Benjamin Kaminski

New Mechanisms of
Optical Harmonic Generation
in Semiconductors

New Mechanisms of
Optical Harmonic Generation
in Semiconductors

Dissertation

presented to the Institute of Physics of the Dortmund Technical University, Germany, in partial fulfilment of the requirements for the degree of Doktor rer. nat.

technische universität
dortmund

presented by

Benjamin Kaminski

Dortmund, September 2009

Accepted by the faculty of the Institute of Physics of the Dortmund Technical University, Germany.

Contents

Motivation

For almost half a century, nonlinear optics has been a highly active field of solid-state physics with important implementations in modern technologies. Within the vast area of nonlinear optics, second and higher harmonics generation, sum and difference frequency generation, and parametric processes play a particularly important role [1, 2]. Harmonic generation is associated with higher order optical susceptibilities, and opens access to the microscopic mechanisms of nonlinear interaction of light with matter and to unique information about the crystallographic, electronic and magnetic structure beyond the limits of linear optics [1, 2, 3].

Second harmonic generation (SHG) has attracted the most vivid interest in fundamental physics because of its exceptional sensitivity symmetry violations in space and time [3]. Another strong point of this phenomenon is its specific sensitivity in the studies of surfaces and interfaces [4, 5]. Various technological applications are based on materials with second order nonlinear susceptibility combined with the possibility to fulfill the phase matching conditions.

In the most general case of multipole approximation, the contributions to the three-photon process of SHG can be written in a matrix form as

$$\left(\begin{array}{c} \mathbf{P}^{2\omega} \\ \mathbf{M}^{2\omega} \\ \mathbf{Q}^{2\omega} \end{array} \right) \propto \left(\begin{array}{ccc} \chi^{eee} & \chi^{eem} & \chi^{emm} \\ \chi^{mee} & \chi^{mem} & \chi^{mmm} \\ \chi^{qee} & \chi^{qem} & \chi^{qmm} \end{array} \right) \left(\begin{array}{c} \mathbf{E}^{\omega}\mathbf{E}^{\omega} \\ \mathbf{E}^{\omega}\mathbf{H}^{\omega} \\ \mathbf{H}^{\omega}\mathbf{H}^{\omega} \end{array} \right), \qquad (1)$$

where $\mathbf{P}^{2\omega}$, $\mathbf{M}^{2\omega}$, and $\mathbf{Q}^{2\omega}$ denote electric polarization, magnetization, and electric-quadrupole polarization, respectively, at the Second Harmonic (SH) frequency; $\mathbf{E}^{\omega}$ and $\mathbf{H}^{\omega}$ are the electric and magnetic fields at the fundamental frequency. Nine nonlinear susceptibilities χ^{lmn} describe various types of coupling of electric dipole (ED),magnetic dipole (MD), and electric quadrupole (EQ) processes for the coherent three-photon SHG processes. They depend on the crystallographic, electronic and magnetic structure, and on the types of nonlinear processes involved in the interaction of light with the medium. The strongest interaction is defined by the electric-dipole (ED) susceptibility χ^{eee} which is only allowed in noncentrosymmetric crystals due to the parity selection rule. Modern technology allows fabrication of controlled artificial structures in which an inversion center is either present or not, which are of high interest for nonlinear optical studies and new applications. In addition, this type of susceptibility can play a dominant contribution in centrosymmetric media at surfaces or interfaces where the inversion symmetry is broken [4, 6, 5, 7, 8, 9, 10]. However, it must be noted that this surface ED contribution is difficult to distinguish from bulk EQ contributions [11].

Most of the fundamental and applied SHG research was devoted to the χ^{eee} ED type of nonlinear susceptibility. It is inherent to piezoelectric and ferroelectric materials which are used in various devices for constructing second, third, and higher order frequency multiplicators, sum and difference frequency generators, optical parametric oscillators, etc. A crucial condition for practical use of these materials is the possibility to fulfill the phase-matching requirements for the fundamental, second, or higher order harmonics, for example, some piezoelectric semiconductors such as GaAs and CdTe with the cubic zinc-blend structure possess high nonlinear ED susceptibilities. However, their cubic structure does not allow phase matching and therefore their efficient use in practical devices. All other susceptibilities χ^{lmn} in Eq. (1) involve various couplings of ED, MD, and EQ processes and, as a rule, are several orders of magnitude smaller, in particular those in which ED processes are not involved. Nevertheless, in centrosymmetric media the SHG susceptibilities involving the electric quadrupole and/or magnetic dipole processes may lead to signals of appreciable magnitude, in particular in the vicinity of electronic resonances. Intuitively, one may expect that EQ processes are more important in centrosymmetric diamagnetic materials, see e.g. [12] and references therein, whereas MD processes are more important in paramagnetic or magnetically ordered materials. However this general rule does not exclude other possibilities. For example, studies of diamagnetic C_{60} fullerene films revealed, on the one hand, the dominant SHG mechanism due to MD coupling at the 689 nm fundamental wavelength [13] and, on the other hand, EQ, EQ and MD coupling at the 1064 fundamental wavelength [14]. Other interesting examples are observations of SHG due to EQ in artificial photonic structures [15], and due to MD resonances in metamaterials [16].

An important trend in the studies of SHG and higher order effects is a search for new mechanisms of nonlinear interaction of light in centrosymmetric and noncentrosymmetric materials induced by phase transitions or external perturbations that break the spatial inversion or time reversal symmetry. Breaking of spatial inversion at the paraelectric-ferroelectric phase transition in $BaTiO_3$ allows ED contributions to SHG which varies with temperature linearly with the order parameter or spontaneous polarization, see e.g. [17]. An ED SHG mechanism may arise at magnetic phase transitions due to particular types of spin ordering, as is the case for crystallographically symmetric Cr_2O_3 [18]. In the very beginning of the studies of induced effects, optical SHG was observed in centrosymmetric calcite $CaCO_3$ as a function of applied dc-electric field [19]. Dc-electric field as a polar vector is the most straightforward and efficient perturbation for inducing a bulk ED contribution to SHG. Another perturbation for inducing ED-SHG may be strain. As an example due to lattice mismatch between a substrate and a thin film grown on it, see e.g. the study of SHG in thin films of magnetic garnets [20, 21]. An ED-SHG was used as an efficient probe for proving enhancement of ferroelectric properties of $BaTiO_3$ films due to biaxial compressive strain [22].

A static magnetic field applied to a medium may induce new contributions to SHG. However, this mechanism is radically different from the action of an electric field or inhomogeneous strain, because the transformation properties of a magnetic field are those of an axial vector. Therefore, it cannot induce ED-SHG and thus, only MD or EQ should be taken into consideration. As noted above, these contributions to SHG are ex-

pected to be much smaller than the ED-SHG. Nevertheless, relatively strong magnetic effects due to spontaneous magnetization and/or magnetic ordering are observed in different ferromagnetic and antiferromagnetic materials. The first magnetization-induced SHG contribution was found in reflection from a ferromagnetic iron surface [23] and then in other materials like silicon as discussed in review papers [3, 24, 25]. In most cases the observed SHG signals could be related to the influence of magnetization on the intrinsic ED-SHG due to inversion symmetry breaking either in the bulk or at the surface of the media.

A large class of semiconductors crystallizing in the zinc-blende (sphalerite), wurtzite, chalcopyrite, and other noncentrosymmetric structures allow for SHG in the electric-dipole approximation. However, nonlinear optical studies of semiconductors using SHG have been, for quite a long time, limited to specific single wavelengths of commercial lasers. Examples of spectroscopic studies of SHG in semiconductors are scarce and mostly limited to narrow spectral ranges [26, 27, 28]. Until recently, not much work has been done in the studies of semiconductors at low temperatures and with high spectral resolution. Cubic semiconductors such as GaAs and CdTe, though possessing high SHG susceptibilities, do not allow phase matching and thus are not of practical importance. On the other hand, striking progress has been made in the development of high optical quality, large size and low absorbing chalcopyrite single crystals of $ZnGeP_2$, $AgGaS_2$ and $CdGeAs_2$. They enable continuous tunable laser sources to be built in wide infrared spectral region [29, 30, 31, 32].

Recently detailed spectroscopic studies of SHG in several groups of semiconductors at low temperatures with high spectral resolution and under applied magnetic fields have been initiated. It was found that the application of a magnetic field in bulk noncentrosymmetric diamagnetic semiconductors GaAs and CdTe, where SHG is allowed in the electric-dipole approximation, induces new optical nonlinearities [33, 34, 35, 36, 37, 38]. They were attributed to Landau-level orbital quantization of the band energy spectrum. In diluted magnetic semiconductors (Cd,Mn)Te the SHG response was found to be induced by the giant spin-splitting of electronic states. Phenomenologically these processes are well described, however, the microscopic understanding is still missing. The involved bands have different parity and thus an excitation by two photon processes should not be possible.

In this work, two novel mechanisms of optical harmonic generation are introduced, whereas the microscopic understanding seems to be given. In the noncentrosymmetric semiconductor ZnO, a material of great interest for application in the UV lasing regime, a second harmonic contribution was found, that is based on the magneto-optical Stark effect. Thereby the magnetic field causes an electric field due to the Lorentz force and enables therefore a mixing of different parity states. Due to this mixing second harmonic processes become allowed even for conduction and valence bands of different parity. This mechanism can not only provide an explanation for ZnO, it might be responsible as well for magnetic field induced SHG in GaAs, CdTe and (Cd,Mn)Te.

The second new type of SHG contribution is found in the centrosymmetric magnetic

semiconductors EuTe and EuSe. These compounds of the group of europium chalco-genides display manifold unique magnetic, electronic and magneto-optical properties, but due to the centrosymmetry of these materials an investigation with SHG seems not to be promising. Nevertheless a novel type of nonlinear optical susceptibility χ^{eem} was found, which is caused by a MD contribution related to spontaneous ferromagnetic or induced paramagnetic magnetization [39]. This new type of spin-induced nonlinear susceptibility can appreciably increase the number of centrosymmetric bulk materials, thin films, and artificial structures accessible to nonlinear optics.

Outline

In Chapter 1 topics of magnetism and symmetry are briefly reviewed and a short introduction to the group theory is given.

Chapter 2 deals with common properties of semiconductors and the investigated material systems: The diamagnetic semiconductor ZnO, the magnetic semiconductors EuSe and EuTe and their crystallographic, electronic and magnetic properties.

Chapter 3 is devoted to nonlinear magneto-optics and gives an introduction to theoretical and phenomenological basics for SHG and THG. Magnetic SHG contributions are briefly reviewed with the main focus given to GaAs, CdTe and (Cd,Mn)Te. The second part of this chapter deals with the experimental setup.

In Chapter 4 a study of nonlinear harmonics generation in the semiconductor ZnO is presented. Crystallographic SHG spectra and magnetic SHG spectra are analyzed in detail and the latter reveal a new contribution based on the magneto-optical Stark effect. The applied external magnetic field interacts via the Lorentz force with the exciton movement and therefore provides a quasi-electric field. This field was the origin of the detected magnetic field contribution being confirmed by temperature dependencies, the polarization dependencies namely rotational anisotropies and theoretical simulations. Moreover, crystallographic third harmonic generation spectra are shown.

Chapter 5 deals with the spin-induced SHG signal in the centrosymmetric magnetic semiconductors EuSe and EuTe. SHG in electric dipole and electric quadrupole approximation is forbidden due to the centrosymmetry of the crystal and the electronic band structure with an odd parity $4f$-$5d$ band gap transition. Nevertheless, a SHG signal in the vicinity of the band gap 2.2-2.4eV of EuTe and EuSe was found. Further magnetic field and temperature investigations reveal that this contribution is induced by a ferromagnetic spin component, which strongly enhances the magnetic-dipole transition. Theoretical and microscopic considerations confirm the origin of the SHG signal. Spin-induced and crystallographic third harmonic generation spectra over broad spectral ranges are displayed as well. This THG signal is of higher magnitude than the SHG signal enhanced by a double resonance of the THG process.

A special feature of nonlinear optics is the polarization dependence, since SHG and THG are typically strongly anisotropic. Therefore, Chapter 6 gives a more detailed

introduction to the theoretical calculation of the rotational anisotropies based on symmetry considerations.

Appendix A is devoted to the used LabView program, its control and the mannerism. The windows for the control of all important devices are shown and explained in detail.

Chapter 1

Magnetism and Symmetry

This chapter gives a review of the magnetism of magnetic disordered and magnetic ordered systems. Symmetry considerations and group theory are helpful tools for analyzing consequences of magnetic structures and will, therefore, be shortly discussed as well. In order to understand and analyze magnetism in matter, quantum-mechanical properties as the spin are needed. A classical point of view is according to the "Bohr van Leuwen-Theorem" not sufficient. If a solid is subject to an external magnetic field, in all materials an internal magnetic field is induced, which is (Lenz's rule) orientated opposite the external field. This behavior is called diamagnetism and is denoted by a negative magnetic susceptibility. However, diamagnetism is only observable if systems possess no other kind of magnetic ordering. Contrary to diamagnetism, solids can have permanent magnetic moments, which order parallel to an external magnetic field and are leading to the so called paramagnetism. The dependence between external magnetic field $\mathbf{H}$ and the magnetization $\mathbf{M}$ is formally described by:

$$\mathbf{M} = \mu_0 \chi_{mag} \mathbf{H}, \tag{1.1}$$

where μ_0 is the permeability of the vacuum and χ_{mag} is the magnetic susceptibility. Ferromagnetism, antiferromagnetism, ferrimagnetism and metamagnetism (see Section 1.2) are different kinds of magnetic order, whose magnetic moments below a certain temperature are aligned parallel or antiparallel to each other. In the following considerations the contributions of the atom core to magnetism are neglected, because they are expected to be of at least one order of magnitude smaller. A magnetic field couples via two different ways to matter, by the minimal-substitution and by the spin [40, 41].

1.1 Disordered magnetic systems

In materials, where the long range order between magnetic moments is missing, in absence of an external magnetic field no magnetic ordering is present. The magnetic moments of these disordered magnetic moments can be aligned by an external magnetic field.
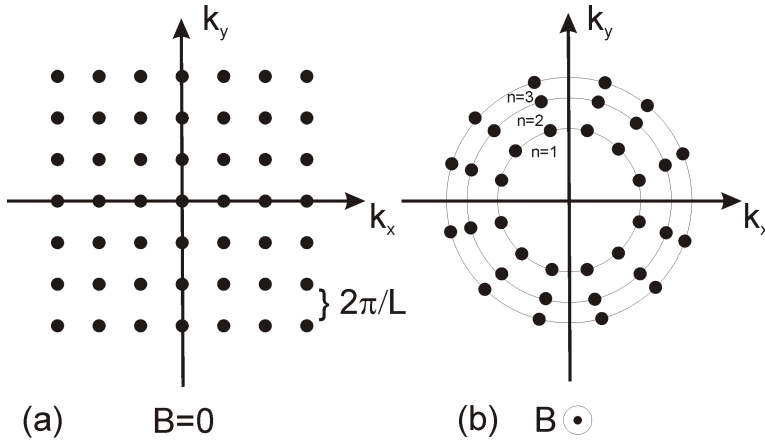
Figure 1.1: *The states of a crystal within the Fermi surface condensate in an external magnetic field on Landau levels. Panel (a) shows the states without and panel (b) with an external magnetic field.*

1.1.1 Diamagnetism

All materials display diamagnetism, but since this kind of magnetism is by far the weakest form of magnetism it can only be observed if no other forms of magnetism and magnetic moments are present. Diamagnetism is induced by the magnetic field itself and not based on permanent magnetic moments as all other forms of magnetism. Therefore, diamagnetism is not sensitive to temperature. In the following, two kinds of diamagnetism are discussed: The Landau-Diamagnetism deals with nearly free electrons and the Larmor-Diamagnetism gives another diamagnetic contribution based on fully-filled shells.

1.1.1.1 Landau-diamagnetism

Since an external magnetic field interacts by means of the Lorentz force with the electron movement, this has to be considered by the minimal substitution of the momentum operator:

$$\mathbf{p} \rightarrow \mathbf{p} + \frac{e}{c}\mathbf{A}(\mathbf{r}) \tag{1.2}$$

with the electron unit charge e, the speed of light in the vacuum c and the magnetic vector potential $\mathbf{A}(\mathbf{r})$. The application of this to N free electrons, an assumption that is e.g. fulfilled for the electrons in the conduction bands of metals, results in the Hamiltonian [42, 41]:

$$\hat{H}_i = \sum_{i=1}^{N} \frac{(\mathbf{p}_i + \frac{e}{c}\mathbf{A}(\mathbf{r}))^2}{2m_e} = \sum_{i=1}^{N} \frac{1}{2m_e}(\mathbf{p}_i^2 + 2\frac{e}{c}\mathbf{p}_i\mathbf{A}(\mathbf{r}_i) + \frac{e^2}{c^2}\mathbf{A}^2(\mathbf{r}_i)), \tag{1.3}$$

where m_e denotes the mass of electrons and the spin and the resulting Zeeman term is neglected. For the case of noninteracting electrons, a homogenous external magnetic B field along the z-axis and the use of the Landau Gauge:

$$rot\mathbf{A} = \mathbf{B} \rightarrow div\mathbf{A} = 0 \rightarrow \mathbf{A} = (0, -Bx, 0).$$

leads to:

$$\hat{H}_i = \frac{p_x^2}{2m_e} + \frac{m_e}{2}\omega_c^2\left(x - \frac{p_y}{m_e\omega_c}\right)^2 + \frac{p_z^2}{2m_e}, \tag{1.4}$$

where the electronic cyclotron frequency $\omega_c = \frac{eB}{mc}$ is used. An approach $\psi(\vec{r}) = C\phi(x)e^{ik_yy}e^{ik_zz}$ for the Schrödinger equation with the Hamiltonian (1.4) results in:

$$\hat{H}_i\psi(\mathbf{r}) = \left(\frac{p_x^2}{2m_e} + \frac{m_e}{2}\omega_c^2\left(x - \frac{\hbar k_y}{m_e\omega_c}\right)^2 + \frac{\hbar^2 k_z^2}{2m_e}\right)C\phi(\tilde{x}) = EC\phi(\tilde{x}), \tag{1.5}$$

thereby the substitution $\tilde{x} = \frac{\hbar c k_y}{eB}$ was used and $\hbar$ denotes the reduced Planck's constant. Equation (1.5) describes a shifted one-dimensional harmonic oscillator with the energy eigenvalues:

$$E_{n,k_y,k_z} = \hbar\omega_c\left(n + \frac{1}{2}\right) + \frac{\hbar^2 k_z^2}{2m_e}, \ \ n = 0, 1, 2\dots. \tag{1.6}$$

The associated eigenfunctions $\phi(\tilde{x})$ are the well known Hermite-polynoms of the harmonic oscillator. The energy values are degenerate with respect to k_y. This degeneracy g for states confined in an area L^2

$$g = \frac{L^2 eB}{\pi\hbar}, \tag{1.7}$$

results, for a noninteracting free electron gas and including the possibility of spin up and down occupation, in the Landau-levels. This corresponds to the quantization of motion of the electrons in the plane perpendicular to the direction of the magnetic field with equidistant discrete energy levels (see Fig. 1.1) and leads to strong variations of the magnetization and the energy values [43]. Calculating the susceptibility with an equation based on statistics and thermodynamics [41]

$$\chi = \frac{\partial\mathbf{M}}{\partial\mathbf{B}}, \tag{1.8}$$

one will see that the Landau-level formation yields a susceptibility $\chi_{dia} < 0$.

1.1.1.2   Larmor-diamagnetism

The previous section dealt with nearly free electrons. Since all orbital angular momenta (operator $\mathbf{L}$), spins (operator $\mathbf{S}$) and also the total angular momentum ($\mathbf{J} = \mathbf{S} + \mathbf{L}$) are compensated in fully-filled ion shells

$$\mathbf{J}|0\rangle = \mathbf{L}|0\rangle = \mathbf{S}|0\rangle = 0$$

($|0\rangle$ denotes the ground state), also these shells give a diamagnetic, but qualitatively different, contribution resulting from the minimal substitution. In order to obtain the Larmor contribution, we use the symmetrical gauge

$$\mathbf{A} = \frac{1}{2}(\mathbf{B} \times \mathbf{r}) = \frac{1}{2}(By, -Bx, 0),$$

with a magnetic field applied in z-direction as well. This results in the Hamiltonian [41, 42]:

$$(\mathbf{p} + \frac{e}{c}\mathbf{A})^2 = \mathbf{p}^2 + \frac{e}{c}(\mathbf{p}\mathbf{A} + \mathbf{A}\mathbf{p}) + \frac{e^2}{c^2}\mathbf{A}^2(\mathbf{r}) = \tag{1.9}$$

$$\mathbf{p}^2 + \frac{eB}{2c}(p_x y + y p_x - p_y x - x p_y) + \frac{e^2 B^2}{4c^2}(x^2 + y^2). \tag{1.10}$$

Thereby is $(p_x y + y p_x - p_y x - x p_y) = -2L_z$, also an orbital angular momentum, which leads to a paramagnetic contribution and is discussed in more detail in Section 1.1.2. However, if we deal initially with fully-filled shells the orbital momentum is zero and this paramagnetic contribution vanishes. Only a diamagnetic part remains:

$$\hat{H}_{dia} = \frac{e^2 B^2}{8 m_e c^2} \sum_{j=1}^{N_e}(x_j^2 + y_j^2) \tag{1.11}$$

with N_e electrons of the atom or ion. In order to analyze the reaction of the system to the external magnetic field, the magnetic moment $\mathbf{m}(B) = \frac{\partial H}{\partial B}$ and then with the assumption of strongly localized electrons the magnetization is calculated by:

$$\mathbf{M}(B) = \frac{N}{V}\langle 0|\mathbf{m}|0\rangle. \tag{1.12}$$

Thereby N is the number of ions in the volume V. Using spherical symmetry $\sum_{j=1}^{N_e}\langle 0|x_j^2|0\rangle = \sum_{j=1}^{N_e}\langle 0|y_j^2|0\rangle = \sum_{j=1}^{N_e}\langle 0|z_j^2|0\rangle = \frac{1}{3}\sum_{j=1}^{N_e}\langle 0|r_j^2|0\rangle$ the expectation value of the magnetization, caused by diamagnetic Larmor term, results in:

$$\mathbf{M}(B) = -\frac{N}{V}\langle 0|\frac{\partial \hat{H}_{dia}}{\partial B}|0\rangle = -\frac{N e^2}{6 m_e c^2 V} B \sum_{j=1}^{N_e}\langle r_j^2\rangle. \tag{1.13}$$

Then the susceptibility in first order perturbation theory for the Temperature T is given by

$$\chi = \mu_0 \left(\frac{\partial M}{\partial B}\right)_T = -\frac{N e^2 \mu_0}{6 m_e c^2 V} \sum_{j=1}^{N_e}\langle r_j^2\rangle. \tag{1.14}$$

Obviously, this susceptibility is negative and results, therefore, in diamagnetism. Diamagnetic susceptibilities are, in contrast to other forms of magnetic order, usually largely temperature independent and typically of the order of magnitude $\chi_{dia} \approx 10^{-6}$ cm^3/Mol. A superconductor is a model of an ideal diamagnet, because the Meissner-Ochsenfeld effect totally shields the external magnetic field; thus, the superconductors has a susceptibility $\chi_{dia}^{SC} = -1$

1.1.2 Paramagnetism

Paramagnetism is a specific characteristic of materials, resulting from the coupling of the external magnetic field to the orbital angular momentum and spins. This requires partially-filled shells or nearly free electrons in the conduction band of metals.
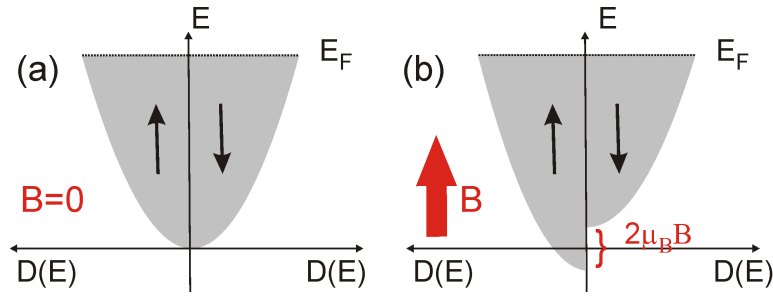
Figure 1.2: *Pauli paramagnetism: Density of states (a) without magnetic field and (b) with magnetic field. The splitting of the sub-bands with magnetic moments parallel and antiparallel to the magnetic field direction leads to a majority of electrons with spins parallel to the direction of the magnetic field.*

Contrary to the induction effect of diamagnetism, paramagnetic materials possess permanent magnetic moments reacting to the applied magnetic field, and have a positive susceptibility χ_{para}.

1.1.2.1 Pauli-paramagnetism

Pauli-spin paramagnetism results from the spins of the band electrons. Following the Dirac theory, with each spin is a magnetic moment connected:

$$\boldsymbol{\mu}_s = -g_e \frac{\mu_B}{\hbar} \mathbf{S}. \tag{1.15}$$

Thereby $\mu_B = \frac{e\hbar}{2m}$ is the Bohr's magneton and g denotes the g-Factor, which is $g = 2$ for free electrons. A homogenous external magnetic field $\mathbf{B} = B_0 \mathbf{e}_z$ interacts with the internal magnetic moments described by the Hamiltonian:

$$\hat{H}_m = -\sum_{i=1}^{N} \mu_s^{(i)} B_0 = g_e \frac{\mu_B}{\hbar} B_0 \sum_{i=1}^{N} S_i^z. \tag{1.16}$$

In the second quantization, the consequences are more obvious:

$$\hat{H} = \sum_{\mathbf{K},\sigma} \epsilon \left(k + z_\sigma \mu_0 B_0 \right) a_{\mathbf{K},\sigma}^+ a_{\mathbf{K},\sigma}, \tag{1.17}$$

thereby are $z_\uparrow = +1$, $z_\downarrow = -1$. Operators $a_{\mathbf{K},\sigma}$ and $a_{\mathbf{K},\sigma}^+$ are named annihilator and creator, according to their ability to decrease or to increase the occupation of an eigenstate by 1. The energy of electrons, with magnetic moments aligned parallel to the external field, is decreased by $\mu_B B_0$ and for electrons with antiparallel alignment, the energy is increased.

At zero magnetic field, all magnetic moments are statistically distributed and no magnetization is expected. But in an external magnetic field, the electrons try to orientate their magnetic moments in order to lower the internal energy $E = \langle H \rangle$. However, this

effort is hindered by the entropy S. Finally, the system remains for a given temperature T in the equilibrium state that minimizes the free energy F [41]:

$$F = E - TS. \tag{1.18}$$

Due to Eq. (1.18) and

$$\chi = \frac{1}{V}\left(\frac{\partial m}{\partial H}\right) = \left(\frac{\partial M}{\partial H}\right),$$

a positive and strongly temperature dependent susceptibility is expected. However, because of the Pauli-principle not all electrons are able to change their energy. Only electrons that are not more than $\mu_B B$ away from the Fermi-level E_F are accessible by the magnetic field.

The electronic density of energy states $D(E) \propto \sqrt{E}$ (see Fig. 1.2) gives at zero magnetic field an energy parabola $E \propto D(E)^2$. Due to different shifts of the energy of electrons with magnetic moments orientated parallel or antiparallel to the direction of the external magnetic field, one spin direction becomes preferential. A distinction between the sub bands, which are split by $2\mu_B B$, is necessary. In the case of $2\mu_B B \ll E_F$, the macroscopic magnetization can be calculated by

$$M = \frac{\mu_B}{V}(N_\downarrow - N_\uparrow) = -\frac{\mu_B^2}{V}B_0\int_0^\infty dy \frac{\partial f}{\partial y}D(y), \tag{1.19}$$

where $f(E) = 1/[exp(\beta(E-\mu))+1]$ is the Fermi-Dirac distribution, taking into account the Pauli-principle. The chemical potential $\mu(T) = E_F(1 - O(T^2))$ influences the density of states $D(E, \mu(T))$ and leads to a weak temperature dependence. At high temperatures, the Fermi statistics passes into the Boltzmann statistics.
The Pauli susceptibility is then given by

$$\chi_{para}(T) = \frac{3}{2}\frac{N}{V}\mu_0\frac{\mu_B^2}{E_F}\left[1 - \frac{\pi^2}{12}\left(\frac{k_B T}{E_F}\right)^2\right], \tag{1.20}$$

where k_B is the Boltzmann constant. For $E_F \gg k_B T$ $\chi_P(0)$ is a good approximation for the susceptibility:

$$\chi_{para}(0) = \chi_{para}(T) = \frac{3}{2}\frac{N}{V}\mu_0\frac{\mu_B^2}{E_F} = -3\chi_{Landau}.$$

1.1.2.2   Langevin-paramagnetism

In a solid, the electrons occupy the orbitals following Hund's rule and the Pauli principle. Since in full orbitals angular momentum and spins compensate, only unpaired electrons of partially filled shells lead to magnetic moments. Due to the spatial distribution of electrons in the orbitals, the spins and electrons can obviously be considered as localized and are not freely propagating (as in conduction bands of metals) through the crystal [44, 45, 46, 47]. This Langevin-paramagnetism of localized magnetic moments is found in materials with partially filled valence bands. Electrons in the valence

shell have the total angular momentum $\mathbf{J}$, composed of the angular momentum $\mathbf{L}$ and the spin $\mathbf{S}$ [42, 48]:

$$\mathbf{J} = \mathbf{L} + \mathbf{S}.$$

With this total angular momentum a magnetic moment is associated:

$$\boldsymbol{\mu}_s = -g_j \mu_B \mathbf{J}. \tag{1.21}$$

and the interaction of the free magnetic moments is neglected. The Landé factor g is calculated by

$$g_j = 1 + \frac{J(J+1) + S(S+1) - L(L+1)}{2J(J+1)}.$$

The macroscopic average of the magnetic moments vanishes due to the statistical distribution without an external magnetic field; thus, time-inversion symmetry remains a symmetry of the system. The application of a magnetic field induces an alignment of the localized magnetic moments along the field direction following the condition Eq. (1.18) in order to minimize the free energy. Therefore, the application of a magnetic field leads to a breaking of symmetry. The Hamiltonian describing the interaction of N particles with the magnetic field is called Zeeman Term:

$$\hat{H} = -\sum_i^N \boldsymbol{\mu}_i \cdot \mathbf{B} = \frac{1}{\hbar} g\mu_B \sum_{i=1}^N \mathbf{J}_i \mathbf{B}. \tag{1.22}$$

Since the scalar product

$$\mathbf{J}_i \cdot \mathbf{B} = \hbar m_i B$$

has the eigenvalues $m_i = -J, -J+1, ..., +J$, one obtains a total number of $(2J+1)^N$ eigenstates. The magnetization can be calculated by the differential of the free energy F:

$$M = -\frac{\partial F}{\partial B} = N g_j \mu_B J B_J \left(\frac{g\mu_B JB}{k_B T} \right), \tag{1.23}$$

where B_J denotes the Brillouin-function

$$B_J(x) = \frac{2J+1}{2J} \coth\left(\frac{2J+1}{2J} x \right) - \frac{1}{2J} \coth\left(\frac{x}{2J} \right)$$

with $x = g_j \mu_B \beta J B$. For high magnetic fields or very low temperatures the magnetization reaches a saturation value $M_0 = N g \mu_B J$. For small fields or high temperatures leading to small x-values, the susceptibility follows the classical Curie-law:

$$\chi = \mu_0 \left(\frac{\partial M}{\partial B} \right)_T = \frac{C}{T} \tag{1.24}$$

with the Curie-constant $C = \frac{N}{V}(g\mu_B)^2 \mu_0 \frac{J(J+1)}{3k_B}$. In order to take into account the spin-orbit interaction, the following Hamiltonian has to be added:

$$\hat{H}_{so} = \frac{\mu_B^2}{e} \frac{1}{r} \frac{dV}{dr} \mathbf{L} \cdot \mathbf{S}.$$

Depending on the strength of the spin orbit coupling, two different cases have to be distinguished: In the case of strong spin-orbit coupling and weak external magnetic fields, the Langevin-paramagnetism is a good approximation, since $[\hat{H}, \mathbf{J}^2] = 0$ and $[\hat{H}, \mathbf{J}_z] = 0$ are valid. This leads to the so called annormal Zeeman splitting of the states with the energy E_{nlj}^0:

$$E_{nlj}^0 + g_j m_j \mu_B B. \tag{1.25}$$

In the case of weak spin-orbit coupling or strong external magnetic fields, the total angular momentum is not a "good" quantum number and

$$E_{nlm_lm_s} = E_{nl}^0 + (m_l + 2m_s)\mu_B B \tag{1.26}$$

has to be used (Paschen-Back effect).

A further kind of paramagnetism exists for $J = 0$. This Van-Vleck-paramagnetism does not depend on the temperature and is induced by excited states. Since the Van-Vleck paramagnetism is weak compared to the above discussed paramagnetic contributions for $J \neq 0$, it will not be considered here.

Typically, the paramagnetic susceptibility is of the order of magnitude of $10^{-6} < \chi < 10^{-3}$ and therefore, the paramagnetic contribution is significantly stronger than the diamagnetic one. Taking into account the discussed diamagnetic and paramagnetic effects, the Hamiltonian has to be written in the following form [40]:

$$\hat{H} = \underbrace{\frac{(\mathbf{p} + \frac{e}{c}\mathbf{A})^2}{2m_e}}_{Diamagnetic\ coupling} - \underbrace{\frac{e}{m_e c}\mathbf{S} \cdot \mathbf{B}}_{Zeeman\ term} + \underbrace{\frac{e\hbar}{2m_e^2 c^2}\frac{dV}{dr}\frac{1}{r}\mathbf{L} \cdot \mathbf{S}}_{Spin-orbit\ coupling} + V(\mathbf{r}). \tag{1.27}$$

1.2 Ordered magnetic systems

In contrast to materials displaying dia- and/or paramagnetic response to an external magnetic field, in the following sections magnetic systems are discussed, which display a spontaneous magnetic ordering below certain temperatures T_N or T_C without any magnetic field applied. This kind of magnetism requires a long range interaction, leading to a collective alignment of magnetic moments. Since time-inversion causes a reversal of spins, the time-inversion symmetry in such systems is broken. Above T_N or T_C, the magnetic ordering vanishes and therefore, crystallographic and magnetic symmetry are the same again for the para- and/or diamagnetic state.

1.2.1 Exchange interactions and Heisenberg model

The long range ordering is caused by an exchange mechanism, based on the Pauli principle and electromagnetic Coulomb interaction leading to an internal molecular field [49]. Due to the Pauli principle antisymmetric wave functions are essential. Therefore, singlet as well as triplet states have to be considered. The energy difference between

these states for two electrons with spatial coordinates, $\mathbf{r}_1$ and $\mathbf{r}_2$, and wave functions, $\psi_a(\mathbf{r}_1)$ and $\psi_b(\mathbf{r}_2)$, is defined as exchange constant or exchange integral J

$$J = \frac{E_S - E_T}{2} = \int \psi_a^*(\mathbf{r}_1)\psi_b^*(\mathbf{r}_2)\hat{H}\psi_a(\mathbf{r}_2)\psi_b(\mathbf{r}_1)$$

with the effective Hamiltonian of the system $\hat{H}$. Hence, the spin dependent part of the Hamiltonian can be written as

$$\hat{H}_{spin} = -2J\mathbf{S}_1\mathbf{S}_2.$$

If $J > 0$ also $E_S > E_T$, the spin triplet is favored and vice versa. The complicated generalization to a many body system with the assumption that above interaction probably exists between all neighbors motivates the Hamiltonian in the Heisenberg model [50]:

$$\hat{H}_{Exchange} = -2\sum_{i\neq j} J_{ij}\mathbf{S}_i \cdot \mathbf{S}_j + g\mu_B \sum_i \mathbf{B}\mathbf{S}_i, \tag{1.28}$$

where J_{ij} is the exchange integral between the spin at position $\mathbf{r}_i$ and the spin at position $\mathbf{r}_j$. J_{ij} displays the overlap of the wave functions of two spins located at the lattice sites i and j. For $J > 0$ a ferromagnetic ordering is preferential and J is called ferromagnetic coupling parameter, for $J < 0$ the antiferromagnetic one is favored and J is named antiferromagnetic coupling parameter. The latter term of Eq. (1.28) is the Zeeman term.

If electrons of neighboring magnetic atoms interact via an exchange interaction without the need of an intermediary, this is known as direct exchange. Very often direct exchange could not be revealed as main mechanism responsible for magnetic properties, because there is insufficient overlap between neighboring magnetic orbitals. This is the case for rare earth compounds (see section EuX), where $4f$ electrons are strongly localized and are very close to the nucleus, with little probability density extending significantly further than about a tenth of the interatomic spacing [51]. These indirect exchange mechanisms, important for materials investigated in this work, are discussed in section 2.3.3

1.2.2   Ferromagnetism

As mentioned above, ferromagnetism can be described by the Heisenberg model with a positive exchange integral $J_{ij} > 0$ [50]. Below a certain temperature T_C, namely the Curie-temperature, this positive exchange integral causes a spontaneous magnetization, even in the absence of an applied magnetic field. All the magnetic moments in a region called domain (see section 1.2.6) align along a single unique direction, which above T_C have compensated mutually in statistical average. Since the order of phase-transitions is classified due to the order of lowest differential of the free energy, which shows a discontinuity at the transition, we have to deal with a second order phase transition (no latent heat) with the order parameter magnetization [41]. With rising temperature the order parameter decreases and vanishes at T_C. Above the phase transition at T_C,
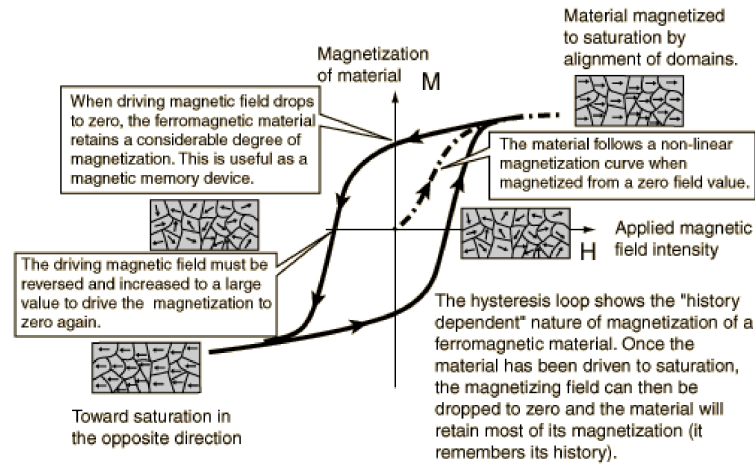
Figure 1.3: *Hysteresis: The magnetization versus the external magnetic field for a ferromagnet according to [52]*

paramagnetism is present and due to the thermal energy above T_C no ordering of the magnetic moments is possible. Therefore, an external magnetic field is necessary to cause a magnetization for $T > T_C$. The positive magnetic susceptibility is of the order of magnitude of 10^2-10^6. For $T > T_C$, the temperature dependence of the magnetic susceptibility is given by the Curie-Weiss law

$$\chi = \frac{C}{T - T_C}.$$
(1.29)

The susceptibility diverges at T_C. A significant feature of ferromagnets below T_C is the so called hysteresis showing the dependence of the magnetization on the magnetic field strength.

Fig. 1.3 shows a hysteresis: With increasing magnetic field strength, the domains, called "Weiss'sche Bezirke" in the case of an ideal ferromagnet, start to align in the external magnetic field direction [49]. The domain walls of different orientated regions are also shifted by the external field. If all moments and domains are orientated, the magnetization saturates asymptotically(M_S). After reducing the magnetic field strength to zero, the magnetization M_r remains. This rest magnetization vanishes at the reverse coercive field strength $-H_C$ or for $T > T_C$.

1.2.3 Antiferromagnetism

Antiferromagnetism is described by a negative exchange integral $J_{ij} < 0$. In antiferromagnetic materials the magnetic moments of the sublattices compensate each other fully within the unit cell ↑↓. Therefore, in opposition to other forms of magnetic ordering, like ferromagnetism or ferrimagnetism, the macroscopic magnetization vanishes and hence antiferromagnetism was predicted first by Néel in 1932 [53] and demonstrated by Bizette, Squire and Tsai in 1938 [54]. Above the Néel temperature T_N,

the paramagnetic phase is present and the temperature dependence of the magnetic susceptibility in this paramagnetic phase is given by

$$\chi = \frac{C}{T + T_N}, \tag{1.30}$$

where C and T_N, the paramagnetic Néel temperature, are material-specific constants. At T_N, a phase transition of second order takes place and the spins are antiferromagnetically aligned. Since the macroscopic magnetization vanishes, the order parameter has to be defined as linear combination of the magnetization of opposite aligned sublattices. For example, the stagged magnetization $M_+ - M_-$ can be used, where $M_\pm$ denote the magnetizations of the different sublattices. In contrast to the magnetization in ferri- and ferromagnetic materials, the antiferromagnetic order parameter is no real physical property [55, 56, 57, 58]. Another complication in antiferromagnetic materials is the large number of possibilities to arrange an equal number of up and down spins on a lattice. In antiferromagnetic EuTe, nearest neighbors are coupled ferromagnetic and next nearest antiferromagnetic. This results in antiferromagnetic coupling of planes in which magnetic moments are aligned parallel; in literature this [↑↓] arrangement is often named AFM type I. EuSe shows this AFM type I phase and moreover, for a different temperature an AFM II type phase [↑↑↓↓] is present.
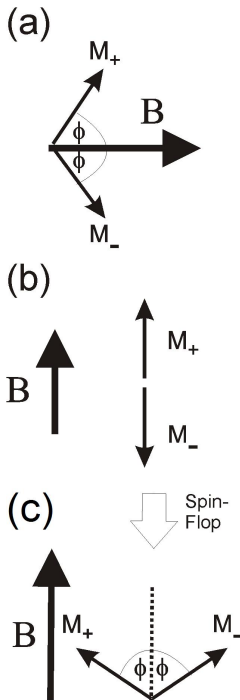
The reaction of an antiferromagnet to an applied external magnetic field at temperatures below T_N is more complicated than for the case of a ferromagnet below T_C [51]. Since there is no energy advantage provided by an orientation of magnetic moments along the applied magnetic field, the direction in which this field is applied is crucial. If a small magnetic field is applied parallel to the magnetization direction of one of the sublattices, only a small term is added or subtracted to the local field of these sublattices depending on their orientation. But both sublattices are saturated and therefore, this external magnetic field has no effect on the magnetization (b). The application of a field perpendicular to the magnetic moments leads to a small tilt of the magnetic moments of both sublattices in field direction and results in a magnetization component in the magnetic field direction (a). Increasing the temperature, but still kept below T_N, decreases, nevertheless,the molecular field of each sublattice. Since one magnetization direction in the case of an external magnetic field applied parallel to the magnetization is energetically favored, this temperature increase effects the net magnetization strongly. For the case of a perpendicularly oriented magnetic field, the magnetization is not influenced by the temperature because the magnetization of both sublattices is affected symmetrically by the magnetic field. Neglecting the thermal fluctuations, the response of the system to a further increase of the external magnetic field depends again on the direction of the applied magnetic field relative to magnetization of the sublattices. In the case of a perpendicular alignment, the magnetic moments are bend more and more over,

resulting in a parallel also ferromagnetic alignment of spins. When the magnetic field is applied parallel to the magnetization, at small fields the moments do not rotate. However, if a critical field is reached the spins suddenly flip into a perpendicular configuration and start to tilt with increasing field as well, leading finally to parallel alignment. This flip is called spin-flop transition(c).

Due to the vanishing macroscopic magnetization, technical applications for antiferromagnets were not given for a long time, but this has changed drastically. An important example is data storage using the exchange bias effect, which is based on directional coupling between the spins in an antiferromagnet and those in an adjacent ferromagnet. Even by means of the vanishing macroscopic magnetization, antiferromagnetic materials enable fast spin manipulation [59, 60]

1.2.4 Ferrimagnetism

Contrary to antiferromagnetism, the sublattices in ferrimagnetic materials are not equal because of crystallographic reasons. Therefore, the magnetization of oppositely orientated sublattices will not cancel out fully and a net magnetization remains. For different ions or different magnetic moments A and B, one can define in each case a Curie constant C_A and C_B in order to obtain the Curie temperature[61]:

$$T_C = \mu(C_A C_B) \tag{1.31}$$

The susceptibility for $T > T_C$ is

$$\chi = \frac{M_A + M_B}{-\mu M_B} = \frac{(C_A + C_B)T - 2\mu C_A C_B}{T^2 - T_C^2}.$$

The exchange integral between spins of the same sublattice is positive, whereas the exchange integral between spins of opposite sublattices is negative. Similar to ferromagnets, in ferrimagnets the formation of domains can be responsible for a net magnetization and the order parameter for the phase transition is the magnetization. In contrast to ferromagnetism, the magnetization of the different sublattices usually shows a different temperature dependence and thus, the macroscopic magnetization within the domains might vanish at a compensation temperature [61].

1.2.5 Metamagnetism

If a material shows a phase-transition from an antiferromagnetic phase to a ferromagnetic one for $H_{applied} > H_c$ and/or $T > T_t$, this is called metamagnetism, where H_c and T_t refer to the critical magnetic field and transition temperature, respectively. Ferromagnetic and antiferromagnetic coupling are both present in the material and the external field or the temperature controls the present phase. In EuSe, the coupling parameters J_1 and J_2 are found to be of comparable magnitude and so this material reveals manifold magnetic-phases, depending sensitively on the applied magnetic field and the temperature.

1.2.6 Domains

Weiss [49] proposed first that a ferromagnet contains a number of small regions called domains, in which spontaneous magnetization is saturated below T_C. However, the direction of the magnetization of different domains needs not to be parallel and therefore ferromagnetic materials can, nevertheless, show no macroscopic magnetization. The domains can cancel each other out and result, thus, in a vanishing macroscopic magnetization. Antiferromagnetic domains, postulated by [62], can be distinguished due to the antiferromagnetic order parameter. Barkhausen [63], Hondo and Kaya [64] proofed the existence of ferromagnetic domains experimentally and the existence of antiferromagnetic domains was demonstrated by Slack [65] and Roth [66]. Between adjacent domains, there is a boundary called domain wall. Although it costs energy to form these domains walls, a formation of domains saves energy associated with dipolar fields [67, 68]. The domain structure, which minimizes the free enthalpy G, is formed.

1.3 Symmetry and group theory

According to the Neumann principle, all physical properties are subject to the symmetry of the system. A physical system is quantum mechanically fully described by the solution of the Schrödinger equation, which in real systems can not be obtained, hindered by the manifold interactions. Symmetry considerations and whose mathematical instrument, the group theory, enable exclusions of solutions and physical properties, being not compatible with symmetry properties of the system [69, 70, 71].

1.3.1 Symmetry groups

In homogenous media, like the vacuum, every movement obeys the conservation of momentum and every rotation follows the conservation of angular momentum. In a crystal the situation is different. Due to internal interactions and the periodical structure, both laws of conservation are not any longer fulfilled [72]. Therefore, the symmetry of the vacuum and the crystal are obviously different. The vacuum is homogenous and isotropic in space and homogenous in time. Thus, the system is invariant for different symmetry operations, in exactly, one object before a symmetry operation and after this operation are not distinguishable. The following symmetry operations are defined:

- $SO(4)$ rotations

- $T_{4\infty}$ translations

- $\hat{I}$ space inversion

- $\hat{T}$ time reversal

- $\hat{C}$ charge reversal

Thereby point groups and space groups are distinguished [73]. Point groups consider only symmetry operations which leave one point fixed. Such symmetry operations are the spatial rotations $SO(3)$, the spatial inversion $\hat{I}$ as well as a combination of both. Space groups include nontrivial spatial translations $T_{3\infty}$ additionally, whereas these translations cannot be described by a linear combination of the lattice vectors.

In matter or electromagnetic fields the symmetry is reduced and not all operations are any longer valid. The residual symmetry operations are called a sub-group of the symmetry group of the vacuum. Since charge reversal $\hat{C}$ is always fulfilled in crystals and the dimension of the unit cell is negligible compared to the optical wavelength, the macroscopic properties are invariant with respect to nontrivial translations and considerations can be mostly reduced to relevant point group symmetry operations [74]:

$$SO(3) \otimes \hat{I} \otimes \hat{T}$$

Only the rotations of the group $SO(3)$ have to be considered for centrosymmetric, nonmagnetic crystals. The rotations and corresponding symmetries are combined in the so called 11 Laue-groups.

Since according to the Noether theorem physical properties have to be invariant for coordinate transformations, tensors χ describing such physical properties must transform for application of elements $\hat{\sigma}$ of the Laue-group $\hat{R}_0$ according to:

$$\chi_{ijk...n} = \sigma_{ii'}\sigma_{jj'}\sigma_{kk'}...\sigma_{nn'}\chi_{i'j'k'...n'}$$

Taking into account the space inversion $\hat{I}$, a parity operation with the eigenvalues ± 1, yields a classification of 32 crystallographic point groups (with translations 230 space groups), showing special transformation characteristics:

- 11 groups of crystals, being invariant under rotations of Laue-groups in combination with space inversion.

- 11 groups, for that only elements of the Laue-group are symmetry operations.

- 10 groups, where inversions only in combination with a few elements of the Laue-group are symmetry operations.

Moreover, the inclusion of the time-reversal operation to these considerations leads to further symmetry groups enabling the description of magnetic materials. The application of the time-reversal operation to a system turns over the spins and thus, the magnetic field itself. Therefore, the crystallographic symmetry is broken and one has to distinguish 122 magnetic point groups (Shubnikov groups [75])M:

- 32 grey groups; every symmetry operation of the cyrstallographic point group is also in combination with time reversal $\hat{T}$ symmetry operation. This group is used to describe para- and diamagnetic materials.

- 32 colorless groups; symmetry according to $\hat{T}$ is definitely broken. These groups allow the description of ferro-, ferri- and antiferromagnetic compounds.

- 58 black-white groups; $\hat{T}$ is only with parts of the crystallographic point group still a symmetry operation.These groups are also used for the description of ferro-, ferri- and antiferromagnetic materials.

Taking the nontrivial translations additionally into account, 1651 magnetic space groups have to be considered. For detailed description of these classifications, see Refs. [76, 77, 78]. In solid state physics the symmetry operations in the majority of cases are given in the Schönflies-notation:

- C_n: uniaxial cyclic rotations, with n=1,2,3,4,6 and $C_n = \frac{2\pi}{n}$

- D_n: C_n additionally twofold axes perpendicular to the main axis

- C_{nh}: C_n additionally σ_h (reflection at a plane parallel to the main axis)

- D_{nh}: D_n additionally σ_h

- C_{nv}: D_n additionally σ_v (reflection at a plane perpendicular to the main axis)

- D_{nd}: D_n additionally σ_d (reflection at a plane diagonal to the main axis)

- T, T_h, T_d, O, O_h cubic groups

1.3.2   Representations of groups

Symmetry operations like rotations, inversion, etc. can be expressed mathematically by matrices. Therefore, several representations Γ_i of a group are possible, linked by matrix multiplications [77, 61]:

$$\Gamma_\beta = X^{-1}\Gamma_\alpha X. \tag{1.32}$$

One can distinguish reducible and irreducible representations. For an irreducible representation, a matrix X can be found for Eq. (1.32), resulting in a diagonal matrix. Different irreducible representations of a group are orthogonal to each other:

$$\sum_{X_i} (\Gamma_\alpha(x_i))_{kp} (\Gamma_\beta(x_i))_{ql} = \frac{g}{n} \delta_{\alpha\beta} \delta_{kl} \delta_{pq}$$

with the order of the group g (number of elements), $\delta_{\alpha\beta}$ Dirac's delta function and the dimension of the matrix n. The character $\chi(X_i)$ of a representation is defined by:

$$\chi(X_i) = Tr\ \Gamma_\alpha(X_i) = \sum_j (\Gamma_\alpha(X_i))_{jj}.$$

For all equivalent representations of a group, the traces (character) are equal. A common representation of a group contains the irreducible representation in the following manner:

$$\Gamma = \sum_{i=1}^n p_\alpha \Gamma_\alpha.$$

Thereby the projection p is $p_\alpha = \sum_{X_i} \chi(X_i)\chi_\alpha^*(X_i)$. The direct product of two representations is defined as

$$\Gamma_\alpha(X_i) \otimes \Gamma_\beta(X_i) = \begin{pmatrix} (\Gamma_\alpha(X_i))_{11}(\Gamma_\beta) & . & . & . & (\Gamma_\alpha(X_i))_{1n_\alpha}(\Gamma_\beta) \\ & . & & & . \\ & . & & & . \\ & . & & & . \\ (\Gamma_\alpha(X_i))_{n_\alpha 1}(\Gamma_\beta) & . & . & . & (\Gamma_\alpha(X_i))_{n_\alpha n_\alpha}(\Gamma_\beta) \end{pmatrix} \qquad (1.33)$$

or shorter written as

$$\Gamma_\alpha \otimes \Gamma_\beta = \sum g_{\alpha\beta\gamma}\Gamma_\gamma \qquad (1.34)$$

with

$$g_{\alpha\beta\gamma} = \frac{1}{g}\sum_{X_i} \chi_\alpha(X_i)\chi_\beta(X_i)\chi_\gamma^*(X_i).$$

The multiplication of commonly used representations is listed in multiplication tables [77]. For a physical system with the Hamiltonian $\hat{H}$, all symmetry transformations form a group of $\hat{H}$. If one considers a symmetry transformation X_i and the associated operator $\hat{\sigma}(X_i)$, then the Hamiltonian $\hat{H}$ and $\hat{\sigma}(X_i)$ have a common set of eigenfunctions, when the commutator $[\hat{H}, \hat{\sigma}(X_i)] = 0$. The application of $\hat{H}$ to the state ψ_{nj}

$$\hat{H}\psi_{nj} = E_n\psi_{nj}, \qquad (1.35)$$

results in eigen-energies with j=1...l, thus with l-fold degeneracy of E_n. Therefore, this leads, due to the vanishing commutator, to

$$\hat{H}\hat{\sigma}(X_i)\psi_{nj} = \hat{\sigma}(X_i)\hat{H}\psi_{nj} = \hat{\sigma}(X_i)E_n\psi_{nj}.$$

Thus, for the application of $\hat{\sigma}(X_i)$ can be written:

$$\hat{\sigma}(X_i)\psi_{nj} = \sum_{k=1}^{l} (\Gamma_\alpha(X_i))_{jk}\psi_{nk}$$

If the matrix $(\Gamma_\alpha(X_i))_{jk}$ has to be determined, one will set the symmetry-transformations X_i fixed and vary j or i, respectively, to obtain a set of matrices. Hence follows, that the matrix is sufficient to estimate a degeneracy of the energy. If the matrix is reducible a degeneracy of energy is given, for irreducible matrices no degeneracy will be found. Therefore, symmetries Γ_α can be assigned to the energy eigenvalues E_n resulting from the eigenfunctions. Considering a semiconductor, then the reaction of the semiconductor to a light field is calculated by Fermi's golden rule consisting of the matrix element $\langle F|\hat{H}_{int}|I\rangle$, which describes the transition probability from the state I to the state F. With above done group theoretical discussions, one has the possibility to estimate, whether this matrix element vanishes and a degeneracy is expected.

$$\langle F|\hat{H}_{int}|I\rangle$$

- $\neq 0$, if

    - the product $\Gamma_I \otimes \Gamma_{Int}$ contains Γ_F
    - $\Gamma_I \times \Gamma_{Int} \otimes \Gamma_F = \Gamma_1$

- $= 0$ otherwise

However, predictions of quantitative values can not be obtained.

Orbitals in crystals show properties of the free atomic orbitals as well. Thus, the symmetries of the electronic states $\psi_{n,s} = \psi_n \chi_s$ (χ_s wave function of spin) can be calculated as direct product of the symmetry of the atomic wave functions and the wave function of the spins.

$$\Gamma = \underbrace{\Gamma_\alpha}_{\psi_n} \otimes \underbrace{\Gamma_{\frac{1}{2}}}_{Spin} = \sum_\beta \Gamma_\beta$$

Chapter 2

Diamagnetic and Magnetic Semiconductors

In this section relevant properties of semiconductors are presented. First, the electronic band structure in view of effective mass considerations is analyzed. Then, the diamagnetic semiconductor ZnO and the quasi particle, the exciton is discussed. Consequences of the application of an external magnetic field and interactions of these excitons with a light wave leading to a polariton are argued as well. The second part deals with magnetic semiconductors, the europium chalcogenides, their crystallographic, electronic and magnetic structure. Finally, mechanisms resulting in the long range ordering are considered. Already in 1913, Nils Bohr claimed for his atom model that the electron orbits around the atom core are discrete energy states. This was established in more detail in the early years of quantum mechanics. If atoms couple to form matter, these discrete states of different atoms overlap and shape energy bands. The energetically highest filled band is called valence band; the lowest empty band is called conduction band.

2.1 Band structure and effective mass

Based on the conductivity, isolators, semiconductors, and metals can be distinguished [40]. The bands of isolators are completely filled or empty, whereas the energy distance, namely band gap E_G, between the valence band and conduction band is large ($E_G > 4$ eV). Therefore, thermal excitations of electrons from the valence- to the conduction band are not possible. Due to the Pauli principle, completely filled or empty bands do not contribute to the conductivity. Thus, for isolators a high resistance R of $R > 10^{14} \Omega$cm is found. However, metals possess partly filled bands resulting in a high number of electrons, which contribute to the conductivity. Therefore, one obtains a very low resistance of $R << 10^{-2}$ Ωcm. In semiconductors, the bands are fully filled or empty for $T = 0$ as for isolators. However, the energy gap is only in the order of a few eV and therefore, thermal excitations of electrons from the valence to the conduction band become possible for temperatures $T \neq 0$. Thus, the resistance $10^{-2} \Omega$cm $< R < 10^9 \Omega$

cm depends strongly on the temperature. The band gap follows

$$\Delta E_G = \frac{-\alpha T^2}{T_0 + T},$$ (2.1)

where ΔE_G is the change of the energy gap depending on the temperature T with the effective temperature T_0 and a constant α. In semiconductors an optical excitation of electrons from the valence to the conduction band is possible. Thereby one can distinguish direct or indirect band gaps of semiconductors. A direct band gap exists if an excitation with a photon $\hbar\omega = E_G$ is feasible and thus, the minimum of the conduction band and the maximum of the valence band are located at the same values of the wave vector k. Otherwise, an indirect band gap is present and only phonon assisted excitations are possible, since the small photon momenta are not sufficient to fulfill the momenta conservation law.

In order to calculate the band structure in a crystal, a lot of interactions have to be taken into account. It was shown, that electrons near the Γ-point behave as free particles with a different mass, providing a good approximation of the band structure. In vicinity of the Γ-point the effective mass m^* can be determined by the slope of the parabolically approximated bands by:

$$\left(\frac{1}{m^*}\right)_{\mu\nu} = \frac{1}{\hbar^2}\frac{d^2E(k)}{dk_\mu dk_\nu},$$

where μ and ν denote cartesian coordinates. The value of the effective mass can differ drastically from the value of free electrons. Negative values are used for the description of holes.

2.2 Diamagnetic semiconductors: ZnO

The importance of the semiconductor ZnO becomes obvious if one has a look at its consumption: Yearly many hundred tons of ZnO are used worldwide [79]. The applications of this material are manifold. ZnO supports as additive the vulcanization process, improves the water-persistency, and handling duration of cement. Moreover, ZnO is applicable as UV-blocker in sunscreen, as dietary supplement and a lot of more. Next to this daily applications, physical interest is based on semiconductor applications for transparent layers in blue light emitter diodes(LED), varistor, solar cells, and TFT-monitors. In the following section, some physical properties of this important material are reviewed that are of relevance for this work and the consequences of the application of an external magnetic field to excitons are discussed.

2.2.1 Crystallographic structure

The II-VI semiconductor ZnO crystallizes with great preference in the wurtzite-type structure (Fig. 2.1). This structure consists of mutual alternating double layers of Zn
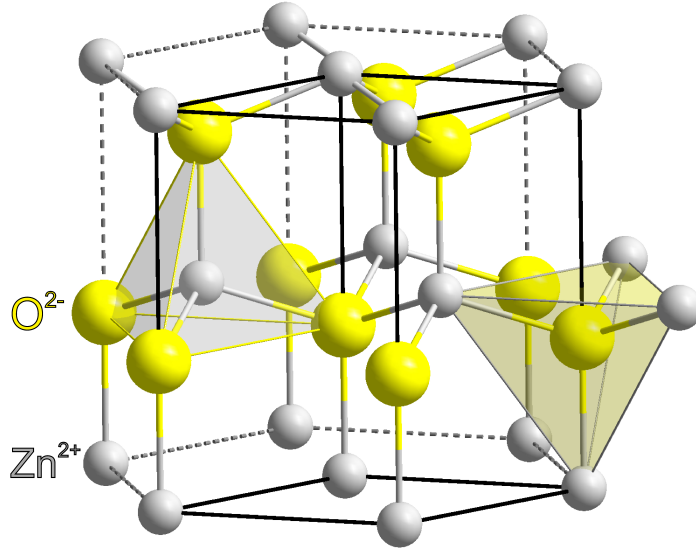
Figure 2.1: *Wurtzite structure of ZnO [80]*

and O atoms in ABAB stacking sequence. The lattice constants of ZnO are $a_0 = 3.23$ Å and $c_0 = 5.213$ Å. The strong ionic binding is provided by Zn^{2+} and O^{2-} ions. Each ion is tetrahedrally surrounded by four ions of the other kind [81]. The corresponding symmetry group C_{6v} ($6mm$-symmetry) contains the following 12 symmetry operations [76]:

$$1, 2_z, 6(\bar{2}_\perp), \pm 3_z, \pm 6_z, \qquad (2.2)$$

where z is the main axis and e.g. $6(\bar{2})$ means a 2 fold rotation around one of the 6 symmetry axes followed by an inversion. The subscripts $\perp$ on the 2 indicates that the twofold axis is perpendicular to the main crystal axis. Due to the sixfold z-axis, the position of the x- and y- axis is not unique. In order to distinguish different crystal directions, 4 Miller indices, h, k, i and l, are used [82]. For a direction perpendicular to the z-axis, one will find:

$$[hki0] \| (h\mathbf{e}_1 + k\mathbf{e}_2 + i\mathbf{e}_3). \qquad (2.3)$$

Thereby for the unit vectors is $-(\mathbf{e}_1 + \mathbf{e}_2) = \mathbf{e}_3$ and therefore, $-(h + k) = i$. So the cartesian coordinates x,y and z can be expressed by the following equivalent indices:

$$\text{x-direction} : [2\bar{1}\bar{1}0], [11\bar{2}0], [\bar{1}2\bar{1}0], [\bar{2}110], [\bar{1}\bar{1}20], [1\bar{2}10] \qquad (2.4)$$

$$\text{y-direction} : [01\bar{1}0], [\bar{1}100], [\bar{1}010], [0\bar{1}10], [1\bar{1}00], [10\bar{1}0] \qquad (2.5)$$

$$\text{z-direction} : [0001] \qquad (2.6)$$

The different directions, perpendicular to the z-axis, denoted by Miller indices are shown in Fig. 2.2. Due to the hexagonal symmetry, ZnO is a uniaxial crystal.
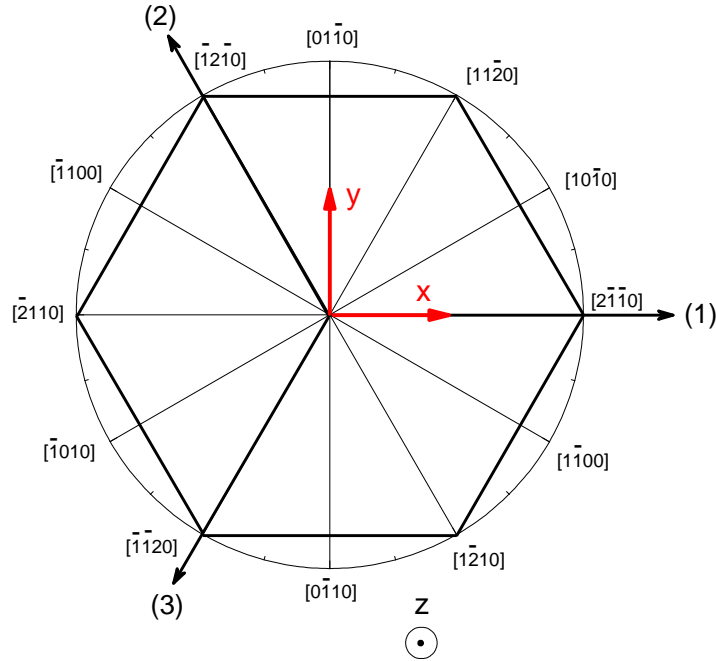
Figure 2.2: *Directions in the wurzite structure denoted by Miller indices for $\boldsymbol{k}\|\boldsymbol{c}$* [81]

2.2.2   Band structure

The valence band of the semiconductor ZnO is formed by $2p^2$ orbitals of O^{2-} and the conductivity band is formed by $4s$ orbitals with an direct band gap around 3.4 eV. In spherical representation, the p- valence bands have D_1^- symmetry and the s-conduction band D_0^+ symmetry. The $2p$-levels (and anti-binding sp^3 orbitals) are split by the hexagonal crystal field into two sub-bands Γ_5 and Γ_1. Adherence of spin and resulting spin-orbit interaction lead to a further splitting into three, two-fold degenerated, valence band states

$$D_0^+ \otimes D_{1/2}^+ \Rightarrow \Gamma_1 \otimes \Gamma_7 = \Gamma_7 \qquad \text{conduction band} \qquad (2.7)$$

$$D_1^- \otimes D_{1/2}^+ \Rightarrow (\Gamma_1 \oplus \Gamma_5) \otimes \Gamma_7 = 2\Gamma_7 \oplus \Gamma_9 \quad \text{valence band} \qquad (2.8)$$

In all wurtzite-type semiconductors, these bands are usually labelled from higher to lower energies as A (Γ_9), B (Γ_7), and C (Γ_7) bands (Fig. 2.3). However, in ZnO an inverted valence band ordering or so called negative spin-orbit coupling is expected [83]. Therefore, an inverted ordering A (Γ_7), B (Γ_9), and C (Γ_7) is more reasonable. Selection rules for transitions from the upper valence bands A (Γ_7) and B (Γ_9) to the conduction band (Γ_7) are essentially the same and are only strongly dipole and spin flip allowed for $\mathbf{E} \perp \mathbf{c}$. On the other hand, transitions from the C (Γ_7) valence band to the conduction band (Γ_7) are only strongly allowed for $\mathbf{E} \parallel \mathbf{c}$. The splitting between the A and B valence bands is amounting to 5 meV.
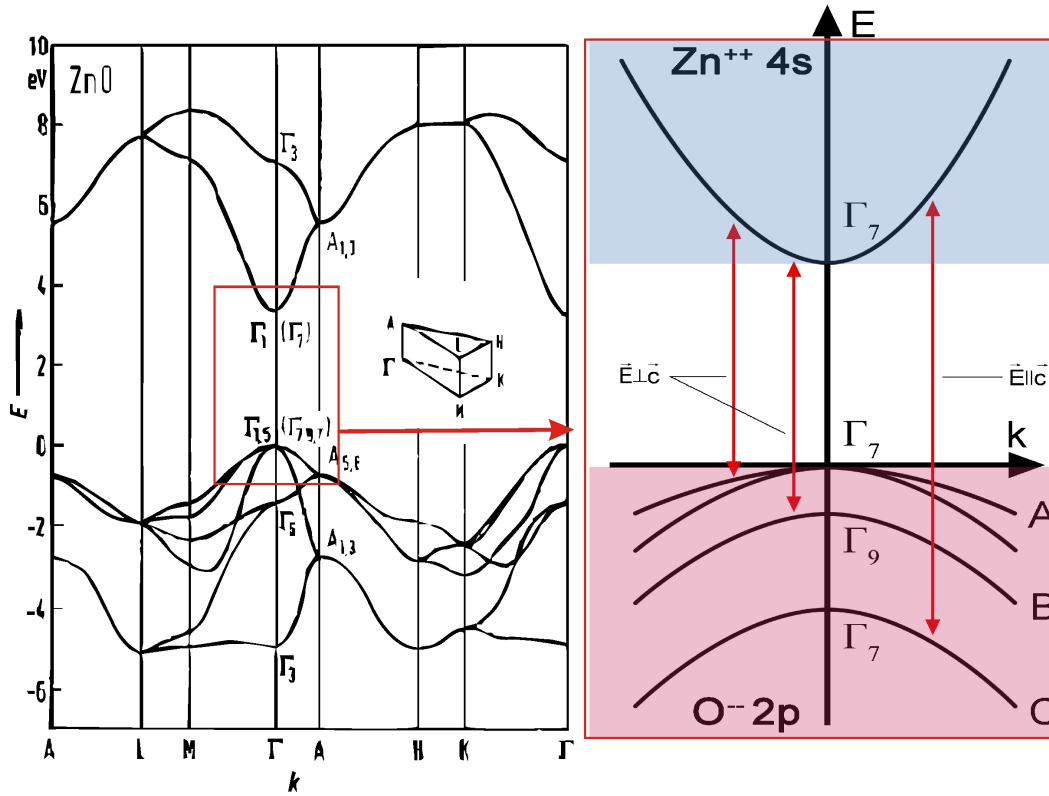
Figure 2.3: *Electronic structure calculated by semi-empirical tight binding theory [84] and the enlarged band structure in vicinity of the Γ-Point. The valence band is formed by the p-orbital of oxygen and the conduction band by the s-orbital of Zn. The valence band is split by the crystal field and the spin-orbit coupling.*

2.2.3 Excitons

If one excites an electron from the filled valence band to the empty conduction band by absorption of a photon, one creates a hole in the valence band simultaneously. In this sense, an optical excitation is a two particle transition. The same is true for the recombination process. An electron in the conduction band can return radiatively or non-radiatively into the valence band only if there is a free place, i.e. a hole. Two (quasi-)particles are annihilated in the recombination process.

However, as a consequence of the Coulomb interaction, these optically generated excitations, namely electron-hole pairs, form a bound state of electron and hole, which can propagate through the crystal. The quanta of these excitations are called excitons in semiconductors and insulators. Binding energies of the excitons E_{exc} depend strongly on the material and varies between 1 meV up to 1000 meV and optical excitations of excitons require photon energies $\hbar\omega \geq E_G - E_{exc}$. Based on the spatial distance and binding energies of electron and hole, two types of excitons can be distinguished. Is the distance between hole and electron small compared with the lattice constant, one speaks about Frenkel-excitons with a large binding energy [85]. On the contrary, Wannier-excitons [86] have a large distance between hole and electron compared with the lattice

constant. Typically, in all semiconductors, we have to deal with Wannier-excitons. Different from the Frenkel-excitons, the two particle problem of Wannier excitons can be considered in the effective mass approximation as hydrogen- or positronium-like problem. For simple parabolic bands and a direct-gap semiconductor, one can separate the relative motions of electron and hole and the motion of the center of mass. One obtains (in cubic materials) a dispersion relation for a hydrogen-like series of states below the gap:

$$E_{exc}(n, \mathbf{K}) = E_G - \frac{Ry^*}{n^2} + \frac{\hbar^2 \mathbf{K}^2}{2m^*_{exc}}, \qquad n = 1, 2, 3.., \tag{2.9}$$

where $Ry^* = e^4 m_e/[32(\pi\varepsilon_0\hbar)^2 \frac{\mu}{m_e\varepsilon_r^2}] = 13.6 \ eV\frac{\mu}{m_e\varepsilon_r^2}$ is the exciton Rydberg energy, $\mathbf{K} = \mathbf{k}_e + \mathbf{k}_h$ the wave vector of the exciton, $m^*_{exc} = m^*_e + m^*_h$ the translation mass and $\mu = (1/m^*_e + 1/m^*_h)^{-1}$ is the reduced mass. ε_0 denotes the dielectric constant of the vacuum and ε_r denotes the dielectric constant of the material. The excitonic bohr radius is defined by

$$a_B^{exc}(n) = a_B\varepsilon_r\frac{m_e}{\mu}n$$

and one can define as condition for Wannier-excitons, using material parameters for typical semiconductors, the following inequalities:

$$1 \ \text{meV} \leq Ry^* \leq 200 \ \text{meV} \leq E_G$$

and

$$50 \ \text{nm} \geq a_B^{exc} \geq 1 \ \text{nm} \geq a_{lattice}.$$

Schematically, one obtains an exciton-wave function by forming wave packets for electrons and holes $\phi_{e,h}(\mathbf{r}_{e,h})$ in the sense of the Wannier-function:

$$\phi(\mathbf{K}, n, l, m) = \Omega^{-1/2}e^{i\mathbf{K}\cdot\mathbf{R}}\phi_e(\mathbf{r}_e)\phi_h(\mathbf{r}_h)\phi_{n,l,m}^{env}(\mathbf{r}_e - \mathbf{r}_h), \tag{2.10}$$

with the center of mass R

$$\mathbf{R} = (m_e\mathbf{r}_e + m_h\mathbf{r}_h)/(m_e + m_h).$$

$\Omega^{-1/2}$ is a normalization factor. The hydrogen-like envelope function ϕ^{env} delineates the relative motion of electron and hole and the plane-wave factor describes the free propagation of the Wannier-exciton through the periodic lattice. $n = 1, 2, 3..$ is the main quantum number, $l = 0, 1, 2, .., n - 1$ is the orbital quantum number and $m = -l, -(l - 1), .., 0, .., l - 1, l$ is the magnetic quantum number as in the hydrogen-like atom. Since exciton features are especially strong for regions of dispersions where electron and hole group velocities are equal, in semiconductors with a direct gap at the Γ point, excitons form preferentially around $\mathbf{K} = 0$.

Furthermore, one has to distinguish singlet and triplet excitons. A singlet exciton possesses antiparallel electron and hole spin. If one starts from the ground state of the crystal, $\mathbf{L}, \mathbf{S}$ and $\mathbf{J}$ are equal to zero, and an optical excitation by an electric dipole transition does not influence the spin. Therefore, the created hole has a spin opposite to the electron and the total spin $\mathbf{S}$ of the electron-hole pair remains zero. A spin

Figure 2.4: *Exciton en-ergy levels at E_G-E_n. (a) Two particle picture (elec-tron, hole): Band struc-ture $E(k_e)$ vs. electron wave vector k_e. Exciton energy levels are schemati-cally shown below the con-duction band [71]. (b) One (quasi-)particle pic-ture (exciton): Exciton dispersion $E_n(K)$ with ex-citon wave vector K [71].*
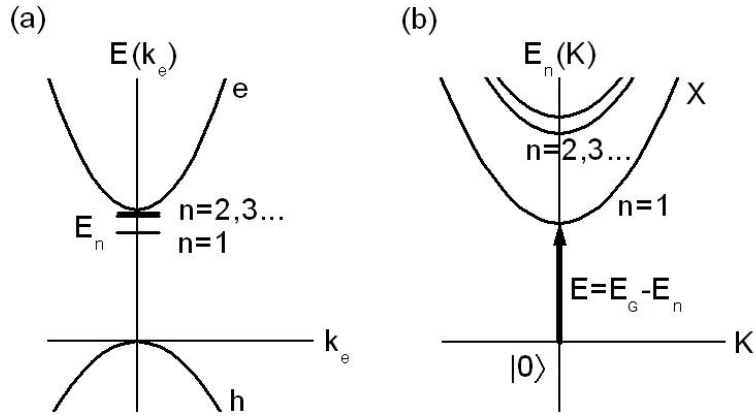
flip in the transition requires an interaction with the magnetic component of the light wave and ends up with $S = 1$ corresponding to the triplet state. Due to an exchange interaction, the triplet state is energetically situated below the singlet excitons. But the triplet excitons are spin-flip forbidden and have consequently small oscillator strengths. The oscillator strength f_n for singlet excitons in direct gap semiconductors with dipole allowed transitions and S-envelope is proportional to:

$$f_n \propto \mid F_{cv} \mid^2 \frac{1}{n^3} \tag{2.11}$$

Thereby $F_{cv} = \langle \phi_{exc} \mid ED \mid 0 \rangle$ is the band to band dipole transition matrix element with the dipole operator ED, the groundstate $\mid 0 \rangle$, and the exciton wave function ϕ_{exc} .

2.2.3.1 Excitons in ZnO

In certain materials like ZnO, triplet and singlet excitons are called para- and orthoex-citons (or dark and bright excitons in quantum dots). Due to the three neighbored valence bands of ZnO (see Section 2.2.2) one obtains three exciton series, denoted as A, B and C-series. These excitons are formed by an electron in the Γ_7 conduction band and a hole in the Γ_7, Γ_9 or Γ_7 valence band. The total symmetry of an exciton can be considered by a direct product of the representation of the symmetry of the envelope and the symmetry of conduction and valence bands

$$\Gamma_{ex} = \Gamma_{Env} \otimes \Gamma_{CB} \otimes \Gamma_{VB}.$$

For uniaxial crystals, the dispersion is dependent on the light direction: Excitons of C-series (Γ_1) can only be excited by a light field with $\mathbf{k} \perp \mathbf{c}$-axis (of the crystal). However, the A- and B- exciton series (Γ_5-Symmetry) requires excitations with $\mathbf{k} \parallel \mathbf{c}$-axis. A further splitting of the S-singlet state into a transversal and a longitudinal exciton and a splitting between singlet and triplet excitons are caused by an exchange interactions between hole and electron, effectuated by their Coulomb interaction. In

ZnO binding-energies of A,B and C series are roughly equal $E_{exc} \approx 60$ meV and the excitonic Bohr radius is $a_B^{exc} \approx 1.8$ nm. Since contrary to cubic materials the Coulomb interaction of hole and electron in wurtzite crystals is anisotropic as well, one has to consider a modified Hamiltonian for the excitons [87, 88, 89, 90]:

$$E_{ex} = E_G + \frac{\hbar^2 \mathbf{k}_{e,x}^2 + \hbar^2 \mathbf{k}_{e,y}^2}{2m_{e\perp}} + \frac{\hbar^2 \mathbf{k}_{e,z}^2}{2m_{e\|}} + \frac{\hbar^2 \mathbf{k}_{h,x}^2 + \hbar^2 \mathbf{k}_{h,y}^2}{2m_{h\perp}} + \frac{\hbar^2 \mathbf{k}_{h,z}^2}{2m_{h\|}}$$
$$- \frac{e^2}{4\pi\varepsilon_0 \sqrt{\varepsilon_\perp \varepsilon_\| (x_e + x_h)^2 + \varepsilon_\perp \varepsilon_\| (y_e + y_h)^2 + \varepsilon_\perp^2 (z_e - z_h)^2}}, \quad (2.12)$$

where the subscripts $\|$ and $\perp$ denote the corresponding masses m, dielectric constants ε, and wave vectors $\mathbf{k}$ of hole (h) and electron (e) for the different polarization directions, parallel and perpendicular to the **c**-axis (For ZnO: $\varepsilon_\| = \varepsilon_{\Gamma_1} = 3.639$, $\varepsilon_\perp = \varepsilon_{\Gamma_5} = 3.591$ [84, 91], and A- and B- excitons: $m_{h\perp} = m_{h\|} = 0.59m_e$, $m_{e\perp} = m_{e\|} = 0.28m_e$ [83]). For this problem, a separation of relative and center of mass movement is not any longer possible. The influence of the anisotropy can be treated by perturbation theory. The use of the anisotropic effective masses $\frac{1}{\mu_\perp} = \frac{1}{m_{e\perp}} + \frac{1}{m_{h\perp}}$, and $\frac{1}{\mu_\|} = \frac{1}{m_{e\|}} + \frac{1}{m_{h\|}}$, enables a description of exciton energies by an averaged dielectric constant $\bar{\varepsilon}$, an averaged reduced mass $\bar{\mu}$, and an anisotropy factor γ:

$$\frac{1}{\bar{\mu}} = \frac{2}{3}\frac{1}{\mu_\perp} + \frac{1}{3}\frac{1}{\mu_\|}\frac{\varepsilon_\perp}{\varepsilon_\|}, \quad \bar{\varepsilon} = \sqrt{\varepsilon_\perp \varepsilon_\|} \quad and \quad \gamma = \bar{\mu}\left(\frac{1}{\mu_\perp} - \frac{1}{\mu_\|}\frac{\varepsilon_\perp}{\varepsilon_\|}\right) \quad (2.13)$$

Hopfield et al. calculated the four lowest exciton lines by [88]:

$$E(1S) = E_G - \frac{e^4\bar{\mu}}{8h^2\varepsilon_0\bar{\varepsilon}^2}$$
$$E(2S) = E_G - \frac{1}{4}\left(\frac{e^4\bar{\mu}}{8h^2\varepsilon_0\bar{\varepsilon}^2}\right)$$
$$E(2P_0) = E_G - \frac{1}{4}\left(\frac{e^4\bar{\mu}}{8h^2\varepsilon_0\bar{\varepsilon}^2}\right)\left(1 + \frac{4}{15}\gamma\right) \quad (2.14)$$
$$E(2P_{\pm 1}) = E_G - \frac{1}{4}\left(\frac{e^4\bar{\mu}}{8h^2\varepsilon_0\bar{\epsilon}^2}\right)\left(1 + \frac{2}{15}\gamma\right)$$

The anisotropy lifts the degeneracy of the P-envelope of the exciton. The envelope P_0 orientated along the **c**-axis, has a different energy as the envelopes $P_{\pm 1}$ orientated in the xy-plane.

2.2.4   Polaritons

Dispersion is the dependence of the energy on a momentum or the wave vector. Due to the kinetic energy for excitons, see Eq. (2.9), a parabolic dependence of energy E and wave vector $\mathbf{k}$ was found. Light waves of the frequency ω are described by

$$E = \hbar\omega = \hbar ck.$$

If a crystal is exposed to light, the dispersion curves of light wave and excitons subtend mutual, leading to a strong interaction if the exciton is dipole allowed.
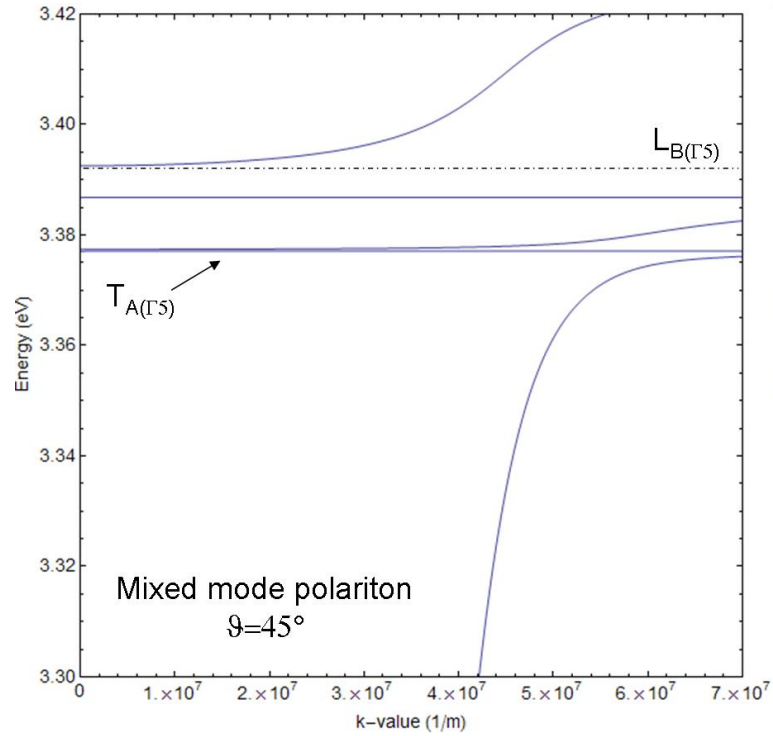
Figure 2.5:   *Mixed mode polariton*

In this case, one is not able to consider the dispersion of excitons and photons separately any further. Classically, one can compare this situation with the coupling of two oscillators. The solution diagonalizing the interaction-hamiltonian is called polariton and describes this coupling of photons and excitons [92, 93, 81, 94, 95, 96, 97, 98]. The dielectric function $\epsilon(\omega)$ of the polaritons in the Sellmeyer-presentation is given by:

$$\epsilon(\omega) = 1 + \sum_i \frac{F_i}{T_i^2 - (\hbar\omega)^2} \tag{2.15}$$

with the oscillator strength F_i and the energy T_i of the i-th exciton. Based on the Maxwell equations (see 3.1-3.4), for the diamagnetic ZnO without free carriers, the propagation of light in ZnO can be considered by the wave equation:

$$\text{rot}(\text{rot } \mathbf{E}) + \frac{\hat{\varepsilon}}{c} \frac{\partial^2 \mathbf{E}}{\partial t^2} = 0. \tag{2.16}$$

It was additionally assumed, that for a small field strength the polarization $\mathbf{P}$ and electric fields $\mathbf{E}$ are linearly connected by the dielectric tensor $\hat{\varepsilon}$:

$$\mathbf{P}(\omega) = \varepsilon_0(\hat{\varepsilon}(\omega) - \hat{1})\mathbf{E}(\omega) = \varepsilon_0\hat{\chi}(\omega)\mathbf{E}.$$

An approach for plane waves $\mathbf{E} = \mathbf{E}_0 e^{i(\mathbf{kr}-\omega t)}$ results in the basic equation of crystal optics:

$$\sum_{j=1}^{3} = (k^2\delta_{ij} - k_i k_j - \frac{\omega^2}{c^2}\varepsilon_{ij})E_j = 0, \qquad i = 1, 2, 3 \tag{2.17}$$

Since ZnO is uniaxial, the dielectric tensor has the form:

$$\hat{\varepsilon} = \begin{pmatrix} \varepsilon_{\Gamma_5} & 0 & 0 \\ 0 & \varepsilon_{\Gamma_5} & 0 \\ 0 & 0 & \varepsilon_{\Gamma_1} \end{pmatrix} \tag{2.18}$$

As mentioned in the last section, the subscripts Γ_5 and Γ_1 denote the symmetry of states with polarizations perpendicular and parallel to the **z**-axis in the point group C_{6v}. The **z**-axis is the optical main axis. Using Eq. (2.17) and the dielectric tensor, one can calculate the dispersion relation for different directions of the incident light field. With $k = (0, 0, k)^T$ one obtains $\varepsilon_{\Gamma_5} = \frac{k^2 c}{\omega}$ for transversal states with polarizations perpendicular to the **z**-axis. For longitudinal states with polarizations parallel to the **z**-axis, this leads to $\varepsilon_{\Gamma_1} = 0$. If **k** is not parallel or perpendicular to the main axis, one obtains so called mixed mode polaritons, an admixture of transversal and longitudinal polaritons, see Fig. 2.5.
A further equivalent representation for polaritons is the Kurosawa-representation:

$$\epsilon(\omega) = \prod_i \frac{L_i^2 - (\hbar\omega)^2}{T_i^2 - (\hbar\omega)^2} \tag{2.19}$$

with the longitudinal energies L_i.

2.2.5   Excitons in magnetic and electric fields

The different types of magnetism and the influence of magnetic fields have been already discussed in chapter 1. For the application to crystals, which possess a periodic lattice, the equations can be easily modified by the effective mass approximation. In the following, the influence of static electro-magnetic fields on the two particle excitation, the exciton is discussed. First, different perturbations caused by a magnetic field are described and finally, energy corrections given for applied electric fields by the Stark-effect are considered.
Based on the comparison of the energy units, the excitonic Rydberg energy $Ry*$ and the cyclotron energy $\hbar\omega_c = \hbar\frac{eB}{\mu}$ (μ reduced exciton mass), one has to distinguish the weak field regime for applications of static magnetic fields [99, 100, 101]:

$$Ry* \gg \hbar\omega_c; \Longrightarrow \gamma = \hbar\frac{eB}{\mu Ry*} \ll 1 \tag{2.20}$$

and the high field regime:

$$Ry* \ll \hbar\omega_c; \Longrightarrow \gamma \gg 1 \tag{2.21}$$

In the weak field regime, the Coulomb energy dominates and the magnetic field can be treated as perturbation. In the case of the high field regime, electrons and holes will be considered as free particles and the coulomb interaction acts as the perturbation. The more complicated intermediate regime $\gamma \approx 1$ is neglected here.

2.2.5.1 Landau-levels or diamagnetic shift

In order to analyze the marginal case of the high field regime in which electron and hole are treated as free particles, the explanations and equations of Section 1.1.1.1 are used. The Lorentz force affects the particles and in the Hamiltonian the interaction of the diamagnetic material ZnO with the field can be treated by the minimal substitution. This results in Landau-levels of hole and electron in the plane perpendicular to $\mathbf{B}$. According to Equation 1.6, one obtains, consequently, in Voigt-geometry($\mathbf{k} \perp \mathbf{B}$):

$$E_{n,\mathbf{k}_\parallel}^{e/h} = \pm\hbar\omega_c \left(n_{e/h} + \frac{1}{2} \right) \pm \frac{\hbar^2 \mathbf{k}_\parallel^2}{2m_{e/h}^*}, \tag{2.22}$$

where $m_{e/h}^*$ is the effective mass of the electron or the hole, respectively. Optical transitions between the Landau-levels of electrons and holes, so called inter-landau-level-transitions, must fulfill the condition: $\delta n = n_e - n_h = 0$ for one-photon-excitation or recombination of an electron/hole pair. In the weak field regime, the considerations of the Larmor-diamagnetism in Section 1.1.1.2 can be used. The Hamiltonian for the relative movement of electron and hole is given by:

$$\hat{H}_{exc} = \frac{\mathbf{p}^2}{2\mu} + V(\mathbf{r}) \tag{2.23}$$

with the reduced mass μ. The minimal substitution and the following transformations result in a diamagnetic contribution:

$$\hat{H} = \frac{e^2}{8\mu c^2}(\mathbf{B} \times \mathbf{r})^2. \tag{2.24}$$

Assuming the magnetic field $\mathbf{B} \parallel \mathbf{c}$ axis, this yields (see Eq. (1.11)):

$$\hat{H} = \frac{e^2 B^2}{8\mu c^2}(x^2 + y^2). \tag{2.25}$$

Since we deal with the relative coordinates of hole and electron, $r_{ex}^2 = x^2 + y^2$ is the radius of the exciton.
For a magnetic field $\mathbf{B} \perp \mathbf{c}$ applied in the Voigt-geometry, one obtains:

$$\hat{H} = \frac{e^2 r_{ex}^2}{8\mu c^2}(B_x^2 + B_y^2). \tag{2.26}$$

Therefore, the energy correction ΔE of the diamagnetic shift constitutes

$$\Delta E_{dia} = C_{dia}\mathbf{B}^2. \tag{2.27}$$

For the wurtzite structure with $\mathbf{B}$ applied in Voigt-geometry, the constant C_{dia} yields [87]:

$$C_{dia} = 6\mu_B^2 \frac{\mu_\perp}{\mu_\parallel} \left(\frac{m_{exc}}{m_e} + \frac{m_{exc}}{m_h} \right) \frac{1}{Ry^*},$$

where m_{exc} is the exciton mass.

2.2.5.2 Zeeman-splitting

By reasons of the spins of electron and holes, excitons can already have a non-vanishing magnetic moment at $\mathbf{B} = 0$, which can be aligned relatively to $\mathbf{B}$ and exhibit in addition the linear Zeeman-term. Due to the relative alignment of hole and spin the resulting splitting depends for singlet and triplet excitons with S-envelope in simplest approximation on the difference or sum of electron and hole g-factors:

$$\Delta E_z = \pm \mid g_e \pm g_h \mid \mu_B B. \tag{2.28}$$

Based on the influence of crystal- and bandstructure, these g-factors can drastically differ from the value $g = 2$, found for free electrons. As already mentioned in Section 1.1.1.2 or discussed in more detail in Section 1.1.2.2, angular momenta give a contribution to the Zeeman-splitting. Therefore, for states $n \geq 2$ additional contributions from the magnetic moment of envelope functions for $l \geq 1$ appear, depending on the orientational quantum number m. Are the states already split because of other reasons by a quantity Δ for $\mathbf{B} = 0$, the Zeeman splitting is suppressed until Δ and ΔE_z are of comparable magnitude.

In the wurtzite structure for a magnetic field applied in Voigt geometry with $\mathbf{B} \perp c$ the dominant Zeeman-term can be written as:

$$\hat{H}_{Z\perp} = \frac{\mu_B}{2} g_{env\perp} B_x L_x \tag{2.29}$$

with

$$g_{env\perp} = 2\sqrt{\mu_\parallel \mu_\perp} \left(\frac{m_{exc}}{m_{e\perp} m_{e\parallel}} - \frac{m_{exc}}{m_{h\perp} m_{h\parallel}} \right).$$

A further Zeeman-term caused by interaction of the magnetic field with the magnetic moments of hole and electron has normally to be taken into account as well, but the analysis shows, that this term gives no contributions for $\mathbf{B} \perp \mathbf{c}$. The influence of the magnetic field on the specific symmetries of the envelope is discussed in more detail in Section 4.1.3.

2.2.5.3 Excitons in static electric fields

The situation of an applied electric field $\mathbf{U}$ to the exciton can be treated analogously to the Stark-effect of the hydrogen-problem in perturbation theory. In the Hamiltonian only the position vectors of hole and electron have additively been taken into account:

$$\hat{H}_{st} = -e\mathbf{U}\mathbf{r} = -e\mathbf{U}(\mathbf{r}_h - \mathbf{r}_e) \tag{2.30}$$

The energy corrections of first and second order for small perturbations of the hydrogen atom are given by [102]:

$$E_n \approx E_n^{(0)} + \langle nl'm_l \mid \hat{H}_{st} \mid nlm_l \rangle + \sum \frac{\mid \langle n'l'm_l \mid \hat{H}_{st} \mid nlm_l \rangle \mid^2}{E_n - E_n'} \tag{2.31}$$

For the ground states of the hydrogen atom, the first order correction term of 2.31 vanishes; thus, initial by the second order perturbation term a quadratic Stark effect correction term is obtained:

$$\Delta E = -const. \ \mathbf{U}^2 \tag{2.32}$$

For excited states of the hydrogen atom $n \geq 2$ the situation is different, since the states are degenerated concerning l and m_l. Therefore, already the first order perturbation term gives a linear correction. For calculations, a diagonalizing of the perturbation operator in the eigenspace of the energies is necessary. The wave function of the $n = 2$ state has even parity for $l = 0$ and possesses odd parity for $l = 1$. Since the Stark-Hamiltonian influences only l, exclusively $\langle 210 \mid \hat{H}_{st} \mid 200 \rangle$ and $\langle 200 \mid H_{st} \mid 210 \rangle$ contribute to the first order correction, resulting in an energy-shift of

$$\Delta E = \pm const.U$$

Hence, the electric field leads for states $n \geq 2$ to an admixture of states with different parity, whereas perturbations induced by magnetic fields can only provide an admixture of states with the same parity.

Excitons are influenced in the same manner as the hydrogen atom and perturbation theory gives a good approximation if the applied electric field $\mathbf{U}$ is small in comparison to the ionization field

$$\mathbf{U}_I = \frac{Ry*}{ea_B^{exc}} \tag{2.33}$$

Lowest 1 S-(envelope) excitons corrections are obtained by the second order perturbation term resulting in a quadratic shift. However, $2P$- and $2S$-exciton correction terms are already given by the first order perturbation leading to an admixture of P- and S- envelope and a linear energy correction term. Besides the influence of the electric field to the envelope, the bands are affected as well, but only bands with "no clear" symmetry like sp-hybrids are corrected in the first order perturbation term. In real solids and also in ZnO, the situation differs for excited states, since for example S and P excitons are not degenerated. These excitons are already split due to lattice polarizations effects, which can be taken into account by replacing the Coulomb interaction of electron and hole by an effective Haken-potential [103]. In order to deal with the situation of this energetically separated S- and P- excitons, one uses a linear combination as approach for the Hamiltonian:

$$\hat{H}|200\rangle = (E_2 + \Delta)|200\rangle \tag{2.34}$$
$$\hat{H}|210\rangle = (E_2 - \Delta)|210\rangle \tag{2.35}$$

The non disturbed energy E_2 for the $n = 2$-state is shifted for S- and P- excitons about the value Δ. The Schrödinger equation for these linear combinations and the system with perturbation $\hat{H} + \hat{H}_{st}$ results in [104]

$$\begin{pmatrix} E_2 + \Delta & \langle 200|\hat{H}_{st}|210\rangle \\ \langle 200|\hat{H}_{st}|210\rangle & E_2 - \Delta \end{pmatrix} \begin{pmatrix} \alpha_1 \\ \alpha_2 \end{pmatrix} = E \begin{pmatrix} \alpha_1 \\ \alpha_2 \end{pmatrix} \tag{2.36}$$

Assuming $\langle 200|\hat{H}_{st}|210\rangle = \langle 210|\hat{H}_{st}|200\rangle = -3ea_B^{exc}U$, the energy-eigenvalues E are given by

$$E = E_2 \pm \sqrt{9e^2(a_B^{exc})^2U^2 + \Delta^2}. \tag{2.37}$$

With the eigenvectors the wave function for the excitons can be written as linear combinations of $|S\rangle$ and $|P\rangle$ states:

$$|\varphi_{2S/2P}\rangle = \alpha_1|P\rangle + \alpha_2|S\rangle \tag{2.38}$$
$$|\varphi_{2P/2S}\rangle = \alpha_1|S\rangle - \alpha_2|P\rangle \tag{2.39}$$
$$\tag{2.40}$$

The coefficients α_1 and α_2 of the eigenvector yield the ratio of the admixture of the the S- ($|200\rangle$) and the P- ($|210\rangle$) excitons.

Several assumptions were made for the calculations but, nevertheless, the treatment by perturbation theory and the discussions above give a good approximation and overview for the resulting effects based on the electric field.
In high electric fields, internal and external lattice strains are present resulting in the inverse piezoelectric effect. But in this work only small fields are considered; therefore, this effect is negligible. Furthermore, in bulk samples the detection of the Stark effect is not easy since the electric field energy $ea_B\mathbf{U}$ must be of the same magnitude as the spectral width of the absorptions bands in order to obtain a detectable shift. Consequently, electric fields in the order of 10^6 V/m are typically required.

2.3 Magnetic semiconductors: Europium chalcogenides

The wide band gap magnetic semiconductors, the europium chalcogenides, display several unique electronic and magnetic properties and are, therefore, an interesting class of materials as well for academic as for device applications [105]. In this section the crystallographic, electronic, magnetic, magneto-optical properties and the responsible indirect exchange mechanisms are discussed.

2.3.1 Crystallographic structure

Europium chalcogenides EuX (X=O, S, Se, and Te) are magnetic semiconductors crystallizing in the centrosymmetric rock salt structure with $m3m$ symmetry.

Figure 2.6 displays the crystal structure for EuTe, where the lattice constant is $a_0 = 6.598$ Å (see Table 2.1). The divalent Eu^{2+} and X^{2-} ions form a strong ionic binding. This ionic binding results in an empty $5d$ state of Europium and a fully filled p-orbital of the chalcogenides. The space lattice is built by a fcc lattice with the basis of

Eu^{2+} at $(1/2,1/2,1/2)$ and X^{2-} ions at $(0,0,0)$ positions. The corresponding symmetry group $m3m$ (O_h symmetry) contains the following 48 symmetry operations [76]:

$$1, \bar{1}, 9(2), 9(\bar{2}), 4(\pm 3), 4(\pm \bar{3}), 3(\pm 4), 3(\pm \bar{4}) \tag{2.41}$$

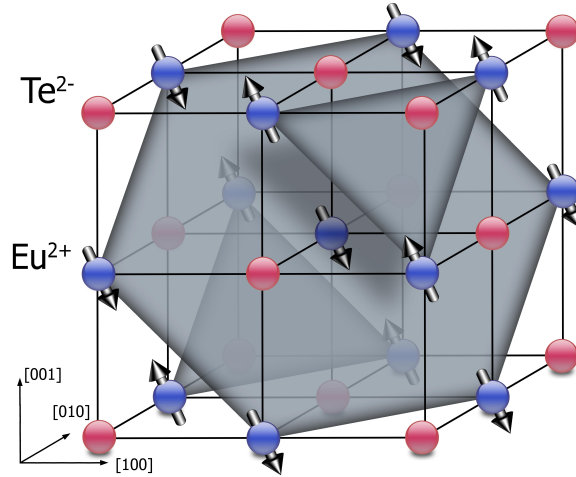where $4(\pm\bar{3})$ means a 3 fold rotation around one of the 4 symmetry axes followed by an inversion (overbar).

Figure 2.6: *Schematic crystal structure and spin structure of EuTe. Arrows show the spin directions, blue and red spheres the Eu^{2+} and Te^{2-}, respectively. The parallel aligned spins are marked by planes. Spins of neighbored planes are aligned antiferromagnetically below the Neel-Temperature.*

2.3.2   Band structure and optical properties

The band structure of EuTe is shown as example for EuX in Fig. 2.7. The differences in the band structure of EuX compounds are mainly based on the main quantum number of the highest filled p-orbital of the chalcogenides leading to an energy shift of the band gap (absorption edge). Material parameters are listed in Table 2.1. Europium $4f^7$ states, which are strongly localized due to Coulomb interaction and shielded by electrons occupying s and p (see Fig. 2.7) chalcogenide orbitals, form the valence band. The conduction band is built by the $5d$ states, that are strongly split by the crystal field into a lower energy three-fold degenerated $5d(t_{2g})$ state and a two-fold degenerated $5d(e_g)$ state lying about 1 eV higher. Due to a resonance between $5d(t_{2g})$ orbitals at neighboring lattice sites, the $5d(t_{2g})$ states are broadened [107] and overlap with the 6s state. Optical absorption measurements have revealed that the conduction band can be described in the framework of tight-binding theory and in EuTe shows a width of about 0.6 eV. In the ground state, the seven valence electrons are in the localized $4f^7$ shell of the Eu^{2+} ion with parallel spins, thus $L = 0$ and total spin $S = 7/2$ represented by the notation $^8S_{7/2}$. The lowest excited state corresponds to an excitation of one valence
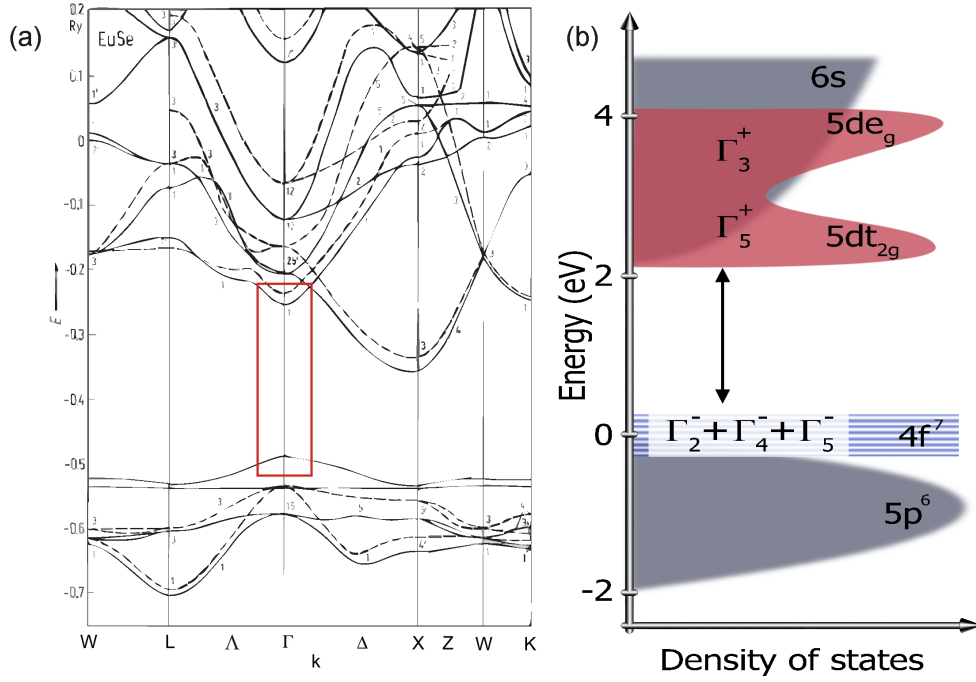
Figure 2.7: *Semi-empirical tight binding bandstructure in EuSe [106] (a) and enlarged schematical bandstructure in the vicinity of the Γ-Point for EuTe (b)*

electron from the $4f^7$ state to the $5d(t_{2g})^1$ state denoted by the notation $4f^65d(t_{2g})$. The remaining six $4f^6$ electrons are described by the orbital quantum number $L = 3$ and spin quantum number $S = 3$ leading to a strong spin-orbit coupling. Therefore, the total momentum quantum number $J = 0, 1, ..., 6$ and resulting magnetic quantum number $M = -J, ..., 0, ..., J$ have to be taken into account and can be represented by the notation $^7F_{JM}X$. Moreover, exchange interaction, characterized by a constant $J_{df}S$, between the excited $5d^1$ electron and the remaining $4f^6$ electrons leads to a further energy splitting:

$$S_T = S_{5d^1} + S_{4f^6}. \tag{2.42}$$

The resulting splitting scheme for EuSe considering all interactions, described by the Hamiltonian

$$\hat{H}_{5d} = p^2/2m + \hat{H}_{cf} + \hat{H}_{so} + \hat{H}_{exchange}, \tag{2.43}$$

is shown in Fig. 2.8. Thereby, H_{cf} denotes the influence of the crystal field, H_{so} takes into account the spin-orbit interaction, and $H_{exchange}$ describes the exchange interaction. Assuming a relative small Zeeman splitting, the shift of the $5d(t_{2g})$ conduction band obeys the Landé-interval rule, depending only on the total momentum quantum number J:

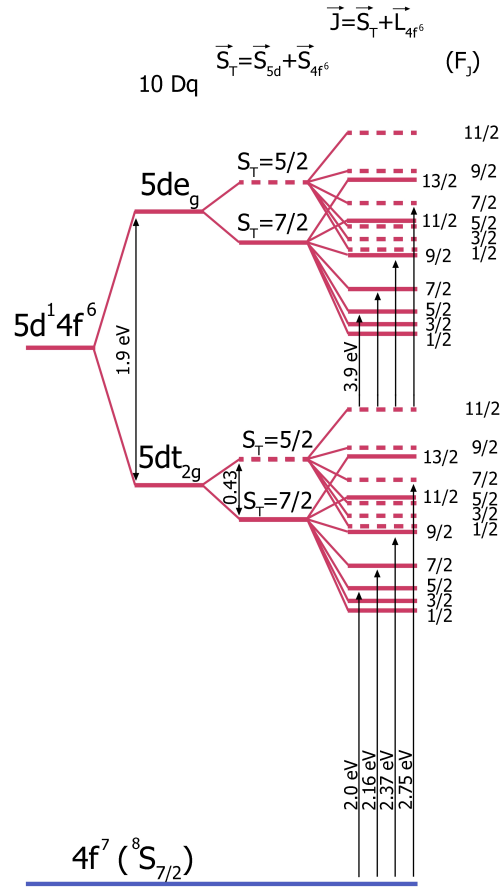$$E_J = E_G + \frac{1}{2}\lambda_{4f}J(J+1), J = 0, ..., 6. \tag{2.44}$$

Figure 2.8: *Level-Splitting of EuSe [108]*

Thereby, E_G is the band gap energy and λ_{4f} is the Landé spin-orbit constant for the corresponding $^7F_{JM}X$ state.

### 2.3.3 Magnetic properties and responsible exchange mechanisms

The Europium chalcogenides possess unique physical properties, determined by the above described electronic structure, in which the strongly localized $4f^7$ electrons of Eu^{2+} ions with spin $S = 7/2$ are involved [109]. EuX are classical Heisenberg magnets, where the competition between the nearest neighbor (NN) and the next-nearest neighbor (NNN) exchange integrals results in magnetic phase diagrams, that can include antiferro- (AFM), ferri- (FIM), and ferromagnetic (FM) ordering, as well as a paramagnetic phase at elevated temperatures [109, 110]. The NN and NNN exchange integrals are denoted by J_1 and J_2. Since the $4f$ electrons are concentrated around

the Europium-core, no overlap of $4f$-wave functions of different Eu-ions is expected. Therefore, the exchange interaction must be indirect.

2.3.3.1 Indirect exchange mechanisms

Several of such indirect exchange interactions have been found, but mechanisms which were claimed to be mainly responsible for long range ordering in the Europium chalcogenides will shortly be discussed in the following. Since there are no free carriers, indirect exchange mechanisms via polarization of conduction electrons, like a Ruderman-Kittel interaction, can be excluded in EuX [111, 112].

Antiferromagnetic next nearest neighbor (NNN) interaction denoted by J_2 is caused by a super exchange according to Kramer and Anderson. Kasuya discussed this in more detail in [113, 114] and concludes that the Kramer-Anderson mechanism for f and p states is too small to explain the magnitude of the NNN exchange constant. Thus, J_2 consists of several competing components, which are considered to involve excitations of the anion p-electrons to neighboring $5d$ states through the $d - f$ exchange. The super-exchange in ionic solids arises because there is a kinetic energy saving for antiferromagnetism.
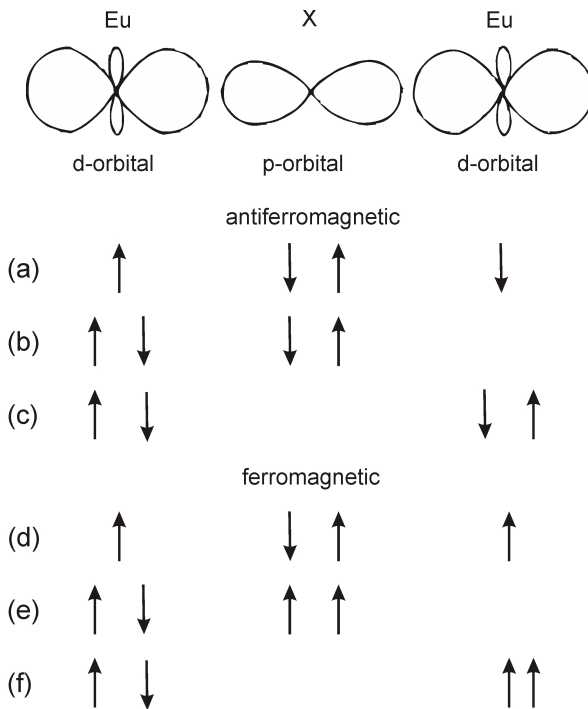
This indirect interaction between two non-neighboring magnetic ions is mediated by a nonmagnetic ion. The left figure shows the mechanism for a simple tri-atomic $p - d$ model. For simplicity, we assume that a single unpaired electron is responsible for the magnetic moment. If the magnetic moments are antiferromagnetically coupled, the ground state (a) can mix with excited states (b)and (c). Therefore, the magnetic moment can be delocalized over the $d - p - d$ unit and lowers the kinetic energy. If the moments on the metal ions are ferromagnetically aligned, the ground state (d) cannot mix with the excited states (e,f) due to the Pauli principle. Consequently, this ordering costs energy U. The antiferromagnetic coupling parameter describing this interaction can be written according to Kramer-Anderson as

$$J_2 = -\frac{1}{2S^2}\frac{t(f,f)^2}{U} \qquad (2.45)$$

Thereby the Coulomb-Energy U gives the energy cost of making an excited state and t the transfer-integral. As mentioned above, Kasuya concludes, that the J_2 value

resulting alone from Eq. (2.45) is too small and the $d - f$ exchange has mainly to be described by

$$J_2 = -\frac{1}{2} \mid \sqrt{2}\frac{2t}{U} \mid^4 \frac{\mid I_{df} \mid^2}{U^5}, \tag{2.46}$$

with the factor I_{df} numbering the value of $d - f$ exchange. Nevertheless, both mechanisms are present and Kasuya takes both contributions and cross terms into account as well and mentions that several other mechanisms contribute to J_2.

As causation for the NN exchange constant J_1, resulting in a ferromagnetic contribution, Methfessel claims an indirect cation-cation super exchange as proposed by Goodenough as most important [115, 116]. Thereby it is assumed, that the $5d$ states (in exactly the $5dt_{2g}$) are so expanded that they even overlap with $4f$ states of neighbored cations and give a ferromagnetic coupling. The parameter can be calculated by:

$$J_1 = \frac{t(f,d)^2 A}{2S^2 U^2}, \tag{2.47}$$

with the transfer-(overlap-)integral $t(f,d)$ representing the probability of a $4f$ electron transfer to an empty $5d$-state. A is an intra atomic exchange energy and U is the energy difference between $4f - 5dt_{2g}$ states. However, according to Kasuya, the appropriate exchange interaction resulting in a ferromagnetic coupling, represented by the positive coupling parameter J_1, consists of a virtual excitation of an $Eu^{2+}4f$ electron to a $5d$ state of a nearest neighbor (NN) cation and a subsequent intra-atomic $d - f$ exchange. Recently, Monte carlo calculations of the exchange mechanisms have been performed revealing that the exchange mechanisms are varying much more strongly with interatomic distances as previously assumed [105]. This can be described by the magnetic Grüneisen law [117], describing the influence of pressure:

$$J(r) = J_0 \left(\frac{r}{r_0}\right)^{-n}, \tag{2.48}$$

where $J_0 = J(r_0)$ and r_0 are the exchange interaction and interatomic distance at 1013 mbar and n is the scaling exponent. For J_1, namely NN exchange interactions, a Grüneisen exponent of $n_1 \approx 20$ was found and for NNN interaction described by J_2, one obtains an exponent of $n_2 \approx 10$. Therefore, particularly the nearest neighbor interaction J_1 depends strongly on the interatomic distance. Considering the mean field theory, taking into account only the Kramer-Anderson mechanism and indirect cation-cation exchange according to Methfessel, the Curie and Néel temperatures can be expressed as functions of exchange parameters J_1 and J_2, extending to nearest and next-nearest Eu-neighbours:

$$T_C = 2/3S(S+1)(z_1 J_1 + z_2 J_2) = 126J_1 + 63J_2 \tag{2.49}$$

$$T_N = 2/3S(S+1)(-z_2 J_2) = -63J_2. \tag{2.50}$$

The number of nearest and next-nearest neighbours in rocksalt structure is $z_1 = 12$ and $z_2 = 6$, respectively. Values of the exchange integrals, as well as of the Néel and Curie temperatures, are listed in Table I.

EuX	$a_0(\mathring{A})$	Mag.Order	$T_C(K)$	$T_{C,N}(K)$	$J_1(K)$	$J_2(K)$	$E_G(eV)$
EuO	5.141	FM	76	66.8	0.63	-0.07	1.12
EuS	5.968	FM	19	16.3	0.20	-0.08	1.65
EuSe	6.195	AFM	9	4.60	0.13	-0.11	1.80
		FiM		3.6			
		AFM		2.8			
EuTe	6.598	AFM	-6	9.58	0.03	-0.15	2.00

Table 2.1: Parameters of EuX materials [109]

.

2.3.3.2 Magnetic structure

For the exchange parameters in EuTe, $\mid J_2 \mid > \mid J_1 \mid$ is valid. Therefore, this compound shows antiferromagnetism below $T_N = 9.58$ K. Absorption and Faraday rotation measurements revealed a critical field of $B_{sat} = 7.2$ T above which EuTe becomes ferromagnetically saturated [118]. The spins or the magnetic moments are parallel within (111) planes and successive (111) planes have the alternative spin orientation [↑↓↑↓]. In EuSe the magnetic behavior is more complicated and is called metamagnetic, the phase diagram is shown in Fig. 2.9. Due to the ferromagnetic and antiferromagnetic
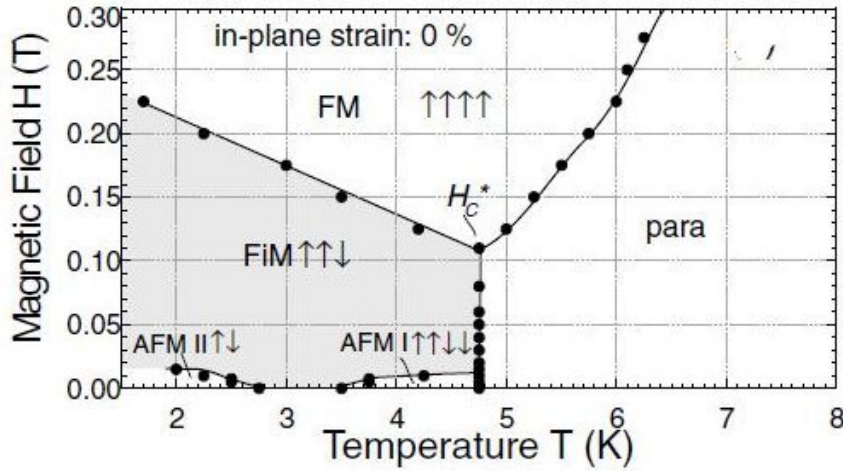
Figure 2.9: *Phase diagram of EuSe [110]. Several different phases are found, depending on magnetic field strength and temperature*

exchange parameters being of comparable magnitudes, this material displays manifold magnetic phases strongly depending on temperature and external magnetic field strength. In zero magnetic field, EuSe becomes antiferromagnetic below $T_N = 4.6$ K with successive spin planes aligned as [↑↑↓↓]. A ferrimagnetic phase is found below $T_C = 3.6$ K with [↑↑↓] spin plane structure. For temperatures lower than $T_N = 2.8$ K, the ordering changes to another antiferromagnetic phase with [↑↓↑↓] ordering. Weak external magnetic fields are already sufficient to change the phases: the two antifer-
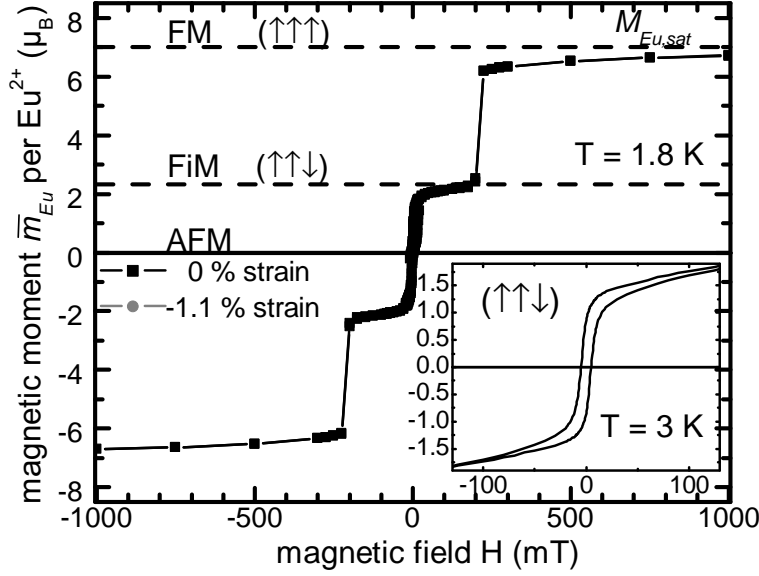
Figure 2.10: *Magnetization dependence of EuSe for T=2K (AFM) and in the inset for T=3K (FiM), measured by squid [110]. At T=1.8K clear steps appear in the magnetization based on the different magnetic phases. In the ferrimagnetic phase for T=3K these magnetization steps vanish and a hysteresis is found.*

romagnetic phases turn into a ferrimagnetic phase and the ferrimagnetic phase into a ferromagnetic phase. In an external magnetic field above a critical value of 0.2 T, EuSe is in a FM phase [110]. The magnetization in dependence on the applied magnetic field is shown for EuSe in Fig. 2.10.

2.3.4 Magneto-optical properties

As mentioned in the last section, europium chalcogenides display unique magnetic properties based on exchange parameters of similar magnitude. Consequently, the behavior in an external magnetic field is of great interest. In an external magnetic field, the band gap energy can be calculated by [118]

$$E_G(B) = E_G(0) - J_{df}S \times \left\{ \begin{array}{ll} \left(\dfrac{B_{int}}{B_{sat}}\right)^2, & B_{int} < B_{sat} \\ 1 & , B_{int} > B_{sat} \end{array} \right\}, \tag{2.51}$$

where the constant $J_{df}S$ describes the exchange interaction, B_{sat} is the saturation field and B_{int} is the internal magnetic field. The saturation field was found to be 7.2 T in EuTe ($\lambda_{4f} = 9.6$ meV, $J_{df}S = 150$ meV) and 0.2 T in EuSe ($\lambda_{4f} = 14$ meV, $J_{df}S = 104$ meV)[109]. In external magnetic fields the europium chalcogenides exhibit a

giant splitting of the conduction band, resulting in exceptionally large magneto-optical effects [119, 120, 121]. According to [122], EuSe has the largest effective g-factor up to 18000 and according to [123], EuTe shows the largest magnetic field induced energy shifts of the interband transitions ever observed in semiconductors. Therefore, EuX attracts interest for potential applications in spin-filter devices based on EuO [124, 125, 126, 127, 128], EuS [129, 130, 131, 132, 133, 134, 135] or EuSe [136] tunnel junctions. These tunnel junctions provide spin-polarized electrons due to different barrier heights for electrons in different spin states [137, 138]. By means of the spin-splitting of the bands, resulting in different refractive indices for left and right circular polarized light, a huge Faraday rotation is observed in europium chalcogenides[139, 140, 141, 142]. Due to this, EuS/EuF$_2$ and EuSe films are applicable for high resolution magneto-optical imaging of the flux distribution in superconductors [143]. Recent works have also demonstrated that EuO can be epitaxially grown on silicon [144] and GaN [145], which opens new possibilities for device realization.

Chapter 3

Nonlinear Magneto-Optics

3.1 Nonlinear optics

The interaction between electromagnetic waves and atomic matter was already carried out to higher orders of perturbation theory in the early years of quantum mechanics [146, 147]. But it was the invention of the laser in 1960 by Maiman [148] based on the theoretical considerations by Schawlow and Townes [149] that cleared the way for experimental nonlinear optics [150, 151]. By means of lasers, the generation of light fields with a field strength of $>10^6$ V/m became possible. The oscillating electric and magnetic fields of electromagnetic waves interact with the charge distribution in the matter. Due to the nonlinear atomic response of the matter, this oscillating light-field induces oscillating electric dipole or higher order moments leading to the coherent emission of radiation with new frequency components [152]. In order to deal with these processes theoretically, one can use the nonlinear wave equation.

3.1.1 Nonlinear wave equation

The basis for the electromagnetic theory and the propagation of electromagnetic waves is provided by the Maxwell equations and the Lorentz force [153]:

$$\text{div}\,\mathbf{E} \;=\; \frac{\rho}{\varepsilon_0}\,, \tag{3.1}$$

$$\text{div}\,\mathbf{B} \;=\; 0\,, \tag{3.2}$$

$$\text{rot}\,\mathbf{E} \;=\; -\frac{\partial \mathbf{B}}{\partial t}\,, \tag{3.3}$$

$$\text{rot}\,\mathbf{B} \;=\; \varepsilon_0\mu_0\frac{\partial \mathbf{E}}{\partial t} + \mu_0\mathbf{j}\,, \tag{3.4}$$

where $\mathbf{E}$ and $\mathbf{B}$ are the electric and the magnetic field, ρ and $\mathbf{j}$ are the electric charge density and the electric current density, and ε_0 and μ_0 are the permittivity and the permeability, respectively. The electric charge density ρ and the electric current density

j can be described by a multipole expansion [154, 1, 2, 71]

$$\rho = \rho_0 - \text{div}\,\mathbf{P} - \text{grad}(\text{div}\,\widehat{Q}) + \ldots, \tag{3.5}$$

$$\mathbf{j} = \mathbf{j}_0 + \frac{\partial}{\partial t}\mathbf{P} + \text{rot}\,\mathbf{M} - \frac{\partial}{\partial t}\text{div}\,\widehat{Q} + \ldots, \tag{3.6}$$

where $\mathbf{P}$ is the electric dipole moment, $\mathbf{M}$ is the magnetic dipole moment and $\widehat{Q}$ is the electric quadrupole moment.

If no free carriers and currents are present in the material, the terms ρ_0 and $\mathbf{j}_0$ vanish. The application of $\nabla\times$ to Eq. (3.3) followed by the use of Eqs. (3.1) and (3.4) results in the inhomogeneous nonlinear wave equation [71]:

$$\text{rot}(\text{rot}\,\mathbf{E}) - \varepsilon_0\mu_0\frac{\partial^2\mathbf{E}}{\partial t^2} = \mu_0\frac{\partial^2\mathbf{P}}{\partial t^2} + \mu_0\text{rot}\frac{\partial\mathbf{M}}{\partial t} - \mu_0\text{div}\frac{\partial^2\widehat{Q}}{\partial t^2} \tag{3.7}$$

The source terms of the inhomogeneous wave equation, the electric dipole moment, the magnetic dipole moment, and the electric quadrupole moment drive the electromagnetic wave. This expresses the fact that, whenever e.g. $\frac{\partial^2\mathbf{P}}{\partial t^2}$ is nonzero, charges are being accelerated, and according to Larmor's theorem from electromagnetism, accelerated charges generate electromagnetic radiation.

Macroscopically, the influence of the light field on the material is described in lowest order by a polarization $\mathbf{P}$. This polarization delineates a displacement of the electric dipoles in the material and may be written in a Taylor expansion in ascending powers of the electric field $\mathbf{E}$:

$$P_i = \varepsilon_0 \sum_{j=1}^{3} \chi_{ij}^{(1)} E_j + \varepsilon_0 \sum_{j,k=1}^{3} \chi_{ijk}^{(2)} E_j E_k + \varepsilon_0 \sum_{j,k,l=1}^{3} \chi_{ijkl}^{(3)} E_j E_k E_l + \ldots, \tag{3.8}$$

where $\chi^{(m)}$ is the electric susceptibility of m-th order and ε_0 is the dielectric constant of the vacuum. The first term of Eq. (3.8) is assigned to coherent processes in linear optics, leading to the refraction index. The response of the material to the light field is described by the susceptibility tensors[71]; the linear response described by $\chi^{(1)}$ is the strongest one and the higher order susceptibilities are negligible in the case of weak light fields. The second term of the expansion treats different situations: The application of the approach $E_i \sim e^{i\omega_i t} + e^{-i\omega_i t}$ to the equation $P_{nl} = \varepsilon_0\chi^{(2)}E_1 E_2$ leads to the nonlinear polarization $P_{nl} \sim e^{i(\omega_1+\omega_2)t} + e^{i(\omega_1-\omega_2)t} + \ldots$, where ω_1 and ω_2 are the frequencies of the incident light waves. The first part of the polarization deals with the Sum Frequency Generation (SFG) corresponding to the elementary process of the annihilation of the two exciting quanta and the generation of a photon with $\omega_3^{SFG} = \omega_1 + \omega_2$. The special case $\omega_1 = \omega_2$ is called second harmonic generation (SHG) (see Sec.3.1.4), which is used as main tool for the investigation of different materials in this work. The second term of the polarization describes the difference frequency generation (DFG), whereby photons with the frequency $\omega_3^{DFG} = \omega_1 - \omega_2$ are generated. All above treated effects are called parametric processes denoting that the crystal itself remains unchanged after the processes, in contrast to an absorption process which changes the population of the

crystal (nonparametric process). DFG is generally known as a parametric conversion process. A consequence of DFG is the parametric amplification that is used to realize wide tunable coherent light sources e.g Optical Parametric Oscillators(OPO). Such an OPO was used in our experiments and is discussed in more detail in Section 3.2.2.

The next expansion term in Eq.(3.8) deals with four interacting photons. If the three incident photons are of the same frequency, this process is called third harmonic generation (THG). The annihilation of these three photons leads to the creation of a photon with $\omega_4^{SFG} = \omega_1 + \omega_2 + \omega_3$.

The intensity of the expansion terms decreases reciprocally with the quadratic fine structure constant, which is a quantity for the coupling strength of the light field to the material. Due to the involvement of multiple photons, nonlinear processes offer higher degrees of freedoms in comparison to linear optics, because the polarization as well as the direction of every photon can be chosen independently. Consequently, the resulting selection rules are different and raise the possibility of detecting transitions which are forbidden in linear optics.

Considering SHG, the source terms in Eq.(3.7) may also be written in the following way:

$$\text{electric dipole moment} \quad : \quad P_i(2\omega) = \varepsilon_0 \chi_{ijk}^{(ED)} E_j(\omega) E_k(\omega) \,, \tag{3.9}$$

$$\text{magnetic dipole moment} \quad : \quad M_i(2\omega) = \frac{c}{\varepsilon_0 n(\omega)} \chi_{ijk}^{(MD)} E_j(\omega) E_k(\omega) \,, \tag{3.10}$$

$$\text{electric quadrupole moment} \quad : \quad \hat{Q}_{ij}(2\omega) = \frac{\varepsilon_0 c}{2i\omega n(\omega)} \chi_{ijkl}^{(EQ)} E_k(\omega) E_l(\omega) \,. \tag{3.11}$$

Thereby the electric quadrupole $\hat{Q}_{ij}$ itself is a tensor. The leading order term is given by the electric dipole moment. Higher order terms contribute only significantly to the SHG signal whether the electric dipole term is forbidden or the higher order terms are enhanced [71].

3.1.2   Symmetry of tensors

Symmetry considerations play a particular role in physics. Already the consideration of symmetry leads to the fundamental laws of the conservation of energy, the conservation of momentum and angular momentum [155]. As mentioned in Section 1.3.1, the Neumann-principle declares that the symmetry of a system must be reflected by the symmetry of the physical properties. If these properties are described by e.g. a tensor, this tensor must have the same symmetry restrictions as the system itself. Thus, the application of symmetry operations to the physical properties, in our case expressed by an optical nonlinear susceptibility tensor $\hat{\chi}$ of the rank n, leads to linear equations giving restrictions and constraints for the vanishing of tensor components. The general transformation of a tensor $\hat{\chi}$ is given by

$$\chi'_{ijk...n} = \sum_p \sum_q \sum_r \cdots \sum_u l_{ip} l_{jq} l_{kr} \ldots l_{nu} \chi_{pqr...u} \,, \tag{3.12}$$

where $l_{i'j'}$ with $i', j' = 1, 2, 3$ are the relative components of the transformation matrix. Therefore, a transformation of the coordinate system of the tensor can be performed by the use of rotation matrices [71].

Tensors could be distinguished by means of their transformation properties. For instance, the application of the spatial inversion operator $\hat{I}$ leads to an inversion of the chirality of the coordinate system by the transformation of the spatial coordinates $\mathbf{r} \to -\mathbf{r}$. With respect to this spatial inversion operation, one can classify tensors in the following way:

$$\text{polar tensor} \quad : \quad \chi'_{ijk...n} = l_{ip}l_{jq}l_{kr} \cdot \ldots \cdot l_{nu} \cdot \chi_{pq...u}, \tag{3.13}$$

$$\text{axial tensor} \quad : \quad \chi'_{ijk...n} = -l_{ip}l_{jq}l_{kr} \cdot \ldots \cdot l_{nu} \cdot \chi_{pq...u}, \tag{3.14}$$

where Einstein's sum convention has to be considered. The components of the inversion matrix (l_{ij}) are given by $l_{ij} = -\delta_{ij}$ using Dirac's delta function. The eigenvalues of the parity operator are $P_{\hat{I}} = \pm 1$, since double application of the operator should re-establish the primary handedness. A more careful consideration is necessary for the time inversion operation $\hat{T}$, which is formally based on the substitution $t \to -t$. Similar to the parity operation, the eigenvalues of the time-inversion are also $P_{\hat{T}} = \pm 1$. Consequently, double application leads to the original "direction of time". The time-inversion operation cannot be understood by means of backwards running clocks. One has to consider this operation as an inversion of movement. Thus, the time-inversion is not applicable if a direction of time/movement is preferential. For macroscopic systems, which maximize their entropy in order to reach the thermodynamical equilibrium, the application of time inversion operation is not reasonable. In optical experiments such a case is given if dissipative processes like absorption effects or transport properties are involved. The time inversion of dynamical effects, e.g. the excitation of a crystal by propagating electromagnetic waves, has to be taken into account as well.

Tensors that are invariant under time inversion are classified as "i"- tensors (reciprocal) and thus, the tensors that change their sign under this operation are called "c"-tensors (non-reciprocal).

The consideration of space- and time inversion for a system leads to a well-defined classification of these tensors. This permits the calculation of their non-vanishing tensor components by group theory [76, 77]. But one should keep in mind that the allowed tensor components are not necessarily non-zero. Due to other conditions, the symmetry allowed components can be nevertheless weak or forbidden.

A first important symmetry restriction for the SHG process in centrosymmetric media is obtained by the application of the space inversion. Due to the centrosymmetry $\hat{\chi}(\overrightarrow{r}) = \hat{\chi}(\overrightarrow{-r})$, the space inversions leads to:

$$(\hat{I}P_i(2\omega)) \propto \hat{I}\chi_{ijk}\hat{I}E_j(\omega)\hat{I}E_k(\omega) = -P_i \, \chi_{ijk}(-E_j(r))(-(E_k(r) = P(2\omega) = 0.$$

Therefore, the crystallographic SHG electric dipole process is forbidden in centrosymmetric media. For harmonic generations are the so called rotational anisotropies typically. The light interacts with the charge distribution; consequently, the angle dependence of the harmonic generation signal reflects the symmetry of the atomic distri-

bution in the crystal and is in opposition to most photoluminescence signals strongly anisotropic.

Thus, the discussed determination of the selection rules for the SHG/THG processes and resulting transformations enable the simulation of the rotational anisotropy and to gain insight into the involved processes.

For example: The diamagnetic semiconductor GaAs possesses zinc-blende structure and is assigned to the point group $\overline{4}$3m. For the third rank tensor χ_{ijk}, describing the electric dipole SHG process, one will find non vanishing tensor components of the χ_{xyz} type and its permutations. The application of the transformation rules leads to Fig. 3.1. A detailed description of the calculation of the rotational anisotropy is given in Ch. 6.
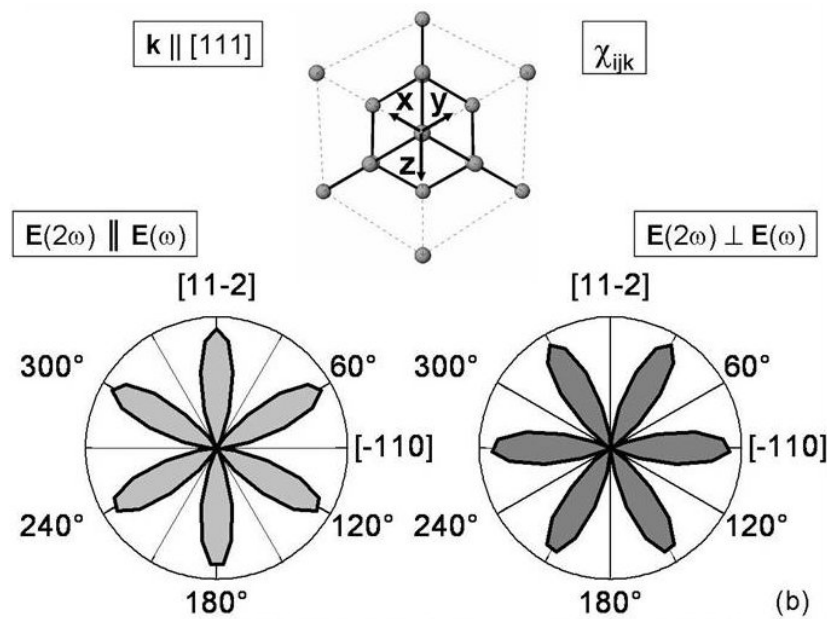
Figure 3.1: *Crystallographic anisotropy simulations for SHG in GaAs. The simulation was done for light incidence in the [111] direction. The crystal shows a sixfold symmetry and the same sixfold symmetry is found in both simulations. The simulation on the left presents the result for a SHG signal polarized parallel to the incident light and the simulation on the right depicts the SHG signal perpendicular to the incident polarization.[71]*

3.1.3 Light-matter interaction

The previous chapters gave a classical and macroscopical discussion of nonlinear optics that is sufficient so far to understand the phenomenological processes and some characteristics of harmonic generation. However, in order to establish understanding for the behavior in the vicinity of resonances and to get a microscopic point of view, a quantum mechanical treatment is unavoidable.

For the description of a quantum mechanical system, the Hamilton operator provides the basis. In the presence of an electromagnetic field the minimal substitution of the momentum operator $\mathbf{p} \to \mathbf{p} + \frac{e}{c}\mathbf{A}$ has to be used. Moreover, the energy contribution of the electric field $\mathbf{E}$ and the magnetic field $\mathbf{B}$ must be taken into account [71, 70]:

$$\hat{H} = \sum_{e^-}[\frac{1}{2m}(\mathbf{p} + \frac{e}{c}\mathbf{A})^2 - eV] \qquad + \frac{1}{8\pi}\int (E^2 + B^2)d^3r \qquad (3.15)$$

$$= \sum_{e^-}(\frac{\mathbf{p}^2}{2m} - eV) + (\frac{e^2}{2mc^2}\mathbf{A}^2 + \frac{e}{mc}\mathbf{p}\mathbf{A}) + \frac{1}{8\pi}\int (E^2 + B^2)d^3r \qquad (3.16)$$

$$= \qquad \hat{H}_e \qquad + \qquad \hat{H}_{int} \qquad + \qquad \hat{H}_{fields}. \qquad (3.17)$$

The properties of the particle are given by the mass m, the charge $q = -e$, the momentum p and the periodic structure of the crystal is included by the potential V.

A transformation of the Hamiltonian leads to the separation of the different contributions $\hat{H}_e$, $\hat{H}_{int}$ and $\hat{H}_{fields}$. The well known part $\hat{H}_e$ describes the motion of non-interacting electrons in the potential V and $\hat{H}_{fields}$ reflects the energy contribution originating from the electric and magnetic fields. $\hat{H}_{int}$ reproduces the interaction between the applied fields, in our case the light field, and the charged particles.
The nonlinear part $\hat{H}'_{int} = \frac{e^2}{2mc^2}\mathbf{A}^2$ is considered for the explanation of the diamagnetic properties of the material. So the diamagnetic shift of the exciton energy in semiconductors, which is proportional to H^2, can be described with this term. The linear part $\hat{H}''_{int} = \frac{e}{mc}\mathbf{p}\mathbf{A}$ deals with the interaction between light and matter and can explain transitions between eigenstates of the material. For the latter, we use an expansion of the vector potential up to the second order:

$$\mathbf{A} = A_0\mathbf{e}e^{\pm i\mathbf{k}(\omega)\mathbf{r}} \approx A_0\mathbf{e}(1 \pm i\mathbf{k}(\omega)\mathbf{r}), \qquad (3.18)$$

where $\mathbf{e}$ is the unit vector and A_0 is the amplitude of the vector potential.

If one has a look at such a possible transition/excitation between two eigenstates induced by the light field

$$\langle f|\hat{H}_{int}|g\rangle = \langle f|\frac{e}{mc}\mathbf{p}\mathbf{A}|g\rangle$$

and then uses Eq. (3.18), different possible transition/excitation sources can be recovered:

electric dipole $\propto A_0\mathbf{e} \cdot \mathbf{1}$ $\hat{H}_{ED} = e\mathbf{E}\mathbf{r}$

magnetic dipole $\propto A_0\mathbf{e} \cdot \mathbf{kr}$ $\hat{H}_{MD} \sim (\mathbf{L} + \mathbf{S})\mathbf{B}$

electric quadrupole $\propto A_0\mathbf{e} \cdot \mathbf{kr}$ $\hat{H}_{EQ} \sim (\mathbf{kr})(e\mathbf{E}\mathbf{r})$

The leading term one obtains already by the first expansion term corresponds to the electric dipole term. An estimate yields [156] that this electric dipole process is stronger by a factor of the reciprocal fine structure constant $\frac{1}{\alpha} \simeq 137$ as the magnetic dipole

electric dipole $\hat{H}_{ED}$	odd	Γ_4^-
magnetic dipole $\hat{H}_{MD}$	even	Γ_4^+
electric quadrupole $\hat{H}_{EQ}$	odd	$\Gamma_3^+ + \Gamma_5^+$

Table 3.1: *Symmetry of process for one photon processes in the cubic space group m3m*

and electric quadrupole term. These both are on the same scale and result from the second expansion term. Since the spin behaves formally like an angular momentum this spin is added to the angular momentum part in the magnetic dipole process. The electric dipole part is the only one in the expansion that is independent of **k** and does consequently not vanish at the Γ point of a crystal. In many cases the optical approach **kr** $<< 1$ is suitable, since $\lambda = \frac{2\pi}{k}$ is much larger than the lattice constant $a \sim |\mathbf{r}|$. Therefore, usually only the electric dipole term is considered. However, as mentioned before symmetry considerations or other conditions can lead to restrictions which prohibit the electric dipole contribution. If so, the magnetic dipole and /or electric quadrupole processes have to be taken into account. By group theoretical considerations, one can ascribe symmetry transformation properties (see Sect. 1.3.1) to this processes as well. For one photon processes in cubic materials, the symmetry representations according to [77] are given in Table 3.1.3. For the symmetry representations of relevant processes in the point group $6mm$, see Section 4.1.1.

3.1.4 Second harmonic generation (SHG)

Although second harmonic generation (SHG) is the lowest-order nonlinear process, it can provide a lot of important information about the electronic and magnetic structure of solids [157, 158, 3, 70]. With its larger number of degrees of freedom, SHG reveals new and complementary information in comparison to linear optics [159, 160, 161]. First SHG experiments were performed by Franken [150] in 1962, using a ruby laser to generate SHG in quartz. It is a special case of the sum frequency generation (SFG), where both incident photons have the same frequency ω and induce a polarization that leads to radiation of the frequency 2ω. The different source terms were already shown in Eqs. (3.9)-(3.11) but will be discussed in more detail in the following [70].

1. $P_i(2\omega) = \varepsilon_0 \chi_{ijk}^{(ED)} E_j(\omega) E_k(\omega)$, χ_{ijk} polar third rank tensor, leading contribution in substances without a center of symmetry.

2. $P_i(2\omega) = \varepsilon_0 \chi_{ijk}^{(MD)} E_j(\omega) H_k(\omega)$, χ_{ijk} axial third rank tensor, second order contribution including a magnetic dipole process that is weaker by a factor of $a \approx 10^{-2}$ compared with the electric dipole process. This process has odd parity and is always allowed in materials without an inversion symmetry. Is this symmetry given or weakly broken this contribution becomes noticeable if the substance owns a resonance with different parity of involved bands.

3. $M_i(2\omega) \propto \varepsilon_0 \chi_{ijk}^{(MD)} E_j(\omega) E_k(\omega)$, χ_{ijk} axial third rank tensor, this term describes a even, magnetic dipole induced transition that is also allowed in materials, in

Figure 3.2: *Illustration of the SHG process. Two photons of the light field $E(\omega)$ generate an excitation from the ground state to the final state. In a coherent process, the SHG light field $E(2\omega)$ is generated. The intermediate states can be real or virtual states. External or internal magnetic fields can be the source of further SHG contributions*
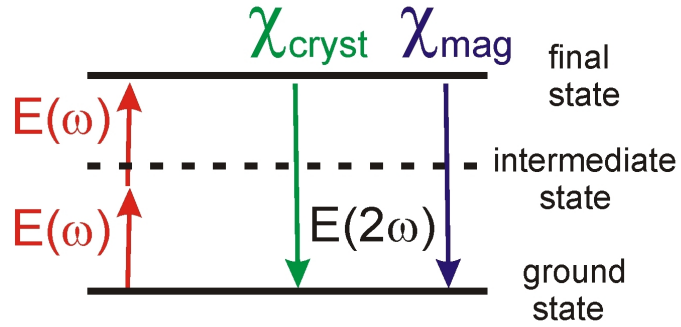
which the inversion symmetry is broken. This process is on the same scale as the previous term but possesses even parity. In materials with given inversion symmetry a contribution makes only transitions/excitations between states with same parity possible.

4. $\hat{Q}_{ij}(2\omega) \propto \varepsilon_0 \chi_{ijkl}^{(EQ)} E_k(\omega) E_l(\omega)$, χ_{ijk} polar fourth rank tensor, as mentioned before the magnetic dipole and electric quadrupole term have the same origin in the expansion and so both these processes are on the same scale. The electric quadrupole has even parity too and previous symmetry considerations are to apply here. But the selection rules for Q_{ij} and M_i are different.

These operators can be inserted into Eq. (3.19) to calculate the transition probability for each process. It will be shown in Section 3.1.5 that this is not always sufficient, especially in the case of magnetic-field-induced SHG in semiconductors.

The process of second harmonic generation for a resonance is shown schematically in Fig. 3.2. Two photons of the applied light field are used to make an excitation of the ground state $|g\rangle$. Thereby the first photon creates a virtual excitation of an intermediate state. The intermediate state is typically a real but nonresonant eigenstate. Thus, only a so called virtual excitation of an energy state with the energy difference ΔE is possible for a short time range Δt obeying the Heisenberg uncertainty principle $\Delta E \cdot \Delta t \geq \hbar$. During this time range, the second photon can generate an excitation from the intermediate state to the final state. The latter decays afterwards by coherent emission of a photon with $E(2\omega)$.

The quantum mechanical description of the process of second harmonic generation is given by means of the transition probability [156]

$$\omega_{fg} \propto \sum_i \frac{\langle g|\hat{H}_{int}(2\hbar\omega)|f\rangle \langle f|\hat{H}_{int}(\hbar\omega)|i\rangle \langle i|\hat{H}_{int}(\hbar\omega)|g\rangle}{(E_f - E_g - 2\hbar\omega)(E_i - E_g - \hbar\omega)} , \qquad (3.19)$$

where E_g, E_i and E_f are the energies of the states $|g\rangle$, $|i\rangle$ and $|f\rangle$, respectively, and $\hat{H}_{int}(\hbar\omega)$ and $\hat{H}_{int}(2\hbar\omega)$ are the operators specifying the interaction. The sum addition takes into account all possible intermediate states. The interaction between light
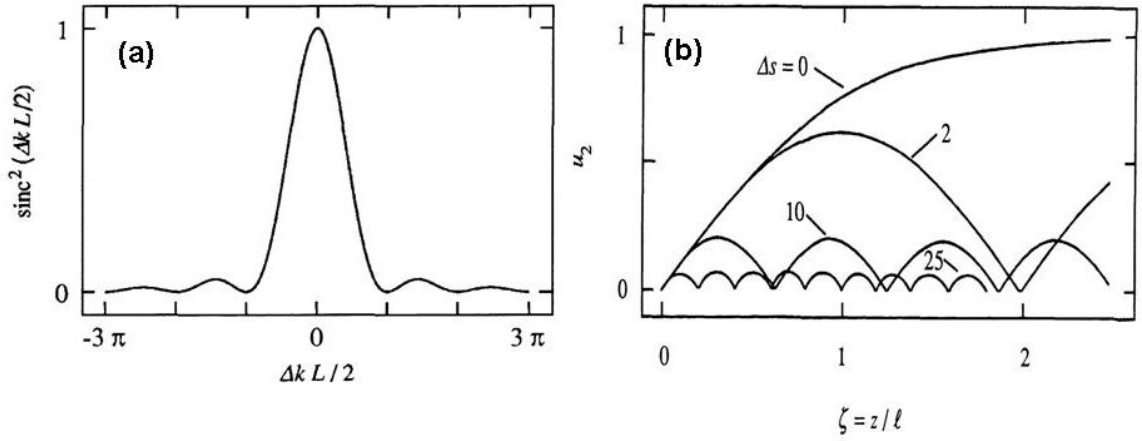
Figure 3.3: *(a) Effect of the wave vector mismatch on the intensity of sum frequency generation and(b)influence of this mismatch on the efficiency of SHG u_2 vs.the normalized propagation distance ξ for different normalized phase mismatch parameter $\Delta s = \Delta k l$.[2]*

and matter is described by the relative interaction Hamilton operators considered in Sect. 3.1.3. The denominator of Eq. (3.19) reveals resonances in the cases that the energy of the first exciting photon is close to the energy difference between the intermediate state and the ground state or the energy of the emitted photon is close to the energy difference between the final state and the ground state. Close to resonances the transition probability increases strongly. This effect leads to very strong and spectrally narrow SHG signals.

3.1.4.1   Phase matching and coherence

Based on the coupled wave equation, one will find the following expression for the SFG intensity $I(\omega_3)_{SFG}$ in media expressed in terms of the incident fields $I(\omega_1), I(\omega_2)$:

$$I(\omega_3)_{SFG} = \frac{512\pi^5\chi^2_{ijk}I(\omega_2)I(\omega_1)}{n_{\omega_1}n_{\omega_2}n_{\omega_3}\lambda^2_{\omega_3}c}L^2\mathrm{sinc}^2(\Delta kL/2) \,, \qquad (3.20)$$

Thereby n_{ω_3} means the refractive index at the frequency ω_3,$n_{\omega_{1,2}}$ the refractive index at the frequency $\omega_{1,2}$, L the length of the media and $\lambda^2_{\omega_3} = \frac{2\pi c}{\omega_3}$. Δk means the so called wave vector mismatch:

$$\Delta k = k_1 + k_2 - k_3$$

with the wave vectors of the three involved photons. The effect of the wave vector mismatch is completely included in $\mathrm{sinc}^2(\Delta kL/2) = \sin^2(\Delta kL/2)/(\Delta kL/2)^2$, which behavior is shown in Fig.3.3. When the condition of perfect phase matching

$$\Delta k = 0$$

	positive uniaxial $(n_e > n_0)$	negative uniaxial $(n_e < n_0)$
Type I	$n_3^o \omega_3 = n_1^e \omega_1 + n_2^e \omega_2$	$n_3^e \omega_3 = n_1^o \omega_1 + n_2^o \omega_2$
Type II	$n_3^o \omega_3 = n_1^o \omega_1 + n_2^e \omega_2$	$n_3^e \omega_3 = n_1^e \omega_1 + n_2^o \omega_2$

Table 3.2: Phase matching conditions for uniaxial crystals

is fulfilled, the generated wave has a fixed phase relation with respect to the linear polarization and the SFG process is most efficient. From the microscopic point of view, this means that the individual atomic dipoles are properly phased and the emitted radiation of each atom contributes coherently in the forward direction [2]. If this condition is not fulfilled, the efficiency of the process decreases as $|\Delta k|L$ increases and the generated wave gets out of phase with its driving polarization. Thus, a coherence length for this interaction can be defined:

$$L_c = \frac{2}{\Delta k}$$

Maker et al. [162] found consequences that are predicted by Eq.(3.20). The SHG intensity of a quartz sample changed strongly as the crystal was rotated. These rotations vary the effective path length through the crystal. Perfect phase matching is often desired but not easy to realize, since e.g. for SHG this condition requires that:

$$n(2\omega) = n(\omega),$$

which is obviously not given in materials with normal dispersion. In order to achieve phase matching, one can use birefringent crystals. Table 3.1.4.1 shows the different phase matching conditions for uniaxial crystals. Methods realizing the phase matching in these birefringent crystals are angle tuning and temperature tuning. Angle tuning is of practical importance for the Optical Parametric Oscillator (OPO) (see Section 3.2.2).

3.1.5   Magnetic second harmonic generation (SHG) contributions

So far, only the SHG of the $\chi_{ijk}^{(2)}$ has been discussed that originates from crystallographic properties. But several magnetic contributions were found giving an insight into magnetic properties determined by the spins of the material. The spins are magnetic moments, which can be described by a current density $\mathbf{j}(\mathbf{r})$. Since the current density changes its direction under time-inversion, the magnetic moments and the spins ,respectively, are also inverted. Thus, the magnetic SHG contribution in magnetically ordered materials behaves as a c-tensor in many cases. Contrary to this, the crystallographic SHG contribution is always time-invariant and characterized by an i-tensor.

An example for long range order of the magnetic moments is the material NiO. A contribution of intrinsic magnetic dipole type

$$P_i(2\omega) = \epsilon_0 \chi_{ijk}(\ell^2) E_j(\omega) H_k(\omega) \tag{3.21}$$
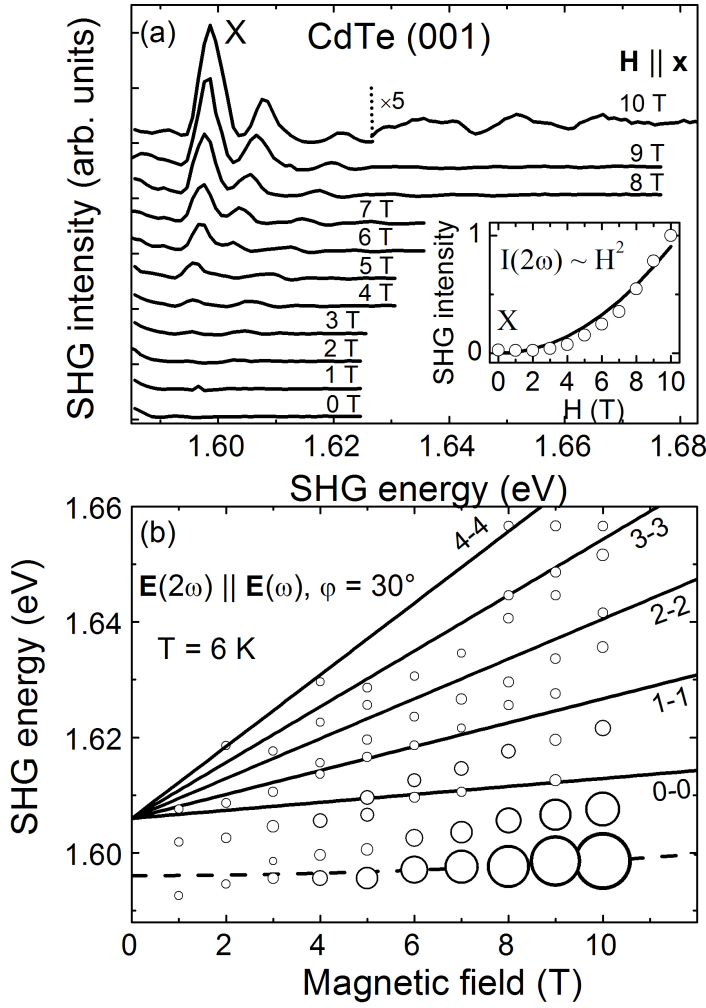
Figure 3.4: *SHG spectra for different magnetic fields and Landau Level fan-chart for CdTe [71, 69]: A set of narrow lines appears in an external magnetic field (a) The shift of the energy vs. magnetic field is shown in (b) A quadratic diamagnetic shift for the excitonic line and a linear shift for the Landau levels are observed. Intensity of SHG signal is given by point size.*

and a susceptibility proportional to the antiferromagnetic ordering parameter ℓ were found. Therefore, this contribution displays the ordering of the moments. As mentioned, tensors of magnetic ordered materials are typically "c-" tensors, but NiO transforms due to the quadratical dependence as an i-tensor[163].

Furthermore, electric-dipole type SHG due to noncentrosymmetric antiferromagnetic ordering was observed in magnetoelectric Cr_2O_3 [18, 164]

In the case of magnetically disordered materials, e.g. diamagnetic or (diluted) paramagnetic semiconductors, a magnetic field induced SHG (MFISH) signal was observed appearing only in an applied magnetic field, which leads to perturbations of the charge and the spin distribution. MFISH contributions can be generally described by

$$\begin{pmatrix} \mathbf{P}^{2\omega} \\ \mathbf{M}^{2\omega} \\ \mathbf{Q}^{2\omega} \end{pmatrix} \propto \begin{pmatrix} \chi^{eeem} & \chi^{eemm} & \chi^{emmm} \\ \chi^{meem} & \chi^{memm} & \chi^{mmmm} \\ \chi^{qeem} & \chi^{qemm} & \chi^{qmmm} \end{pmatrix} \begin{pmatrix} \mathbf{E}^{\omega}\mathbf{E}^{\omega}\mathbf{H} \\ \mathbf{E}^{\omega}\mathbf{H}^{\omega}\mathbf{H} \\ \mathbf{H}^{\omega}\mathbf{H}^{\omega}\mathbf{H} \end{pmatrix}, \qquad (3.22)$$

where $\mathbf{H}^\omega \equiv \mathbf{H}(\omega)$ is the magnetic field at the fundamental frequency and $\mathbf{M}^{2\omega} \equiv \mathbf{M}(2\omega)$ and $\mathbf{Q}^{2\omega} \equiv \mathbf{Q}(2\omega)$ are the magnetization and electric-quadrupole polarization at the MFISH frequency, respectively. Consequently, for e.g. GaAs the leading order SHG contribution in a static magnetic field $\mathbf{H}(\equiv \mathbf{H}(0))$, which has to be distinguished from $\mathbf{H}(\omega)$ of the light field, can be described by

$$P_i(2\omega) = \epsilon_0 \mathrm{i} \chi_{ijkl} E_j(\omega) E_k(\omega) H_l. \tag{3.23}$$

The external magnetic field leads to a nonlinear susceptibility χ_{ijkl} that can be classified as an axial fourth-rank i-tensor.

The zinc-blende structure ($\bar{4}$3m symmetry) and the corresponding non vanishing tensor components of the xyz-type for $\chi_{ijk}^{(2)}$ enable the elimination of the strong crystallographic SHG and a detection of pure MFISH. Since the exciton binding energy in GaAs and CdTe is only 4.2 meV, weak magnetic fields of about 2 Tesla are sufficient to form Landau levels. This orbital quantization was claimed to be the origin of the MFISH signal in these diamagnetic materials. Figure 3.4 (a) displays spectra for different magnetic fields in CdTe. The strongest peak of the spectra increasing with

$$I(2\omega) \propto H^2 \tag{3.24}$$

was identified as an exciton-peak. Energetically higher situated peaks correspond to intra Landau level transitions. The energy shift versus magnetic field is shown in Fig. 3.4 (b). The exciton shows a quadratic shift and the intra-Landau-Level transitions are shifting linearly. The size of data points is scaled by the SHG intensity of the corresponding peaks.

Based on detailed analysis of the detected anisotropy, it was found that electric dipole type MFISH is not sufficient to describe the MFISH process in these alloys. The spatial dispersion mechanism, including magnetic dipole and electric quadrupole contributions, has also to be taken into account to explain the shape of the measured anisotropy.

$$P_i(2\omega) = \epsilon_0 \chi_{ijklm} E_j(\omega) E_k(\omega) k_l(\omega) H_m, \tag{3.25}$$

The nonlinear susceptibility tensor χ_{ijklm} is an axial time-invariant fifth-rank tensor [33, 36]. Because of the tensor components for electric dipole processes, a signal in Faraday geometry should vanish. Despite a weak signal was detected in this configuration as well.

If one replaces cations of CdTe by strongly paramagnetic ions as Manganese (Mn), the magnetic properties are significantly changed. Since the integration of the foreign ion influences, the lattice constant linearly (Vegards law), a shift of the band gap according to [165, 166] is observed. SHG spectra of these, so called, diluted magnetic semiconductors reveal features based on these changes. Due to $d-d$ and $d-f$ exchange interaction of the Mn-ions, a giant Zeeman splitting is expected and found in the spectra. Fig. 3.5 shows SHG spectra for different $Cd_{1-x}Mn_x$Te compounds. The spectra differ obviously. Next to a shift of the band gap, the number of lines appearing in external magnetic fields varies as well. By means of a significant degradation of the quality of the crystals for higher concentrations of Mn, the lines are obviously broadened and a decrease of SHG intensity is observed. The main mechanism for the SHG
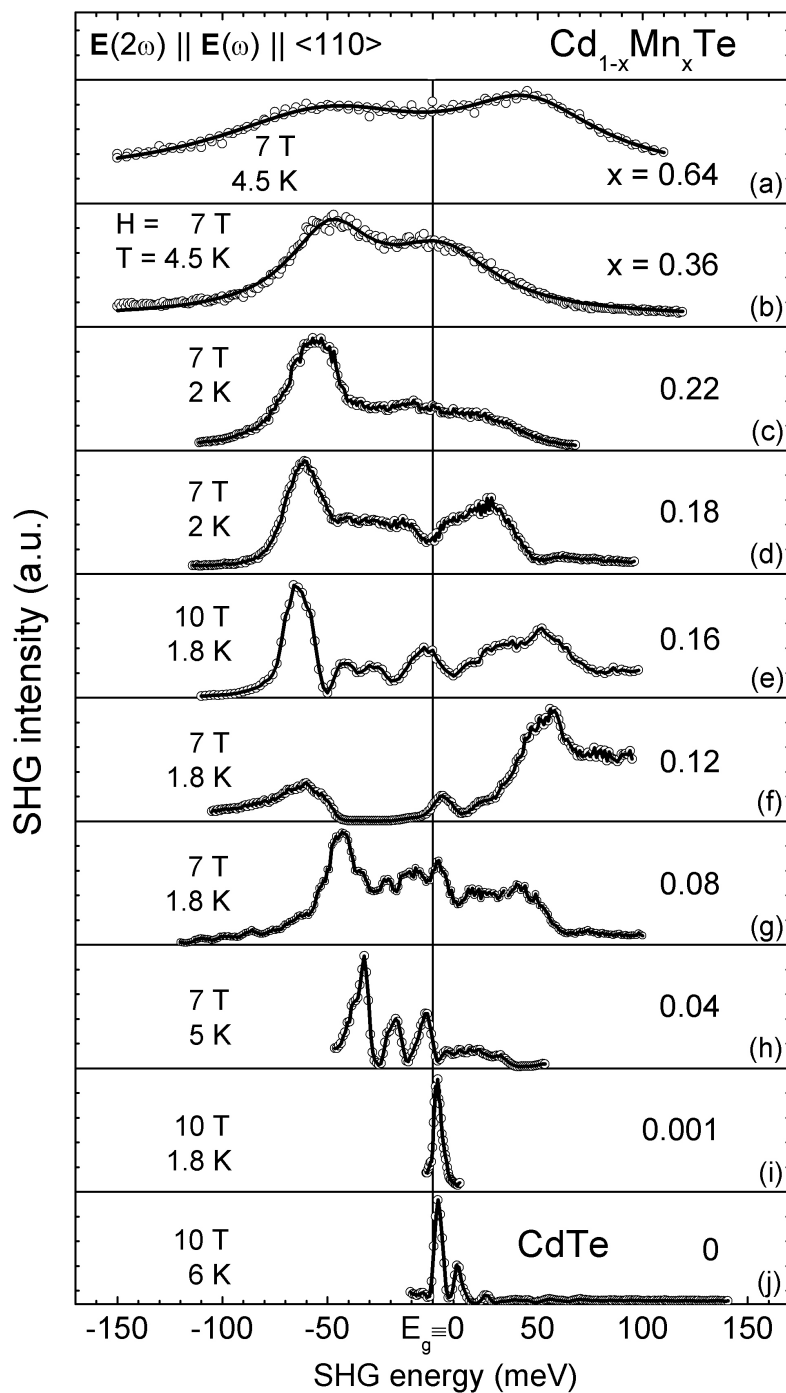
Figure 3.5: *Spectra for different compounds $Cd_{1-x}Mn_xTe$: The Mn-concentration significantly influences the shape of the spectra*
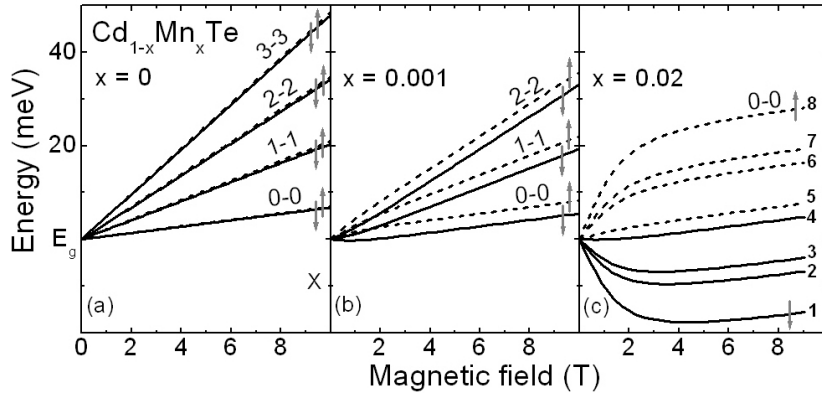
Figure 3.6: *Comparison of mechanisms for different Mn-concentrations: In CdTe (a) slightly diluted (b) and diluted (c) $Cd_{1-x}Mn_x Te$*

contribution in these diluted semiconductors is the spin quantization, that can also be phenomenologically described by Eqs. (3.23) and (3.25). The increase of the intensity vs. the magnetic field for the spin-quantization induced contribution is given by [34]:

$$I(2\omega) = P^2(2\omega) \propto M \qquad (3.26)$$

A more detailed investigation of weakly diluted compounds revealed that indeed both spin- and orbital-quantization induced contributions are present and a sort of a competition takes place. Fig. 3.6 compares the behavior of peaks for pure CdTe, a slightly diluted compound and a material with a higher concentration of Mn. The quadratic line shift of the exciton line and linear shift of Landau levels for CdTe is slightly changed in Fig. 3.6 (b) and becomes drastically dominated for higher concentrations by the spin quantization displayed in Fig. 3.6 (c). Phenomenologically the mechanisms seem to be understood, but a microscopic understanding of these diamagnetic semiconductors and alike of these diluted compounds is still missing. Due to the specific bandstructure and the parity of its bands, for these materials electric dipole SHG contributions should not be allowed. But the situation is quite similar for ZnO and conformities are discussed in Section 4.4. The later discussed mechanism responsible for SHG contribution in ZnO could probably provide a microscopic understanding of these materials, too.

Furthermore, in magnetic ordered materials whose magnetic SHG is described by a c-tensor, the magnetic contribution vanishes in the magnetically disordered phase and only crystallographic SHG is observable. This effect is observed e.g. in CuB_2O_4.

A consideration of polarization selection rules and the non-vanishing tensor components enables the discrimination of magnetic and crystallographic contributions. The magnetic contribution is typically orders of magnitudes weaker than the crystallographic SHG [167].
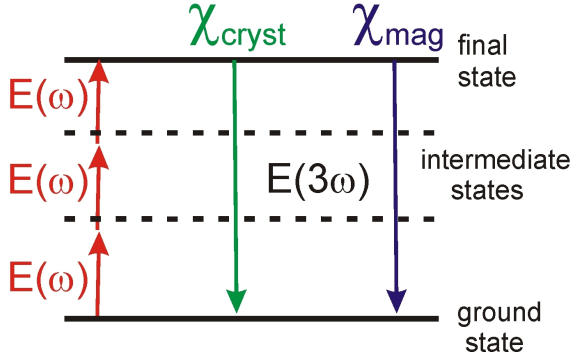
Figure 3.7: *THG process: Three incident photons excite, via two intermediate states, the final state and THG light is coherently emitted. Analogue to SHG crystallographic and magnetic contributions exist as well*

3.1.6 Third harmonic generation (THG)

The process of four interacting waves has already been shown for the corresponding electric dipole process in Eq. (3.8). As a higher order expansion term of the polarization, the THG contribution is obviously weaker than the SHG contribution. Contrary to the electric dipole process of SHG, the THG-process has no restrictions in centrosymmetric materials. Further different source terms of third harmonic generation are written analogously to SHG as:

$$\text{electric dipole moment} \quad : \quad P_i(3\omega) = \varepsilon_0 \chi_{ijkl}^{(ED)} E_j(\omega) E_k(\omega) E_l(\omega)\,, \qquad (3.27)$$

$$\text{magnetic dipole moment} \quad : \quad M_i(3\omega) = \frac{c}{\varepsilon_0 n(\omega)} \chi_{ijkl}^{(MD)} E_j(\omega) E_k(\omega) E_l(\omega)\,, \quad (3.28)$$

$$\text{electric quadrupole moment} \quad : \quad Q_{ij}(3\omega) = \frac{\varepsilon_0 c}{2i\omega n(\omega)} \chi_{ijklm}^{(EQ)} E_k(\omega) E_l(\omega) E_m(\omega) \quad (3.29)$$

As well as for SHG magnetic THG contributions can be found. Such a contribution is discussed for the Europium chalcogenides in Sect. 5.3.

Also the formulation in a microscopic picture leads to a similar transition-probability:

$$\omega_{fg} \propto \sum_i \frac{\langle g|\hat{H}_{int}(3\hbar\omega)|f\rangle \langle f|\hat{H}_{int}(\hbar\omega)|i2\rangle \langle i2|\hat{H}_{int}(\hbar\omega)|i\rangle \langle i|\hat{H}_{int}(\hbar\omega)|g\rangle}{(E_f - E_g - 3\hbar\omega)(E_i - E_g - \hbar\omega)(E_{i2} - E_g - 2\hbar\omega)}\,, \qquad (3.30)$$

The excitation from the ground state happens via two virtual excitations of nonresonant eigenstates, allowed again by the Heisenberg uncertainty principle, see Fig. 3.7. The three incident photons are annihilated and one photon of the frequency 3ω is generated in the same elementary process. The denominator clarifies that in the vicinity of resonances again sharp and narrow lines are expected. Already a simple approach shows a further fundamental consequence of a third harmonic generation process. Based on the nonlinear polarization

$$\mathbf{P}^{(3)}(t) = \chi^{(3)} \mathbf{E}(t)^3, \qquad (3.31)$$

containing an axial tensor of fourth rank χ_{ijkl}, with the Use of the approach of an applied monochromatic light field:

$$\mathbf{E} = \mathbf{E}_0 \cos \omega t, \qquad (3.32)$$

Figure 3.8: *The $\chi^{(3)}$ response of the media to the incident light field leads to intensity dependent refractive index n_2 at the frequency of the incident beam. For positive n_2 the media acts as a positive lens for the beam and self-focussing takes place.*
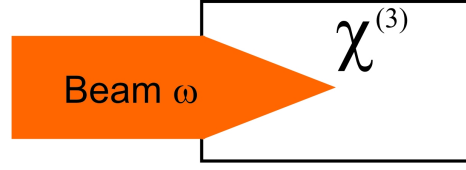
and the additions theorem $\cos^3 \omega t = \frac{1}{4} \cos(3\omega t) + \frac{3}{4} \cos(\omega t)$, the nonlinear polarization can be expressed as:

$$\mathbf{P}^{(3)}(t) = \frac{1}{4} \cos(3\omega t) \chi^{(3)} \mathbf{E}_0^3 + \frac{3}{4} \cos(\omega t) \chi^{(3)} \mathbf{E}_0^3. \tag{3.33}$$

In this expression the expected third harmonic term of the frequency 3ω appears. It describes a response of the material with the frequency 3ω due to an incident light field of the frequency ω. In each elementary event three photons of the light wave are destroyed and a photon of 3ω is generated. In Eq. (3.33) a further nonlinear contribution at the frequency of the incident light field is found. This leads to an intensity dependent refractive index experienced by a light wave at the fundamental frequency. The refractive index n, in the presence of this type of nonlinearity, is expressed by

$$n = n_0 + \underbrace{\frac{12\pi^2}{n_0^2 c} \chi^{(3)}}_{n_2} I, \tag{3.34}$$

where n_0 is the normal refractive index and I the intensity of the incident field. A consequence of this intensity dependent refractive index is self focussing. When a light beam has a nonuniform transverse intensity distribution and propagates through a medium with a positive n_2, the material acts as a positive lens causing the rays to curve toward each other (Fig. 3.8). The practical importance of that process is not to neglect, since the intensity of the self focussed spot often leads to a damage of the material [2]. Thus, the detection of THG is further hindered, the process itself is very weak making high laser intensities necessary. However, in some materials these high intensities could be further focussed inside the sample due to the self-focussing and can lead to a damage of the sample.

3.2 Experimental setup

The field of nonlinear optics requires high intensity light beams and first was accessible with the invention of the laser. In order to provide the desired laser fields, a laser-system consisting of a Nd:YAG-Laser and a BBO based Optical Parametric Oscillator (OPO) were used. The latter allocates a wide tunable spectral region for nonlinear spectroscopy. Low temperatures and high magnetic fields for the investigation of the magnetic properties could be provided by a split coil cryostat.

3.2.1 Nd:YAG-laser

The pump light field for the OPO pumping is provided by a Nd:YAG laser, (Spitlight 600, Innolas) [168]. This laser is divided in the oscillator, the amplifier and the harmonic generators. The oscillator consists of a convex output coupler with a variable reflectivity coating together with a high reflectivity rear mirror to ensure the proper collimation at a specified output. For the pumping of the oscillator and the laser rods, a single xenon flashlamp driven by a high stability power supply is used. The pumped laser rods consisting of a yttrium aluminium garnet crystal, doped with neodymium, produce infrared light of 1064 nm with a repetition rate of 10 Hz.
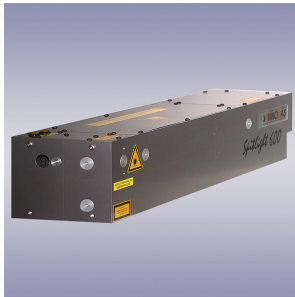
Flashlamp and laser rods are precisely temperature controlled provided by flowing deionized water. A Pockels-cell containing a KD*P crystal and a polarizer enable the Q-Switching. The amplifier rods are mounted in the same pumping chamber as the oscillator and pumped by the same flashlamp. This guarantees perfect synchronization of the oscillator and the amplifier. The output light of 1064 nm is converted by harmonic generation assemblies composed of two type I KD*P crystals. These hygroscopic crystals are mounted in temperature controlled ovens, preventing damage due to moisture, and generate the second and the third harmonic of the fundamental light wave subsequently. Thus, the wave of 1064 nm is transformed to 532 nm(SHG) and then to 355 nm (THG). The maximal output adds up to about 800 mJ per pulse for the fundamental beam. A maximal THG conversion of about 30% can be achieved. This THG output is used to pump the OPO.

3.2.2 Optical parametric oscillator (OPO)

The used OPO, PremiScan midband version (MB) [169], consists of two nonlinear BBO-crystals placed in a computer controlled rotation stage in an optical resonator. Inside the resonator the incident third harmonic beam of the Nd:YAG laser induces two light fields in the chosen crystal by a reversed sum frequency generation process. The induced beams are called idler (I) and signal (S) beams, where the latter is conventional the light wave with the higher energy (Fig. 3.9 (a)). Amplification is achieved by parametric amplification of the difference frequency generation process.

Thereby, the presence of a field of ω_1 stimulates the downward transition that leads to the generation of the ω_2 (Fig. 3.9 (b)). The generation of the ω_1 field reinforces the generation of ω_2 and vice versa. In our case, i.e. the generation of the idler also reinforces the generation of the signal. But the parametric amplification for the used pumping laser is not sufficient so far to accomplish the difference generation process with desired efficiencies. A back coupling of the amplified light field is provided by the optical resonator that already enables the oscillation with weak pumping intensities if the amplification compensates the losses of the resonator.
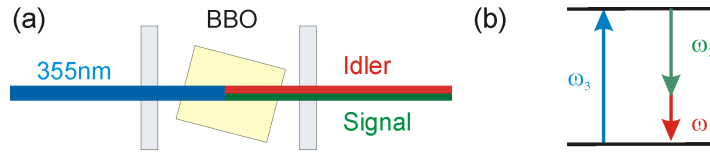
Figure 3.9: *Optical components of an OPO: The OPO consists of a pivoted BBO crystal and a resonator with dielectric mirrors (reflection coefficients R_i). The third harmonic of the light beam emitted by a Nd:YAG laser generates two light waves with different frequencies, the so-called signal and idler light waves, in the BBO crystal.*

Above this threshold, an efficient conversion of the pumping beam into signal and idler beam is possible. For the nonlinear process of the parametric oscillation, conservation of energy and momentum are given by:

$$\text{Conservation of energy:} \quad \omega_P = \omega_S + \omega_I, \tag{3.35}$$

$$\text{Conservation of momentum:} \quad n_P\omega_P = n_S\omega_S + n_I\omega_I, \tag{3.36}$$

$$\text{with} \quad k_i = n_i\omega_i/c,$$

where ω_i is the frequency, k_i is the wave number and n_i is the refraction index of the light wave i. Energy tuning of the idler and signal light waves is achieved by using angle tuning following the phase matching condition Eq. (3.36). Thereby a rotation of the BBO crystal leads to a variation of the extraordinary refractive indices n_S and n_I and consequently to a variation of the energy of the idler and signal beams. The ordinary incident pump beam (355nm) and the ordinary signal beam are polarized perpendicular to the extraordinary idler beam. Thus, type II phase matching is realized.

Two dielectric mirrors, arranged in the plan-parallel Fabry-Perot configuration [170], build up the resonator. Through the first mirror the THG beam is injected and the idler and signal light waves are extracted by means of the second mirror. The mirrors are suitable for the full spectral range of 412-2550 nm, and possess a reflectivity of 99 % and 70 %, respectively, with respect to the signal energy. Two nonlinear crystals beta barium borate β-BaB$_2$O$_4$ (BBO) with a special antireflection coating for the conversion of the third harmonic (355 nm) of the Nd:YAG laser are used. The strong birefringence enables the energy tuning of the signal and idler waves in a large spectral region by means of small rotation angles [171, 172]. The two crystals are optimized for different spectral regions: typical tuning range for the "red" crystal is 514-1145 nm and the typical ranges for the "blue" crystal are 412-514 nm (signal) and 1145-2550 nm (idler). Due to low dispersion and high transmission of the crystals, a large spectral range is accessible; thus, the pumped OPO can provide a light source in a spectral range 412-2550 nm [173]. Most experiments of this work were performed using only the idler light wave in a spectral range of 710-2550 nm (0.5-1.75 eV) allowing measurements of SHG spectra in regions of 1.0 to 3.5 eV. The intrinsic linewidth of the OPO is shown in figure 3.10(b). Typical conversion efficiencies are about 20% and are shown in figure 3.10(a). Dielectric and polarization optics are used to separate the horizontally polarized idler and vertically polarized signal beams and channel them to different output windows.
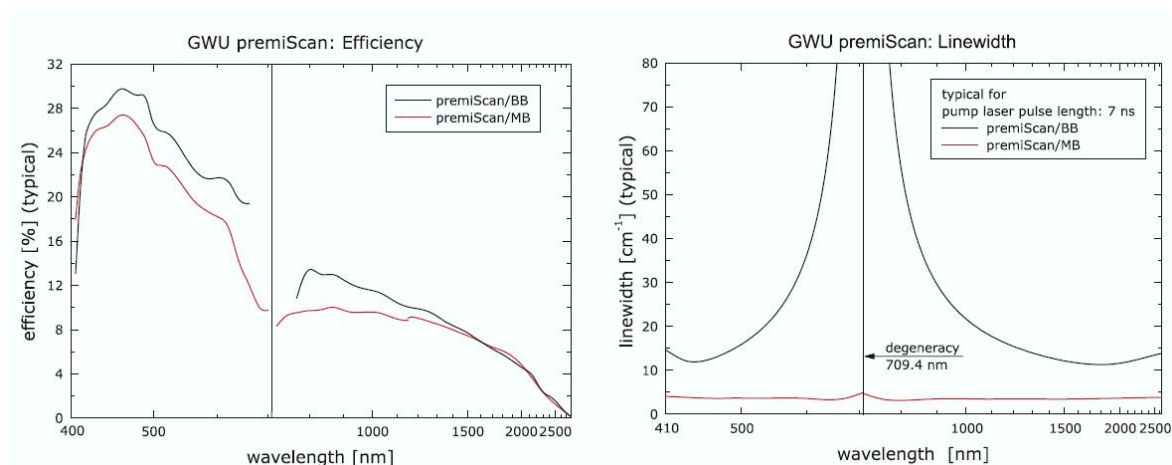
Figure 3.10: *Efficiency (a) and linewidth (b) of the used Optical Parametric Oscillator (PremiScan-MB Version)* [169]

A compensator crystal compensates the spatial shift of the idler/signal output caused by the angle tuning of the crystals. A maximum pulse energy of 70 mJ at 2.3 eV can be achieved with a pulse duration of about 5 ns.

3.2.3   Optical components and split coil magnet cryostat

A Glan-Thompson prism is applied to ensure proper linear polarization of the light beam and a lambda-half wave-plate in front of the Glan-Thompson is used to regulate the beam intensity. Since idler and signal beams are polarized perpendicularly to each other, a selection could easily be provided by this Glan-Thomson prism as well. A second lambda-half wave-plate mounted on a motorized rotation stage enables computer controlled alignment of the polarization of the idler/signal beam. Therefore, this component is called polarizer. Different lenses map the OPO output and focus the incident beam on the sample. A set of filters, see Appendix Table A.1, in a motorized filter wheel, placed in front of the sample, erases second harmonic light of optical components. The sample is usually mounted in an Oxford splitcoil cryostat. This Oxford cryostat enables the feed of external magnetic fields up to 11T in the Voigt-geometry, perpendicular to the direction of the light propagation, and the Faraday-geometry, parallel to the direction of the light propagation [174]. High magnetic fields are generated by a superconducting coil bedded in liquid helium. The liquid helium vessel is isolated by vacuum chambers and liquid nitrogen shields. A needle valve connects the helium vessel and the sample chamber; thus, a cooling to low temperatures becomes possible. By means of a heater and by the application of a pump to the sample chamber, temperatures between 1.6-300 K can be realized. Further lenses behind the cryostat image the induced second harmonic light of the sample to the spectrometer and the CCD-camera. The observed SHG/THG intensities are normalized by the squared/cubic pulse energy of the light transmitted through the sample, using a quartz plate and a photo diode.
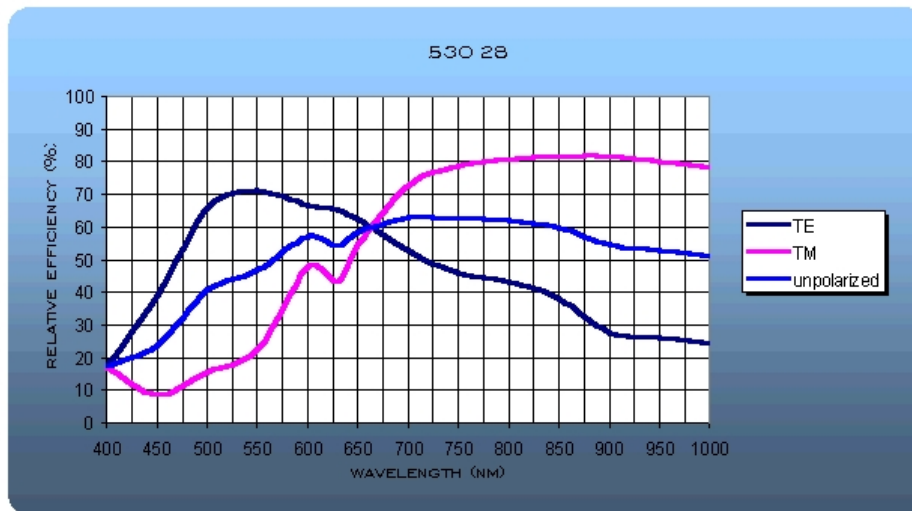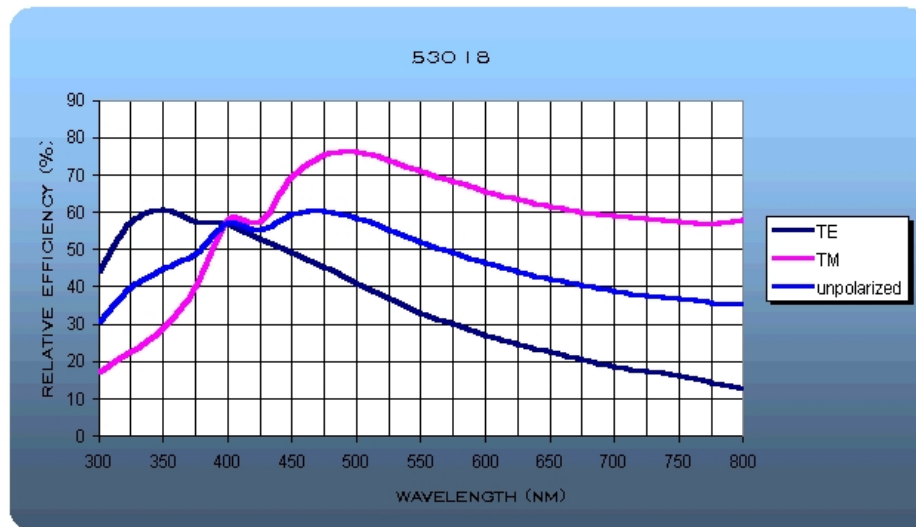
Figure 3.11: *The efficiencies for the grating 530289 blazed at 750 nm. Different colors denote Transversal Electric (TE) and Transversal Magnetic (TM) polarizations and unpolarized light* [176]

Another motorized filter wheel eliminates the transmitted fundamental light wave, see Appendix Table A.2). The analyzer is a polymer polarizing foil mounted on a motorized rotation stage too and offers the polarization dependent detection of the SHG/THG signal. Then a depolarizer depolarizes the light before the spectrometer to avoid detection discrepancies by means of different spectrometer efficiencies for transverse electric and transverse magnetic polarized light fields. The wavelength selective detection is realized by use of a spectrometer.

3.2.4   Spectrometer

The spectrometer HR460, Jobin Yvon, with an aperture (f/5.3) uses a special Czerny-Turner configuration, utilizing an aspheric optical correction [175]. Astigmatism inherent to classical Czerny-Turner Systems is negligible. The incident light beam is focussed onto the entrance slit and collimated by a collimation mirror. This mirror reflects the beam to the dual Grating Turret, consisting of two different gratings that can be chosen computer controlled. One grating is blazed at 400m and is applicable for a spectral range of 200-600nm. The second grating is blazed at 750 nm and is applicable for a higher spectral range of 600-1000nm. The wavelength dependencies for the different gratings are shown in Figs. 3.11 and 3.12. The light is spectrally widened in dependency of the groove density of the grating. The desired wavelength region is computer controlled chosen by the grating reflection angle and the light beam is reflected to a mirror that focusses the beam to the exit slit and the connected CCD. Two swing away mirrors enable the use of side exit and side entrance slits.

Figure 3.12: *The efficiencies for the grating 530183 blazed at 400 nm. Different colors denote Transversal Electric (TE) and Transversal Magnetic (TM) polarizations and unpolarized light* [176]

3.2.5 CCD-camera

An air cooled Pixis charge-coupled device (CCD) camera 256 was used. The Camera core is the CCD-array chip, consisting of a semiconductor. Due to the internal photo-effect, electron-hole pairs are created when a photon incidents. Thereby carriers are collected in a quantum well, which can controlled by an external voltage. Variation of this voltage causes migration of the carriers in the counting direction. The used Pixis-CCD camera possesses an array with a resolution of 256×1024 pixels and a pixel size of 26×26 μm[177]. High sensitivity is given in the range of $200 - 1100$nm. Dark current of this CCD-array is reduced through thermoelectric cooling down to $-70°C$, a four stage Peltier cooling in combination with circulating air. To prevent condensation and contamination, the camera is evacuated. The camera is triggered by the laser pulses to assure the same number of pulses for each measurement period and is connected to the PC via USB 2.0. The camera itself is sensitive to strong magnetic fields. Variations of the cooling temperature and the noise level were observed. In order to avoid such fluctuations, the CCD was shielded by a antimagnetic cage of 0.5mm μ-metal.

3.2.6 Software

The realization of the experiments requires manifold simultaneously performed controls of above discussed and further devices. A program for the control and automatization of measurements was written in LabView and an introduction for the "use of this software" is given in the appendix A.

3.2.7   Experimental configuration

The main interest of the investigations in this work were the spectral dependencies of
the SHG signal and the polarization dependence called anisotropy. The idler or signal
light of the tunable OPO is used for nonlinear optical studies of the materials. The
polarization of the fundamental beam is properly chosen by the polarizer. This polar-
ized light beam is focussed onto the sample, placed in the split coil cryostat providing
the desired fields (0-11 T) in Voigt or Faraday geometry and temperatures (1.6-300 K).
The reference detects the pulse energy of the light transmitted through the sample.
The SHG or THG polarization is chosen by the analyzer. Optical filters separate the
fundamental and SHG light behind the sample. Scattered light as well as two-photon
luminescence, which is strong in semiconductors at low temperatures, is suppressed by
the use of the spectrometer connected to the CCD, that is readout by the computer.
Spectral dependencies are measured by simultaneous tuning of the wavelength of the
OPO and the wavelength of the spectrometer. Desired magnetic fields, temperatures
or polarizations can be regulated by computer control. The polarization dependencies
at a fixed wavelength are investigated by simultaneous rotation of polarizer and the
analyzer foil. Thereby the polarization planes of the incident and SHG light waves are
simultaneously changed. Fig. 3.13 shows the experimental setup.
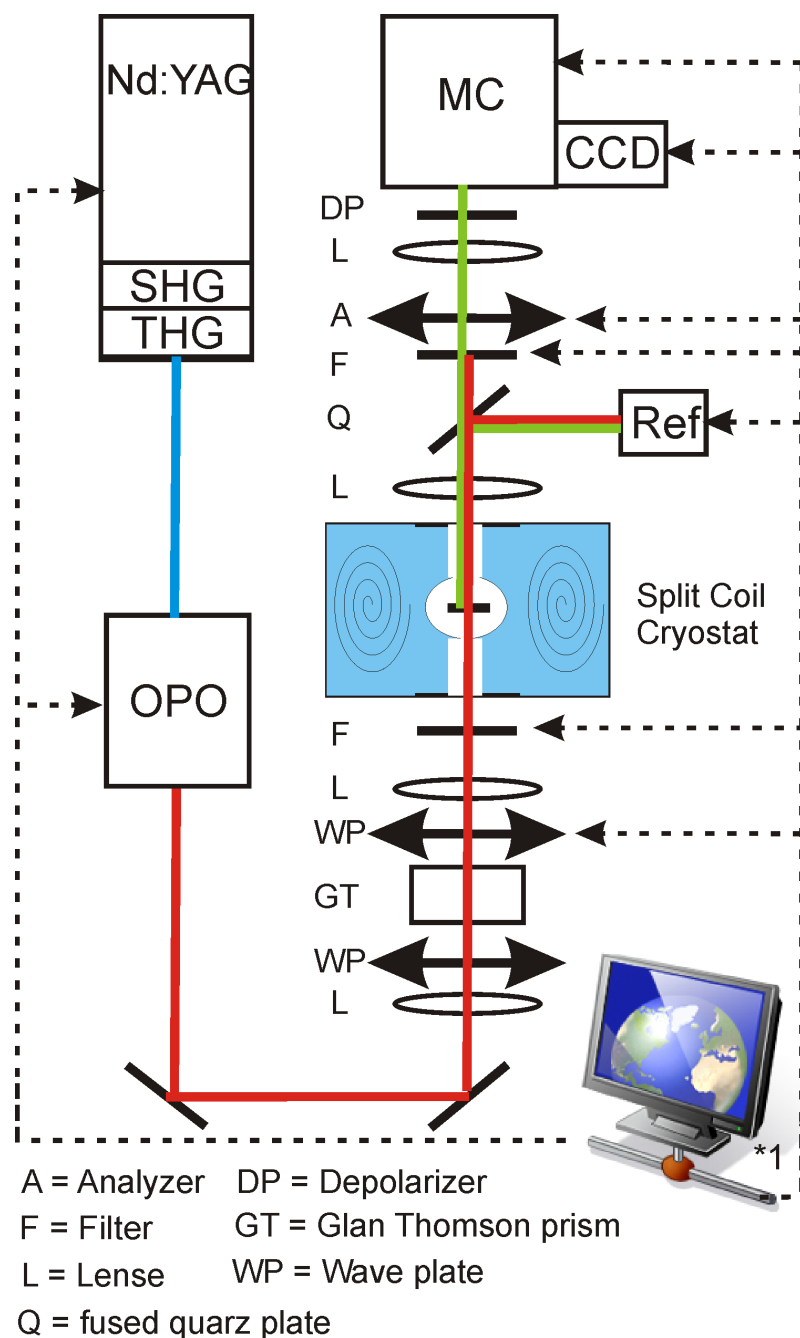
Figure 3.13: *Experimental setup: The fundamental output of the laser is converted into 355 nm (SHG/THG: second/third harmonic), this wavelength is used to pump the OPO: optical parametric oscillator. Proper polarizations of the OPO output are selected by use of a GP: Glan prism and a computer controlled WP: λ/2 wave plate. The SHG/THG signal of the sample in the cryostat is incident via an A: analyzer foil, to the MC: monochromator, and detected by a CCD: charged-coupled-device camera.*

Chapter 4

Nonlinear Magneto-Optics in Zinc Oxide

Already in 1930 the research started on the II-VI compound ZnO. The emphasis of this early research period was aimed at doping, transport, deep centers, band structure, excitons, bulk- and surface-polaritons, luminescence, high excitation or many particle effects and lasing. Because n and p doping of ZnO were not possible, the interest faded away in the 80s. Then the interest relives a revival around 1995 because ZnO holds promises as an alternative compound to GaN in blue/UV optoelectronics, as a cheap, transparent, conducting oxide and as a material for electronic circuits which are transparent in the visible [83]. Therefore, ZnO was subject to manifold linear as well as nonlinear optical studies. As discussed in detail in the last chapter, nonlinear optics has been an active field of scientific and applied research since the 1960s with the optical harmonics generation playing a particular role [1, 2]. These processes involve higher order nonlinear optical susceptibilities and can consequently reveal new and complimentary information about electronic and magnetic structure of solids in comparison to linear optics [159, 160, 70, 178, 179]. The leading role in these studies without any doubt belongs to the second harmonic generation (SHG). In the electric dipole approximation, the SHG process is allowed only in non-centrosymmetric materials and thus, ZnO, a material without a center of symmetry, has already been studied in several works. Although symmetry considerations forbid any SHG for $\mathbf{k}\|\mathbf{c}$, we report on a new contribution in the vicinity of the band gap for this configuration in an external magnetic field.

4.1 Theoretical consideration of harmonic generation in ZnO

Three valence bands A,B, and C are found in ZnO split by the crystal field and spin-orbit interaction (see Fig. 2.3). Due to the mentioned "Neumann" principle, the symmetries of the crystal, the bands and the excitons give us several restrictions for

1 S exciton	strong	weak	paraexciton
A Γ_7	$\Gamma_5(2)$	$\Gamma_1(1)$	$\Gamma_2(1)$
B Γ_9	$\Gamma_5(2)$		$\Gamma_6(2)$
C Γ_7	$\Gamma_1(1)$	$\Gamma_5(2)$	$\Gamma_2(1)$

Table 4.1: Twelve S-excitons: The strong and weak orthoexcitons are allowed. Paraexcitons are spin flip forbidden. The value in brackets gives the degeneracy [81]

all kinds of optical experiments. In the following, these consequences will be discussed in view of the generation of optical harmonics.

4.1.1   Polarization selection rules

According to the group theory, the symmetry of the excitons Γ_{Exc} is obtained by the direct product of the representation of envelope, valence band and conduction band:

$$\Gamma_{Exc} = \Gamma_{Env} \otimes \Gamma_{CB} \otimes \Gamma_{VB} \tag{4.1}$$

For the $1S$-exciton series, twelve $1S$ excitons are found and given in Table 4.1: Paraexcitons are triplet states, spin forbidden and have, therefore, no oscillator strength for electric dipole transitions. The triplet singlet admixture states, Γ_5 and Γ_1 excitons, are called orthoexcitons, are dipole allowed and have an oscillator strength. Since ZnO is uniaxial, these orthoexcitons can be assigned to unique polarizations. The polarization of Γ_5 excitons is perpendicular to the **c**-axes of the crystal, the polarization of Γ_1 excitons is parallel to the **c**-axes. The envelope of P-excitons transforms in C_{6V} as Γ_1 if the envelope is aligned along the **c**-axis (P_0) and as Γ_5 for an envelope perpendicular to the **c**-axis (P_1). Consequently, the P_0 excitons have the same symmetries ($\Gamma_{1S} \oplus \Gamma_1$) as the S-excitons in Table 4.1. Contributions to the $P_{\pm 1}$ envelope of the A, B, and C exciton states are obtained by coupling of the envelope to the S-state [87]:

$$\text{A}2P_{\pm 1}: \quad \Gamma_{\text{A}1S} \otimes \Gamma_5 = \Gamma_1 \oplus \Gamma_2 \oplus \Gamma_6 \oplus \quad\quad \Gamma_5 \quad\quad \oplus \quad\quad \Gamma_5 \tag{4.2}$$

$$\text{B}2P_{\pm 1}: \quad \Gamma_{\text{B}1S} \otimes \Gamma_5 = \Gamma_1 \oplus \Gamma_2 \oplus \Gamma_6 \oplus \quad\quad - \quad\quad \oplus \Gamma_1 \oplus \Gamma_1 \oplus \Gamma_1 \tag{4.3}$$

$$\text{C}2P_{\pm 1}: \quad \Gamma_{\text{C}1S} \otimes \Gamma_5 = \underbrace{\Gamma_5}_{strong} \oplus \underbrace{\Gamma_1}_{weak} \oplus \underbrace{\Gamma_2 \oplus \Gamma_6 \oplus \Gamma_5}_{forbidden} \tag{4.4}$$

By further group theoretical considerations, one can get selection rules for the electric dipole excitation:

$$\langle \varphi_{exc} | ED | g \rangle \neq 0, \quad \Rightarrow \Gamma_{exc} = \Gamma_{ED}. \tag{4.5}$$

Since the ground state g is of Γ_1 symmetry, the excitons can only be excited for the same symmetry of the ED operator. The symmetry and polarizations for the excitation of multi-photon processes (only electric dipole processes) are shown in Table 4.2. Higher order contributions could be calculated as well, but since they are at least one order of magnitude smaller, they are neglected in the following. For the two photon process, an

process	reduction
one photon	$\Gamma_1 = \Gamma_1$
	$\Gamma_5 = \Gamma_5$
two photon	$\Gamma_1 \otimes \Gamma_1 = \Gamma_1$
	$\Gamma_1 \otimes \Gamma_5 = \Gamma_5$
	$\Gamma_5 \otimes \Gamma_5 = \Gamma_1 \oplus \Gamma_2 \oplus \Gamma_6$
three photon	$\Gamma_1 \otimes \Gamma_1 \otimes \Gamma_1 = \Gamma_1$
	$\Gamma_1 \otimes \Gamma_1 \otimes \Gamma_5 = \Gamma_5$
	$\Gamma_1 \otimes \Gamma_5 \otimes \Gamma_5 = \Gamma_1 \oplus \Gamma_2 \oplus \Gamma_6$
	$\Gamma_5 \otimes \Gamma_5 \otimes \Gamma_5 = \Gamma_3 \oplus \Gamma_4 \oplus 3\Gamma_5$

Table 4.2: Symmetries of the states for different numbers of exciting photons in ZnO with wurtzite structure C_{6v}

Figure 4.1: *1- and 2- photon absorption spectra: 1-photon absorption spectrum shown by dashed line. Only S-excitons are observed. Contrary in the corresponding 2-photon absorption spectrum, shown as line, only excitons of P-envelope are excited*[180].
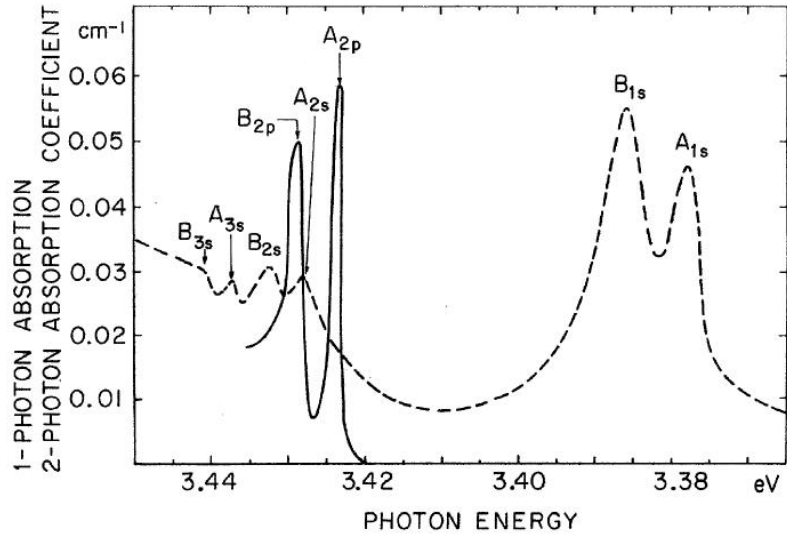
excitation of the Γ_5 exciton requires a polarization component in **c**-direction (Γ_1) and a component perpendicular to the **c**-axes (Γ_5). A light beam with **k**$\|$**c** can only excite the *P*-excitons. Figure 4.1 displays one- and two-photon absorption spectra. Due to the symmetry caused selection rules, the different processes excite different envelope functions of the excitons. However, for SHG electric-dipole processes the situation is different: The required relaxation of the excitation to the ground state must be "electric-dipole" allowed for an one photon process. Therefore, for **k**$\|$**c** normally no SHG contribution of ED-type is expected. However, the relaxation of *S*-excitons to the ground state would be possible, since these excitons are one-photon allowed, but a two-photon excitation is not feasible.

But for a tilted sample with polarization components parallel and perpendicular to the **c**-axes, see Table 4.2, Γ_5 excitations become feasible and the SHG process of electric dipole type allowed:

$$P_i^{ED}(2\omega) = \varepsilon_0 \chi_{ijk}^{(2)} E_j(\omega) E_k(\omega), \tag{4.6}$$

where $\chi_{ijk}^{(2)}$ is a polar third rank i-tensor with nonvanishing tensor components for $6mm$ (C_{6v}) point group:

$$\chi_{xxz}(3) = \chi_{yyz}(3), \chi_{zzz}. \tag{4.7}$$

$\chi_{xxz}(3)$ denotes the distinct unrestricted permutations of the indices xxz. A further restriction has to be taken into account: since the last two indices denote the electric fields or photons, respectively, of the light wave with the same polarization, these indices have to be permutable. The components reveal the necessity of polarization contributions perpendicular and parallel to $\mathbf{z}$ for this SHG-process as well. External perturbations given by external magnetic and/or electric fields enable SHG processes for normal incidence ($\mathbf{k}\|\mathbf{c}$), too. It was found that a magnetic field caused a further perturbation resulting in an electric field next to the well known, the diamagnetic shift and the Zeeman splitting. This magneto-optical Stark effect is explained in more detail in Section 4.1.3. The static electric field SHG contribution can be described by:

$$P_i^{ED}(2\omega) = \varepsilon_0 \chi_{ijkl}^{(SHG)} E_j(\omega) E_k(\omega) E_l(0), \tag{4.8}$$

where χ_{ijkl}^{SHG} denotes a polar, fourth-rank, i-tensor with the remaining tensor components:

$$\chi_{xxxx} = \chi_{yyyy} = \chi_{yxyy} + \chi_{yyxx} + \chi_{yxxy}, \; \chi_{zzzz},$$
$$\chi_{xxyy} = \chi_{yyxx}, \; \chi_{xyxy} = \chi_{yxyx}, \; \chi_{xyyx} = \chi_{yxxy},$$
$$\chi_{xxzz} = \chi_{yyzz}, \; \chi_{yzzy} = \chi_{xzzx}, \; \chi_{yzyz} = \chi_{xzxz},$$
$$\chi_{zzyy} = \chi_{zzxx}, \; \chi_{zyyz} = \chi_{zxxz}, \; \chi_{zxzx} = \chi_{zyzy}, \tag{4.9}$$

The second and third indices denote again the electric fields of the light wave and have, therefore, to be permutable for the electric dipole process given by Eq. (4.8). This leads to a further reduction of remaining tensor components. Since no polarization in $\mathbf{z}$-direction is provided for normal incidence, in this geometry all components with a subscript z vanish as well. According to table 4.2, depending on the direction of polarizations S- or P-excitons THG electric dipole processes are allowed. The ED-THG contribution is given by:

$$P_i^{ED}(2\omega) = \varepsilon_0 \chi_{ijkl}^{(THG)} E_j(\omega) E_k(\omega) E_l(\omega), \tag{4.10}$$

where $\chi_{ijkl}^{(3)}$ is again a polar fourth rank tensor with the nonvanishing tensor components given by Eq.(4.9) likewise. But for the ED-THG process the permutation must be given for the last three indices. Therefore, for ED-THG processes and $\mathbf{k}\|\mathbf{c}$, only the χ_{xxxx} and χ_{yyyy} are excitable.

4.1.2 Modeling of rotational anisotropy

The rotational anisotropy of the second harmonic intensity, detected for simultaneous rotation of linear polarizers for fundamental and SHG light, is a characteristic feature

of the coherent harmonic generation processes and a consequence of above discussed selection rules. The components in Eqs. (4.7) and (4.9) are given in respect to the crystal coordinate system. The crystallographic coordinate system is defined by the crystallographic axes $\mathbf{x}$, $\mathbf{y}$ and $\mathbf{z} \| \mathbf{c}$. The laboratory system is spanned by the light wave vectors $\mathbf{k}(\omega) \| \mathbf{k}(2\omega)$ and the electric field vectors $\mathbf{E}(\omega)$ and $\mathbf{E}(2\omega)$ of the fundamental and the second harmonic (SH) light wave, respectively. In order to obtain the modeling, the photons and the tensor components have to be transformed in the same coordinate system. This can be realized either by the transformation of the electromagnetic field or by transformation of the crystal components. A transformation of the coordinate system of a tensor can be performed by use of Eq. (3.12). The respective transformation matrix depends on the experimental geometry. For crystallographic SHG-contributions, polarizations along and perpendicular to the $\mathbf{c}$-axis are required. Therefore, the (0001) sample was tilted around ϑ between the $\mathbf{c}$-axis and the wave vector $\mathbf{k}$; this experimental geometry is shown in Fig. 4.2. After the transforma-
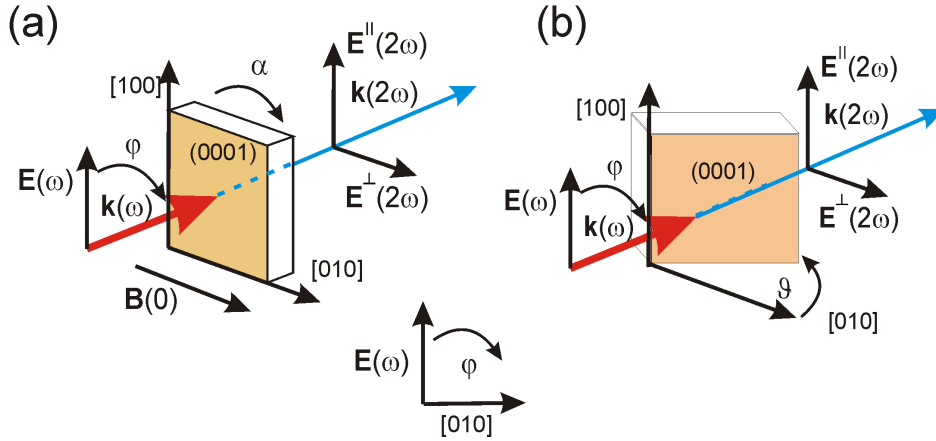
Figure 4.2: *Experimental geometry for normal incidence (a) and tilted sample (b)*

tion, the tensor in the laboratory coordinate system will be inserted in the respective equation for the polarization (here Eq. (4.6)). For $\mathbf{E}(2\omega) \| \mathbf{E}(\omega)$, one obtains the crystallographic contribution $I(2\omega) \propto |\mathbf{P}^{ED}(2\omega)|^2$:

$$
\begin{aligned}
I_\|(2\omega) \propto \quad & (\sin(\alpha + \varphi)(2(2\chi_{xxz} + 2\chi_{yyz} + \chi_{zxx} + \chi_{zyy} + \chi_{zzz}) \\
& + (2\chi_{xxz} + 2\chi_{yyz} + \chi_{zxx} + \chi_{zyy} - 2\chi_{zzz})\cos(2(\alpha + \varphi)) \\
& + \sqrt{3}(2\chi_{xxz} - 2\chi_{yyz} + \chi_{zxx} - \chi_{zyy})\sin(2(\alpha + \varphi))))^2 \ ,
\end{aligned} \tag{4.11}
$$

and for the crossed geometry $\mathbf{E}(2\omega) \perp \mathbf{E}(\omega)$):

$$
\begin{aligned}
I_\perp(2\omega) \propto \quad & ((-3(2\chi_{xxz} - 2\chi_{yyz} - \chi_{zxx} + \chi_{zyy})\cos(\alpha + \varphi) - 3(2\chi_{xxz} - 2\chi_{yyz} + \chi_{zxx} \\
& - \chi_{zyy})\cos(3\alpha + \varphi)) + 2\sqrt{3}(2(\chi_{xxz} + \chi_{yyz} - \chi_{zxx} - \chi_{zyy} - \chi_{zzz}) \\
& + (2\chi_{xxz} + 2\chi_{yyz}\chi_{zxx} + \chi_{zyy} - 2\chi_{zzz})\cos 2(\alpha + \varphi))\sin(\alpha + \varphi))^2,
\end{aligned} \tag{4.12}
$$

where φ is the angle between the polarization plane of the fundamental light and the crystallographic [100] axis and α is the sample azimuthal angle. Detection of
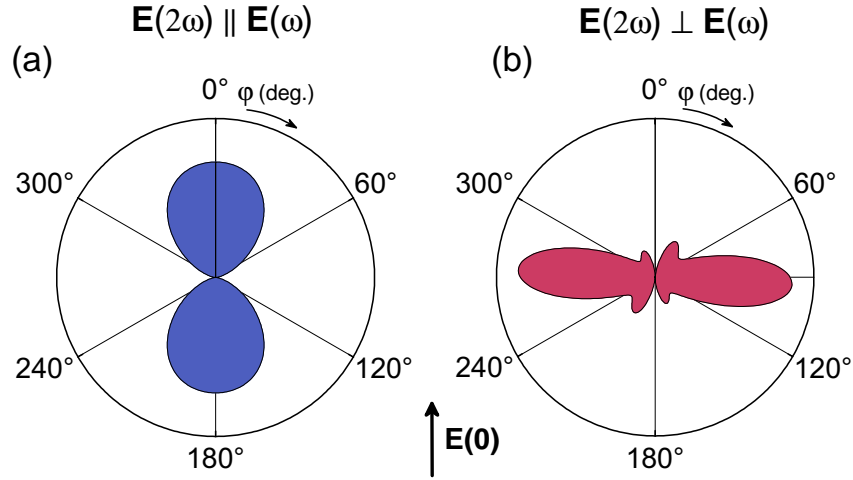
Figure 4.3: *Modeled anisotropies for parallel (a) and crossed (b) polarization configuration.*

the magnetic/electric field induced SHG contribution is also possible for normal light incidence with $\mathbf{k}\|\mathbf{c}$. Modeling of the rotational anisotropy for this process described by Eq. (4.8) results with the tensor components (4.9) and a static electric field in x-direction in

$$I_\|(2\omega) \propto [U((\chi_{yxxy} + 11\chi_{yyxx})\cos(\varphi) + (-\chi_{yxxy} + \chi_{yyxx})\cos(4\alpha + 5\varphi))]^2, \quad (4.13)$$
$$I_\perp(2\omega) \propto [U((3\chi_{yxxy} + \chi_{yyxx})\sin(\varphi) + (\chi_{yxxy} - \chi_{yyxx})\sin(4\alpha + 5\varphi))]^2. \quad (4.14)$$

Theoretically modeled rotational anisotropies are given in Fig. 4.3. The shape of the anisotropy depends strongly on the field direction, but only weakly on crystal orientation.

The simulation for the third harmonic generation process, described by Eq. (4.10), leads to:

$$I_\|(3\omega) \propto [\chi_{xxxx}(3 + \cos 4(\alpha + \varphi))]^2, \quad (4.15)$$
$$I_\perp(3\omega) \propto [(\chi_{xxx}\sin(4\alpha + 4\varphi))]^2. \quad (4.16)$$

4.1.3   Phenomenological description and microscopic model

As discussed in the last section, the crystallographic contribution is allowed only for tilted samples resulting in polarization contributions parallel and perpendicular to the $\mathbf{c}$-axis. For $\mathbf{k}\|\mathbf{c}$ and due to the above discussed selection rules, SHG-contributions should be forbidden. The perturbation induced by an external magnetic field influences only states of the same parity and cannot enable the transitions. The magneto-Stark

Figure 4.4: *SHG electric dipole process for exciton states in ZnO: a two-photon excitation of the 2P excitons is electric dipole allowed, but the relaxation is forbidden. For 2S excitons, the two photon excitation is not electric dipole allowed, but the relaxation would be possible. An admixture caused by the magneto-optical Stark effect enables the SHG process.*
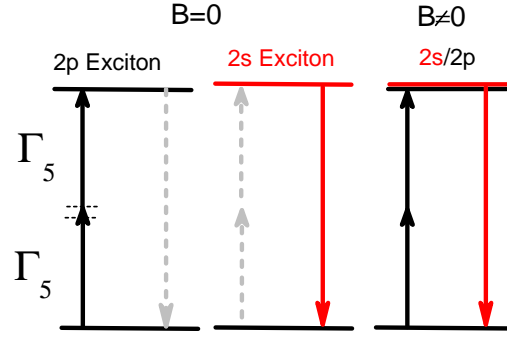
effect found by Thomas and Hopfield in CdS in 1960 is established to be the origin of the observed SHG signal [88, 181, 182]. An external magnetic field produces three different perturbations of the excitonic energy levels, thereby the ordinary Zeeman effect and the ordinary diamagnetic shift are well known. The third perturbation resulting from the center of mass motion of the exciton in the magnetic field with the velocity $\mathbf{v}$ leads to a perturbation equivalent to an electric field $\mathbf{U}$:

$$\mathbf{U} = n\frac{\hbar}{m^*_{exc}}\mathbf{k} \times \mathbf{B} = n\mathbf{v} \times \mathbf{B}, \tag{4.17}$$

representing the effect of oppositely directed Lorentz forces on the electron and hole. The refractive index n of ZnO is $n \approx 2$ for the used spectral region. Equation (4.17) is rightly in most calculations neglected [183].

This effect causes an admixture of the energetically neighbored $2S$ and $2P$ exciton states and higher exciton levels, resulting in a SHG parity allowed transition, see Fig. 4.4.

The $2S$ and $2P$ and higher exciton lines in ZnO are in the vicinity of each other and consequently these are verifiable influenced by the small electric field caused by the magneto-Stark effect. According to Eq. (4.17) with an exciton mass $m^*_{exc} = m^*_h + m^*_e = 0.59m_e + 0.28m_e = 0.89m_e$, a magnetic field of 10 T equates $U \approx 444$ V/cm.

The influence of this quasi electric field can be treated as the typical Stark effect, which is discussed in Section 2.2.5.3. Based on discussions in Section 3.1.4, the transition probability for the SHG process and the oscillator strength can be calculated for example for the $2P/2S$ state by:

$$\omega_{fg} \propto \sum_i \frac{\langle 0|\hat{H}_{ED}(2\hbar\omega)|\varphi_{2P/2S}\rangle\langle\varphi_{2P/2S}|\hat{H}_{ED}(\hbar\omega)|\varphi_{1S}\rangle\langle\varphi_{1S}|\hat{H}_{ED}(\hbar\omega)|0\rangle}{(E_{2P/2S} - E_g - 2\hbar\omega)(E_{1s} - E_g - \hbar\omega)}. \tag{4.18}$$

The state $\varphi_{2P/2S}$ denotes the addition of a contribution of the $2S$ state to the exciton state with $2P$ envelope function, caused by an electric field according to Eq. (2.40), and vice versa:

$$|\varphi_{2S/2P}\rangle = \alpha_1|\varphi_{2P}\rangle + \alpha_2|\varphi_{2S}\rangle, \tag{4.19}$$

and

$$|\varphi_{2P/2S}\rangle = \alpha_1|\varphi_{2S}\rangle - \alpha_2|\varphi_{2P}\rangle. \tag{4.20}$$

The constants α_1 and α_2 can be obtained by calculations considered in Sect. 2.2.5.3 and by the normalization condition $\alpha_1^2 + \alpha_2^2 = 1$:

$$\alpha_1 = \frac{M(U)}{\sqrt{M^2(U) + \left[\Delta + \sqrt{\Delta^2 + M^2(U)}\right]^2}} \tag{4.21}$$

and

$$\alpha_2 = \frac{\Delta + \sqrt{\Delta^2 + M^2(U)}}{\sqrt{M^2(U) + \left[\Delta + \sqrt{\Delta^2 + M^2(U)}\right]^2}}, \tag{4.22}$$

where $M(U) = 3eUa_B^{exc}$ and a_B^{exc} is the excitonic Bohr radius. Δ denotes the half of the splitting of S and P states: $\Delta = (E_S - E_P)/2$. The values of the splitting were read from Fig.(4.1). For the energy distance between A$2S$ and A$2P$ states $\Delta = 2$ meV and for B$2S$ and B$2P$ $\Delta = 1$ meV were found. Since the electric field is expected to be very small, both S- and P- excitons get only small additions of the different parity state. The shifted positions of energy of the S- and P- states are given by:

$$E_{2P/2S} = E_{A,B} - \sqrt{(3ea_B^{exc}U)^2 + \Delta^2}, \tag{4.23}$$

$$E_{2S/2P} = E_{A,B} + \sqrt{(3ea_B^{exc}U)^2 + \Delta^2}. \tag{4.24}$$

$E_{A,B}$ denotes the energy positions, E_A or E_B, of the degenerated A and B states, for example $E_A = (E_{AS} + E_{AP})/2$. For the equivalent quasi electric field of $U \approx 444$ V/cm caused by a 10 T magnetic field, the resulting energy shift is only of the order of magnitude 10^{-5} eV and can, therefore, be neglected.
The total intensity of the SHG signal can be derived by

$$I_{SHG}^{MSE} = P^2(2\omega) \propto \alpha_1^2 \alpha_2^2 \tag{4.25}$$

According to Eq. (4.17), the effect takes only place for **k** being not parallel to **H** and vanishes in the Faraday geometry. Consequently, the investigation of the SHG on ZnO was mainly performed in the Voigt geometry. Due to the applied magnetic field, the diamagnetic shift according to Eq. (2.27) and the Zeeman-term according to Eq. (2.29) have to be included in the considerations as well. A calculation of the Zeeman-term can be done with group theoretical representations; the specific wave functions can be neglected [87]. The P-excitons have the symmetries, see Eqs. (4.2)- (4.4), $P_0(\Gamma_5)$ and $P_{\pm 1}(\Gamma_1, \Gamma_2$ and $\Gamma_6)$. Two Γ_6 states can be distinguished according to the quantum number of the angular momentum of the envelope and are, therefore, denoted as Γ_{6+} and Γ_{6-}. It is found that Γ_1 and Γ_2 states are not eigenstates of the magnetic field

operator, but states that diagonalize this operator can be created by:

$$^P\psi_+ = \frac{1}{\sqrt{2}}(^P\psi_1 - i\,^P\psi_2),$$

$$^P\psi_- \frac{1}{\sqrt{2}}(^P\psi_1 + i\,^P\psi_2), \tag{4.26}$$

where the states with the symmetry Γ_i are denoted by the functions $^P\psi_i$. Furthermore, the magnetic field leads to an admixture of P_0 and $P_{\pm 1}$ excitons; thus, the states $^P\psi_{6-}, ^P\psi_{6+}, ^P\psi_+, ^P\psi_-$ and additively $^P\psi_{5,1}$ and $^P\psi_{5,2}$ have to be taken into account. The diagonalization of the corresponding 6×6 matrix leads to three two-fold degenerated states. One of these states is not influenced by the Zeeman term, whereas the other two states are subject to the Zeeman splitting with the effective $g_{env\perp}$- value, see Eq. (2.29). For A- and B- excitons in ZnO one obtains: $g_{env\perp} \approx 3.27$. A further splitting of the twofold degenerated states proportional to $g_{env\perp}$, based on triplet 2P excitons, was found by Hopfield et al. in CdS [88], Wheeler et al. in CdSe [89] and Miklosz et al. in ZnS [90].

4.2   Samples

ZnO substrate samples (TD1 and TD2) with a thickness of 0.5 mm were hydrothermally grown by the company Crystek. Sample TD1 and TD2 vary in the surface side, which is formed in the case of sample TD1 by Zn-atoms and in the case of sample TD2 by O-atoms. In the following, only results of transmission experiments performed on polished sample TD1 (Zn side) are presented. Crystal orientations within the c-plane were revealed by Laue-measurements.

4.3 Experimental results and discussion

In the following, the experimental results are presented and discussed in view of the above explained selection rules and mechanisms.

4.3.1 Crystallographic SHG
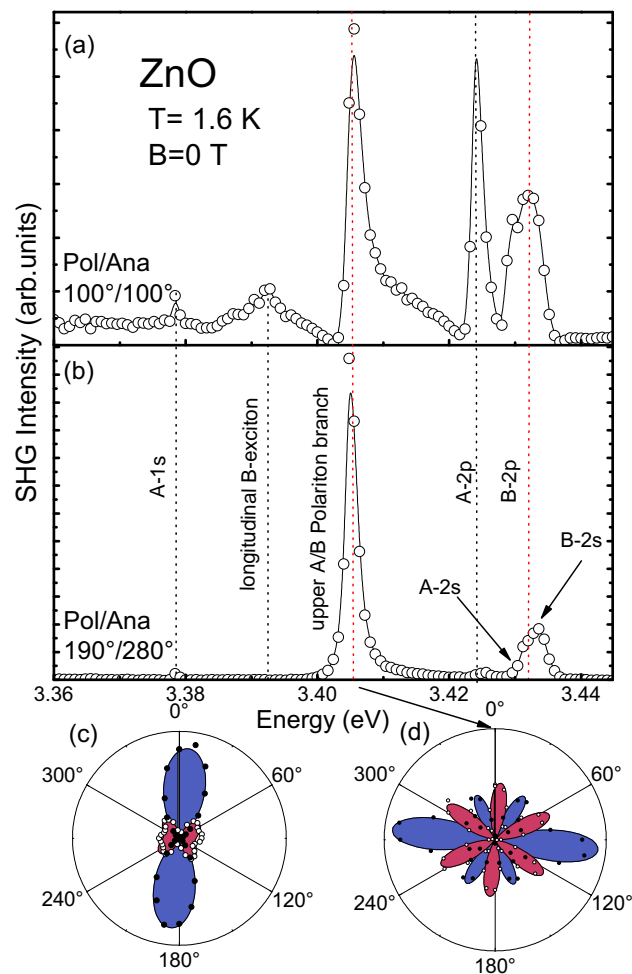
Figure 4.5: *SHG signal due to crystallographic contribution for tilted sample, shown for different polarizer and analyzer configurations in panel (a) and (b). The exciton lines in absorption according to Refs. [91, 180, 184] are signed in as dashed lines and agree with detected resonances. The measured (points) and simulated (shaded areas) anisotropies at 3.4 eV next to a resonance are shown for $E(2\omega)\|E(\omega)$ (blue areas and light points) and $E(2\omega) \perp E(\omega)$ (red areas and dark points) in panel (c) The rotational anisotropies of the resonance at 3.405 eV are displayed in panel (d).*
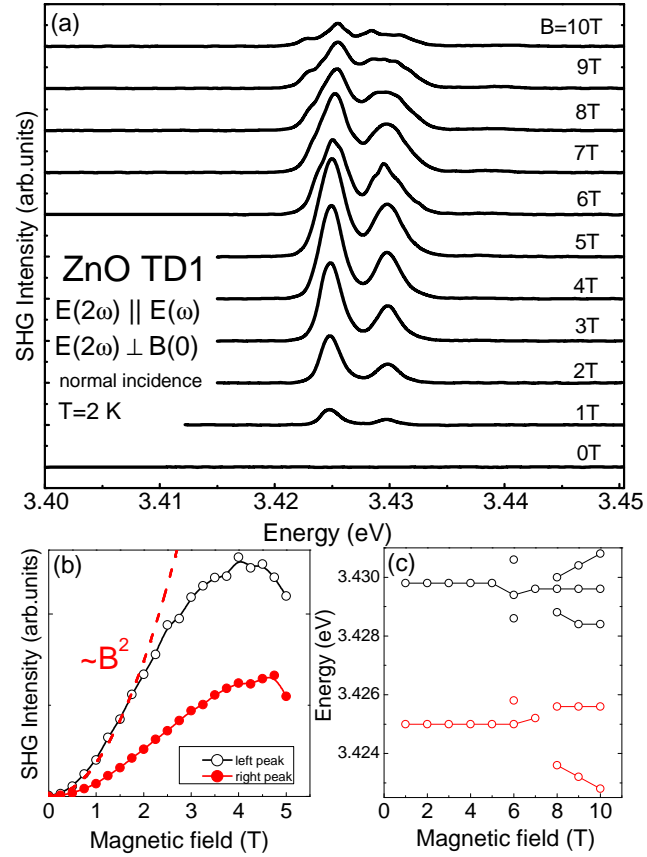
Figure 4.6: *(a) SHG spectra in Voigt-geometry at different magnetic fields. (b) The intensity vs. magnetic field is shown. For comparison, a quadratic plot is displayed. (c) Line shift vs. magnetic field*

Figure 4.5 shows the crystallographic spectra for $E(2\omega)||E(\omega)$ and $E(2\omega) \perp E(\omega)$ and their angular dependencies (anisotropies) for $\mathbf{k}$ being tilt to $\mathbf{c}$ on $\vartheta \approx 45$ (see Fig.4.2). The modeled anisotropies are depicted as shaded areas and experimental data as points. Both are showing good agreement. The strongest contributions are observed for $\varphi = 90°$. One can identify different S and P exciton lines according to Fig. 4.1 [83]. As mentioned in previous sections, for tilted samples the Γ_5 S-excitons are in SHG allowed, since needed polarization components parallel Γ_1 and perpendicular Γ_5 to $\mathbf{c}$ are present. Therefore, different polarization combinations can be provided and SHG light emitted with polarization components parallel to $\mathbf{c}$ could be observed as well. At 3.405 eV the strongest peak is detected. This peak is caused by a mixed-mode exciton-polariton of the upper polariton-branch. The polariton dispersion for the mixed mode polariton is shown in Fig. 2.5.

4.3.2   Magneto-Stark effect induced SHG in ZnO

For normal light incidence ($\mathbf{k}||\mathbf{c}$) without an external magnetic field, the SHG signal should vanish according to the selection rules. Figure 4.6 (a) displays SHG spectra of ZnO for $\mathbf{k}||\mathbf{c}$ recorded at different magnetic fields in Voigt geometry. Indeed, at zero field, no SHG signal is detected in a wide spectral range. However, SHG appears in
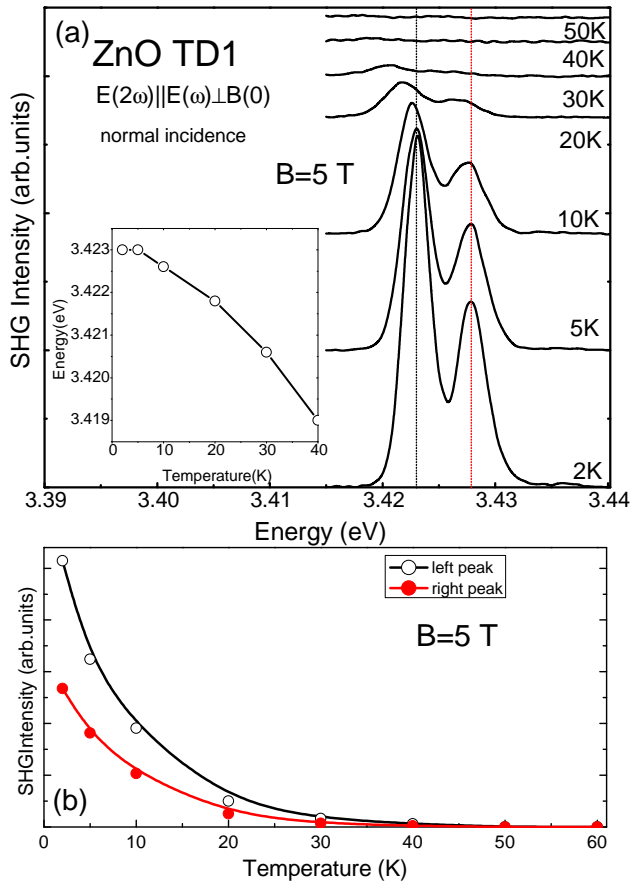
Figure 4.7: *(a) Temperature dependence of SHG spectra for B=5 T. The inset displays the line shift of the lower exciton peak vs. temperature Panel (b) shows the SHG intensity vs. temperature of both exciton peaks.*

an applied magnetic field B in the vicinity of the band gap. Its double peak structure with maxima at 3.425 eV and 3.43 eV is in good agreement with ZnO two-photon absorption spectra shown in Fig. 4.1 [180, 184]. As shown in Fig. 4.6 (b), the integrated SHG intensity increases with an increasing magnetic field strength up to 4 T and decreases again for higher fields. At a fixed magnetic field of $B = 5$ T, the SHG signal continuously decreases with increasing temperature and vanishes at about 40 K (Fig. 4.7(b)). As demonstrated by the insert of Fig. 4.7(a), an energy shift of the peaks is found showing typical band gap behavior [83].

Peaks which only appear in an external magnetic field can be assigned to positions of A and B excitons, having an odd $2P$ and even $2S$ envelope. In lower energy regions no SHG signal is found and no $1S$ exciton is observed. For an external magnetic field applied in Faraday geometry, no SHG signal was detected. Applied magnetic fields up to 10 T do not influence the bandstructure or parity of bands in ZnO. Due to strong exciton binding energies of 60 meV, the applied magnetic field gives only a small perturbation of the excitons according to Eq. (2.20); the condition for the "weak field regime" is fulfilled. Therefore, a change of electronic states by a Landau-level quantization might be excluded. Furthermore, all direct magnetic perturbations are only able to influence and mix states of same parity because a magnetic field perturbation

has even parity. In order to make the SHG contribution for P-Excitons and S-Excitons allowed, an odd parity perturbation is required [185]. This odd perturbation could only be provided by an external static electric field, but in our experiment only a static magnetic field was applied. Consequently, the magneto-Stark effect (Thomas-Hopfield effect) might be responsible for this mixing of states. The magnetic field interacts with the relative movement of hole and electron, resulting in an electric field according to Eq. (4.17). S- and also P- excitons are mixed and should, thus, be observable in an external magnetic field. Therefore, four peaks would be expected due to the S- and P-excitons for A and B bands. However, only two lines are observed. Fig. 4.8 displays
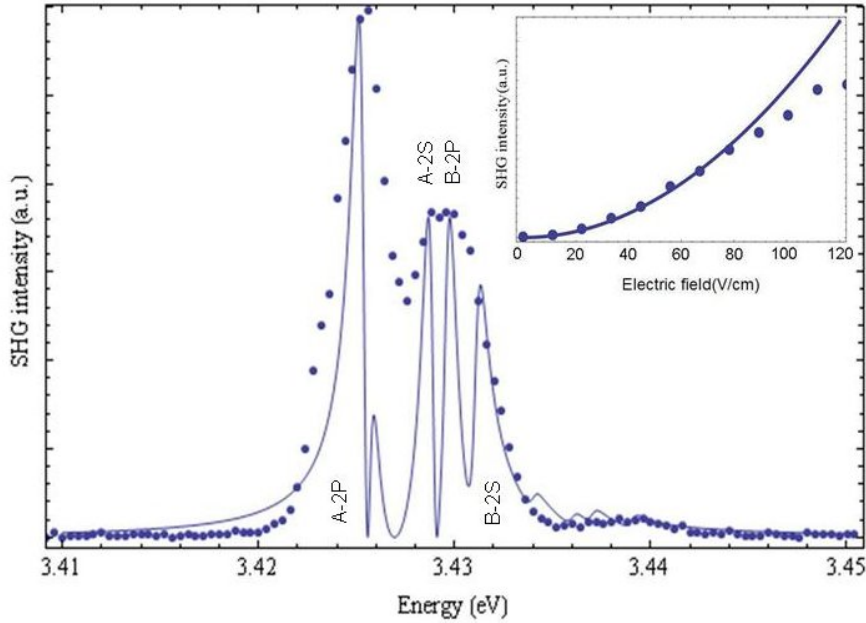
Figure 4.8: *Comparison of simulated spectra (line) and experimental data (points) for $B = 5T$. Inset shows detected and calculated SHG intensity vs. calculated quasi electric field.*

a comparison of a theoretically simulated spectrum, obtained by calculations based on squared Eq. (4.18) for $2S$, $2P$, $3S$ and $3P$ excitons. The energy positions taking into account the influence of the electric fields are given by Eqs. (4.23) and (4.24) and can be used with small changes for other excitons as well. The needed start parameters $E_{A/B}$ of the energy positions and splittings of the excitons were obtained by Fig. 4.1 and the references [180, 81]:

$$E_{A2} = (3.427 \pm 0.001) \text{ eV},$$
$$E_{B2} = (3.430 \pm 0.001) \text{ eV},$$
$$E_{A3} = (3.435 \pm 0.001) \text{ eV},$$
$$E_{B3} = (3.438 \pm 0.001) \text{ eV},$$
$$E_{1S} = (3.37599 \pm 0.00003) \text{ eV}. \tag{4.27}$$

For A2 excitons a splitting parameter $\Delta = 2$ meV and B2 and higher excitons $\Delta = 1$ meV were used. In order to avoid a divergence of the denominator at resonances of Eq.

(4.18), a complex damping $-i\Gamma$-term has to be added in the brackets of the denominator. This damping constant Γ influences the linewidth and was chosen for modeling to $\Gamma = 0.0004$ eV.

Good agreement is obtained between theoretically modeled spectra and experimental data. As one can see, the second peak (around 3.43 eV) consists of three lines: The A-2S exciton line and B-2S and B-2P exciton peaks. But due to line broadening and the limited resolution of the experimental setup (0.4 meV), these neighboring peaks could not be resolved experimentally. The inset of Fig. 4.8 shows the intensity dependency of the detected and calculated SHG signal vs. the quasi electric field. Experimental data points were obtained from magnetic field dependencies (Fig. 4.6 and are plotted versus the quasi electric field determined by Eq. (4.17). Below a quasi electric field of 80 V/cm being consistent with about 2 T, a good agreement is found. Discrepancies and the decrease of the intensity for higher fields can be explained by the ordinary magnetic perturbations [88], because these effects influence the energy positions of S- and P- exciton states (see Eqs. (2.29) and (2.27)) and lift the degeneracy.

The absence of $1S$ exciton lines in the SHG spectra is a further proof of the magneto-Stark effect. Since the distances between odd parity states and the $1S$ states are large ($\frac{3}{4}Ry^*$) and the according dipole transition elements are small, a significant admixture could not be realized by the quasi electric fields applied in our experiments. Moreover, effects on the band structure itself can be excluded. Based on Eq. (4.17), a necessary condition for the Faraday geometry is that the electric field has to vanish and hence the SHG signal as well. Indeed, no SHG signal was detected in Faraday geometry.
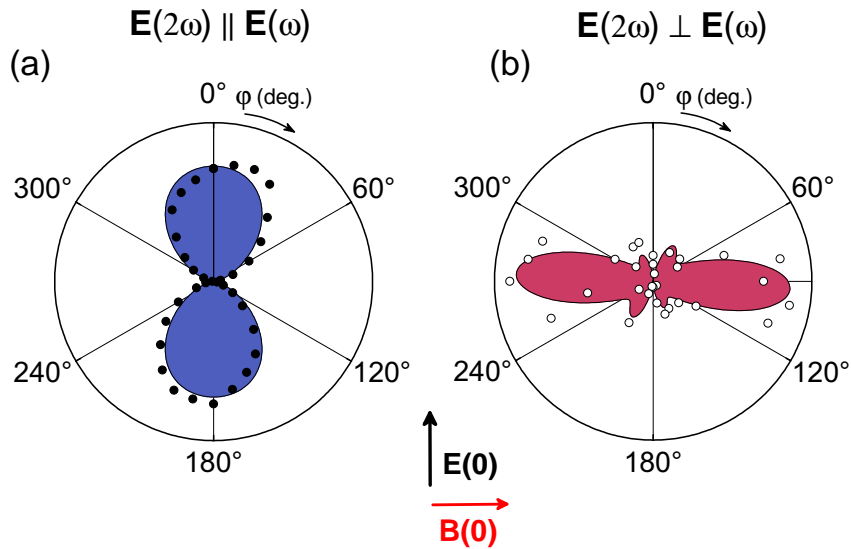
Figure 4.9: *Detected anisotropies for the magneto-Stark effect induced SHG signal are displayed for parallel (a) and crossed (b) configuration. The agreement between theory and experiment confirms the magneto-Stark effect as origin of the SHG signal*

But this criteria is not sufficient, since due to the symmetry of the tensor components

the SHG signal for the Faraday geometry should vanish as well. Modeled (shaded areas) and measured (points) anisotropies are shown in Fig. 4.9. The good agreement for $E(2\omega)\|E(\omega)$ and $E(2\omega)\perp E(\omega)$ confirms the process given by Eq. (4.8) as main mechanism of the detected SHG signal. Strongest contributions are observed in resulting electric field direction for $E(2\omega)\|E(\omega)$. Perpendicular to this induced electric field, no SHG signal is found. Deviations from this calculated behavior, especially for the crossed rotational anisotropy, are due to noise because the detected signal for this configuration was weak.

4.3.3   Third harmonic generation in ZnO

The crystallographic ED-Third Harmonic spectrum is shown in Fig.4.10. It was measured for normal incidence and without magnetic fields. Peaks could be clearly linked
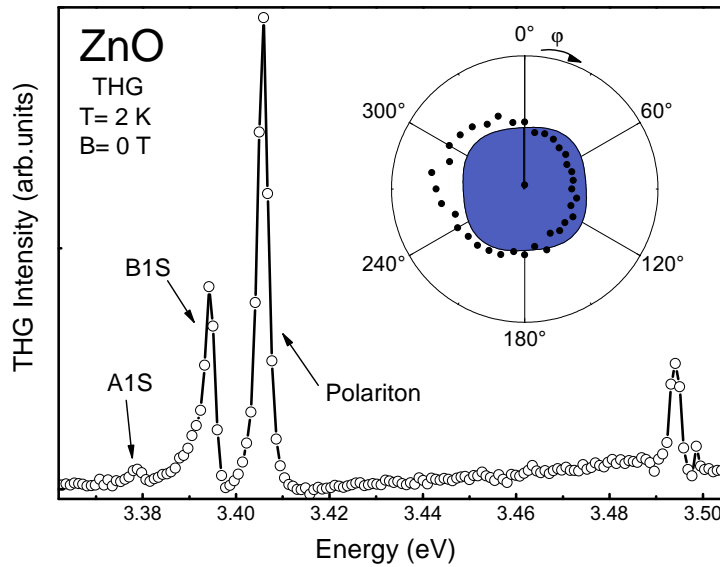
Figure 4.10: *Third Harmonic Generation in ZnO: The process is allowed for the 1s exciton states.*

to excitonic lines and a strong (transverse) polariton peak [81] was observed. By means of the selection rules for three photon process, one recognizes clearly that only Γ_5 excitations are allowed for $\mathbf{k}\|\mathbf{c}$:

$$\Gamma_5 \otimes \Gamma_5 \otimes \Gamma_5 = \Gamma_3 \oplus \Gamma_4 \oplus 3\Gamma_5$$

In normal incidence only Γ_5 polarizations perpendicular to the $\mathbf{c}$ axes could provided. Therefore, a detection of P-excitons is not expected. However, in opposite to the crystallographic and magnetic SHG spectra neither $2S$ excitons nor the $2P$ excitons are observed. The corresponding measured and modeled anisotropies for $\mathbf{E}(2\omega)\perp\mathbf{E}(\omega)$ are shown as inset in Fig.4.10.

4.4   Comparison with GaAs and CdTe

In this section the results of this chapter are compared with another materials where magnetic-field-induced SHG was observed. As accomplished in more detail in Section 3.1.5 in previously studied noncentrosymmetric GaAs and CdTe SHG is allowed at zero magnetic field and the magnetic-field induced SHG signals were shown to be due to Landau-level splitting [37, 186]. But here, a microscopic understanding leading to an allowed transition is still missing. In both material systems, GaAs and CdTe with zinc-blende structure and ZnO with wurtzite-structure, the nonvanishing tensor-components of xyz-type require polarization components in **x**, **y** and **z** direction for crystallographic SHG. Due to this type of nonvanishing tensor components, the crystallographic SHG contribution can easily be suppressed by a proper choice of experimental geometry; thus, a detection of pure MFISH signal is possible. Since the exciton binding energy in GaAs and CdTe adds up to only 4.2 and 10 meV, respectively, magnetic fields below 10 T already cause a Landau-level quantization opposite to the excitonic states in ZnO, which are only weakly disturbed due to the high binding energy of about 60 meV. The above discussed magneto-Stark effect is also present in GaAs and CdTe and influences the parity of involved states as well. According to [71], the excitonic line was identified by its energy position and since the energy saving due to binding energy for example of 4.2 meV in GaAs is only small, higher excitons are energetically situated close to this $1S$ exciton and a detection of a SHG signal caused by an admixture with $2P$ and/higher excitons is possible. The increase of SHG intensity $\propto H^2$ in GaAs and CdTe could be as well be described by the increase of intensity caused by the magneto-Stark effect. However, the detection of a MFISH signal in Faraday geometry contradicts strongly the MFISH signal caused by the magneto-Stark effect. But as discussed in Section 3.1.5 and in several references [71, 69], this 5 times weaker MFISH signal was surprisingly found although an analysis of nonvanishing tensor-components yields the vanishing of electric dipole SHG in Faraday geometry. Therefore, it is obvious that only higher order contributions provide the signal in the Faraday geometry and an inclusion of the spatial dispersion mechanism including magnetic dipole and electric dipole contributions was necessary for detailed explanation of measured anisotropies. A further significant point of the MFISH signal in CdTe and GaAs is the observation of a signal below the critical field at which the orbital quantization starts. The magneto-Stark effect could provide a microscopic explanation and these material systems have to be investigated in more detail in view of this magneto-Stark effect.

4.5   Conclusions

Crystallographic SHG, symmetry allowed for tilted sample, was shown and all features were explained by group theoretical analysis. Based on symmetry considerations and resulting selection rules as well, it was established that no SHG signal is expected even in the presence of an external magnetic field for **k**∥**c**. Because the parity of the involved excitons can not provide simultaneously needed SHG transitions either for the two photon excitation or for the one photon relaxation process. The magnetic

field itself mixes states of same symmetry and in Voigt geometry an admixture of the $P_0(\Gamma_6)$ and $P_{\pm 1}(\Gamma_1$ and $\Gamma_2)$ is caused. Only an electric field could provide such an admixture of odd parity states and this electric field is caused by the magneto-Stark effect, found by Thomas and Hopfield in 1961. Comparisons of experimental data and theoretical considerations of spectra and increase of intensity, modeled anisotropies, symmetry considerations and resulting selection rules proved that this effect could give a microscopic and phenomenological explanation of observed SHG-signals. Further diamagnetic materials for example as GaAs and CdTe, where microscopic models for detected SHG signal are still missing, are definitively subject to this magneto-Stark-effect and several accordances suggest that this effect could be as well responsible for detected magnetic electric dipole SHG signal in the Voigt geometry.

The third harmonic spectrum was shown as well and S-excitons for normal incidence were observed.

Chapter 5

Nonlinear Magneto-Optics in Europium Chalcogenides

As mentioned in Section 2.3, Europium chalcogenides EuX (X=O, S, Se, and Te) are magnetic semiconductors crystallizing in the centrosymmetric cubic rock salt structure $m3m$. They possess unique physical properties determined by the electronic structure in which the strongly localized $4f^7$ electrons of Eu^{2+} ions with spin $S = 7/2$ are involved [109]. EuX are classical Heisenberg magnets, where the competition between nearest and next-nearest neighbor exchange integrals results in magnetic phase diagrams that can include antiferro- , ferri- (FIM), and ferromagnetic (FM) ordering as well as a paramagnetic phase at elevated temperatures [109, 110]. EuTe is antiferromagnetic with a critical field $B_c = 7.2$ T and a Néel temperature T_N=9.6 K, above which it becomes ferromagnetically saturated. EuSe is metamagnetic with $T_N = 4.6$ K and shows a mixed AFM and FIM ordering below 3.4 K. At $T < 4.6$ K and in a magnetic field above a critical value of ≈ 0.2 T, EuSe is in the FM phase [110]. EuX exhibit strong linear magneto-optical effects [109, 120, 121], due to which they attract interest for potential applications in spin injection and magneto-optical devices [145, 128, 134, 125, 127]. Nonlinear optical properties of these materials have not yet been explored.

In this chapter, we report on spectroscopy of the centrosymmetric magnetic semiconductors EuTe and EuSe revealing spin- induced optical second harmonic generation (SHG) in the band gap vicinity at 2.1-2.4 eV. The magnetic field and temperature dependencies demonstrate that the SHG arises from the bulk of the materials due to a novel type of nonlinear optical susceptibility caused by the magnetic dipole contribution combined with spontaneous or induced magnetization. This spin-induced susceptibility opens access to a wide class of centrosymmetric systems by harmonics generation spectroscopy. Furthermore spin-induced optical third harmonic generation was observed and is presented in this Chapter as well.

The Chapter is organized as follows: Section 5.1 deals with theoretical, phenomenological and microscopical considerations of optical harmonic generation. Details of investigated samples are given in Section 5.2, which is followed by Section 5.3, where experimental results are presented and discussed, before we conclude in Section 5.4

5.1 Theoretical consideration of harmonic generation in centrosymmetric solids

5.1.1 Polarization selection rules for SHG

Based on the crystallographic symmetry and the band structure parity, the selection rules for different SHG processes will be determined and used as a basis for the analysis of the azimuthal rotational anisotropy of the SHG signal. Already the centrosymmetry of the EuX delivers a first and strong restriction for the SHG process. So the strongest SHG contribution, the electric dipole contribution, is forbidden in centrosymmetric materials. Further information is revealed by more detailed analysis of the parity of involved bands and possible optical excitation processes. The odd symmetry of the $4f$ valence band is described by $\Gamma_2^- + \Gamma_4^- + \Gamma_5^-$, the symmetry of the even conduction band $5d(t_{2g})$ is Γ_5^+ and for the $5d(e_g)$ band the symmetry is Γ_3^+.

Therefore, in linear optics as well as in the third harmonic generation (THG) the electric dipole induced transitions characterized by Γ_4^- are allowed due to their odd parity.

Since in a SHG process two incident and one outcoming photons (electric fields) are involved, the strongest ED excitation requires two Γ_4^- transitions. It has, therefore, again even parity and is in the present case parity forbidden. Higher order SHG processes, electric quadrupole $\Gamma_3^+ + \Gamma_5^+$ and magnetic dipole Γ_4^+ contributions, have even parity and can consequently not induce a resonant transition in linear optics as well as in nonlinear optics, see Section 3.1.4. For the resonant excitation, an odd SHG process is needed; this can only be provided by the magnetic dipole process [1, 2]:

$$P_i^{CMD}(2\omega) = i\varepsilon_0 \chi_{ijk}^{(2)} E_j(\omega) H_k(\omega), \tag{5.1}$$

consisting of an even magnetic dipole transition and an odd electric dipole excitation [187]. Thereby $E_j(\omega)$ and $H_k(\omega)$ are the electric and magnetic fields of the fundamental light wave, respectively. This polarization is in the following called crystallographic magnetic dipole (CMD) contribution. $\chi_{ijk}^{(2)}$ is an axial third-rank tensor allowed in any medium [76].The crystallographic ED-third-order nonlinear SHG susceptibility χ_{ijk} has been investigated in several works [188, 189].

The same type of tensor describes the Faraday effect if in Eq. (5.1) the light field $H_k(\omega)$ is replaced by an external magnetic field $H_k(0)$, and the polarization $P_i(\omega)$ is excited at the fundamental frequency. In view of the strong Faraday effect in EuX compounds achieving 10^6 deg/cm [119], a significant MD contribution to the SHG is expected [187].

In bulk EuX compounds with the point group $m3m$, the tensor $\chi_{ijk}^{(2)}$ has only one non-vanishing independent component $\chi_{xyz}(c3)$=-$\chi_{xzy}(c3)$ [76], which, however, for all crystal orientations does not lead to any SHG intensity $I(2\omega) \propto |\mathbf{P}^{CMD}(2\omega)|^2$, because of the alternating sign for every axis permutation.

Layers of EuTe and EuSe grown on BaF$_2$ substrate (see chapter 5.2) are known to acquire a small mismatch between sample and substrate lattice constants resulting

in a weak trigonal distortion along the [111]-axis. Evidently this causes a symmetry reduction of the thin EuTe and EuSe layers to the trigonal centrosymmetric point group $\overline{3}m$ in the proximity of the interface [190, 191, 192, 193, 20]. Nevertheless, the centrosymmetry remains and ED as well as EQ contributions cannot be induced. The tensor $\chi_{ijk}^{(2)}$ in this point group has one independent component [76]

$$\chi_{xyz} = \chi_{xzy} = \chi_{yxz} = \chi_{yzx} = \chi_{zxy} = \chi_{zyx}, \tag{5.2}$$

which may produce a small crystallographic MD contribution to the SHG signal if the wave vector of the incident light beam $\mathbf{k}$ is not parallel to one of the fundamental crystal axis $\mathbf{x}$, $\mathbf{y}$ or $\mathbf{z}$.

A new type of nonlinear polarization can be induced if the parent crystal symmetry is broken by either magnetic field or magnetic ordering, both of which we introduce with the magnetic parameter $\mathbf{M}(0)$. The induced magnetic dipole (IMD) nonlinear polarization is

$$P_i^{IMD}(2\omega) = \varepsilon_0 \chi_{ijkl}^{(3)} E_j(\omega) H_k(\omega) M_l(0), \tag{5.3}$$

where $\chi_{ijkl}^{(3)}$ is a polar fourth-rank tensor [76] with non-vanishing tensor components:

$$-\chi_{xyyx} = \chi_{xzzx} = \chi_{yxxy} = \chi_{yzzy} = \chi_{zxxz} = \chi_{zyyz},$$
$$-\chi_{xyxy} = \chi_{xzxz} = \chi_{yxyx} = \chi_{yzyz} = \chi_{zxzx} = \chi_{zyzy},$$
$$\chi_{xxyy} = \chi_{xxzz} = \chi_{yyxx} = \chi_{yyzz} = \chi_{zzxx} = \chi_{zzyy},$$
$$\chi_{xxxx} = \chi_{yyyy} = \chi_{zzzz}. \tag{5.4}$$

5.1.2 Modeling of rotational anisotropies

The polarization dependence of the SHG signal, namely its rotational anisotropy, will be calculated in the following. This rotational anisotropy of the SHG intensity detected for simultaneous rotation of linear polarizers for the fundamental and SHG light is a characteristic feature of the coherent SHG process giving an in-depth view on the symmetries involved. To accomplish modeling of the rotational anisotropy, the components given by Eqs. (5.2) and (5.4) with respect to the crystal coordinate system have to be transformed in the laboratory coordinate system, depending on the experimental geometry. This geometry is shown in Fig. 5.1.

The laboratory system is spanned by the light wave vectors $\mathbf{k}(\omega) \parallel \mathbf{k}(2\omega)$ and the electric field vectors $\mathbf{E}(\omega)$ and $\mathbf{E}(2\omega)$ of the fundamental and the second harmonic (SH) light wave, respectively. The crystallographic coordinate system is defined by the crystallographic axes $\mathbf{x}$, $\mathbf{y}$ and $\mathbf{z}$. Then the transformed tensors will be inserted in the equations for the polarizations. Since EuX samples were grown in [111] direction and experiments were performed in normal light incidence with $\mathbf{k} \parallel$ [111], this geometry will be considered. In the configuration $\mathbf{E}(2\omega) \parallel \mathbf{E}(\omega)$, one obtains for crystallographic contribution $I(2\omega) \propto |\mathbf{P}^{CMD}(2\omega)|^2$:

$$I_\parallel(2\omega) \propto |-\chi_{xyz} \cos 3(\alpha + \varphi)|^2, \tag{5.5}$$
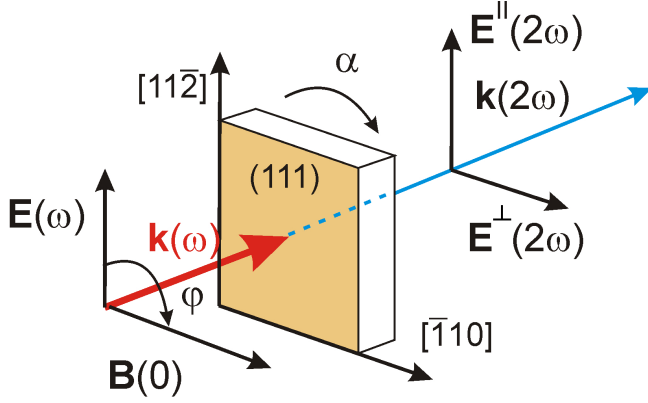
Figure 5.1: *Experimental geometry for SHG in EuX. Same geometry is used for THG experiments.*

and for the crossed arrangement $\mathbf{E}(2\omega) \perp \mathbf{E}(\omega)$

$$I_\perp(2\omega) \propto |\chi_{xyz}\sin 3(\alpha + \varphi)|^2. \tag{5.6}$$

Thereby φ is the angle between the polarization plane of the fundamental light and the crystallographic $[11\bar{2}]$ axis and α is the sample azimuthal angle (Fig. 5.1). As shown in Fig. 5.2(b,d), one gets a sixfold rotation pattern.

The $I(2\omega) \propto |\mathbf{P}^{IMD}(2\omega)|^2$ contribution triggered by an external magnetic field can be modeled by:

$$I_\parallel(2\omega) \propto |\frac{M}{6}(\chi_{xxxx} + 5\chi_{xxyy} - \chi_{xyxy} - \chi_{xyyx})\cos\varphi|^2 \tag{5.7}$$

in the case of $\mathbf{E}(2\omega) \parallel \mathbf{E}(\omega)$. For $\mathbf{E}(2\omega) \perp \mathbf{E}(\omega)$ you will get

$$I_\perp(2\omega) \propto |\frac{M}{6}(\chi_{xxxx} - \chi_{xxyy} + 5\chi_{xyxy} - \chi_{xyyx})\sin\varphi|^2, \tag{5.8}$$

where M is the magnetization. One may pay attention to the fact that this magnetic contribution shows a two-fold pattern Fig. 5.2 (a,c) and is not depending on the orientation of the sample, but strongly on the direction of the magnetization.

In ideal bulk or unstrained films as well as for $\mathbf{k}$ parallel to one of the fundamental crystal axes $\mathbf{x}$, $\mathbf{y}$ or $\mathbf{z}$, the crystallographic magnetic dipole contribution vanishes. But for the present experimental geometry and samples in external magnetic fields, the crystallographic contribution is not absent. Therefore, for proper modeling the interference between IMD [Eq. (5.3)] and CMD [Eq. (5.1)] contributions should be taken into account

$$I(2\omega) \propto |\mathbf{P}^{IMD}|^2 + |\mathbf{P}^{CMD}|^2 \pm 2|\mathbf{P}^{IMD}\mathbf{P}^{CMD}|. \tag{5.9}$$

Here the signs $\pm$ correspond to opposite orientations of $\mathbf{M}(0)$. The SHG intensities for the parallel and perpendicular configurations of fundamental and SHG light polarizations are

$$I_\parallel(2\omega) \propto [\pm\frac{M}{6}(\chi_{xxxx} + 5\chi_{xxyy} - \chi_{xyxy} - \chi_{xyyx})\cos\varphi - \chi_{xyz}\cos 3(\alpha + \varphi)]^2,$$

$$I_\perp(2\omega) \propto [\pm\frac{M}{6}(\chi_{xxxx} - \chi_{xxyy} + 5\chi_{xyxy} - \chi_{xyyx})\sin\varphi + \chi_{xyz}\sin 3(\alpha + \varphi)]^2.$$

The phases of the rotation patterns in Fig. 5.2 are signed by $\pm$ to distinguish between possible constructive and destructive interference geometries.
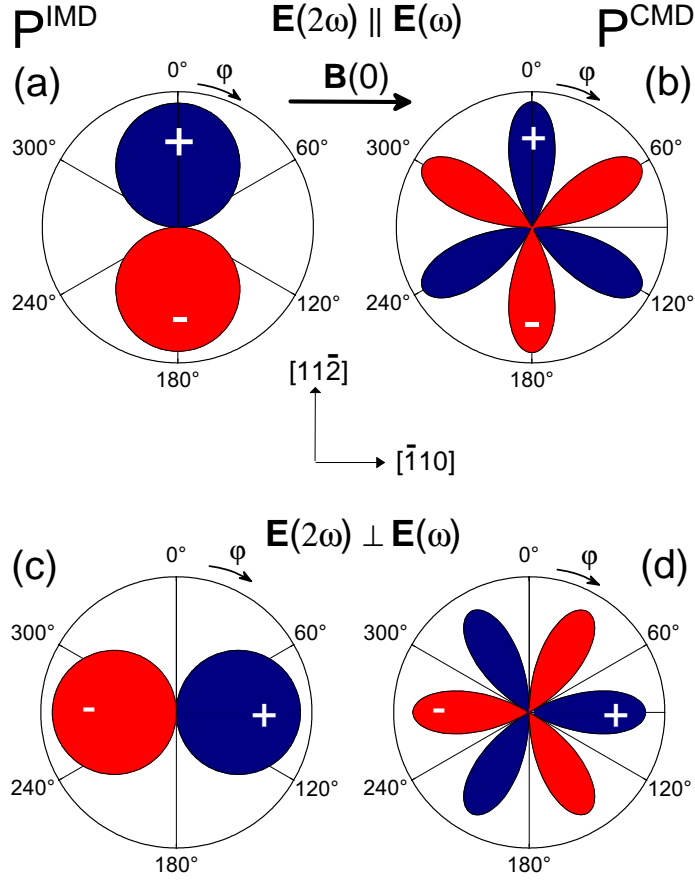
Figure 5.2: *Polar plots for SHG for calculated IMD and CMD nonlinear polarizations. Different colors/signs denote different phases of the SHG contributions.*

5.1.3   Phenomenological description

Below T_N magnetic ordering in, for instance, EuTe can be characterized by the magnetic moments $\mathbf{m}_1$ and $\mathbf{m}_2$ of the two sublattices with $|m_1| = |m_2|$. To describe the magnetic behavior of an antiferromagnet in external magnetic fields, we introduce a FM vector $\mathbf{F}=\mathbf{m}_1+\mathbf{m}_2$ and an AFM vector $\mathbf{A}=\mathbf{m}_1$-$\mathbf{m}_2$. Though $\mathbf{F}$ and $\mathbf{A}$ are composed of the same vectors $\mathbf{m}_1$ and $\mathbf{m}_2$, their transformation properties are different. $\mathbf{F}$ changes sign under time reversal, but not under space inversion; consequently, $\mathbf{F}$ transforms as a MD. The AFM vector $\mathbf{A}$ does not induce any SHG signal, which can be qualitatively understood as follows: at $\mathbf{B} = 0$ vectors $\mathbf{m}_1$ and $\mathbf{m}_2$ are oriented antiferromagnetically. Each magnetic sublattice induces a SHG signal via MD according to Eq. (5.3) with $\mathbf{M}(0) = \mathbf{m}_{1,2}$, but destructive interference from oppositely oriented sublattices annihilates the SHG signal, since the relevant nonlinear polarization is an odd function of $\mathbf{M}(0)$. With increasing magnetic field the AFM ordering is transformed into a FM one

and the destructive interference is continuously reduced. In this case, $\mathbf{M}(0)$ in Eq. (5.3) should be associated with the ferromagnetic vector $\mathbf{F}$. The SHG signal increases with the magnetic field and reaches saturation when the two sublattices become ferromagnetically oriented . Above T_N in the paramagnetic phase $\mathbf{M}(0) = \chi_p \mathbf{B}$, where χ_p is the paramagnetic susceptibility. In EuSe, this spin induced mechanism is responsible for the detected signal as well.

5.1.4 Microscopic model

On the basis of the detected results and the above described mechanism, quantum mechanical calculations were performed [107, 194]. In order to describe the band-edge SHG process in EuX theoretically, we shall consider the restricted set of electronic states described in Sec.2.3.2 and summarized in Fig 2.8. Of course, in real EuX systems, a continuous energy band is present in the background of the ${}^7F_{JM}X$ states [195], but the simplified level scheme is justifiable because it has very successfully described the complex magneto-optical properties observed at the absorption band-edge in EuTe and EuSe [120, 121]. Namely, the electronic levels considered in the analysis consist of a $4f^7 \left({}^8S_{7/2}\right)$ ground state, and ${}^7F_{JM} X$ excited states, where ${}^7F_{JM}$ represents the state of the Eu^{3+} remainder left behind by an electron that has been transferred into an X state. The X state represents a Bloch state belonging to the $5d(t_{2g})$ conduction band, which in the tight-binding scheme is given by

$$X(\mathbf{k}, \mathbf{r}) = \frac{1}{\sqrt{\mathcal{N}}} \sum_{\mathbf{R}} e^{i\mathbf{R}\cdot\mathbf{k}} \phi(\mathbf{r} - \mathbf{R}). \tag{5.10}$$

Here $\phi(\mathbf{r})$ represents one of the $5d(t_{2g})$ Europium orbitals (d_{xy}, d_{yz} or d_{zx}), $\mathbf{R}$ is the position vector of an Eu atom in the lattice, and $\mathcal{N}$ is the number of lattice sites inside the Born-Karmán volume.

Ignoring the Zeeman energies, which are very small in comparison to, for instance, the giant magnetic field dependent $d - f$ exchange interaction, the ${}^7F_{JM}$ levels will have a $2M + 1$ degeneracy. Therefore, the energy of an electronic excitation depends only on quantum numbers J and X, and measured from the ground state, it is given by

$$E_{JX} = E_G + E_J + \epsilon_X(\mathbf{k}), \quad J = 0, \ldots, 6. \tag{5.11}$$

Here $\epsilon_X(\mathbf{k})$ is the energy dispersion of the $5d(t_{2g})$ narrow conduction band (width ~ 100 meV), and E_G is the magnetic field dependent energy bandgap of the EuX system, given by Eq.(2.51) for EuTe. We also assume $T = 0$ K, meaning that the unperturbed electronic system is in the ground state $4f^7 \left({}^8S_{7/2}\right)$.

Two fundamental characteristics of the energy level scheme considered may be pointed out: (i) the energy spread of the excited states is much smaller than the band gap; (ii) all excited states have the same parity, which is opposite to the parity of the ground state. From the first property, it can be surmised that the dominant second order induced polarization will be strongly resonant when the photon energy is about $\hbar\omega \sim \frac{1}{2}E_G$, Therefore, we may discard the anti-resonant contributions [2, 1] to the

induced second order dipole moment. From the second property, electric-dipole matrix elements between excited states vanish. Therefore, the main contribution to the complex amplitude of second-order polarization, parallel to the polarization vector of the exciting light, will be given by

$$P_{x0}^{(2)}(2\omega) = \frac{Ne^3 E_x B_y}{8m_0\hbar\omega} \cdot \tag{5.12}$$

$$\sum_{\substack{JMX \\ J'M'X'}} E_{J'X'} \frac{\langle {}^8S_{7/2}| \sum x_q |{}^7F_{JM}X\rangle \langle {}^7F_{JM}X| \sum (L_y)_q |{}^7F_{J'M'}X'\rangle \langle {}^7F_{J'M'}X'| \sum x_q |{}^8S_{7/2}\rangle}{(E_{J'X'} - \hbar\omega + i\Gamma)(E_{JX} - 2\hbar\omega + i\Gamma)}$$

where $N = 4/a^3$ is the concentration of Eu^{2+} in the lattice, a is the parameter of the face centered cubic lattice of EuX. The relaxation between all excited and the ground state is described by a common parameter Γ. In the above equation, x_q and $(L_y)_q$ represent the x-coordinate and y-component of the angular momentum, respectively, of the $q-$th electron, and the sum is taken over all seven electrons involved in the electronic transitions.

The matrix elements figuring in Eq. (5.12) involve seven electrons, which complicates their calculation. We can, however, convert them into single-electron matrix elements by exploring spin conservation [120, 121]. This is done by first performing a Clebsch-Gordan expansion of the ${}^7F_{JM}$ states, which is then represented by a series of terms with defined electronic spin. Second, we explore the fact that the spin of all electrons is a good quantum number in the ground state. Therefore, the matrix elements of Eq. (5.12) can be expanded in terms of a series of matrix elements of operators that act only on the spatial part of the wave functions, between states with well defined spin.

We can simplify Eq. (5.12) still further by exploring the narrowness of the conduction band, and the non-conservation of the Bloch wave-vector **k** in the matrix elements. The latter is a consequence of the spatial localization of the ground state electrons. Therefore it can be anticipated that a rigorous account of the conduction band energy width will ultimately lead to broadening of the resonances that are characteristic of Eq. (5.12). Taking into account the energy narrowness of the conduction band, we shall incorporate the non-zero conduction band heuristically, in a two-step calculation. In a first step, we ignore the conduction band dispersion, and as a result Eq. (5.12) is converted into

$$P_{x0}^{(2)}(2\omega) = \frac{Ne^3 E_x B_y}{8m_0\hbar\omega} \sum_{JM\phi,J'M'} E_{J'} \left[C^{JM}C^{J'M'} \right]^2 \frac{\langle\phi|x|4fm'\rangle\langle 4fm'|L_y|4fm\rangle\langle 4fm|x|\phi\rangle}{(E_{J'} - \hbar\omega + i\Gamma)(E_J - 2\hbar\omega + i\Gamma)}$$

$$+ \frac{Ne^3 E_x B_y}{8m_0\hbar\omega} \sum_{JM\phi,\phi'} E_J \left[C^{JM} \right]^2 \frac{\langle 4fm|x|\phi\rangle\langle\phi|L_y|\phi'\rangle\langle\phi'|x|4fm\rangle}{(E_J - \hbar\omega + i\Gamma)(E_J - 2\hbar\omega + i\Gamma)}, \tag{5.13}$$

where $m = -M + 3$ and $m' = -M' + 3$, $|4fm\rangle$ represent single-electron $4f$ orbitals of the Eu^{2+} ion, $|\phi\rangle$ is a $5d(t_{2g}$ orbital, and $C^{JM} = (LSM_LM_S|JM)$ is a compact representation of Clebsch-Gordan coefficients with $L = S = M_S = 3$, $M_L = M - 3$.

The conduction band energy width is taken into account in a second step, by convoluting the second harmonic generated intensity that corresponds to Eq. (5.13) with a density of states, $\mathcal{D}(E)$, characteristic of a $5d(t_{2g})$ conduction band

$$I_{SHG}(2\hbar\omega) \propto \int dE \; \mathcal{D}(E - 2\hbar\omega) \left\{Re \; [P_{x0}(2\omega)]\right\}^2. \tag{5.14}$$

To calculate matrix elements $\langle 4f \, m| \, x \, |\phi\rangle$, $\langle 4f \, m'| \, L_y \, |4f \, m\rangle$, and $\langle \phi| \, L_y \, |\phi'\rangle$ appearing in Eq.(5.13), it is first required that the wave functions for the atomic $|4fm\rangle$ state and for the $|\phi\rangle$ state are expressed in the coordinates of the reference frame that is used to describe the propagating light, in which operators L_y and x are defined. This can be done using Wigner functions $D_{m_1 m_2}^{(j)}(\alpha, \beta, \gamma)$, as described in [121], were α, β and γ are angles that define Euler rotations [196].

The amplitude of the second order induced polarization generated by separate magnetic domains present in the sample was calculated using Eq. (5.13). The total polarization was obtained by averaging over all magnetic domains and both spin sublattices. The SHG intensity was calculated using Eq. (5.14).

Although, the Zeeman energies do not enter, the energy level scheme described, which is justifiable because Zeeman energies are negligible in comparison with the $d - f$ exchange interaction, a magnetic field has a profound effect on the SHG efficiency in EuX, because the intensity and direction of an external magnetic field determines the orientation of the Eu^{2+} spins in the EuX lattice [197]. Obviously, the Euler rotation angles will depend on the orientation of an Eu^{2+} spin relative to the reference frame for the propagating light, which has an immediate impact on the matrix elements.

5.1.5 Polarization selection rules for THG

The next higher order of harmonic generation is the third harmonic generation (THG) nearly allowed in all materials. The strongest THG ED process is not complied to such strong symmetry restrictions as SHG. But it is normally about one order weaker than typical ED-SHG contributions. As already mentioned above, the optical band gap at about $2.2 - 2.4$ eV is determined by $4f^7 \rightarrow 5d(t_{2g})$ (Γ_5^+) transition, which for four-photon processes related to THG are allowed in ED approximation. As leading order THG contribution, this will be treated in the following. In the ED approximation the third-order nonlinear optical polarization $P_i(3\omega)$ can be written as [1]

$$P_i^{CED}(3\omega) = \varepsilon_0 \chi_{ijkl}^{(3)} E_j(\omega) E_k(\omega) E_l(\omega), \tag{5.15}$$

where $\chi_{ijkl}^{(3)}$ is a polar forth-rank tensor [76] with non-vanishing tensor components:

$$\chi_{zyyz} = \chi_{xzzx} = \chi_{yxxy} = \chi_{yzzy} = \chi_{zxxz} = \chi_{xyyx},$$
$$\chi_{xyxy} = \chi_{xzxz} = \chi_{yxyx} = \chi_{yzyz} = \chi_{zxzx} = \chi_{zyzy},$$
$$\chi_{xxyy} = \chi_{xxzz} = \chi_{yyxx} = \chi_{yyzz} = \chi_{zzxx} = \chi_{zzyy},$$
$$\chi_{xxxx} = \chi_{yyyy} = \chi_{zzzz}. \tag{5.16}$$

Due to permutability of the three incident photons, described by the last three of the four indices, $\chi_{xyxy} = \chi_{xxyy} = \chi_{xyyx}$ must be valid. Therefore, one can reduce the number of independent components to two, namely χ_{xxyy} and χ_{zzzz}. As a result, we can easily write down $I(3\omega) \propto |\mathbf{P}^{CED}(3\omega)|^2$ for the parallel configuration $\mathbf{E}(3\omega) \parallel \mathbf{E}(\omega)$

$$I_\parallel(3\omega) \propto |(\chi_{xxxx} + 3\chi_{xxyy})|^2 \tag{5.17}$$

and for the crossed configuration $\mathbf{E}(2\omega) \parallel \mathbf{E}(\omega)$

$$I_\perp(3\omega) = 0. \tag{5.18}$$

Only for $\mathbf{E}(3\omega) \parallel \mathbf{E}(\omega)$ a THG signal should appear and show an isotopic behavior (Fig. 5.3).

In the presence of an external magnetic field applied in the Voigt geometry or a resulting magnetization, respectively, a further induced ED contribution appears:

$$P_i^{IED}(3\omega) = i\varepsilon_0 \chi_{ijklm}^{(4)} E_j(\omega) E_k(\omega) E_l(\omega) M_m(0), \tag{5.19}$$

where $\chi_{ijkl}^{(4)}$ is an axial fifth-rank tensor [76]. The full set of non-vanishing tensor components is given by [198, 76]

$$\begin{aligned}
-\chi_{xyzxx} &= \chi_{xzyxx} = \chi_{yxzyy} = -\chi_{yzxyy} = -\chi_{zxyzz} = \chi_{zyxzz}, \\
-\chi_{xyzzz} &= \chi_{xzyyy} = \chi_{yxzzz} = -\chi_{yzxxx} = -\chi_{zxyyy} = \chi_{zyxxx}, \\
-\chi_{xzyzz} &= \chi_{xyzyy} = \chi_{yzxzz} = -\chi_{yxzxx} = -\chi_{zyxyy} = \chi_{zxyxx}, \\
-\chi_{xyxzx} &= \chi_{xzxyx} = \chi_{yxyzy} = -\chi_{yzyxy} = -\chi_{zxzyz} = \chi_{zyzxz}, \\
\chi_{xxyzx} &= \chi_{xxzyx} = \chi_{yyxzy} = -\chi_{yyzxy} = -\chi_{zzxyz} = \chi_{zzyxz}, \\
-\chi_{xyxxz} &= \chi_{xzxxy} = \chi_{yxyyz} = -\chi_{yzyyx} = -\chi_{zxzzy} = \chi_{zyzzx}, \\
-\chi_{xxyxz} &= \chi_{xxzxy} = \chi_{yyxyz} = -\chi_{yyzyx} = -\chi_{zzxzy} = \chi_{zzyzx}, \\
-\chi_{xyyzy} &= \chi_{xzzyz} = \chi_{yxxzx} = -\chi_{yzzxz} = -\chi_{zxxyx} = \chi_{zyyxy}, \\
-\chi_{xyyyz} &= \chi_{xzzzy} = \chi_{yxxxz} = -\chi_{yzzzx} = -\chi_{zxxxy} = \chi_{zyyyx}, \\
-\chi_{xxxyz} &= \chi_{xxxzy} = \chi_{yyyxz} = -\chi_{yyyzx} = -\chi_{zzzxy} = \chi_{zzzyx}.
\end{aligned} \tag{5.20}$$

Here the second, third, and fourth index of the susceptibility denote the direction of the incident photons, which are undistinguishable. Thus, these indices have to be permutable. By means of this permutability and the given direction of the applied magnetic field, only four independent components remain.

For simulations of the rotational anisotropies of the spin-induced contribution in the Voigt-geometry, these components lead to the following dependencies for $\mathbf{E}(3\omega) \parallel \mathbf{E}(\omega)$

$$\begin{aligned}
I_\parallel(3\omega) \propto |\sqrt{6}M(3\chi_{xyzzz} + 6\chi_{zyxzz} + 2\chi_{zyyyx} - 3\chi_{zyzzx})\cos 3(\alpha + \varphi)\sin\varphi + \\
3\sqrt{6}M(\chi_{xyzzz} - 2\chi_{zyxzz} - 2\chi_{zyyyx} + 3\chi_{zyzzx})\cos\varphi\sin 3(\alpha + \varphi)|^2, \quad (5.21)
\end{aligned}$$

and for the crossed arrangement $\mathbf{E}(3\omega) \perp \mathbf{E}(\omega)$

$$\begin{aligned}
I_\perp(3\omega) \propto |\sqrt{6}M(3\chi_{xyzzz} - 6\chi_{zyxzz} + 4\chi_{zyyyx} + 3\chi_{zyzzx})\cos\varphi\cos 3(\alpha + \varphi) + \\
3\sqrt{6}M(3\chi_{xyzzz} + \chi_{zyyyx})\sin\varphi\sin 3(\alpha + \varphi)|^2. \quad (5.22)
\end{aligned}$$
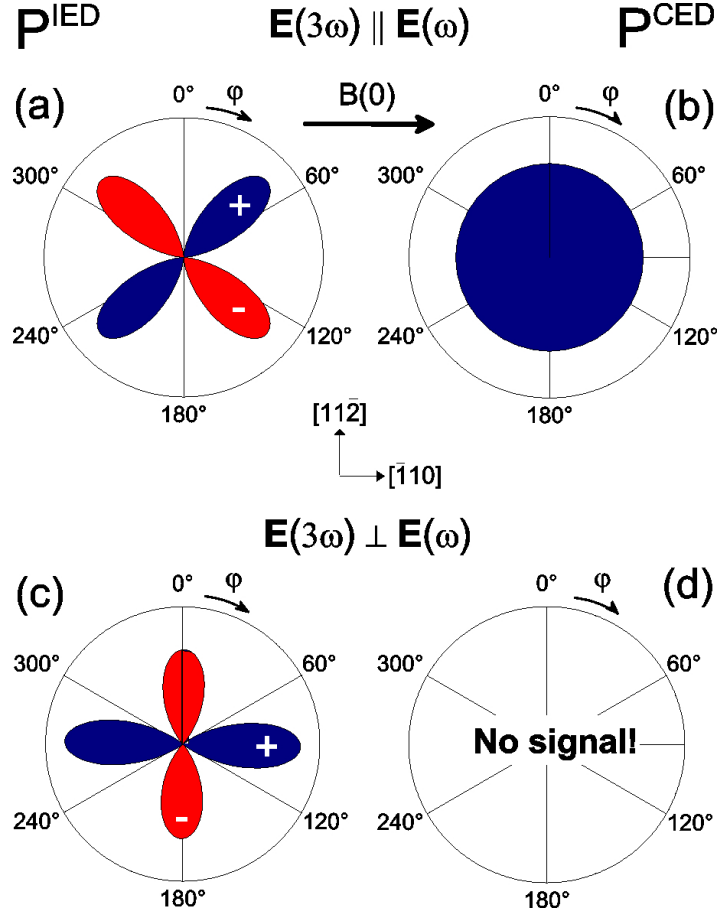
Figure 5.3: *Polar plots for THG for calculated IED and CED nonlinear polarizations with m3m symmetry.*

Once again, both contributions are present in an applied magnetic field. So for THG the interference between IED [Eq. (5.21)] and CED [Eq. (5.17)] contributions should be taken into account

$$I(3\omega) \propto |\mathbf{P}^{IED}|^2 + |\mathbf{P}^{CED}|^2 \pm 2|\mathbf{P}^{IED}\mathbf{P}^{CED}|. \tag{5.23}$$

The THG intensities for the parallel and perpendicular configurations of fundamental and THG light polarizations, thus, are given by

$$I_{\parallel}(3\omega) \propto | -18(\chi_{xxxx} + 3\chi_{xxyy}) \pm \sqrt{6}M(3\chi_{xyzzz} + 6\chi_{zyxzz} + 2\chi_{zyyyx} - 3\chi_{zyzzx})\cos 3(\alpha + \varphi)$$
$$\sin\varphi \pm 3\sqrt{6}M(\chi_{xyzzz} - 2\chi_{zyxzz} - 2\chi_{zyyyx} + 3\chi_{zyzzx})\cos\varphi\sin 3(\alpha + \varphi)|^2, \tag{5.24}$$

$$I_{\perp}(3\omega) \propto | \pm \sqrt{6}M(3\chi_{xyzzz} - 6\chi_{zyxzz} + 4\chi_{zyyyx} + 3\chi_{zyzzx})\cos\varphi\cos 3(\alpha + \varphi) \pm$$
$$3\sqrt{6}M(3\chi_{xyzzz} + \chi_{zyyyx})\sin\varphi\sin 3(\alpha + \varphi)|^2. \tag{5.25}$$

Figures 5.3 (a,b) show the rotational anisotropies for a specific choice of tensor components and the shapes varies strongly with the choice of values for χ_{xyyx} and χ_{yxyx}.

5.2   Samples

The investigated EuX samples have been grown by molecular-beam epitaxy (MBE) on (111) BaF$_2$ substrate [123, 120]. One sample EuTe (7074) was grown in Brazil and the other EuTe samples (Va496 and Va494) were grown in Linz. The 1 μm thick EuTe layers were capped with a 40-nm-thick BaF$_2$ protective layer. EuSe samples (Va497 and Va495) with an epilayer thickness of 500 nm, grown by MBE on (111)BaF$_2$ substrate as well, were also capped with a 40-nm-thick BaF$_2$ protective layer. BaF$_2$ is transparent in the desired SHG region and no substrate SHG and THG contributions were found. The high sample quality was confirmed by X-ray analysis. Differences in lattice constants of epilayer (EuTe, 6.598Å / EuSe, 6.195 Å) and substrate (BaF$_2$, 6.200 Å) lead to a lattice mismatch of about 6% for EuTe and 0.08% for EuSe. In explored EuTe and EuSe samples this mismatch results in a residual trigonal distortion in the [111] direction. In the case of our one micron thick films, X-ray diffraction revealed a residual perpendicular strain of about 0.1%. A further mismatch, increasing the distortion, is a difference in the thermal expansion coefficients. The stronger influence of crystallographic contributions for EuSe, despite the smaller lattice mismatch, is based on less thickness.

It is important to mark that, although, the detected spin induced SHG originates from the bulk, epilayers have been used for the investigations: Thin homogeneous epilayers grown by the use of MBE own very high quality in comparison to bulk single crystals. The superior quality of MBE grown materials in comparison to bulk crystals was proved in several studies in the last decade [110, 199]. As the presented results are higher order nonlinear effects,a high sample quality is a very important and sometimes even decisive factor for observing second harmonic generation, irrespective of the microscopic mechanisms involved. Requirements such as chemical stoichiometry and stability of sample, structural and optical homogeneity, absence of impurities, partial SHG phase matching conditions, etc. are easier to fulfill in MBE epilayers than in bulk crystals. Epilayers used in this study have a thicknesses of about 1 μm, which can be regarded as bulk-like epilayers with physical properties similar, but superior, to those in bulk crystals.
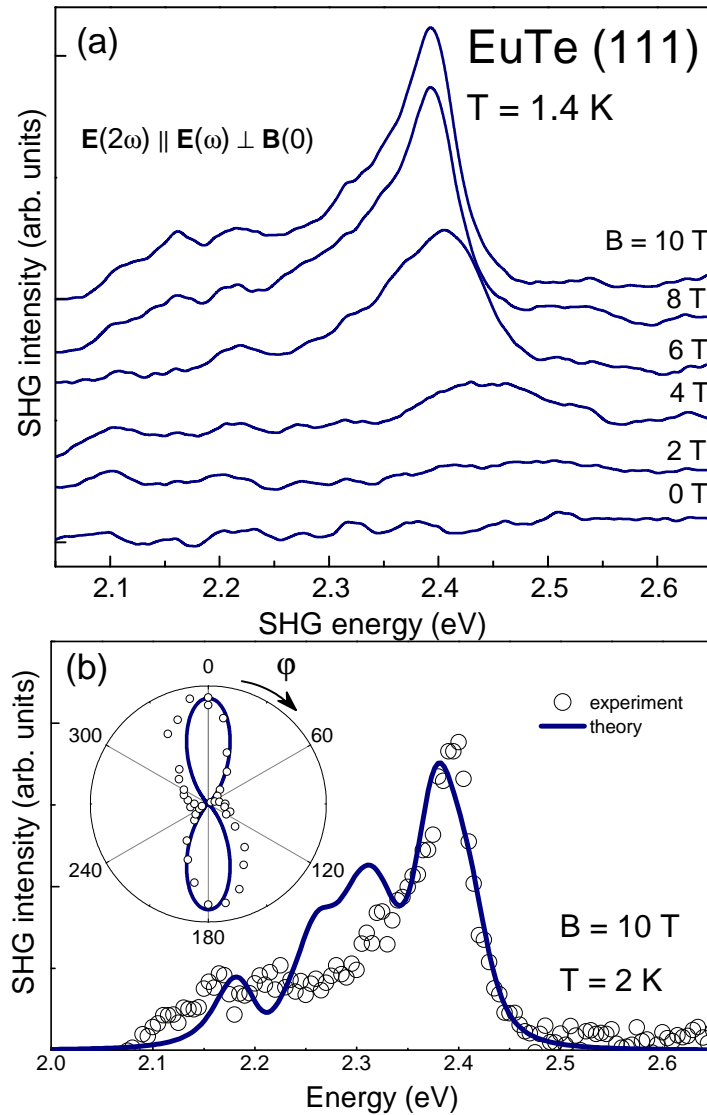
Figure 5.4: *(a) SHG spectra of EuTe (sample VA 496) shown for different magnetic fields applied in the Voigt-geometry. (b) Comparison of calculated SHG spectra (line) [107] and experimental results (points) for 10 T.*

5.3 Experimental results and discussion

5.3.1 Second Harmonic Generation in EuTe

Figure 5.4(a) displays the SHG spectra of EuTe recorded at different magnetic fields. At zero field, no SHG signal was detected in a wide temperature range below and above T_N. Consequently, we can conclude that the symmetry reduction caused by the trigonal strain is very weak and not sufficient to break the inversion symmetry.
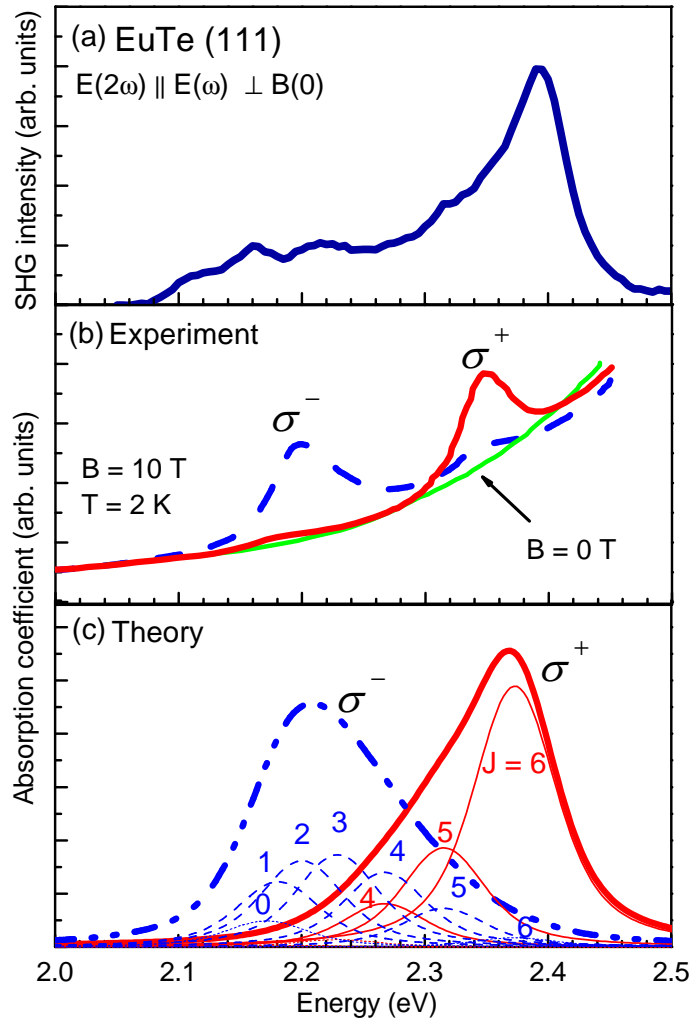
Figure 5.5: *Comparison of detected SHG spectra (samples VA 496 and 7074)(a) and linear absorption spectra (b). Panel (c) shows that the observed broad absorptions peaks are built of an overlap of seven peaks with the different quantum numbers J.*

However, SHG appears at finite B in the vicinity of the band gap and its spectral shape with a maximum at 2.4 eV and a shoulder at 2.2 eV is in good agreement with EuTe absorption spectra (Fig. 5.5) [120, 121]. Two lines were observed in these absorption measurements. It was revealed that two different sets of the seven transitions could be separately excited by circular polarized light, σ^+ and σ^- polarizations, see Fig. 5.5 (c).

In Figure 5.6, the integrated SHG intensity is shown increasing with field and saturating for $B > 7.5$ T. As is indicated by the arrows, this magnetization stems from a continuous transformation of the AFM ordering at $B = 0$ to the FM one above B_{sat}.
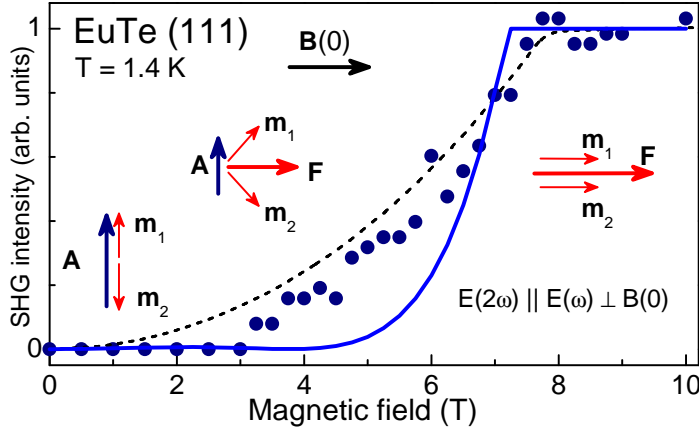
Figure 5.6: *Integral SHG intensity as function of magnetic field. Solid line gives theoretical calculated SHG increase vs. magnetic field. Dashed line gives normalized $M^2(T)$ after Ref. [200].*

The calculated intensity increase is shown as solid line and the correspondence of the theory and experiment is remarkable, although, the calculations neglected interference of crystallographic and spin induced magnetic dipole contributions. Therefore, it is evident that the SHG mechanism in EuTe is controlled by the spin polarization of Eu^{2+} induced by external magnetic fields. SHG spectra for different temperatures are shown in Fig. 5.7. At a fixed magnetic field of $B = 10$ T, the SHG intensity in the vicinity of the gap decreases continuously with increasing temperature and vanishes at about 50 K. As demonstrated by the inset of Fig. 5.7, this decrease follows approximately a $M^2(T)$ dependence [200]. Above T_N, the SHG signal is obviously related to the paramagnetic spin polarization.

Detected rotational anisotropies for EuTe are displayed in Fig. 5.8. The clearly two-fold rotation patterns are obviously based on the P^{IMD}. In Figure 5.8, the pure magnetic dipole contribution is depicted as a line. Experimental data (points) and IMD contribution are in satisfactory agreement. The quasi-twofold patterns induced by P^{IMD} can be qualitatively understood as follows: The external magnetic field induces a magnetic dipole in the sample and the incident light wave interacts via the oscillating electric or magnetic field with this magnetic dipole. In the case when the exciting fields are applied in the magnetic dipole direction, the strongest interaction takes place. The oscillating magnetic dipole moment is the source of the SHG signal and since electric and magnetic fields in light waves are perpendicular to each other, an outgoing SHG polarization can only be provided perpendicular to the magnetic dipole. The negligible role of the CMD contribution for EuTe is confirmed by the fact that the magnetic field dependence of the SHG intensity $I(2\omega) \propto M^2$, as seen in Fig. 5.4(b). However, taking into account the weak sixfold crystallographic contribution caused by strains, the accordance could be significantly increased. Thus, both contributions and their interference are verified to be involved. The fit taking into account P^{IMD} and P^{CMD}, with a ratio for $P^{IMD} : P^{CMD}$ of 6 : 1, are illustrated as shaded areas.
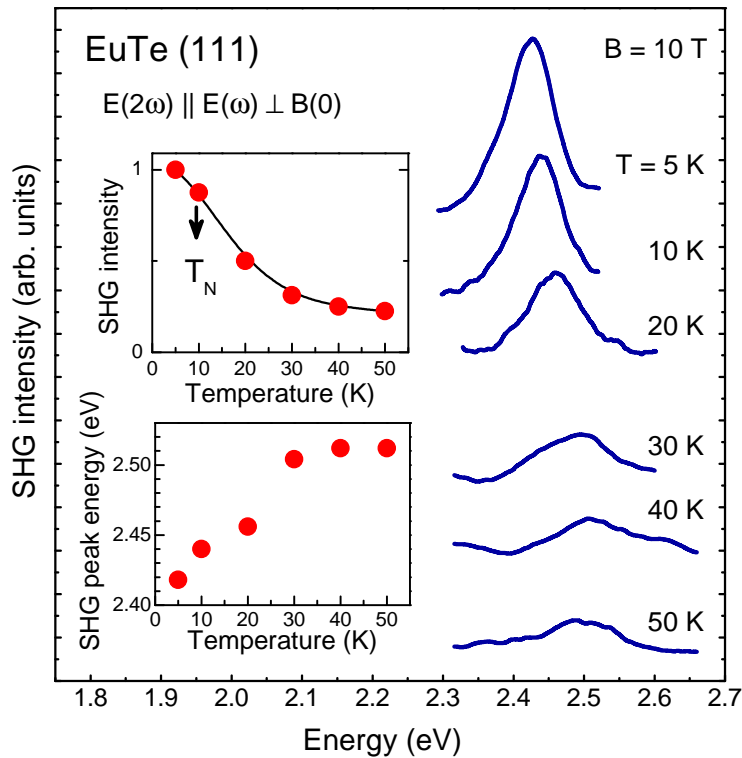
Figure 5.7: *SHG spectra of EuTe (sample VA 496) for different temperatures. Spectra are offset by 0.2 relative to each other. Upper inset shows peak SHG intensity as function of temperature. Lower inset shows peak energy shift vs. temperature.*

5.3.2   Second Harmonic Generation in EuSe

The experiments on EuSe confirm the spin induced mechanism despite its complicated magnetic phase diagram [110]. Figure 5.9(a) shows that in the vicinity of the optical band gap around 2.1-2.4 eV again a clear SHG signal appears at finite B, which is absent at $B = 0$. However, for different polarization geometries $\mathbf{E}(2\omega) \perp \mathbf{E}(\omega) \| \mathbf{B}(0)$ and $\mathbf{E}(2\omega) \| \mathbf{E}(\omega) \perp \mathbf{B}(0)$, peaks at different energy positions are detected. The magnetic field dependence of the corresponding SHG intensity is shown in Fig. 5.9(b) for two experimental geometries with $\mathbf{E}(2\omega) \perp \mathbf{E}(\omega)$ and $\mathbf{E}(2\omega) \| \mathbf{E}(\omega)$. In both cases, the SHG intensity increases in a steplike manner with increasing field, and shows two saturation regions, one between 0.01 and 0.2 T and a second one above 0.2 T.

These steps are in good agreement with the critical fields for the magnetic phase transitions of EuSe [110]. It gives us a clear proof that the measured SHG arises from the bulk of the sample and not from the surface [11], because critical fields at the surface, and in particular in antiferromagnets, differ radically from those in bulk.

To account for the interference of CMD and IMD contributions in EuSe, we compare in Fig. 5.9(b) $I(2\omega)$ with a $[a + bM(B)]^2$ dependence taking $b/a = 4$ similar to
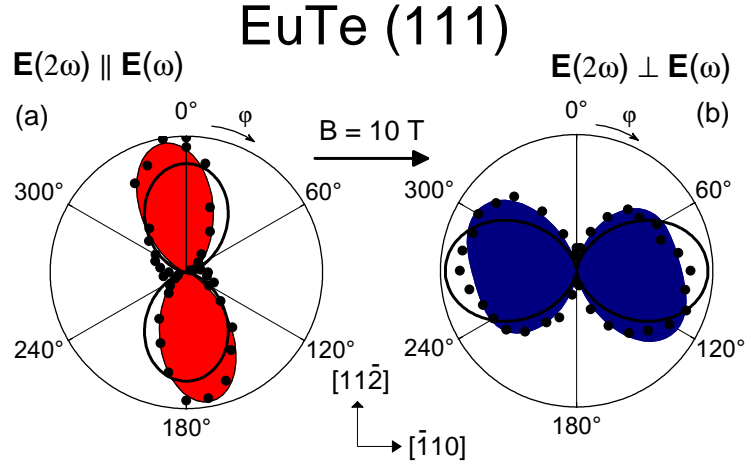
Figure 5.8: *Polar plots of experimental SHG (sample 7074) intensity data (dots) at 2.4 eV and T= 2 K. Best fits based on Eqs. (4) and (5), taking into account the IMD (IMD and CMD) are shown by solid lines (shaded areas).*

$P^{IMD}/P^{CMD} = 4$ for the saturated magnetization. The observed asymmetry in the field dependence of EuSe is well explained. Detected SHG signals are based on the FM component of the spin system in EuX, which induces the MD contribution to SHG. The role of the external magnetic field is to induce the ferromagnetic component **F**. SHG signals are also observed above T_N, when the magnetic field polarizes the Eu^{2+} spins in a paramagnetic phase. Thus, an application of the magnetic field to EuX leads to a new type of MD nonlinearity. It can be treated as a counterpart to electric field application to centrosymmetric media, which breaks space inversion symmetry and allows ED-SHG processes. The shape of SHG spectra is sensitive to the temperature, as illustrated in Fig.5.10. At temperatures below 1.8 K (in AFM I phase) a double peak structure is observed for $\mathbf{E}(2\omega)\perp\mathbf{E}(\omega)$ that was not observed for other temperatures.

As already mentioned in Section 2.3.3, EuSe shows manifold magnetic phases due to the competition of ferromagnetic and antiferromagnetic interactions of nearest neighbors and next nearest neighbors, respectively. This leads to a strong temperature and magnetic field dependence; therefore, one would expect a strong influence of the temperature to the spin induced SHG signal in EuSe, too. The temperature dependence of the SHG signal for $B = 1$ T is shown in Fig. 5.10(c). Indeed, the SHG signal decreases rapidly and already about 15 K it vanishes completely.

Figure 5.11 presents the rotational anisotropies for different field directions $B = 1$ T or -1 T, respectively. Evidently, the anisotropies depend strongly on the field direction and show clear discrepancies to the pure induced magnetic dipole contribution (P^{IMD}, thin line). A stronger influence of the crystallographic contribution was found and a modeling taking into account both contributions results in a ratio of $P^{IMD}/P^{CMD} = 4$. The shape of the anisotropies of Fig. 5.11(a),(d) and Fig. 5.11(b),(c), even for different
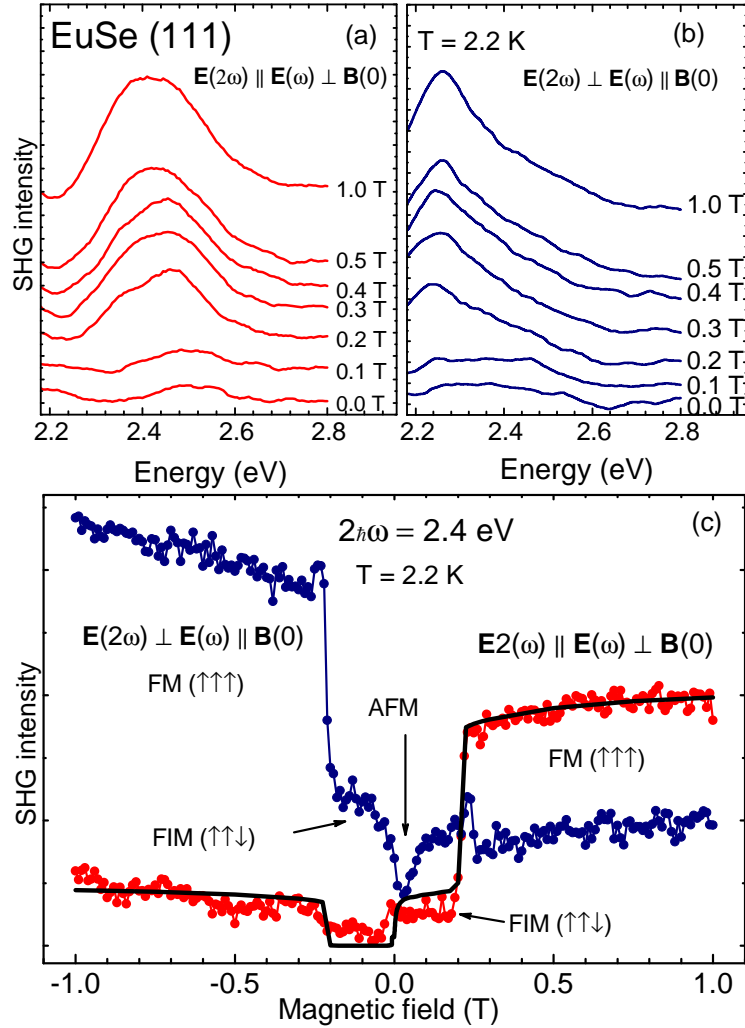
Figure 5.9: *(a,b) Magnetic-field-induced SHG spectra in EuSe (sample VA 497) shown for different magnetic fields and two different measurement geometries. (c) SHG intensity vs magnetic field. The line gives normalized $[a + bM(B)]^2$ with $b/a = 4$ and $M(B)$ after Ref. [110].*

geometries, is similar.

The influence of the sample orientation on the anisotropy shape is displayed in Figs. 5.12. The angle α between the crystallographic $[\bar{1}10]$ axes and the applied magnetic field was changed and then the anisotropy measurements performed. An alteration of two-fold to four-fold anisotropies and vice versa is observed. Sample rotations about $\alpha = 60°$ (Fig. 5.12) yield the same influence as an inversion of the magnetic field direction (Fig. 5.11). Reflecting the crystal symmetry, the system is invariant to rotations about $\alpha = 120°$. The behavior of the shape in dependence on the magnetic field direction and on the sample orientation could be understood as follows: The
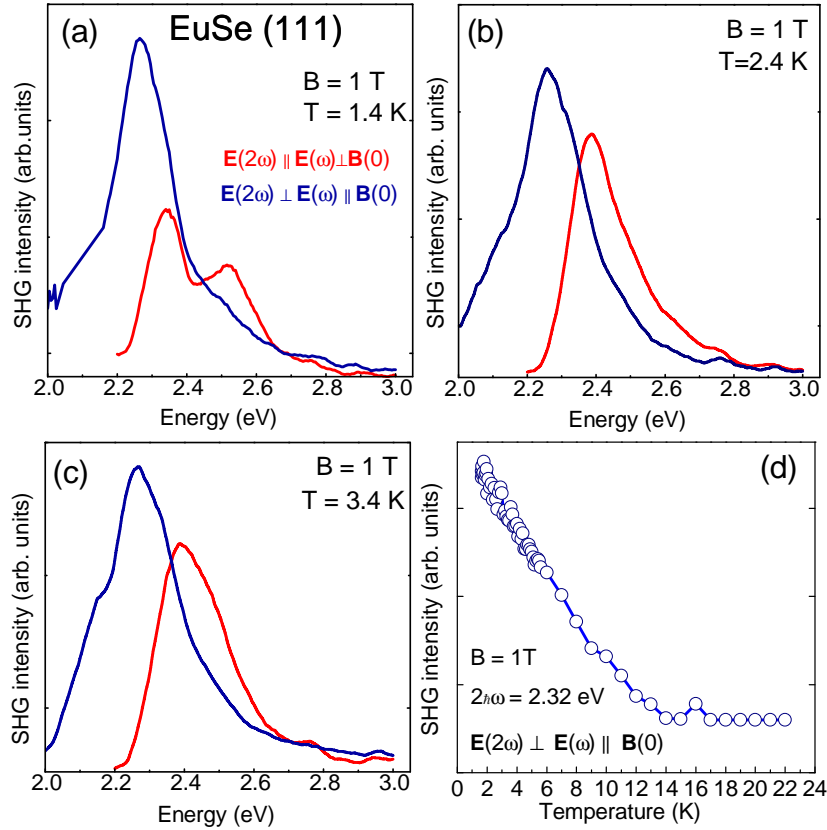
Figure 5.10: *(a)-(c) SHG spectra of EuSe (sample VA 495) for different temperatures below $T_N = 4.8$ K and two different experimental geometries.(d) Peak intensity vs. temperature*

twofold magnetic contribution is always aligned perpendicular to the magnetic field for $\mathbf{E}(2\omega)\|\mathbf{E}(\omega)$ geometry, only depending on the orientation of the magnetic moments. The crystallographic contribution itself is completely independent of the magnetic field but logically influenced by crystal orientation. As it was shown in Fig. 5.2, the different patterns of the anisotropies possesses different phases. When, therefore, the sample is rotated, the sixfold crystallographic contributions are rotated as well and interfere with the fixed twofold magnetic contribution. Thereby an overlap of patterns with different phases leads to destructive interference, of patterns with same phases to constructive interference. An inversion of the magnetic field results in an inversion of the phases of the magnetic contribution. Analogy is found to the Faraday effect in linear optics. This Faraday effect is an interference phenomenon as well, however, consisting of a strong crystallographic contribution responsible for the refractive index and a smaller magnetic contribution.
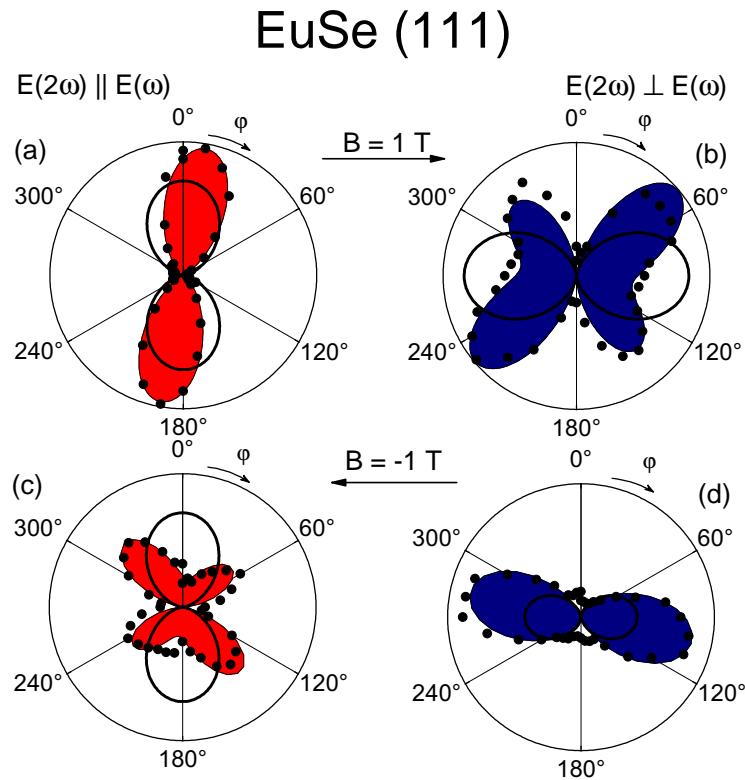
Figure 5.11: *Polar plots of experimental SHG intensity data (dots) in EuSe (sample VA 497) (a,b,c,d)(for different field directions) measured at 2.4 eV. Best fits based on Eqs. (5.1) and (5.3), taking into account the IMD (IMD and CMD) are shown by solid lines (shaded areas).*

5.3.3   Conclusions on SHG in Eu*X*

In the last sections, we report on spin-induced SHG in the centrosymmetric magnetic semiconductors EuTe and EuSe. No SHG was detected in the antiferromagnetic (AFM) and paramagnetic phases. However, when a magnetic field is applied, SHG arises due to the breaking of the antiferromagnetic order or by polarization of the paramagnetic phase, both resulting in appearance of a net magnetization. The observed spin-related nonlinearities arise due to a novel type of nonlinear optical susceptibility caused by the MD contribution in combination with spontaneous or induced magnetization. A nonlinear reciprocal effect appears as well, especially in EuSe, and is explained by the interference of strain caused crystallographic and spin-induced contributions.
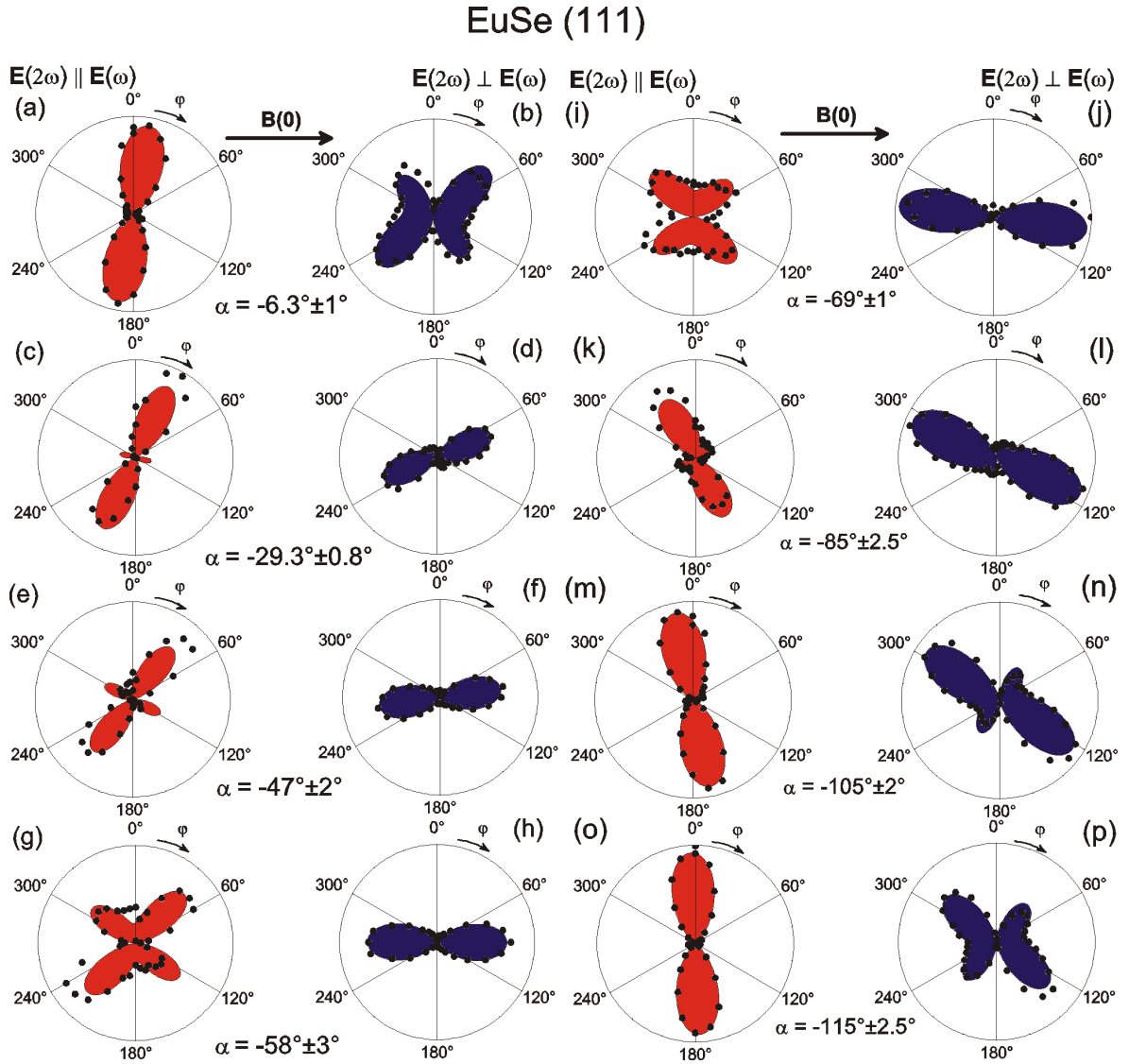
Figure 5.12: *Polar plots of experimental SHG intensity data (dots) in EuSe (sample VA 497) measured at 2.4 eV and with different sample in plane rotations. Angle α given between crystallographic axes and [11$\overline{2}$] direction. Fits based on Eqs. (5.1) and (5.3), taking into account the IMD (IMD and CMD), are shown by solid lines (shaded areas).*

5.3.4   Third Harmonic Generation in EuTe

Figure 5.13(a) displays the SHG spectra of EuTe recorded at different magnetic fields below $T_N = 9.6$ K. As mentioned in Section 5.1.5, the ED-THG process is allowed in these materials even without external magnetic fields. Indeed, several features are found in the spectrum at zero magnetic field. The peak around 2.4 eV corresponds to the band gap seen in SHG spectra and linear optical measurements as well. A further feature is observed between energy ranges of 2.8 eV up to 3.3 eV with a stronger peak
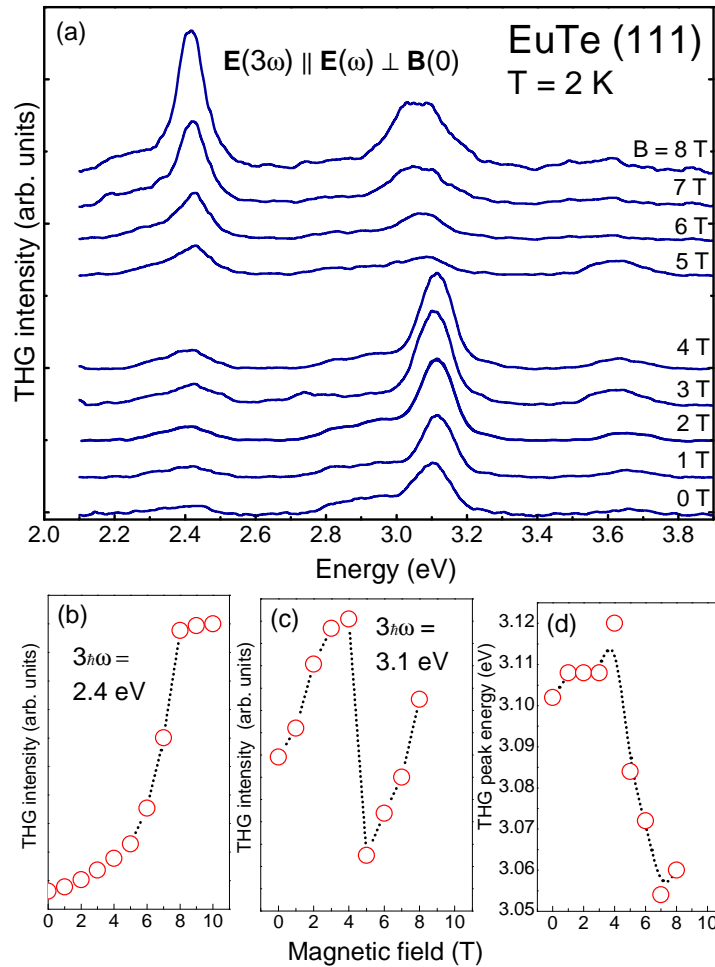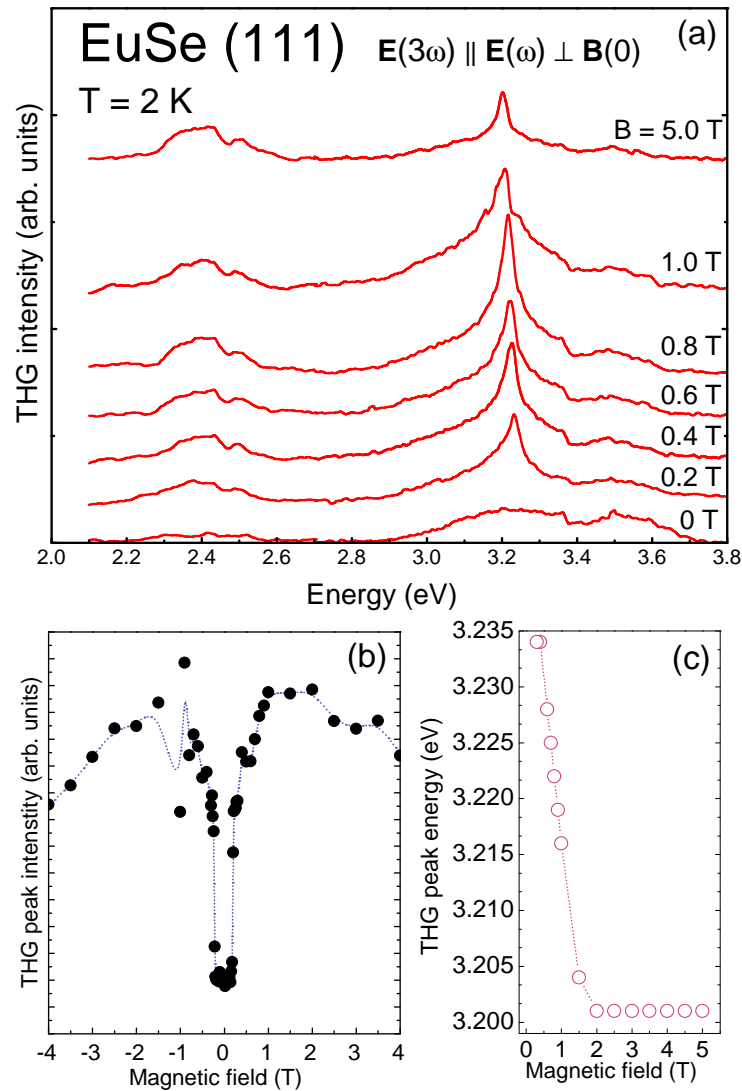
Figure 5.13: *(a) THG spectra of EuTe shown for different magnetic fields up to 8 T. Insets show intensity dependence for peak at 2.4 eV (b) and 3.2 eV (c). (d) Energy shift of line at 3.2 eV vs. magnetic field.*

around 3.1 eV; another smaller line is seen around 3.6 eV. Figure 5.14 illustrates the different mechanisms involved. The first peak at 2.4 eV is resonantly excited by the sum of the energy of all three incident photons. Broad background stems from the same mechanism of higher level $5d$ band. However, the second and stronger peak around 3.15 eV is based on a double resonant excitation. Thereby two incident photons excite the excitonic state that was found around 2.1 eV [110, 123], then the third photon excites, again resonantly, a $5d/6s$ energy level. By means of this double resonant excitation, the strong feature and its behavior for increasing fields can be explained as well. The latter is based on the fact that again a spin induced contribution P^{IED} produces an increase of signal around 2.4 eV and a shift of energy levels. An increase of the SHG intensity vs. the magnetic field is found for the peak around 3.15 eV likewise. But in advanced external magnetic fields, the intensity decreases surprisingly.

We suggest that the decrease is caused by the magnetic field induced energy level shift
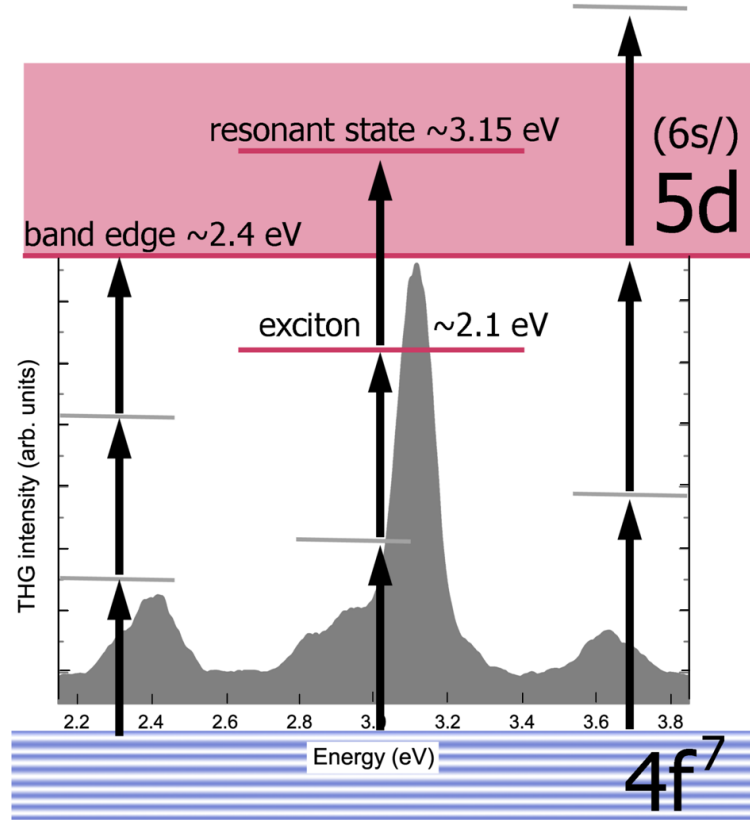
Figure 5.14: *The different types of resonances linked to peaks of THG spectra in EuTe (sample VA 496). Spectrum (dark grey) is shown for B= 4T and T= 2K and* $\mathbf{E}(3\omega)\|\mathbf{E}(\omega)$

leading to a shifting out of resonance.

For the intensity accession of the first line (2.4 eV), the P^{IED} as causation is evidently established; however, for detailed description interference of P^{IED} and P^{CED} has to be taken into account, see Fig. 5.13(b). Energy shift and intensity vs. magnetic field are shown for the double resonant peak in Fig. 5.13. The anisotropies measured at different peak positions are depicted in Fig. 5.15 (points) and confirm by means of the different shapes that probably different mechanisms are involved. For sufficient modeling again both contributions P^{IED} and P^{CED} have to be considered for $\mathbf{E}(3\omega)\|\mathbf{E}(\omega)$ (shaded red areas). Anisotropies measured in $\mathbf{E}(3\omega)\perp\mathbf{E}(\omega)$ geometry, can be modeled only with P^{IED} process (shaded blue areas).

5.3.5   Third Harmonic Generation in EuSe

Also in EuSe, see THG spectra Fig.5.16, above described features are observed. In comparison with EuTe an increase of intensity based on the spin induced contribution
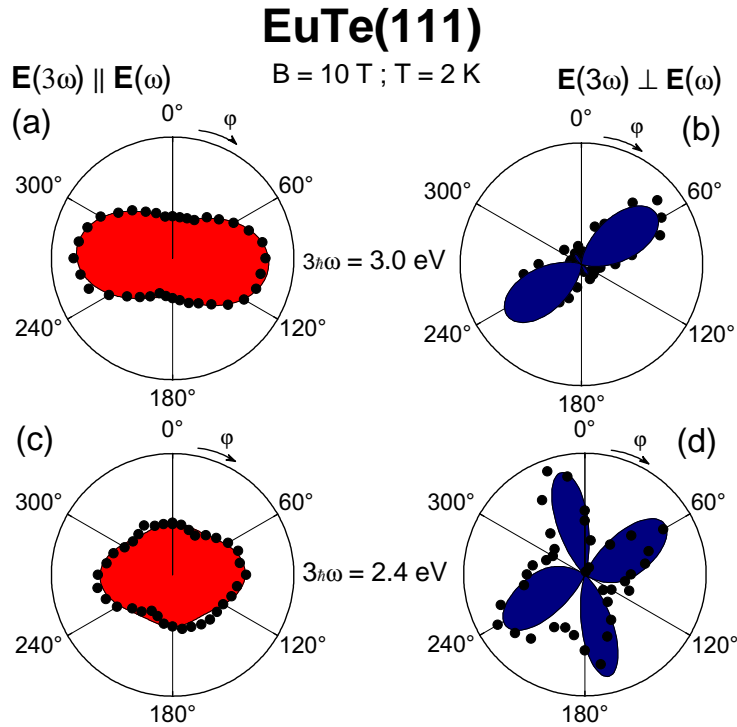
Figure 5.15: *Polar plots of experimental THG intensity data (dots) in EuTe (Sample VA 496) measured at 3.0 eV (a),(b) and at 2.4 eV (c),(d). Best fits based on Eqs. (5.15) and (5.19), taking into account the IED (IED and CED) are shown by solid lines (shaded areas).*

P^{IMD} is significantly found at 3.2 eV. A sharp peak appears for fields above 0.2 T ascribed to this process. Already fields about 0.5 T are sufficient to reach the saturation of spin alignment and consequently a saturation in SHG intensity (Fig. 5.16). In advanced magnetic fields, a loss of intensity is monitored due to energy shift of the resonant levels caused by the external magnetic field. At zero magnetic field, again several features at 2.4 eV and between 2.9 and 3.7 eV can be identified. Origin of THG signal is thereby the crystallographic contribution P^{CED}. Intensity versus magnetic field and peak energy versus magnetic field are displayed in Fig. 5.16 (b) and (c). The field dependence of the integral intensity is in good agreement with the function $I(3\omega) \propto (M + M^2)$, in accordance with Eq. (5.23). With increasing magnetic fields the narrow peak is shifted to lower energies by 30 meV; this shift is saturated above 1.5 T. THG spectra at fixed magnetic fields are shown for temperatures up to 15 K in Fig. 5.17(a). The sharp peak at 3.2 eV, whose line width does not change with increasing temperature, vanishes already about 10 K and decreases its intensity much faster than the broad THG background [Fig. 5.17(b)]. It can be explained in terms of a strongly temperature dependent spin-induced mechanism, which controls the nar-

Figure 5.16: *(a) THG spectra of EuSe (Sample VA 497) shown for different magnetic fields up to 5 T. (b) shows intensity dependence for peak at 3.2 eV. (c) shows the energy shift of line at 3.2 eV vs. magnetic field.*

row line fully. THG broad band crystallographic contributions show a much weaker temperature dependence. The line shift depending on the temperature is illustrated in Fig. 5.17(c). The value of the shift is rather big, larger than 100 meV in the temperature range of 2-8 K, especially if we compare it with the shift of about(30 meV) of this line caused by magnetic fields. Peculiar is the comparison of the EuSe THG peak intensity and the initial magnetic susceptibility [109], see Fig. 5.17(d), clarifying that magnetization and harmonic generation are linked.
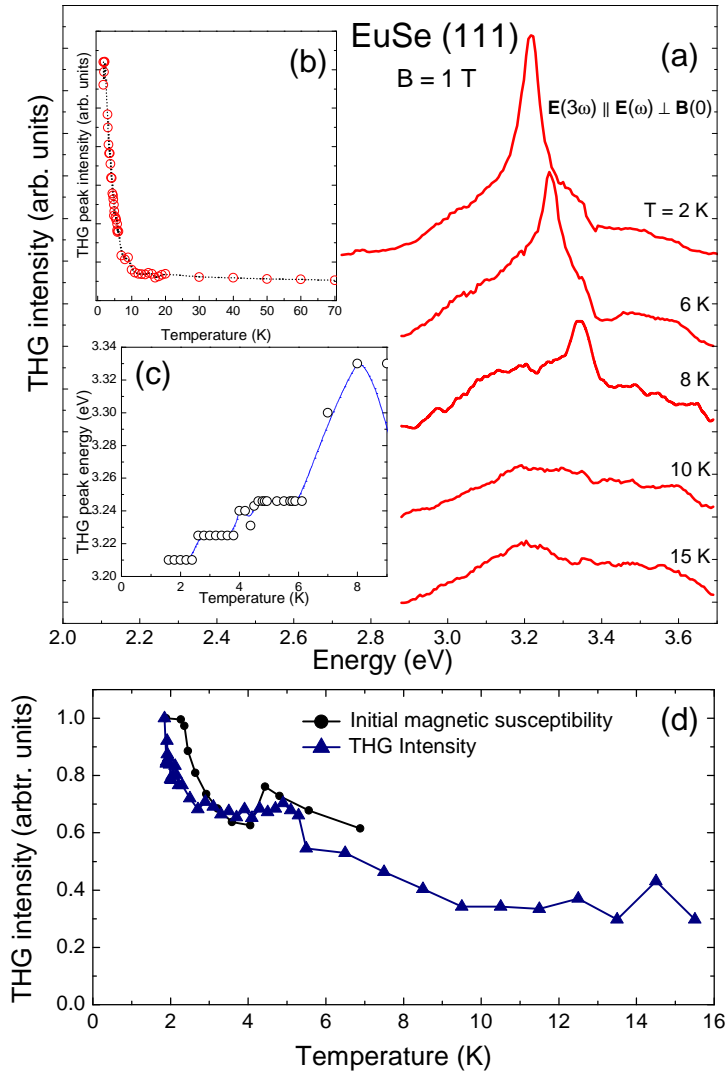
Figure 5.17: *(a)THG spectra (EuSe, Sample VA 497) at 10T for different temperatures. Insets show integral THG intensity as function of temperature. (b)Energy of the THG Peak vs. Temperature*

Figure 5.18 displays anisotropies for different field directions (a),(b); the anisotropies measured at zero magnetic field (c) and for a temperature above $T_N = 4.6$ K (d). For all anisotropies measured in a magnetic field, the shape is always twofold and does surprisingly not change neither for different field directions nor for different temperatures. In comparison with the SHG anisotropies of EuSe, normally stronger interferences and therefore stronger changes of the shape would be expected. Nevertheless, for sufficient modeling, both contributions P^{CED} and P^{IED} have to be taken into account. These modeled anisotropies are again illustrated as shaded areas.
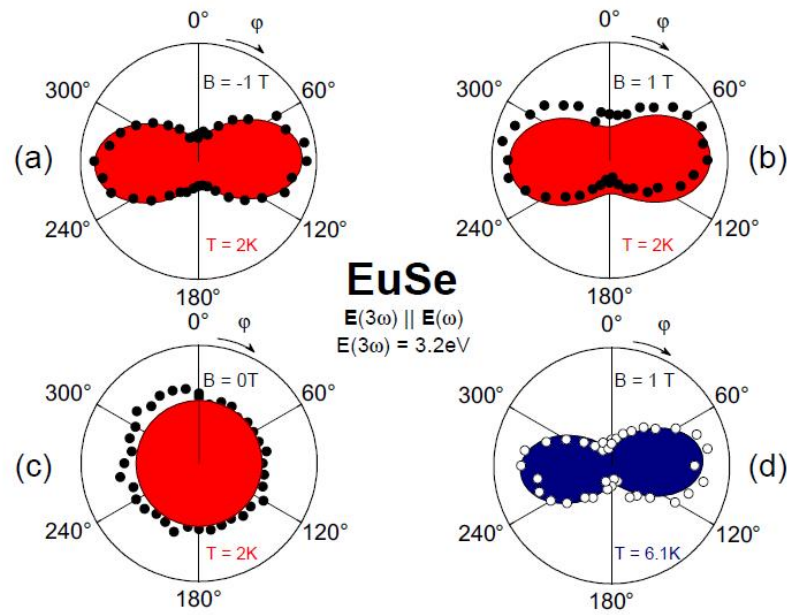
Figure 5.18: *Polar plots of experimental THG intensity data (dots) in EuSe(Sample VA 497) (a,b,c) measured at 3.2 eV for different magnetic fields and above the $T_N = 4.6$ K. Best fits, based on Eqs. (5.15) and (5.19) taking into account the IED and CED, are shown as shaded areas.*

Experimental results for the magnetic-field-induced THG in EuSe confirm the suggested model. Therefore, the spin-induced THG process in EuSe is allowed in ED approximation due to the ferromagnetic component as well.

5.4   Conclusions

The EuX materials show a spin induced $P \propto M$ contribution in the vicinity of the
band gap in SHG as well as in THG
The established magnetic-dipole mechanism induces bulk SHG polarizations either by
the ferromagnetic component of the magnetic structure, or by the spin polarization
in the paramagnetic phase and reaches saturation, when all spins are aligned. This
was evidently proven by several field- and temperature dependencies illustrated in the
sections before. Also anisotropies, typical for harmonic generation and allowing to
analyze involved processes, confirmed the induced IMD/IED and an interference with
strain based CMD/CED processes. A verification for a weaker higher order magnetic
dipole term in SHG as main mechanism is given by the fact that the intensities of THG
and SHG were of same magnitude. The electric dipole effect is usually a hundred times
stronger than next higher order process. Since the THG itself is typically more than a
hundred times weaker than SHG this is a clear evidence, that only higher order provides
the SHG contribution and the centrosymmetry of the material is still given. Peaks
observed around 2.2-2.4 eV are caused by the described processes and can be clearly
identified with the absorption edge, that was observed in linear optical experiments
(Fig. 5.5). Furthermore, a microscopic model for the SHG process was established
and presented shortly in section 5.1.4, taking into account quantum mechanical energy
levels. This quantum mechanical model and experimental data were compared and
revealed that spectra as well as the increase of intensity of the SHG signal versus the
magnetic field could be well described by the theoretical model. Since the theoretical
model neglected interference of crystallographic and induced SHG contributions, small
discrepancies between theory and experiment could be explained, too. This accordance
approves significantly that the dominant and driving process for generation of the SHG
light in this magnetic centrosymmetric semiconductor is based on the spin induced
magnetic dipole process. The calculated anisotropy, neglecting the interference term,
also corresponds with the observed two-fold anisotropy of EuTe. Moreover, in nonlinear
optics a sufficient microscopic model can seldom be given and for the first time a
new SHG contribution could be explained phenomenologically and microscopically,
accounting also for the electronic structure of the material.
Spin induced-electric dipole third harmonic generation was observed and could be
microscopically explained as well. An interesting feature of these THG spectra is a
double resonant peak situated about 3.2 eV. These new types of spin-induced nonlinear
susceptibilities can appreciably increase the number of centrosymmetric bulk materials,
thin films, and artificial structures accessible to nonlinear optics.

Chapter 6

Anisotropy Simulations of SHG Processes

6.1   Introduction

In opposition to photoluminescence or absorption, the generation of optical harmonics is typically strongly anisotropic. Therefore, these polarization dependencies of the detected harmonic signal give the opportunity to distinguish between desired SHG or THG signals and undesired PL contributions. Furthermore, the identification of potentially involved processes as electric-dipole, magnetic dipole or electric quadrupole processes, field induced contributions and interferences of different contributions becomes often possible by a detailed analysis of these anisotropies. As discussed before in Section 3.1.2, these anisotropies are consequences of the symmetry of the media and of involved processes. Therefore, the interpretation and simulation of theoretical anisotropies were of great importance for this work and should be discussed in this section.

6.2   Anisotropy simulation in ZnO

The symmetry properties of materials are taken into account by the description in the point groups (Section 1.3). For every point group, symmetry restrictions result for the susceptibility tensors. To classify the tensors, one has to consider time inversion and space inversion operations (Section 3.1.2).

6.2.1   Crystallographic SHG in ZnO

Since ZnO is a diamagnetic material, it should be invariant under time inversion and thus, the susceptibility must be an i-tensor. ZnO has no center of symmetry and consequently the electric dipole SHG process should be allowed. Regarding the accordant

process

$$P_i(2\omega) = \epsilon_0 \chi_{ijk} E_j(\omega) E_k(\omega) \tag{6.1}$$

reveals that the susceptibility of third order describing the crystallographic contribution is a polar tensor. Since the electric fields and the polarization itself are polar tensors and these polar tensors change their sign under application of space inversion, the susceptibility must be polar as well to fulfill the equation. The remaining tensor components for a polar third rank i- tensor are listed in several tables [76]. For ZnO with the wurtzite structure and the point group $6mm$, the following nonzero tensor components are found:

$$\chi_{zzz},$$
$$\chi_{xxz} = \chi_{yyz},$$
$$\chi_{yzy} = \chi_{xzx},$$
$$\chi_{zxx} = \chi_{zyy}. \tag{6.2}$$

The coordinates $\mathbf{x}$,$\mathbf{y}$ and $\mathbf{z}$ are given in respect to the crystal framework. The last two indices of the tensor describe the electric fields or photons of Eq. 6.1. Therefore, both indices must be permutable without restrictions and components in line two and in line three of 6.2 have to be equal [201]. Already here only 3 independent components remain. Furthermore, we have to deal with restrictions given by the execution of the experiment. The laboratory frame work is spanned by $\mathbf{k}$ of the incident light field and polarization vectors in the plane perpendicular to $\mathbf{k}$. Assuming an [0001] orientated sample relative to the laboratory framework, then it is obvious that polarizations in z-direction cannot be provided. The incident light beam provides only one polarization perpendicular to $\mathbf{k}$ and therefore, both photons must have the same index for this configuration. Detection is only possible for polarizations perpendicular to $\mathbf{k}$. Consequently, one can conclude that for this sample orientation the electric dipole type SHG has to vanish independent of the polarization geometry, $E(2\omega) \perp E(\omega)$ or $E(2\omega) \| E(\omega)$. If one tilts the sample-[111] direction parallel to the $\mathbf{k}$ vector, the situation is different. In respect to the laboratory coordinate system, we have now $[111]\|(k)\|\mathbf{z}'$ and can assume for $\mathbf{x}'\|[11-2]$ and $\mathbf{y}'\|[1-10]$ relative to the laboratory coordinate system. The normalized transformation matrix between the $\mathbf{x}, \mathbf{y}, \mathbf{z}$ and $\mathbf{x}', \mathbf{y}', \mathbf{z}'$ for the [111] orientated sample is

$$\hat{T}_{x,y,z \to x',y',z'} = \begin{pmatrix} -\frac{1}{\sqrt{6}} & -\frac{1}{\sqrt{6}} & \sqrt{\frac{2}{3}} \\ -\frac{1}{\sqrt{2}} & -\frac{1}{\sqrt{2}} & 0 \\ \frac{1}{\sqrt{3}} & \frac{1}{\sqrt{3}} & \frac{1}{\sqrt{3}} \end{pmatrix}. \tag{6.3}$$

The following measurement of the anisotropy implies a simultaneous rotation of the polarizer and analyzer or equivalent to this, a rotation of the sample around $\mathbf{k}$

$$\hat{A} = \begin{pmatrix} \cos\alpha + \varphi & \sin\alpha + \varphi & 0 \\ -\sin\alpha + \varphi & \cos\alpha + \varphi & 0 \\ 0 & 0 & 1 \end{pmatrix}. \tag{6.4}$$

Both matrices have to be multiplied $\hat{R} = \hat{A} \cdot \hat{T}_{x,y,z \to x',y',z'}$ in order to obtain the final transformation matrix for the tensor:

$$\hat{R} = \begin{pmatrix} -\frac{\cos\alpha+\varphi}{\sqrt{6}} + \frac{\sin\alpha+\varphi}{\sqrt{2}} & -\frac{\cos\alpha+\varphi}{\sqrt{6}} - \frac{\sin\alpha+\varphi}{\sqrt{2}} & \sqrt{\frac{2}{3}}\cos\alpha + \varphi \\ \frac{\cos\alpha+\varphi}{\sqrt{2}} + \frac{\sin\alpha+\varphi}{\sqrt{6}} & -\frac{\cos\alpha+\varphi}{\sqrt{2}} + \frac{\sin\alpha+\varphi}{\sqrt{6}} & -\sqrt{\frac{2}{3}}\sin\alpha + \varphi \\ \frac{1}{\sqrt{3}} & \frac{1}{\sqrt{3}} & \frac{1}{\sqrt{3}} \end{pmatrix}. \tag{6.5}$$

According to the Eq. 3.12, the tensor transformation for different frameworks is given. In the case of our polar third-rank i- tensor, this ends up to:

$$\chi_{i'j'k'} = \sum_p \sum_q \sum_r \hat{R}_{i'p}\hat{R}_{j'q}\hat{R}_{k'r}\chi_{pqr}. \tag{6.6}$$

For the case of $E(2\omega)\|E(\omega)$, one can choose $P_{x'}(2\omega) = \epsilon_0 \chi_{x'x'x'} E_{x'}(\omega) E_{x'}(\omega)$ without loss of generality or equivalent $P_{y'}(2\omega) = \epsilon_0 \chi_{y'y'y'} E_{y'}(\omega) E_{y'}(\omega)$. Consequently, the Eq. 6.6 results in:

$$\chi_{x'x'x'} = \sum_p \sum_q \sum_r \hat{R}_{x'p}\hat{R}_{x'q}\hat{R}_{x'r}\chi_{pqr}, \tag{6.7}$$

where for example $\hat{R}_{r'q}$ denotes the component of the transformation matrix $\hat{R}$ in row r'(x',y',z' =1,2,3) and column q(x,y,z =1,2,3). Determination of this equation yields

$$\chi_{x'x'x'} = \frac{1}{3\sqrt{6}}(\sin(\alpha+\varphi)(2(2\chi_{xxz} + 2\chi_{yyz} + \chi_{zxx} + \chi_{zyy} + \chi_{zzz})$$
$$+(2\chi_{xxz} + 2\chi_{yyz} + \chi_{zxx} + \chi_{zyy} - 2\chi_{zzz})\cos(2(\alpha+\varphi)) +$$
$$\sqrt{3}(2\chi_{xxz} - 2\chi_{yyz} + \chi_{zxx} - \chi_{zyy})\sin(2(\alpha+\varphi)))) \tag{6.8}$$

for the $[111]\|\mathbf{k}$ orientated sample and $E(2\omega)\|E(\omega)$ geometry. Considering $E(2\omega) \perp E(\omega)$ also $P_{y'}(2\omega) = \epsilon_0 \chi_{y'x'x'} E_{x'}(\omega) E_{x'}(\omega)$ Eq. 6.6 leads to:

$$\chi_{y'x'x'} = \sum_p \sum_q \sum_r \hat{R}_{y'p}\hat{R}_{x'q}\hat{R}_{x'r}\chi_{pqr}, \tag{6.9}$$

Executing the calculation, one obtains finally:

$$\chi_{y'x'x'} = (-3(2\chi_{xxz} - 2\chi_{yyz} - \chi_{zxx} + \chi_{zyy})\cos(\alpha+\varphi) - 3(2\chi_{xxz} - 2\chi_{yyz} + \chi_{zxx} - \chi_{zyy})$$
$$\cos(3\alpha+\varphi)) + 2\sqrt{3}(2(\chi_{xxz} + \chi_{yyz} - \chi_{zxx} - \chi_{zyy} - \chi_{zzz}) \tag{6.10}$$
$$+(2\chi_{xxz} + 2\chi_{yyz} + \chi_{zxx} + \chi_{zyy} - 2\chi_{zzz})\cos 2(\alpha+\varphi))\sin\alpha+\varphi)\frac{1}{(18\sqrt{2})}.$$

Then the intensity for $E(2\omega)\|E(\omega)$ can be calculated by

$$I = P_{x'}(2\omega)^2 = |\epsilon_0 \chi_{x'x'x'} E_{x'}(\omega) E_{x'}(\omega)|^2, \tag{6.11}$$

and for $E(2\omega) \perp E(\omega)$ by

$$I = P_{y'}(2\omega)^2 = |\epsilon_0 \chi_{y'x'x'} E_{x'}(\omega) E_{x'}(\omega)|^2. \tag{6.12}$$

If we assume $E_x = 1$, the qualitative results are not changed and the theoretical anisotropy can be plotted for an estimate of the shape and/or fitted to the experimental data. An equivalent calculation of theoretical rotational anisotropy is given in [21].

6.2.2 Magnetic-field-induced SHG in ZnO

External perturbations like magnetic fields also result in new sources for SHG signals:

$$P_i(2\omega) = \epsilon_0 \chi_{ijkl} E_j(\omega) E_k(\omega) H_l(0) \tag{6.13}$$

Thereby χ_{ijkl} is a fourth rank tensor and since the Eq. 6.13 consists on the right side of two polar ($\mathbf{E}$) and an axial tensor $\mathbf{H}$, χ_{ijkl} is also an axial tensor. But as discussed in detail in Section 4.1.3, the external magnetic field leads to a third perturbation resulting in a quasi electric field. Therefore, the mechanism responsible for detected SHG signal is given by

$$P_i(2\omega) = \epsilon_0 \chi_{ijkl} E_j(\omega) E_k(\omega) E_l(0) \tag{6.14}$$

Only polar tensors are involved in this process and consequently we have to deal with a polar fourth rank i-tensor with the non-vanishing tensor components:

$$\chi_{xxxx} = \chi_{yyyy} = \chi_{yxyy} + \chi_{yyxx} + \chi_{yxxy},$$
$$\chi_{zzzz}, \ \chi_{xxyy} = \chi_{yyxx}, \ \chi_{xyxy} = \chi_{yxyx}, \ \chi_{xyxy} = \chi_{yxyx},$$
$$\chi_{xxzz} = \chi_{yyzz}, \ \chi_{yzzy} = \chi_{xzzx}, \ \chi_{yzyz} = \chi_{xzxz},$$
$$\chi_{zzyy} = \chi_{zzxx}, \ \chi_{zyyz} = \chi_{zxxz}, \ \chi_{zxzx} = \chi_{zyzy}, \tag{6.15}$$

Here according to the process 6.14, the second and third index denote the electric fields and have, therefore, to permutate. The fourth index specifies the direction of the applied magnetic field. Moreover, the magnetic contribution appears already for a sample orientation of $\mathbf{z} = [001] \| \mathbf{k}$ in the Voigt-geometry and is calculated only for this in the following. Therefore, all tensor components with subscripts z can not be excited and are zero.

Due to the fact that the crystallographic contribution is suppressed for this sample orientation, a detection of pure magnetic contributions is possible. Then the calculation of the transformation matrix $\hat{R} = \hat{A}$ becomes quite simple, because only the matrix $\hat{A}$ has to be considered. However, with the application of the rotation matrix the magnetic field or electric field has to be hold fixed, and both possible magnetic field directions $\mathbf{x}$ and $\mathbf{y}$ must be considered for each geometry:

$$\chi_{x'x'x'x'} = \sum_p \sum_q \sum_r \sum_s \hat{R}_{x'p} \hat{R}_{x'q} \hat{R}_{x'r} \hat{R}_{x's} \sin(\varphi) \chi_{pqr}, \tag{6.16}$$

and

$$\chi_{x'x'x'y'} = \sum_p \sum_q \sum_r \sum_s \hat{R}_{x'p} \hat{R}_{x'q} \hat{R}_{x'r} \hat{R}_{y's} \cos(\varphi) \chi_{pqr}, \tag{6.17}$$

for $E(2\omega) \| E(\omega)$ and for $E(2\omega) \perp E(\omega)$

$$\chi_{y'x'x'x'} = \sum_p \sum_q \sum_r \sum_s \hat{R}_{y'p} \hat{R}_{x'q} \hat{R}_{x'r} \hat{R}_{x's} \sin(\varphi) \chi_{pqr}, \tag{6.18}$$

and

$$\chi_{y'x'x'y'} = \sum_p \sum_q \sum_r \sum_s \hat{R}_{y'p}\hat{R}_{x'q}\hat{R}_{x'r}\hat{R}_{y's}\cos{(\varphi)}\chi_{pqr}\,. \tag{6.19}$$

The additive $\sin{(\varphi)}$ or $\cos{(\varphi)}$ terms are used to compensate the rotation and thus holding the magnetic field or the quasi electric field U, respectively, fixed. All following calculations are exactly the same discussed in the previous section and result in the intensity dependencies:

$$I_\parallel(2\omega) \propto [U((\chi_{yxxy} + 11\chi_{yyxx})\cos{(\varphi)} + (-\chi_{yxxy} + \chi_{yyxx})\cos{(4\alpha + 5\varphi)})]^2, \tag{6.20}$$
$$I_\perp(2\omega) \propto [U((3\chi_{yxxy} + \chi_{yyxx})\sin{(\varphi)} + (\chi_{yxxy} - \chi_{yyxx})\sin{(4\alpha + 5\varphi)})]^2. \tag{6.21}$$

6.3   Anisotropy simulation of SHG in Eu*X*

6.3.1   Crystallographic anisotropy of SHG in Eu*X*

In centrosymmetric europium chalcogenides with the point group $m3m$, electric dipole contributions as well as electric quadrupole processes are forbidden due to the different parity of valence and conduction band. Only one kind of a magnetic dipole SHG contribution is allowed, since this process only possesses odd parity:

$$P_i(2\omega) = i\epsilon_0\chi_{ijk}E_j(\omega)H_k(\omega) \tag{6.22}$$

This equation consists of an axial tensor **H** and two polar tensors **E** and **P**, hence χ_{ijk} has to be an axial tensor as well. Since the europium chalcogenides are magnetic compounds, one would expect an i tensor. But for this point group c and i tensor have the same non-vanishing components and the tensor is, therefore, not distinguishable for paramagnetic or magnetic phases. For a third rank axial tensor the non-vanishing tensor-components are given by:

$$\chi_{xyz} = -\chi_{xzy} = \chi_{yxz} = -\chi_{yzx} = \chi_{zxy} = -\chi_{zyx}, \tag{6.23}$$

However, for this magnetic dipole process the permutability of the last two indices is not any longer given, since H and E excitations have to be perpendicular to each other because of experimental restrictions. The samples were grown in [111]-direction and the experiments performed for **k**‖[111]. Therefore the transformation matrix $\hat{R}$ according to 6.5 has to be used. Due to the four-fold symmetry axis, the calculation of the transformation of this process according to Eq. (3.12) leads to

$$\chi_{x'x'y'} = \sum_p \sum_q \sum_r \hat{R}_{x'p}\hat{R}_{x'q}\hat{R}_{y'r}\chi_{pqr} = 0\,, \tag{6.24}$$

$$\chi_{y'x'y'} = \sum_p \sum_q \sum_r \hat{R}_{y'p}\hat{R}_{x'q}\hat{R}_{y'r}\chi_{pqr} = 0\,, \tag{6.25}$$

for parallel and perpendicular geometry as well. But the europium chalcogenides samples were grown on BaF$_2$ substrate leading to a trigonal strain in the epilayer. This

strain is the origin of a symmetry reduction of the point group $m3m$ to the centrosymmetric point group $\bar{3}m$, with the non-vanishing tensor components:

$$\chi_{xyz} = \chi_{xzy} = \chi_{yxz} = \chi_{yzx} = \chi_{zxy} = \chi_{zyx}. \qquad (6.26)$$

Further calculations are done as above, but it has to be kept in mind, that the permutability of the last two indices is not feasible [202, 191]. The intensity dependencies are resulting for $\mathbf{E}(2\omega) \perp \mathbf{E}(\omega)$ in

$$I(2\omega)_{\parallel}^{SHG} \propto |-\chi_{xyz}\cos 3(\alpha + \varphi)|^2 \qquad (6.27)$$

and for the crossed arrangement $\mathbf{E}(2\omega) \perp \mathbf{E}(\omega)$ in

$$I(2\omega)_{\perp}^{SHG} \propto |\chi_{xyz}\sin 3(\alpha + \varphi)|^2. \qquad (6.28)$$

6.3.2 Magnetic-field-induced anisotropy of SHG in Eu*X*

A magnetic contribution depending on the magnetization was observed. This contribution is described by:

$$P_i^{IMD}(2\omega) = \varepsilon_0 \chi_{ijkl}^{(3)} E_j(\omega) H_k(\omega) M_l(0) \qquad (6.29)$$

Since this process includes two axial tensors, the magnetic field of the light field and the magnetization triggered by the external magnetic field, $\chi_{ijkl}^{(3)}$ is a polar fourth rank tensor. This tensor consists of the non-zero tensor components:

$$-\chi_{xyyx} = \chi_{xzzx} = \chi_{yxxy} = \chi_{yzzy} = \chi_{zxxz} = \chi_{zyyz},$$
$$-\chi_{xyxy} = \chi_{xzxz} = \chi_{yxyx} = \chi_{yzyz} = \chi_{zxzx} = \chi_{zyzy},$$
$$\chi_{xxyy} = \chi_{xxzz} = \chi_{yyxx} = \chi_{yyzz} = \chi_{zzxx} = \chi_{zzyy}.$$
$$\chi_{xxxx} = \chi_{yyyy} = \chi_{zzzz} \qquad (6.30)$$

Here, again the permutability of the second and third index describing the electric and magnetic field of the light wave is not given [202, 191]. The external magnetic field was applied in Voigt-geometry. For the application of the transformation matrix trigonometric functions have additively to be taken into account as well, to compensate the rotation for the applied external field by splitting it into the projections for the rotating crystal axis. Further calculations are similar as done for ZnO in magnetic fields: First application of $\hat{R}$, then the transformation of the tensors are considered:

$$\chi_{x'x'y'x'} = \sum_p \sum_q \sum_r \sum_s \hat{R}_{x'p} \hat{R}_{x'q} \hat{R}_{y'r} \hat{R}_{x's} \sin{(\varphi)} \chi_{pqr}, \qquad (6.31)$$

$$\chi_{x'x'y'y'} = \sum_p \sum_q \sum_r \sum_s \hat{R}_{x'p} \hat{R}_{x'q} \hat{R}_{y'r} \hat{R}_{y's} \cos{(\varphi)} \chi_{pqr}, \qquad (6.32)$$

for $E(2\omega) \| E(\omega)$ and for $E(2\omega) \perp E(\omega)$

$$\chi_{y'x'y'x'} = \sum_p \sum_q \sum_r \sum_s \hat{R}_{y'p} \hat{R}_{x'q} \hat{R}_{y'r} \hat{R}_{x's} \sin{(\varphi)} \chi_{pqr}, \qquad (6.33)$$

$$\chi_{y'x'y'y'} = \sum_p \sum_q \sum_r \sum_s \hat{R}_{y'p} \hat{R}_{x'q} \hat{R}_{y'r} \hat{R}_{y's} \cos{(\varphi)} \chi_{pqr}, \qquad (6.34)$$

Consequently, the $I(2\omega)\propto|\mathbf{P}^{IMD}(2\omega)|^2$, contribution triggered by an external magnetic field yields:

$$I(2\omega)^{SHG}_{\parallel} \propto |\frac{M}{6}(\chi_{xxxx} + 5\chi_{xxyy} - \chi_{xyxy} - \chi_{xyyx})\cos\varphi|^2 \qquad (6.35)$$

in the case of $\mathbf{E}(2\omega) \parallel \mathbf{E}(\omega)$ and for $\mathbf{E}(2\omega) \parallel \mathbf{E}(\omega)$ you will get

$$I(2\omega)^{SHG}_{\perp} \propto |\frac{M}{6}(\chi_{xxxx} - \chi_{xxyy} + 5\chi_{xyxy} - \chi_{xyyx})\sin\varphi|^2, \qquad (6.36)$$

where M is the magnetization. This twofold anisotropy depends only on the direction of the magnetic field and the magnetization. According to these equations, only the trigonometric factors added to compensate the rotation for the magnetic field are left and therefore, the crystal orientation should be completely irrelevant. No signal was detected without a magnetic field and the crystallographic contribution could not be measured. Nevertheless, variances are found, which are especially obvious in EuSe, showing strong dependencies on the sample orientation. Firstly, the anisotropies and the modeling have revealed that an interference of the small crystallographic and strong magnetic contribution are necessary to explain the detected shape and their changes with sample rotations or field inversions. Thereby the crystallographic SHG signal is enhanced by the magnetic one and is rotated for sample rotations leading to the observed changes. The final SHG contributions for both geometries are given by:

$$I_{\parallel}(2\omega) \propto [\pm\frac{M}{6}(\chi_{xxxx} + 5\chi_{xxyy} - \chi_{xyxy} - \chi_{xyyx})\cos\varphi - \chi_{xyz}\cos 3(\alpha + \varphi)]^2, \quad (6.37)$$

$$I_{\perp}(2\omega) \propto [\pm\frac{M}{6}(\chi_{xxxx} - \chi_{xxyy} + 5\chi_{xyxy} - \chi_{xyyx})\sin\varphi + \chi_{xyz}\sin 3(\alpha + \varphi)]^2, \quad (6.38)$$

Considerations and modeling for third harmonic generation are exactly the same, only the higher order tensor components have to be taken into account and the relative permutability of the involved processes.

Summary and Outlook

Two novel mechanisms of optical harmonic generation have been found experimentally and are discussed in this work.

The first one is found in ZnO and is caused by the magneto-optical Stark effect. Due to the parity of the exciton states, the SHG electric-dipole process is forbidden. But the magneto-optical Stark effect causes a quasi electric-field that mixes exciton states of different parity and thus the SHG electric-dipole process becomes allowed for 2S and 2P and higher excitons. This magneto-Stark effect is based on a perturbation resulting from the center of mass motion of the exciton in the magnetic field. In calculations the term leading to this magneto-Stark effect is typically neglected and in most experiments this effect is screened by stronger contributions of other mechanisms. But SHG processes are very symmetry sensitive and therefore, also this small symmetry breaking effect has to be taken into account, especially in situations when efficient mechanisms of electric-dipole allowed SHG processes are symmetry forbidden. In the future further experiments, planned in static electric fields, should finally prove the magneto-Stark effect. Other materials, in which the microscopic SHG mechanism is not clear, have to be investigated also in view of this magneto-optical Stark effect.

The second mechanism is found in centrosymmetric europium chalcogenides. Since the electric-dipole SHG contribution is forbidden in centrosymmetric materials, the investigation with SHG did not seem to be promising. Nevertheless, spin-induced SHG is found in the centrosymmetric magnetic semiconductors EuTe and EuSe. The established magnetic-dipole mechanism induces bulk SHG polarizations either by the ferromagnetic component of the magnetic structure, or by the spin polarization in the paramagnetic phase. Also a spin-induced THG signal was observed and discussed in detail.

This new type of spin-induced nonlinear susceptibility can appreciably increase the number of centrosymmetric bulk materials, thin films, and artificial structures accessible to nonlinear optics. In the future the remaining europium chalcogenides, EuO and EuS, have to be investigated also with SHG. However, since this SHG contribution is also present in centrosymmetric materials, manifold experiments are thinkable.

Appendix A

Software and Data Acquisition

A.1 Introduction

All experiments often require similar series of measurements only changing a few parameters. Original producer software is normally designed to control their own product and no information transfer between several different devices and software can be provided. For this demand, a LabView program was written that can afford the interface between different devices.

LabView is a graphically programming language designed by National Instruments with the acronym denoting "**Lab**oratory **V**irtual **I**nstrumentation **E**ngineering **W**orkbench". For every device, a so called SubVI (Virtual Instrument) can be created and then be independently executed. These SubVIs can easily be linked to each other and therefore, the transfer of information configured. Typically, LabView-drivers for all new devices are available and an easy implementation can be achieved. The interface program "Manager" written by Georgy Astakhkov at the University of Würzburg provides the basis for the used program and was adopted to the Nonlinear Optical Setup and the devices [203]. In the following, the main parts and devices of the used LabView program will shortly be introduced.

A.2   Main Program

The interface between all devices and for the control and execution of measurements is the "Manager" main window, see Fig. A.1.

The major part consists of an x-y graph displaying current measurement results. According to the different measurement types, different assignments of the x-y axes are possible. On the left side, one can find the controls relevant for measurements and at the top, characteristics of the x-y graph can be changed. Every measurement type requires a feed back signal of specific devices. If all of this specific devices are opened, are in the status "Ready", and the measurement type is chosen (shown by the blazing lamp "Ready"), the measurement can be started by the "Start" button.
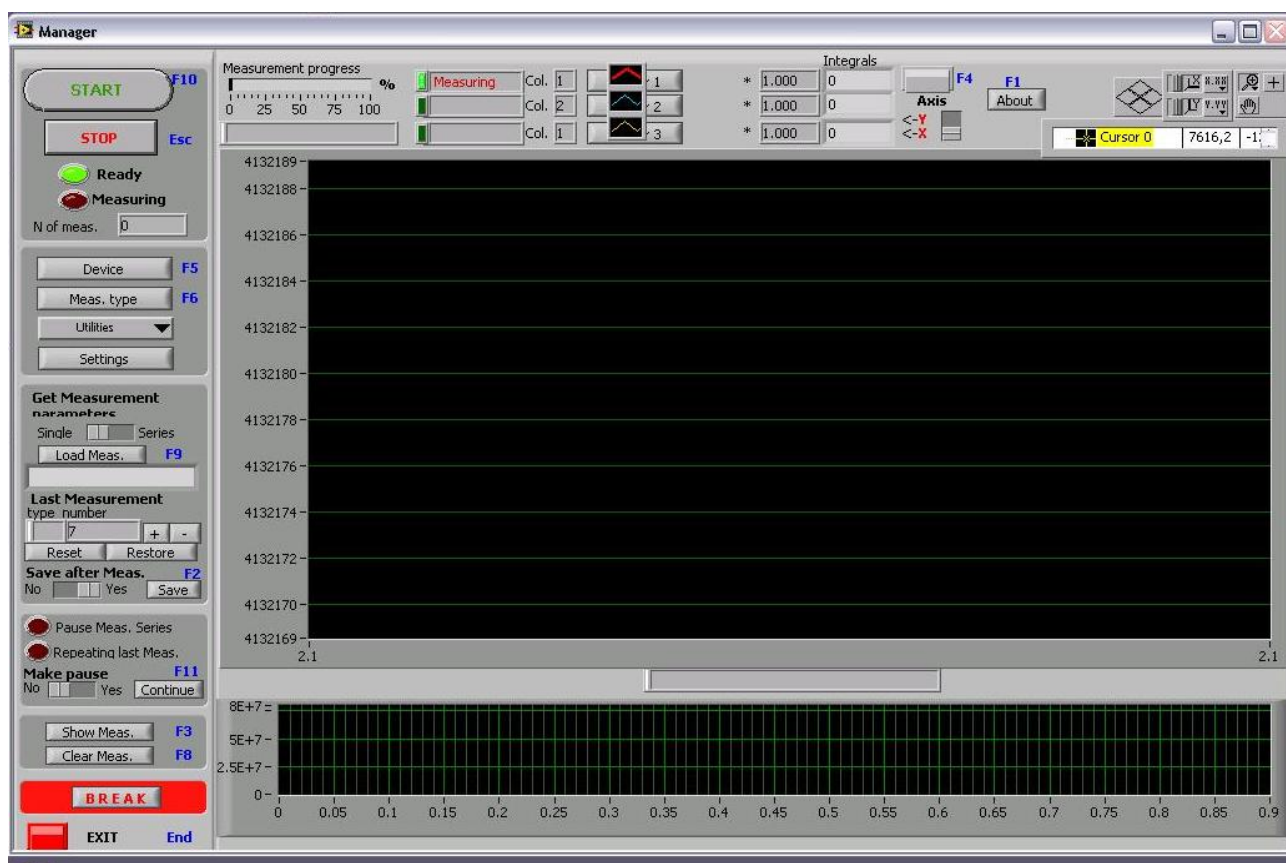
Figure A.1: *Manager*

A.3 Devices

Several devices are fully implemented in the LabView program. If one presses the button devices on the left in the main program, a further window (Figure A.2) opens, and enables the selection of the desired and for the Nonlinear Optical Measurement necessary components. Further windows open for each chosen device. For different

Figure A.2: *Devices*

measurement types, different components can be required. But typically, the program opens necessary components for the chosen measurement type autonomously. The Sub-VIs of the different devices will shortly be presented in the following.

A.3.1 Spectrometer

The spectrometer HR460 can easily be controlled by the buttons in the monochromator window. The desired wavelength or energy can be keyed in the fields and by the "GO" button, to these values the grating will be moved by the motor of the spectrometer. Grating 0, grating 53028 blazed at 400 nm (grooves no.1800), and Grating 1, grating 53018 blazed at 750 nm (grooves no.1200), are installed (see Section 3.2.4) and can be used by entering the number (0 or 1) and pressing the button "GO". During initialization or driving to the desired position, the red "Busy" lamp is bright. If the position is reached, the green "Ready" lamp indicates this. Next to the right wavelength, one can choose the type of measurement. If an experiment is performed by the main program, it uses the dependence given here for OPO energy and spectrometer energy. If SHG is chosen the spectrometer is driven to the $2\times$OPO energy (eV), for THG to $3\times$ OPO energy and for fundamental $1\times$ OPO energy.

A.3.2 Adjustment of spectrometer

During long measurement periods and uncontrolled computer shutdowns a misalignment of the spectrometer is possible.

An adjustment can be provided by producer software but often conflicts appear if the LabView program is still open, because both are trying to accost the devices. Therefore, it is recommended to close the LabView software before opening the manufacturer software.

After that the adjustment of the spectrometer can easily be achieved by using the software "Hardware Configuration and Control". The left window opens and one has to choose the right computer connection of the spectrometer to the computer before one activates the "Add Controller" button. Then the software should recognize the connected spectrometer and one has to press the

"Start" button. Another window A.3 opens. The initialization values for the HR460 can be taken from the manual. After that one has to choose the menu item "Initialize" and can control the proper initialization by the menu item "Control". The window changes and one can choose "Grating motor commands" and "absolute motor position". (The initialize motor position should be 205760 for the used spectrometer). Afterwards one can start the LabView software again.
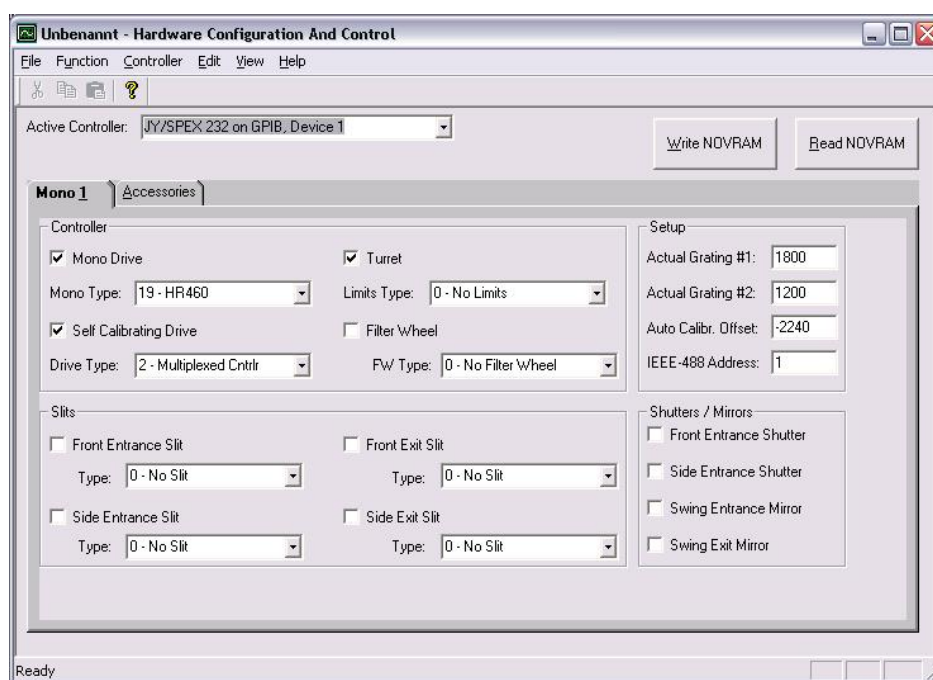
Figure A.3: *Producer software for adjustment of the spectrometer HR460*

A.3.3 Magnetic field and temperature

The implemented SubVIs for the magnetic field and temperature control are constructed for Oxford cryostats. The panels are similar to the hardware devices; therefore, the controls are self-explaining and can be used as usual.

A.3.4 CCD-software

Since the performed experiments were mainly interested in the detection of the intensity of the harmonic generation signal, the CCD usage was mainly photon counting. The exciting light was provided by a pulsed laser and one has, therefore, to ensure that the detected signal always includes same numbers of pulses. This was accomplished by triggering the CCD with the flash lamp trigger of the laser. The triggering can be switched on by changing "Free Run" to "external presync preopen" in the panel A.4. Typically, only a small region of the CCD array is of interest for the experiment
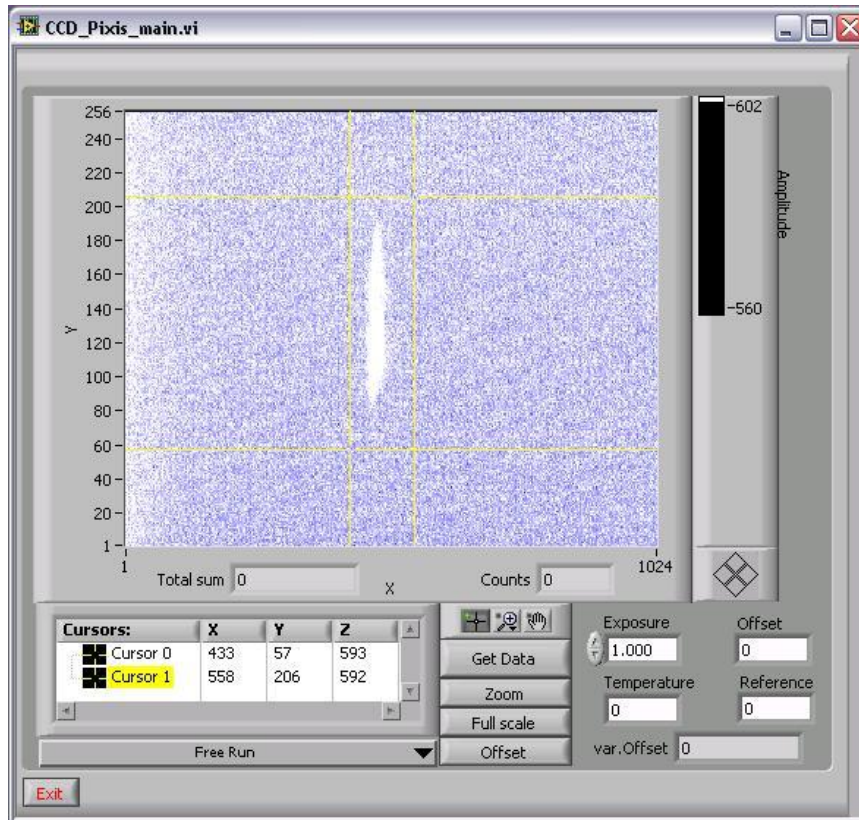
Figure A.4: *CCD-panel consisting mainly of the image of the camera chip*

and the cursors have to be arranged (manually) around the detected spot. Nonlinear optical experiments often involve very low intensities and consequently long exposure times are needed. Thus, the noise level can significantly increase. To ensure a precise substraction of the changing noise level caused by external circumstances, a neighbored region of same spot size is used to afford a new offset with every measurement.

Moreover, the CCD-camera is sensitive to the external magnetic field. Since the experimental setup is quite compact, the distance between camera and magnet cryostat is only about 1 m. For magnetic fields about 8 T a strong increase of noise level and fluctuations of the chip temperature were observed. In order to avoid this influence of the magnetic field, a 0.5mm μ-metal shield was built around the CCD, which was sufficient to suppress the perturbations. Furthermore, it was observed that the noise level depends on room temperature as well. Therefore, the above discussed variable offset, which is measured during every measurement, is important for the quality of the experimental results.

A nitrogen cooled CCD-camera might be a good alternative: Since the cooling is directly provided by nitrogen, influences to cooling electronics are not expected. Moreover, the CCD camera and the controller are separated and thus, a bigger distance between cryostat and the controller could be easily achieved. Nonlinear optical signals are often very weak and nitrogen cooled CCD-cameras possess higher quantum

efficiencies and a better signal-noise ratio. Therefore, the change to a nitrogen cooled CCD-camera sounds promising and might provide an significant improvement of the present setup.

A.3.5 OPO

The optical parametric oscillator software requires the started producer software of the pumping laser, otherwise the LabView software will indicate an error (glazing light-blue error lamp of OPO panel). For the laser software one has to choose right parameters, typically "OPO-normal" was used (640 V, about 170mJ per pulse 355nm output with $215\mu s$ Q-switch delay and 90 % threshold). If errors in the OPO Lab-View software appear, one can increase the OPO window size and scroll below the OPO panel, where the error number will be found. These error numbers are listed in the manufacturer table (GWU) and are helpful for debugging. After installation or OPO/Laser movement a calibration of dependence between OPO motor position and wavelength becomes important. Therefore, one has to connect the Lambda-meter and change in the opo main.dat file (Folder of GWU software PremiScan) the entry for the connected Lambda meter. Then a calibration can be executed with the manufacturer software. Afterwards one has to undo the change in the opomain.dat file before the LabView software is started. The OPO-LabView-subVI is shown in Fig. A.5. Be-
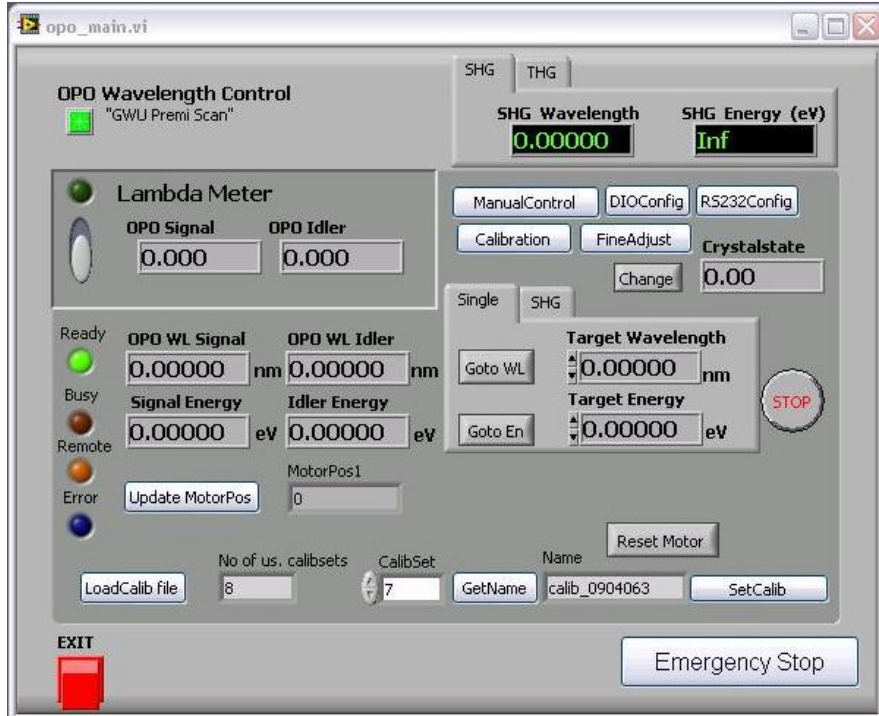
Figure A.5: *OPO-software*

fore the OPO software can be used for changing the wavelength, the calibration file

has to be loaded and set. On the left the OPO idler and signal wavelengths or energies, respectively, for the actual motor position are given. In the upper right corner, one can choose SHG/THG wavelength/energy for the display. The position can be changed by input of the desired fundamental wavelength/energy and the "GOTOWL" or "GOTOEn" buttons. After long measurements it is recommended to do some easy calibration procedure for the OPO before continuing. The OPO hardware saves the home position of the OPO motor. The OPO motor possesses two end switches and the zero (middle) position can be adjusted by using the buttons "ManualControl" and in the opening window "Find Home". When this procedure is finished one should press "Define home" and close this window.

A.3.6 Filterwheels and polarizer
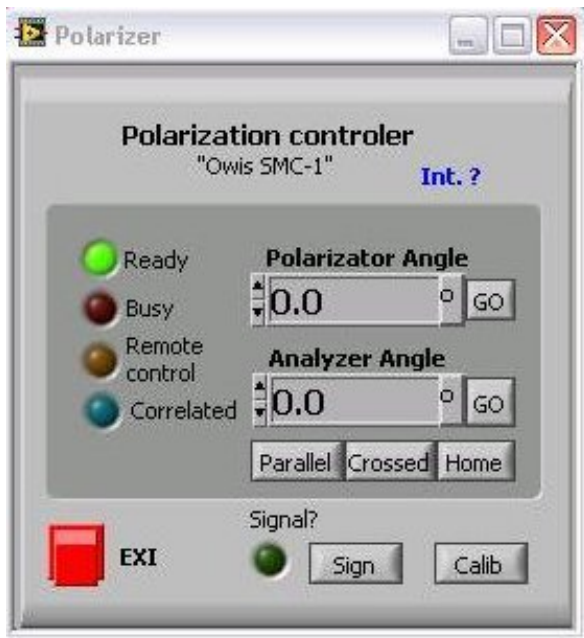
The polarization angle in the plane perpendicular to **k** of polarizer and analyzer can be chosen independently by the software controlling the rotation stages. Since mostly crossed or parallel polarization geometries are used, buttons for these configurations are implemented as well. The status of these devices is indicated by the lamps on the left side. For calibration the "Calib" button can be used. The rotation stages have Hall-switches indicating the home position. By pressing the button the motors go back to their home position, then are driving to the motor position, which was found by polarizations optics to be the polarization angle 0° of the idler. Furthermore, this value is set as new home-position and end-positions are limited. Since the Hall-switches are magnetic devices, the rotation stages are sensitive to applied magnetic fields. Fields in Voigt-geometry are not so critical, but fields in Faraday direction disturb the movement of the rotation stages for $B \geq 8$T.

Also the filter regions can be chosen by computer control. Every wheel consists of six filter insertions. Thereby the first set of filters should erase the undesired SHG contributions of components placed before the sample. The second filter set behind the cryostat and the sample should separate SHG/THG light and fundamental. The harmonics have to pass through and the fundamental must be blocked. The inserted filters and applicable SHG regions are given in table A.1 and A.2.

The filterwheels are sensitive to the magnetic field as well, especially the filter-wheel placed before the cryostat is so close that already fields about 4T are sufficient to disturb the functionality of the wheel.

Figure A.6: *Filterwheel-software*

Pos.	Filter/mm	SHG (eV)	SHG (nm)	blocks (nm)
1	Si/1	1.20-1.84	673-1032	1346-2064
2	RG850/3	1.48-2.48	500-838	1000-1676
3	OG590/3	2.26-4.07	305-550	610-1100
4	GG385/3	3.48-6.02	206-356	412-712

Table A.1: Filter in filterwheel 1 (before the sample)

A.3.7 Reference

Since the OPO output can differ significantly for different wavelengths, a normalization is necessary. A quartz-plate reflects a marginal fraction of the fundamental beam to a photodiode. The detection of this photodiode is triggered by the flash lamp trigger of the laser and connected to an integrator. The integrated signal is transmitted to the PC via an USB connection and read out by the software.

Pos.	Filter/mm	SHG (eV)	SHG (nm)	blocks (nm)
1	RG 9/3	1.21-1.70	730-1025	1460-2050
2	KG 2/2	1.55-2.48	500-800	1000-1600
3	BG39/3	1.95-3.64	340-636	680-1272
4	UG11/1	3.28-4.61	269-378	538-756
5	UG5/1	3.76-5.39	230-330	460-660

Table A.2: Filter in filterwheel 2 (behind the sample)

A.4   Measurement-type

The measurement types of most importance are spectra or anisotropies and should be mentioned shortly in the following. Other parameters which are not driven automatically for chosen measurement type can be regulated manually by the above explained panels. By activating the button "Measurement Type"; the "Types" window and a "Header" window show up. The header input values are written in the measurement file as header. SHG ("S-Type") measurement types simultaneously change the spectrometer and OPO-energy in the dependence, that was selected in the monochromator panel. Other parameters like polarizations, temperature, magnetic fields etc. have to be regulated manually with the panels. The spectrometer energy, the detected signal, with subtracted variable offset, and the reference values are written in the columns of the measurement file.
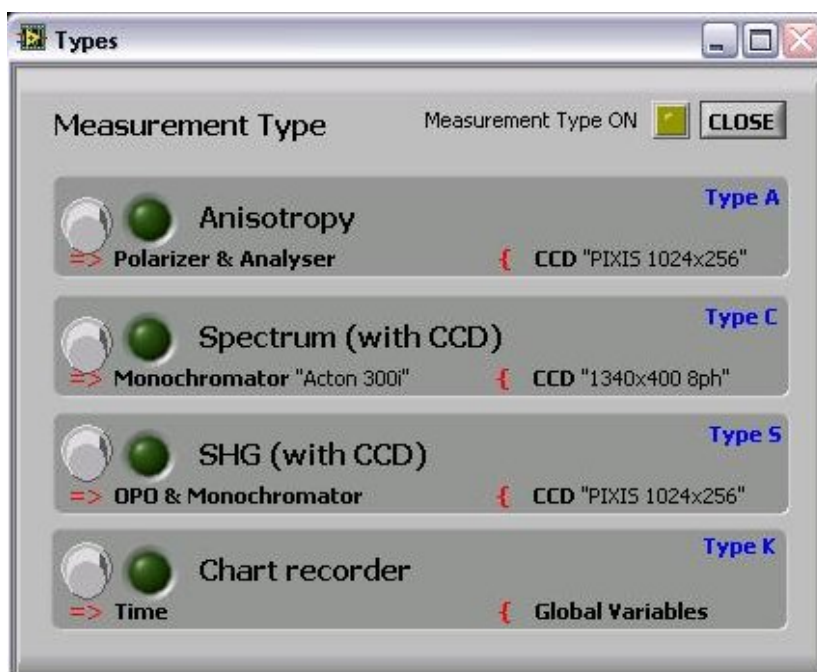
Figure A.7: *measurement-types*

In the "SHG" window the fundamental "Start"- and "End"- energy and the step width for the spectrum have to be filled in. The lower part is greyed out for single measurements. In the "Manager" window the single/series actuator can be used to enable this series measurements. Anisotropy measurements ("A-Type") only vary polarizer and analyzer angle and the desired energy has consequently to be regulated for spectrometer and OPO before. "Start", "End" angles and the step width, as well as the relative angle between polarizer and analyzer have to be entered. If all desired values are filled in, by the button "Read" the values are transmitted to the main program and the measurement can be started. By the menu item "Utilities" and "Measurement file" in the main program, more complicated series of measurements can be entered and

then be saved. These measurement files can then be loaded in the main program, but require the filename ending ".mes" and the "series" setting.

A.5   Further problems and recommendations

Besides the problems caused by an external magnetic field, we observed problems with the moving parts of the OPO and electronic parts of the Laser.

A.5.1   Problems and service of the laser Spitlight

An electronic trigger box responsible for the control of the Q-switch had to be exchanged. This box is situated below the bottom cover. Moreover, a discrepancy of the voltage applied to the laser and the voltage regulated by the software was found. This problem was caused by a substandard potentiometer; thus, the electronic board of the power supply was transposed. A further problem with the shutter appears. This shutter controlled by the software could not be opened by the program. Responsible for this problem was a pull relief of the cable connection between power supply and laser head, which was not well fixed. For a proper functioning of the laser, deionizer cartridges and filters of the power supplies have to be replaced semiyearly. The manufacturer recommends for the flashlamp lifetime only 20 million pulses. Every few weeks a small and easy readjustment of the laser output intensity by THG and SHG screws on the top of the laser is advised.

A.5.2   Problems and service of OPO PremiScan

The moving parts of OPO caused most problems. The crystal step motor and the electronic board of the controller had to be replaced because given specifications for the velocities of the motor could not be kept. However, most problems appeared for software and hardware due to the motor of the crystal changer. Some screws of this motor were unscrewed during frequent use, leading to problems with the end switches. For the OPO an implementation of the lambda meter delivered by the manufacturer into the LabView software would be desirable. For the actual software no LabView drivers for the lambda meter were available and no strong maladjustment of the OPO was observed. Consequently, a casual calibration and/or inspection are sufficient for proper measurements.

Publications

Parts of this work are or will be published as follows:

1. "*Orbital Quantization of Electronic States in Magnetic Field as Origin of Second Harmonic Generation in Diamagnetic Semiconductors*"
   I. Sänger, D. R. Yakovlev, **B. Kaminski**, and M. Bayer
   V. V. Pavlov, and R. V. Pisarev
   *Phys. Rev. B **74** (16), 165208 (2006)*

2. "*Magnetic-Field-Induced Second-Harmonic Generation in the Diluted Magnetic Semiconductors $Cd_{1-x}Mn_xTe$*"
   I. Sänger, D. R. Yakovlev, **B. Kaminski**, and M. Bayer
   V. V. Pavlov, and R. V. Pisarev
   *Phys. Rev. B **74** (23), 235217 (2006)*

3. "*Spin-Induced Optical Second Harmonic Generation in the Centrosymmetric Magnetic Semiconductors EuTe and EuSe*"
   B. Kaminski,M. Lafrentz, R. V. Pisarev, D. R. Yakovlev, V. V. Pavlov, V. Lukoshkin, A. B. Henriques, G. Springholz, G. Bauer, E. Abramof, P. H. O. Rappl and M. Bayer.
   *Phys. Rev. Lett. **103**, 057203 (2009)*

4. "*Optical second harmonic generation in the centrosymmetric magnetic semiconductors EuTe and EuSe*"
   B. Kaminski,M. Lafrentz, R. V. Pisarev, D. R. Yakovlev, V. V. Pavlov, V. Lukoshkin, A. B. Henriques, G. Springholz, G. Bauer, E. Abramof, P. H. O. Rappl and M. Bayer.
   Phys. Rev. B.
   Submitted to PRB (2010)

5. "*Third Harmonic Generation in EuTe and EuSe*"

   B. Kaminski,M. Lafrentz, R. V. Pisarev, D. R. Yakovlev, V. V. Pavlov, V. Lukoshkin, A. B. Henriques, G. Springholz, G. Bauer, E. Abramof, P. H. O. Rappl and M. Bayer.

   In preparation (2010)

6. "*Novel Mechanisms of Optical Harmonics Generation in Semiconductors*"

   R. V. Pisarev, **B. Kaminski**, M. Lafrentz, V. V. Pavlov, D.R.Yakovlev, and M. Bayer

   Phys. Stat. Sol. (c)- Proc. 26 conference in St. Petersburg

   (2009)

7. "*Magneto Stark Effect Induced SHG in ZnO*"

   B. Kaminski, M. Lafrentz, R.V. Pisarev, D.R. Yakovlev, V.V. Pavlov, et al.

   In preparation (2010)

8. "*Self-Organized Optical Anisotropies in CuCl:NaCl*"

   H. J. Weber , **B.Kaminski** and M.Lafrentz

   In preparation. (2010)

Symbols and abbreviations

symbol	meaning
$|0\rangle$	ground state
$|4fm\rangle$	state of EuX (one electron picture)
$5d$, $4f$, $6s$	Eu^{2+} sites in EuTe or EuSe (EuX
$5de_g$, $5dt_{2g}$	split $5d$ band in EuX
a_0	lattice constant
$a_{lattice}$	variable for lattice constant
$\hat{A}$	matrix for anisotropy simulation
AFM	antiferromagnetic
$\mathbf{A}$	vector potential
α	fine structure constant, $\alpha \simeq 1/137$
α_1	constant giving admixture of S/P-excitons
α_2	constant giving admixture of S/P-excitons
α	angle in experimental geometry
a_B	Bohr radius
a_B^{exc}	exitonic Bohr radius
α, $\alpha(\omega)$	absorption coefficient
b_0	lattice constant
B	magnetic field
B_{int}	internal magnetic field
B_{sat}	saturation magnetic field
$\mathbf{B}$	magnetic induction
B$_J$(y)	Brillouin function
BaF$_2$	barium fluoride
BBO	β-BaB$_2$O$_4$
c	speed of light in vacuum (299 792 458 m s^{-1})
c_0	Lattice constant
$\mathbf{c}$	c-axis of the wurtzite structure
C	Curie constant
C$_{6v}$	Symmetry of wurtzite structure
C^{JM}	Clebsch-Gordan coefficients

CB	conduction band
CCD	charge-coupled device camera
CED	crystallographic electric dipole
CdTe	cadmium telluride
$Cd_{1-x}Mn_xTe$	cadmium manganese telluride
CMD	crystallographic magnetic dipole
Cr_2O_3	chromium oxide
Cu^{2+}	copper ions
CuB_2O_4	copper borate
d	label for d electrons
$D_i^{\pm}$	symmetry of bands in spherical presentation for $6mm$
DMS	diluted magnetic semiconductors
δ_{ij}	Dirac's delta function
ΔE	energy difference
$D(E)$	density of states
$\Delta E_{A,B}$	Energy shift of A and B excitons series due to Stark effect
ΔE_Z	Zeeman splitting
DFG	difference frequency generation
e	electron, unit charge ($1.602176 \cdot 10^{-19}$ C)
E, E_{ex}	energy, exchange energy
E_F	Fermi level
E_G	band gap energy
$E(\mathbf{k}), E_{e,h}(\mathbf{k})$	dispersion, of the conduction/valence band
$\mathbf{E}$	electric field vector
E_i	i-th electric light field
ED	electric dipole
EQ	electric quadrupole
EuTe	europium telluride
EuSe	europium selenite
EuX	europium chalcogenides
eV	electron volt ($1.602176 \cdot 10^{-19}$ J)
$\hat{\varepsilon}, \varepsilon_r, \varepsilon_0$	dielectric tensor, dielectric constant, in vacuum
$\bar{\varepsilon}$	averaged dielectric constant
fcc	face-centered cubic
$f(E)$	Fermi-Dirac distribution
F	free energy
F_i	oscillator strength of the i-th exciton
f_n	oscillator strength of S-excitons
$F_{JM}X$	state of EuX (seven electron picture)
FM	ferromagnetic
FiM	ferrimagnetic
$|f\rangle$	final state

FWHM	full width at half maximum
ϕ_{nlm}	eigenfunctions of the hydrogen atom
g_e	electron g factor
g_h	hole g factor
g_{env}	envelope g factor
$|g\rangle$	ground state
g_J	Landè factor
G	free enthalpy
GaAs	gallium arsenide
Γ_i	symmetry of valence-, conduction bands, excitons and optical processes
Γ-point	point of high symmetry
$\overline{\gamma}$	anisotropy factor
h	hole
h	Miller index
$\hat{H}$	Hamiltonian
$\hat{H}_{cf}$	Hamiltonian of interaction with the crystal field
$\hat{H}_{dia}$	Hamiltonian of diamagnetic interaction
$\hat{H}_e$	Hamiltonian of free electrons
$\hat{H}_{exchange}$	Hamiltonian of Heisenberg exchange interaction
$\hat{H}_{field}$	Hamiltonian of electro-magnetic field energy
$\hat{H}_{int}$	Interaction hamiltonian
$\hat{H}_{so}$	Hamiltonian of spin orbit interaction
$\hat{H}_{spin}$	Hamiltonian of spin dependent part
$\hat{H}_{st}$	Hamiltonian of the Stark effect
$H_{N_e}(y)$	Hermite polynomials
$\mathbf{H}$	magnetic field strength
H_C	coercive field strength
HeNe	helium-neon laser
$\hbar$	$h/2\pi = 1.054571 \cdot 10^{-34}$ J s$= 6.582118 \cdot 10^{-16}$ eV s
i	integer index $i = 0, 1, 2 \ldots$
i	complex unity
i	Miller index
$|i\rangle$	intermediate state
I	light intensity
$\hat{I}$	inversion operator
IED	induced electric dipole
IMD	induced magnetic dipole
j	integer index $j = 0, 1, 2 \ldots$
$\mathbf{j}$	electric current
$\mathbf{J}$	total angular momentum

J_z	z-component of the angular momentum
J_{ij}	exchange integral
J_1, J_2	ferromagnetic, antiferromagnetic exchange integral
$J_0(r_0)$	exchange integral under normal pressure
k_B	Boltzmann constant $1.38062 \cdot 10^{-23} J/K$
$\mathbf{k}$	wave vector
k	Miller index
$\Delta \mathbf{k}$	wave vector mismatch
K	Kelvin
KD*P	KH_2PO_4
L	Length
L_c	coherence length
l	Miller index
$\mathbf{l}$	antiferromagnetic order parameter
$\mathbf{L}$	orbital angular momentum
L_z	z-component of the orbital momentum
LO, LA	longitudinal optical, longitudinal acoustic
λ	wavelength
λ_{4f}	Landè spin-orbit constant
m	z-component of the angular momentum
m_e	electron mass ($9.109381 \cdot 10^{-31}$ kg)
m^*	effective mass
m_e^*, m_h^*, m_X^*	effective electron/hole/exciton mass
$\mathbf{M}$	magnetization, magnetic dipole moment
M_S	saturated magnetization
Mn^{2+}	manganese ions
MD	magnetic dipole
MFISH	magnetic-field-induced second harmonic generation
MSHG	magnetic second harmonic generation
meV	milli electron volt
mJ	milli joule
μm	micrometer
μ	magnetic moment
μ	reduced mass
μ_r, μ_0	permeability, in vacuum
$\overline{\mu}$	averaged effective mass
μ_S	magnetic moment
μ_B	Bohr magneton
$\mu(T)$	chemical potential
n	refractive index
N	Number of electrons or other atoms

NNN	next nearest neighbors
NN	nearest neighbors
Nd:YAG	yttrium aluminium garnet doped with neodymium
Ni^{2+}	nickel ions
NiO	nickel oxide
nm	nanometer
OPO	optical parametric oscillator
O_h	symmetry of EuX
p	label for p (band) electrons
P	label for P excitons
$\mathbf{P}$	polarization, electric dipole moment
$\mathbf{p}$	impulse operator
PL	photoluminescence
Φ	Wannier-wavefunction
ps	picosecond
Ψ	wavefunction
φ	angle in experimental geometry
$|\varphi_{exc}\rangle$	exciton wavefunction
$\hat{Q}$	electric quadrupole moment
R	resistivity, reflectivity
$\hat{R}$	rotation matrix for anisotropy simulation
r, r_0	interatomic distance, at normal pressure
$\mathbf{r}, \mathbf{R}$	spatial position
Ry	Rydberg constant
Ry^*	Rydberg constant for excitons
ϱ	electric charge density
s	label for s (band) electrons
S	entropy
$\mathbf{S}$	spin
$< \mathbf{S} >$	averaged spin
S_z	z-component of the spin
S_i	spin of the i-th electron, ion or atom
SHG	second harmonic generation
SFG	sum frequency generation
$\sigma_\pm$	circular polarization
$\sigma_{x,y,z}$	Pauli-matrices
$\hat{\sigma}$	elements of the Laue group
$t(f,f), t(f,d)$	transfer integral

t	time
T	temperature, Tesla
T_0	effective temperature
T_C	Curie temperature
T_N	Neèl temperature
$\hat{T}$	transformation matrix for anisotropy simulation
ϑ	angle in experimental geometry
$\hat{T}$	time inversion operator
τ	relaxation time
$\mathbf{U}$	external electric field
U	energy difference
VB	valence band
ω	photon frequency
ω_c	cyclotron frequency
Ω	Ohm
x	manganese concentration
X	exciton
χ_{para}, χ_{dia}, χ_{mag}	para/dia/magnetic susceptibility
$\chi_{N_e}(\tilde{x})$	eigenfunctions of the harmonic oscillator
$\chi_{ijk..}$	nonlinear optical susceptibilities
ZnO	zinc oxide

Bibliography

[1] Y. Shen, *The Principles of Nonlinear Optics* (Wiley, New York, 1984).

[2] R. Boyd, *Nonlinear Optics* (Academic, New York, 1992).

[3] M. Fiebig, V. V. Pavlov, & R. V. Pisarev, J. Opt. Soc. Am. B **22**, 96 (2005).

[4] T. F. . Heinz, C. K. Chen, D. Ricard, & Y. R. Shen, Phys. Rev. Lett. **48**, 472 (1982).

[5] P.-F. Brevet, *Surface Second Harmonic Generation* (Presses polytechniques et universitaires romandes, 1997).

[6] W. C. P. Guyot-Sionnest & Y. R. Shen, Phys. Rev. B **33**, 8254ff. (1986).

[7] A. Liebsch, Surf. Science **307**, 1007 (1994).

[8] J. Chen, S. Machida, & Y. Yamanoto, Opt. Lett. **23**, 676 (1998).

[9] K. Veenstra, A. Petukhov, A. de Boer, & T. Rasing, Phys. Rev. B **58**, R16020 (1998).

[10] A. Kirilyuk, J. Phys. D **35**, R189 (2002).

[11] J. Sipe, V. Mizrahi, & G. I. Stegeman, Phys. Rev. B **35**, 9091ff (1987).

[12] H. Hoshi, T. Yamada, K. Ishikawa, H. Takezoe, & A. Fukuda, J. Chem. Phys. **107**, 1687ff (997).

[13] B. Koopmans, A.-M. Janner, H. T. Jonkman, G. A. Sawatzky, & F. V. der Woude, Phys. Rev. Lett. **71**, 3569 (1993).

[14] D. Wilk, D. Johannsmann, C. Stanners, & Y. R. Shen, Phys. Rev. B **51**, 10057 (1995).

[15] T. Ishihara, K. Koshino, & H. Nakashima, Phys. Rev. Lett. **91**, 253901ff. (2003).

[16] M. V. Klein, C. Enkrich, M. Wegener, & S. Linden, Science **313**, 5786 (2006).

[17] A. Q. Jiang, J. F. Scott, H. Lu, & Z. Chen, J. Appl. Phys. **93**, 1180 (2003).

[18] M. Fiebig, D. Fröhlich, B. Krichevtsov, & R. Pisarev, Phys. Rev. Lett. **73**, 2127 (1994).

[19] R. W. Terhune, P. Maker, & C. M. Savage, Phys. Rev. Lett. **73**, 404 (1972).

[20] V. Pavlov, R. Pisarev, A. Kirilyuk, & T. Rasing **78**, 2004 (1997).

[21] V. Gridnev, V. Pavlov, R. Pisarev, A. Kirilyuk, & T. Rasing, Phys. Rev. B **63**, 4407 (2001).

[22] K. J. Choi, M. Begalski, Y. L. Li, & A. Sharan, Science **305**, 1005 (2004).

[23] J.Reif, J. C. Zink, C. M. Schneider, & J. Kirschner, Phys. Rev. Lett. **67**, 2878 (1991).

[24] A. Kirilyuk, J. Phys. D: Appl. Phys. **35**, R189 (2002).

[25] A. Kirilyuk & T. Rasing, J. Opt. Soc. Amer. B **22**, 148 (2007).

[26] M. Y. Shen, S. Koyama, M. Saito, T. Goto, & N. Kuroda, Phys. Rev. B. **53**, 477 (1996).

[27] H. P. Wagner & E. Al., Phys. Rev. B **58**, 10494 (1998).

[28] S. Bergfeld & W. Daum, Phys. Rev. Lett. **90**, 036801 (2001).

[29] K. L. Vodopyanov, G. M. H. Knippels, A. F. G. V. der Meer, J. P. Maffetone, & I. Zwieback, Optics Commun. **202**, 205 (2002).

[30] K. L. Vodopyanov, F. Ganikhanov, J. P. Maffetone, I. Zwieback, & W. Ruderman, Optics Lett. **25**, 841 (2000).

[31] G. A. Medvedkin & V. G. Voevodin, J. Opt. Soc. Amer. B **22**, 1884 (2005).

[32] A. Godard, Comp. Rendue Phys. **8**, 1100 (2007).

[33] V. V. Pavlov, A. M. Kalashnikova, R. V. Pisarev, I. Sänger, D. R. Yakovlev, & M. Bayer, J. Opt. Soc. Am. B **22**, 168 (2005).

[34] I. Sänger, B. Kaminski, D. Yakovlev, R. Pisarev, M. Bayer, G. Karczewski, T. Wojtowicz, & J. K. J, Phys. Rev. B **74**, 235217.

[35] I. Sänger, D. R. Yakovlev, M. Bayer, V. V. Pavlov, R. V. Pisarev, G. K. an T. Wojtowicz, & J. Kossut, Phys. Rev. Lett. **96**, 117211 (2006).

[36] I. Sänger, B. Kaminski, D. R. Yakovlev, M. Bayer, V. V. Pavlov, & R. V. Pisarev, Phys. Rev. B (2006).

[37] V. V. Pavlov, A. M. Kalashnikova, R. V. Pisarev, I. Sänger, D. R. Yakovlev, & M. Bayer, Phys. Rev. Lett. **94**, 157404 (2005).

[38] V. Venkataramanan, K. Noguchi, M. Aono, & T. Suzuki, Appl. Phys. B **74**, 683 (2002).

[39] B. Kaminski, M. Lafrentz, R. V. Pisarev, D. R. Yakovlev, V. V. Pavlov, V. Lukoshkin, A. B. Henriques, G. Springholz, G. Bauer, E. Abramof, P. H. O. Rappl, & M. Bayer, Phys. Rev. Lett. **103**, 057203 (2009).

[40] C. Kittel, *Introduction to Solid State Physics* (Wiley, New York, 2005).

[41] W. Nolting, *Grundkurs theoretische Physik*, vol. 6 — Statistische Physik (Vieweg, Braunschweig / Wiesbaden, 1997).

[42] G. Czycholl, *Theoretische Festkörperphysik* (Springer, Heidelberg, 2004), 2nd edn.

[43] L. Landau & E. Lifschitz, *Lehrbuch der theoretischen Physik*, vol. V — Statistische Physik (Akademie, Berlin, 1970).

[44] M. Bellae, *Quantum and Statistical Field Theory* (Oxford Science Publications, London, 1991).

[45] K. Huang, *Statistical Mechanics* (Wiley, Singapore, 1987), 2. edn.

[46] L. Rosenfeld, *Theory of Electrons* (Interscience, New York, 1951).

[47] S. Krupicka & J. Sternberk, *Elements of Theoretical Magnetism* (CRC Press, Cleveland, Ohio, 1968).

[48] J. Smart, *Effective Field Theories of Magnetism* (W.B. Saunders, 1966).

[49] P. Weiss, J. Physique Rad. **6**, 661 (1907).

[50] W. Heisenberg, Z. Physik **49**, 619 (1928).

[51] S. Blundell, *Magnetism in Condensed Matter* (Oxford University Press, USA, 2001).

[52] H. D. Young, *University Physics* (Addison-Wesley, 1992), 8th edn.

[53] L. Néel, Ann. Phys. Paris **18**, 5 (1932).

[54] H. Bizette, C. Squire, & B. Tsai, Comptes Rendus Acad. Sci. Paris **207**, 449 (1938).

[55] I. Dzyaloshinskii, Sov. Phys. JETP **5**, 6 (1957).

[56] L. Néel, Ann. de Phys. **4**, 249 (1949).

[57] Y. Y. Li, Phys. Rev. **101**, 1450 (1956).

[58] S. Foner, Phys. Rev. **130**, 183 (1963).

[59] A. V. Kimel, A. Kirilyuk, A. Tsvetkov, R. V. Pisarev, & T. Rasing, Nature **429**, 850 (2004).

[60] M. Fiebig, N. P. Duong, T. Satoh, B. B. V. Aken, K. Miyano, Y. Tomioka, & Y. Tokura, J. Phys. D: Appl. Phys. **41**, 164005 (2008).

[61] A. Cracknell, *Magnetism in Crystalline Materials* (Pergamon, Oxford, 1975).

[62] L. Néel, Proceedings of International Conference in Theoretical Physics Kyoto (Science Council of Japan, Tokyo, 1953).

[63] H. Barkhausen, Z. Physik **20**, 401 (1919).

[64] K. Honda & S. Saya, Sci. Rept. Tohoku Imp. Univ. (1926).

[65] G. Slack, J. Appl. Phys. **31**, 1571 (1960).

[66] W. Roth, J. Appl. Phys. **31**, 2000 (1960).

[67] L. Landau & E. Lifschitz, *Lehrbuch der theoretischen Physik*, vol. VIII — Elektrodynamik der Kontinua (Akademie, Berlin, 1970).

[68] A. Hubert & R. Schäfer, *Magnetic Domains* (Springer, Berlin, 2000).

[69] B. Kaminski, Zweiphotonenspektroskopie an Halbleitern, Diploma Thesis, Universität Dortmund (2006).

[70] M. Fiebig, *Nichtlineare Spektroskopie und Topografie an antiferromagnetischen Domänen*, Ph.D. thesis, Universität Dortmund (1996).

[71] I. Sänger, *Magnetic - Field - Induced Second Harmonic Generation in Semiconductors and Insulators*, Ph.D. thesis, TU Dortmund (2006).

[72] G. Burns, *Introduction to Group Theory with Applications* (Academic, New York, 1977).

[73] T. Hahn, ed., *International Tables for X-Ray Crystallography, Vol. A: Space-Group Symmetry* (Reidel, Boston, 1987).

[74] J. Nye, *Physical Properties of Crystals* (Oxford University Press, London, 1969).

[75] A. Shubnikov & N. Belov, *Colored Symmetry* (Pergamon, Oxford, 1964).

[76] R. R. Birss, *Symmetry and Magnetism* (North-Holland, Amsterdam, 1966).

[77] G. Koster, J. Dimmock, J. Wheeler, & H. Statz, *Properties of the Thirty-Two Point Groups* (M.I.T. Press, Cambridge/Massachusetts, 1963).

[78] S. Joshua, *Symmetry Principles and Magnetic Symmetry in Solid State Physics* (Adam Hilger, New York, 1991).

[79] C. Klingshirn, M. Grundmann, A. Hoffmann, B. Meyer, & A. Waag, Physik Journal 33 (2006).

[80] S. State, Wurtzite polyhedra.png, Internet Wikipedia.

[81] J. Wrzesinski, *Zwei- und Dreiphotonenspektroskopie an Exziton-Polaritonen in ZnO unter Uniaxialem Druck*, Ph.D. thesis, Universität Dortmund (1997).

[82] K. Kopitzki, *Einführung in die Festkörperphysik* (Teubner, Stuttgart, 1993).

[83] C. Klingshirn, phys. stat. sol. (b) **244**, 3027 (2007).

[84] D. Bimberg, R. Blachnik, M. Cardona, P. J. Dean, T. Grave, G. Harbeke, K. Hübner, U. Kaufmann, W. Kress, O. Madelung, W. V. Münch, U. Rössler, J. Schneider, M. Schultz, & M. Solknick, *Landolt-Börnstein, Zahlenwerte und Funktionen Aus Naturwissenschaft und Technik, Neue Serie, Gruppe III und III-V Halbleiter,* (Springer Verlag, Berlin, Heidelberg, New York, 1982).

[85] J. Frenkel, Phys. Rev. **31**, 17 (1931).

[86] G. H. Wannier, Phys. Rev. **52**, 191 (1937).

[87] C. Schweitzer, *Nichtlineare Spektroskopie and Halbleitern mit Großer Bandlücke*, Ph.D. thesis, Universität Dortmund (2002).

[88] D. Thomas & J. Hopfield, Phys. Rev. **124**, 657 (1961).

[89] R. Wheeler & J. Dimmock, Phys. Rev. **125**, 1805 (1965).

[90] J. Miklosz & R. Wheeler, Phys. Rev. **153**, 913 (1967).

[91] M. Fiebig, D. Fröhlich, & C. Pahlke-Lerch, phys. stat. sol. (b) **177**, 187 (1993).

[92] F. Bassani, F. Ruggiero, & A. Quattropani, *Microscopic Quantum Theory of Exciton Polartions with Spatial Dispersion*, vol. 7D (Il Nuovo Cimento).

[93] J. Hopfield, Phys. Rev. **112** (1958).

[94] G. Blattner, *Der Einfluss Externer Magnetfelder Auf Die Freien und Gebundenen Exzitonen in ZnO*, Ph.D. thesis, Universität Karlsruhe (1982).

[95] W. Nieswand, *Nichtlineare Spektroskopie an Polaritonen in CuCl unter Dem Einfluss Äusserer Störungen*, Master's thesis, University Dortmund (1994).

[96] Pahlke-Lerch, *Experimentelle Untersuchungen Zu Den Maxwellschen Randbedingungen in der Nichtlinearen Spektroskopie*, Ph.D. thesis, University Dortmund (1993).

[97] F.Bassani & L. Andreani, *Exciton-Polartion States in Insulators and Semiconductors* (XCVI Corso, 1987).

[98] P. Köhler, *Nichtlineare Optik an Exzitonen-Polaritonen-Systemen*, Ph.D. thesis, Universität Dortmund (1991).

[99] C. F. Klingshirn, *Semiconductor Optics* (Springer-Verlag, Berlin, Germany, 1995).

[100] W. Schäfer & M. Wegener, *Semiconductor Optics and Transport Phenomena* (Springer-Verlag, Berlin, 2002).

[101] G. Landwehr & E. I. Rashba, *Landau Level Spectroscopy* (Elsevier Science, Amsterdam, 1991).

[102] W.Nolting, *Grundkurs: Theoretische Physik - Quantenmechanik, Teil2*, vol. 5 (Verlag Zimmermann Neufang, Ulmen, 1993).

[103] H.Haken, Fortschritte der Physik **6**, 271 (1958).

[104] S. Gasiorowicz, *Quantenmechanik* (Oldenbourg, München, 2005).

[105] W. Söllinger, W. Heiss, R. T. Lechner, K. Rumpf, P. Granitzer, H. Krenn, & G. Springholz, cond-mat **arXiv:0907.3836v1**.

[106] Landolt-Börnstein, *Numerical Data and Functional Relationships, New Series, Group III, Vol.* **41b** (Springer-Verlag, Berlin, 1999).

[107] A. Henriques, E. Abramof, & P. H. O. Rappl, submitted to PRB (2009).

[108] W. Reim & J. Schoenes, *Ferromagnetic Materials*, vol. 5 (1990).

[109] P. Wachter, *Handbook on the Physics and Chemistry of Rare Earths*, vol. 11 (K. A. Gschneider and L.R. Eyring, North Holland , Amsterdam, 1979).

[110] R. Lechner & Et.Al., Phys. Rev. Lett. **94**, 157201 (2005).

[111] W. Zinn, Journal of Magnetism and Magnetic Materials **3**, 23 (1976).

[112] A. Mauger, phys. stat. sol. b **84**, 761 (1977).

[113] T. Kasuya, Critical Reviews in Solid State and Materials Sciences **3**, 131 (1972).

[114] T. Kasuya, IBM J. Res. Developm. **14**, 214 (1970).

[115] G. Methfessel, Z. Angew. Phys. **18**, 414 (1965).

[116] J. B. Goodenough, *Magnetism and Chemical Bond* (Interscience Wiley, New York, 1963).

[117] D. Bloch, J. Phys. Chem. Solids **27**, 881 (1966).

[118] L.K.Hanamoto, A.B.Henriques, N. Jr., P.Rappl, E.Abramof, & Y.Ueta, J. Phys. Condens. Matter **16**, 5597 (2004).

[119] J. Schoenes & P. Wachter, IEEE Trans. Magnetics MAG **12**, 81 (1976).

[120] A. B. Henriques & E. al, Phys. Rev. B **72**, 155337 (2005).

[121] A. B. Henriques, M. A. Manfrini, P. H. O. Rappl, & E. Abramof, Phys. Rev. B **77**, 035304 (2008).

[122] R. Kirchschlager, W. Heiss, R. T. Lechner, G. Bauer, & G. Springholz, Appl. Phys. Lett. **85**, 67 (2004).

[123] W.Heiss, G.Prechtl, & G.Springholz, Phys. Rev. B **63**, 165323 (2001).

[124] P. G. Steeneken, L. H. Tjeng, I. Elfimov, G. A. Sawatzky, G. Ghiringhelli, N. B. Brookes, & D.-J. Huang, Phys. Rev. Lett. **88**, 47201 (2002).

[125] T. S. Santos & J. S. Moodera, Phys. Rev. B **69**, 241302 (2004).

[126] T. S. Santos, J. S. Moodera, K. V. Raman, E. Negusse, J. Holroyd, J. Dvorak, M. Liberati, Y. U. Idzerda, & E. Arenholz, Phys. Rev. Lett. **101**, 147201 (2008).

[127] G.-X.Miao, M.Müller, & J.S.Moodera, Phys. Rev. Lett. **102**, 076601.

[128] G. Springholz & et al, Appl. Phys. Lett. **79**, 1225 (2001).

[129] J. S. Moodera, X. Hao, G. A. Gibson, & R. Meservey, Phys. Rev. Lett. **61**, 637 (1988).

[130] X. Hao, J. S. Moodera, & R. Meservey, Phys. Rev. B **42**, 8235 (1990).

[131] A. T. Filip, P. LeClair, C. J. P. Smits, J. T. Kohlhepp, H. J. M. Swagten, B. Koopmans, & W. J. M. de Jonge, Appl. Phys. Lett. **81**, 1815 (2002).

[132] P. LeClair, J. K. Ha, H. J. M. Swagten, J. T. Kohlhepp, C. H. V. de Vin, & W. J. M. de Jonge, Appl. Phys. Lett. **80**, 625 (2002).

[133] C. J. P. Smits, A. T. Filip, J. T. Kohlhepp, H. J. M. Swagten, B. Koopmans, & W. J. M. de Jonge, J. Appl. Phys. **95**, 7405 (2005).

[134] J. Trbovic, C. Ren, P. Xiong, & S. V. Molnar, Appl. Phys. Lett. **87**, 082101 (2005).

[135] C. Ren, J. Trbovic, R. L. Kallaher, J. G. Braden, J. S. Parker, S. V. Molnar, & P. Xiong, Phys. Rev. B **75**, 205208 (2007).

[136] J. S. Moodera, R. Meservey, & X. Hao, Pyhs. Rev. Lett. **70**, 853 (1993).

[137] D. D. Awschalom, D. Loss, & N. Samarth, *Semiconductor Spintronics and Quantum Computation* (Springer-Verlag, Berlin, 2002).

[138] D. Bouwmeester, A. Ekert, & A. Zeilinger, *The Physics of Quantum Information* (Springer-Verlag, Berlin, 2000).

[139] G. Busch, J. Schoenes, & P. Wachter, Solid State Commun. **8**, 1841 (1970).

[140] J. Schoenes & P. Wachter, Physica B+C **86-88** (1977).

[141] M. Suekane, G. Kido, N. Miura, & S. Chikazumi, J. Magn. Mater. **31-34**, 589 (1983).

[142] H. Hori, R. Akimoto, M. Kobayashi, S. Miyamoto, M. Fu-Rusawa, N. Kreines, A. Yamagishi, & M. Date, Physica B **201**, 438 (1994).

[143] M. R. Koblischka & R. J. Wijngaarden, Supercond. Sci. Technol. **8**, 199 (1995).

[144] J. Lettieri, V. Vaithyanathan, S. K. Eah, J. Stephens, V. Sih, D. D. Awschalom, J. Levy, & D. G. Schlom, Appl. Phys. Lett. **83**, 975 (2003).

[145] A. Schmehl, V. Vaithyanathan, A. Herrnberger, S. Thiel, C. Richter, M. Liberati, T. Heeg, M. Rockerath, L. F. Kourkoutis, & S. Muhlbauer, Nature Mat. **6**, 882 (2007).

[146] M. Göppert-Maier, *Über Elementarakte mit Zwei Quantensprüngen*, Ph.D. thesis, Universität Göttingen (1931).

[147] J. Armstrong, N. Bloembergen, J. Ducuing, & P. Pershan, Phys. Rev. **127**, 1918 (1962).

[148] T. Maiman, Nature **187**, 493 (1960).

[149] A. Schawlow & C. Townes, Phys. Rev. **112**, 1940 (1958).

[150] P. Franken, A. Hill, C. Peters, & G. Weinreich, Phys. Rev. Lett. **7**, 118 (1961).

[151] N. Bloemberg, *Nonlinear Optics* (Benjamin, New York, 1965).

[152] *Proceedings of the International School of Physics ENRICO FERMI Course LXIV*.

[153] J. D. Jackson, *Classical Electrodynamics* (John Wiley and Sons, New York, 1975).

[154] P. S. Pershan, Phys. Rev. **130**, 919 (1963).

[155] L. Landau & E. Lifschitz, *Lehrbuch der theoretischen Physik*, vol. I — Mechanik (Akademie, Berlin, 1970).

[156] R. Loudon, *The Quantum Theory of Light* (Clarendon, Oxford, 1983).

[157] E. Matthias & F. Träger, Proceedings of the Topical Conference: Nonlinear Optics at Interfaces (NOPTI 1998), Appl. Phys. B **68** (1999).

[158] F. Träger, Proceedings of the Topical Conference: Nonlinear Optics at Interfaces (NOPTI 2001), Appl. Phys. B **74** (2002).

[159] K. Bennemann, *Nonlinear Optics in Metals* (Clarendon, Oxford, 1998).

[160] B. D. Bartolo, *Nonlinear Spectroscopy of Solids: Advances and Applications* (Plenum, New York, 1994).

[161] Y. Uesu, S. Kurimura, & Y. Yamamoto, Appl. Phys. Lett. **66**, 2165 (1995).

[162] P. Maker, R. Terhune, M. Nisenhoff, & C. Savage, Phys. Rev. Lett. **8**, 21 (1962).

[163] M. Fiebig, D. Fröhlich, T. Lottermoser, V. V. Pavlov, R. V. Pisarev, & H.-J. Weber, Phys. Rev. Lett. **87**, 137202 (2001).

[164] H.-J. Thiele, *Nichtlineare optische Untersuchungen magnetischer Phasen von Cr_2O_3 und α-Fe_2O_3*, Master's thesis, Universität Dortmund (1995).

[165] J. K. Furdyna & J. Kossut, *Semiconductors and Semimetals* (Academic Press, Boston, 1998).

[166] D. R. Yakovlev, *Habilitation: Exciton Magnetic Polarons in Diluted Magnetic Semiconductor Heterostructures (in Russian)* (A. F. Ioffe Physico-Technical Insitute, St.Petersburg, Russia, 1998).

[167] V. Muthukumar, R. Valentí, & C. Gros, Phys. Rev. Lett. **75**, 2766 (1995).

[168] Innolas, *Innolas Spitlight 600*, Innolas, Krailing (2007).

[169] GWU, *GWU Premiscan*.

[170] F. Kneubühl & M. Sigrist, *Laser* (Teubner, Stuttgart, 1995).

[171] A. Yariv, *Optical Waves in Crystals* (John Wiley and Sons, Inc., New York, 1984).

[172] A. Fix, *Untersuchung der spektralen Eigenschaften von optischen parametrischen Oszillatoren aus dem optisch nichtlinearen Material Betabariumborat*, Ph.D. thesis, Universität Kaiserslautern (1995).

[173] K. Kato, IEEE J. Quantum Electron. **22**, 1013 (1986).

[174] OxfordInstruments, *Manual Oxford*.

[175] JobynIvon, *HR460 Spectrometer*.

[176] JobynIvon, Specs gratings HR460, Homepage Jobyn Ivon.

[177] PIXIS, *Pixis CCD*.

[178] D. Fröhlich, International School of Atomics and Molecular Spectroscopy, Erice 1993 on: Nonlinear Spectroscopy of Solids: Advances and Applications Series B: Phys. **339**, 289 (Plenum Press, New York 1994), edited by B. di Bartolo, B. Bowlby.

[179] R. Pisarev, M. Fiebig, D. Fröhlich, S. Leute, & T. Lottermoser, Physica B **284–288**, 1404 (2000).

[180] R. Dinges, D. Fröhlich, B. Staginnus, & W. Staude, Phys. Rev. Lett. **25**, 922 (1970).

[181] J. Hopfield & D. Thomas, Physical Review **122**, 35 (1961).

[182] J. J. Hopfield & D. G. Thomas, Phys. Rev. **132**, 563 (1963).

[183] B. Gerlach, D. Richter, & J.Pollmann, Z. Phys. B - Condensed Matter **66**, 419 (1987).

[184] R.Dinges, *2-Photonabsorptionsmessungen an ZnO*, Master's thesis, Universität Frankfurt (1970).

[185] D.Fröhlich, private communications (2009).

[186] V. V. Pavlov, A. M. Kalashnikova, R. V. Pisarev, I. Sänger, D. R. Yakovlev, & M. Bayer, SPIE Proceedings, in press (2006).

[187] P. Pershan, Phys. Rev. **130**, 919 (1963).

[188] S. Bergfeld & W. Daum, Phys. Rev. Lett. **90**, 036801 (2003).

[189] M.-Z. Huang & W. Y. Ching, Phys. Rev. B **47**, 9464 (1993).

[190] H.-J. Weber, private communications (2008-2009).

[191] V. Pavlov, private communications (2008-2009).

[192] Pisarev, private communications (2006-2009).

[193] R. V. Pisarev, B. B. Krichevtsov, V. N. Gridnev, V. P. Klin, D. Fröhlicht, & Ch.Pahlke-Lerch, J. Phys.: Condens. Matter **5**, 8621 (1993).

[194] B. Kaminski, M. Lafrentz, R. V. Pisarev, D. R. Yakovlev, V. V. Pavlov, V. Lukoshkin, A. B. Henriques, G. Springholz, G. Bauer, E. Abramof, P. H. O. Rappl, & M. Bayer, Submitted to Phys. Rev. B (2010).

[195] A. Mauger & C. Godart, Phys. Rev. **141**, 51 (1986).

[196] D. A. Varshalovich, A. N. Moskalev, & V. K. Khersonskii, *Quantum Theory of Angular Momentum* (World Scientic, Singapore, 1988).

[197] A. B. Henriques, G. D. Galgano, B. Díaz, P. H. O. Rappl, & E. Abramof, J. Phys. Condens. Matter **19**, 406234 (2007).

[198] S. V. Popov, Y. P. Svirko, & N. I. Zheludev, *Susceptibility Tensors for Nonlinear Optics* (Institute of Physics Publishers, Philadelphia, 1995).

[199] E. Abramof & et al, Phys. Rev. B **78**, 134423 (2008).

[200] N. F. Oliveira, S. Foner, Y. Shapira, & T. B. Reed, Phys. Rev. B **5**, 2634 (1972).

[201] A. Pasquarello & A.Quattropani, Phys. Rev. B **43**, 3837 (1991).

[202] M. Fiebig, private communications (2008-2009).

[203] M. Gerbracht, *Optically Detected Resonances Induced by Far Infrared Radiation in Quantum Wells and Quantum Dots*, Ph.D. thesis, TU Dortmund (2008).

List of Figures

Index

Curriculum vitae

Personal details

Name: Benjamin Kaminski

Date of birth: 01.06.1981

Place of birth: Werl

Family status: unmarried

Education and qualifications

08.1987 - 07.1991 Basic primary school: Marien-Grundschule, Werl

09.1991 - 06.2000 Grammar school: Marien-Gymnasium, Werl

09.2000 - 07.2001 basic military service

10.2001 - 07.2006 Diploma course of studies: physics

Diploma thesis:

"Zweiphotonenspektroskopie an Halbleitern"

Supervisor: Priv.-Doz. Dr. D.R. Yakovlev

University of Dortmund

since 09.2006 Ph.D. student at the chair of Prof. Dr. M. Bayer

Topic of the presented Ph.D. thesis:

"New Mechanisms of Optical Harmonic Generation

  in Semiconductors"

Ph.D. thesis supervisor: Prof. Dr. D. R. Yakovlev

Dortmund Technical University

Acknowledgements